https://ntrs.nasa.gov/search.jsp?R=19790016917 2020-03-21T22:16:15+00:00Z

The Deep Space Network Progress Report 42-51

March and April 1979

(NASA-CR-158704) THE DEEP SPACE NETWORK Progress Reports, Mar. 1979 - Apr. 1979 (Jet Propulsion Lab.) 230 p HC A11/MF A01
CSCL 14B
G3/12
N79-25088
THRU
N79-25116
Unclas
26547

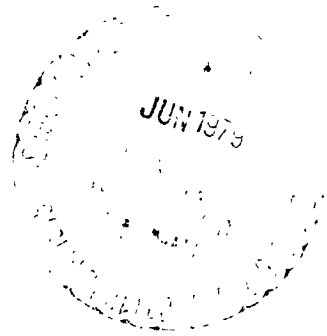

June 15, 1979

National Aeronautics and
Space Administration

Jet Propulsion Laboratory
California Institute of Technology
Pasadena, California

The Deep Space Network Progress Report 42-51

March and April 1979

June 15, 1979

National Aeronautics and
Space Administration

Jet Propulsion Laboratory
California Institute of Technology
Pasadena, California

Contents

DESCRIPTION OF THE DSN

MISSION SUPPORT

Ongoing Planetary/Interplanetary Flight Projects

SUPPORTING RESEARCH AND TECHNOLOGY

Tracking and Ground-Based Navigation

PRECEDING PAGE BLANK NOT FILMED

Communications—Spacecraft/Ground

Station Control and Operations Technology

Network Control and Data Processing

NETWORK AND FACILITY ENGINEERING AND IMPLEMENTATION

Deep Space Stations

OPERATIONS

Network Operations

N79-25089

Network Functions and Facilities

N. A. Renzetti
Office of Tracking and Data Acquisition

The objectives, functions, and organization of the Deep Space Network are summarized; deep space station, ground communication, and network operations control capabilities are described.

The Deep Space Network was established by the National Aeronautics and Space Administration (NASA) Office of Space Tracking and Data Systems and is under the system management and technical direction of the Jet Propulsion Laboratory (JPL). The network is designed for two-way communications with unmanned spacecraft traveling approximately 16,000 km (10,000 miles) from Earth to the farthest planets and to the edge of our solar system. It has provided tracking and data acquisition support for the following NASA deep space exploration projects: Ranger, Surveyor, Mariner Venus 1962, Mariner Mars 1964, Mariner Venus 1967, Mariner Mars 1969, Mariner Mars 1971, and Mariner Venus-Mercury 1973, for which JPL has been responsible for the project management, the development of the spacecraft, and the conduct of mission operations; Lunar Orbiter, for which the Langley Research Center carried out the project management, spacecraft development, and conduct of mission operations; Pioneer, for which Ames Research Center carried out the project management, spacecraft development, and conduct of mission operations; and Apollo, for which the Lyndon B. Johnson Space Center was the project center and the Deep Space Network supplemented the Manned Space Flight Network, which was managed by the Goddard Space Flight Center. The network is currently providing tracking and data acquisition support for Helios, a joint U.S./West German project; Viking, for which Langley Research Center provided the Lander spacecraft and project management until May, 1978, at which time project management and mission operations were transferred to JPL, and for which JPL provided the Orbiter spacecraft; Voyager, for which JPL provides project management, spacecraft development, and is conducting mission operations; and Pioneers, for which the Ames Research Center provides project management, spacecraft development, and conduct of mission operations. The network is adding new capability to meet the requirements of the Galileo mission to Jupiter, for which JPL is providing the Orbiter spacecraft, and the Ames Research Center the probe. In addition, JPL will carry out the project management and the conduct of mission operations.

The Deep Space Network (DSN) is one of two NASA networks. The other, the Spaceflight Tracking and Data Network (STDN), is under the system management and technical direction of the Goddard Space Flight Center (GSFC). Its function is to support manned and unmanned Earth-orbiting satellites. The Deep Space Network supports lunar, planetary, and interplanetary flight projects.

From its inception, NASA has had the objective of conducting scientific investigations throughout the solar system. It was recognized that in order to meet this objective, significant supporting research and advanced technology development must be conducted in order to provide deep space telecommunications for science data return in a cost effective

manner. Therefore, the Network is continually evolved to keep pace with the state of the art of telecommunications and data handling. It was also recognized early that close coordination would be needed between the requirements of the flight projects for data return and the capabilities needed in the Network. This close collaboration was effected by the appointment of a Tracking and Data Systems Manager as part of the flight project team from the initiation of the project to the end of the mission. By this process, requirements were identified early enough to provide funding and implementation in time for use by the flight project in its flight phase.

As of July 1972, NASA undertook a change in the interface between the Network and the flight projects. Prior to that time, since 1 January 1964, in addition to consisting of the Deep Space Stations and the Ground Communications Facility, the Network had also included the mission control and computing facilities and provided the equipment in the mission support areas for the conduct of mission operations. The latter facilities were housed in a building at JPL known as the Space Flight Operations Facility (SFOF). The interface change was to accommodate a hardware interface between the support of the network operations control functions and those of the mission control and computing functions. This resulted in the flight projects assuming the cognizance of the large general-purpose digital computers which were used for both network processing and mission data processing. They also assumed cognizance of all of the equipment in the flight operations facility for display and communications necessary for the conduct of mission operations. The Network then undertook the development of hardware and computer software necessary to do its network operations control and monitor functions in separate computers. A characteristic of the new interface is that the Network provides direct data flow to and from the stations; namely, metric data, science and engineering telemetry, and such network monitor data as are useful to the flight project. This is done via appropriate ground communication equipment to mission operations centers, wherever they may be.

The principal deliverables to the users of the Network are carried out by data system configurations as follows:

(1) The DSN Tracking System generates radio metric data, i.e., angles, one- and two-way doppler and range, and transmits raw data to Mission Control.

(2) The DSN Telemetry System receives, decodes, records, and retransmits engineering and scientific data generated in the spacecraft to Mission Control.

(3) The DSN Command System accepts spacecraft commands from Mission Control and transmits the commands via the Ground Communication Facility to a Deep Space Station. The commands are then radiated to the spacecraft in order to initiate spacecraft functions in flight.

(4) The DSN Radio Science System generates radio science data, i.e., the frequency and amplitude of spacecraft transmitted signals affected by passage through media such as the solar corona, planetary atmospheres, and plantetary rings, and transmits this data to Mission Control.

(5) The DSN Very Long Baseline Interferometry System generates time and frequency data to synchronize the clocks among the three Deep Space Communications complexes. It will generate universal time and polar motion and relative Deep Space Station locations as by-products of the primary data delivery function.

The data system configurations supporting testing, training, and network operations control functions are as follows:

(1) The DSN Monitor and Control System instruments, transmits, records, and displays those parameters of the DSN necessary to verify configuration and validate the Network. It provides the tools necessary for Network Operations personnel to control and monitor the Network and interface with flight project mission control personnel.

(2) The DSN Test and Training System generates and controls simulated data to support development, test, training and fault isolation within the DSN. It participates in mission simulation with flight projects.

The capabilities needed to carry out the above functions have evolved in the following technical areas:

(1) The Deep Space Stations, which are distributed around Earth and which, prior to 1964, formed part of the Deep Space Instrumentation Facility. The technology involved in equipping these stations is strongly related to the state of the art of telecommunications and flight-ground design considerations, and is almost completely multimission in character.

(2) The Ground Communications Facility provides the capability required for the transmission, reception, and monitoring of Earth-based, point-to-point communications between the stations and the Network Operations Control Center at JPL, Pasadena, and to the JPL Mission Operations Centers. Four communications disciplines are provided: teletype, voice, high-speed, and wideband. The Ground Communications Facility uses the capabilities provided by common carriers throughout the world, engineered into an integrated system by Goddard Space Flight Center, and controlled from the

communications Center located in the Space Flight Operations Facility (Building 230) at JPL.

The Network Operations Control Center is the functional entity for centralized operational control of the Network and interfaces with the users. It has two separable functional elements; namely, Network Operations Control and Network Data Processing. The functions of the Network Operations Control are:

(1) Control and coordination of Network support to meet commitments to Network users.

(2) Utilization of the Network data processing computing capability to generate all standards and limits required for Network operations.

(3) Utilization of Network data processing computing capability to analyze and validate the performance of all Network systems.

The personnel who carry out the above functions are located in the Space Flight Operations Facility, where mission operations functions are carried out by certain flight projects. Network personnel are directed by an Operations Control Chief. The functions of the Network Data Processing are

(1) Processing of data used by Network Operations Control for control and analysis of the Network.

(2) Display in the Network Operations Control Area of data processed in the Network Data Processing Area.

(3) Interface with communications circuits for input to and output from the Network Data Processing Area.

(4) Data logging and production of the intermediate data records.

The personnel who carry out these functions are located approximately 200 meters from the Space Flight Operations Facility. The equipment consists of minicomputers for real-time data system monitoring, two XDS Sigma 5s, display, magnetic tape recorders, and appropriate interface equipment with the ground data communications.

N79-25090

Voyager Support

J. E. Allen and H. E. Nance
Deep Space Network Operations Section

This is a continuation of the Deep Space Network report on tracking and data acquisition for Project Voyager. This report covers the Jupiter encounter period for Voyager 1, from 1 January through March 1979.

I. Voyager Operation – Status

Voyager 1 made its closest approach to Jupiter and its largest satellites on the morning of March 5, 1979, 18 months to the day after its launch. This event was preceded by the Observatory Phase, which started on 4 January 1979, and was followed by the Movie and Far Encounter Phases. The closest Encounter Phase was followed by the Post Encounter Phase that continued through March 1979. The entire period went well with the spacecraft performing in an excellent manner and the Deep Space Network (DSN) acquiring and processing the data without undue incidents.

II. DSN Operations

As the Encounter time approached, a modified configuration control/freeze was imposed on the supporting facilities to ensure that the encounter activities were supported with known hardware and software capabilities. This required that any known or newly discovered anomalies had acceptable work around procedures to ensure continued support. The control essentially was within three categories.

A. SFOF Physical Plant and Data Systems

Soft freeze from 0000Z 4 December 1978 through 2400Z 28 August 1979, except for the following hard freeze periods (0000Z first day through 2400Z last day):

12/12/78 through 12/14/78	Voyager 1 NET
1/29/79 through 3/14/79	Voyager 1 TCM 3, Movie, FE1, FE2, TCM 4, NE and PE1

B. DSN Facilities

Modified configuration control is in effect from 4 December 1978 through 30 September 1979. The Voyager NOPE defined, prior to 1 December 1978, modified configuration control to encompass level of support for encounter (OB through PE2), spacecraft maneuvers and tracking cycles, the Movie Phase, Far Encounter 2, Near Encounter, and Post-encounter 1 Phase, the Near Encounter Test, and the major scan platform calibration preceding each encounter. The definition of a normal DSN freeze was modified to accommodate regular alternating tracking between Voyager and Pioneer Venus.

C. Encounter Configuration

The Jupiter encounter phase for Voyager 1 began on 4 January 1979 and will continue through 9 April 1979. Supplemental procedures and configurations were required by the DSN to support the Jupiter encounter activity. Generally, only the telemetry configuration changed significantly while other subsystem configurations remained essentially the same as they were for the Cruise Phase.

Figure 1 shows the standard 64-m telemetry configuration which is 7.2 kb/s to 115.2 kb/s convolutionally encoded TLM on the X-band carrier with simultaneous 40 b/s uncoded TLM on the S-band carrier.

There were times when the Project configured the spacecraft for the same high rate encoded telemetry transmission via both RF carriers (360 kHz and 22.5 kHz). This was normally done when the Project wished to ensure full recovery of critical data. Figure 2 shows the S/X-band configuration that was used when the Project exercised its option to put the same telemetry rate on both carriers (S/X-band carriers). This configuration was also used when Voyager Project had important TLM data on the S-band carrier and the X-band carrier was not in use, or vice versa.

In order for the Project to optimize the telemetry return and to ensure that each experiment objective was met, there were frequent bit rate changes during the encounter period. To support this operation, the DSN was required to be cognizant of the changes and the supporting equipment configuration. To obtain maximum data it was necessary to determine whether the first bit of the new rate or the last bit of the old rate would result in maximum return. When a determination was made, the following procedure was used to support the decision.

Obtaining the First Bit of Data

(1) The station initialized for the new bit rate per the time in the SOE when the subcarrier frequency and modulation index remain the same as for the previous rate. The Subcarrier Demodulator Assembly (SDA) had to be in lock prior to stream initialization.

(2) When the SDA subcarrier or modulation index was changed simultaneously with data rate, it was impossible to get the first bit of data since there was a delay in acquiring SDA lock.

(3) Whenever the first bit of data was important, the station did not wait for TLM stream lock to put TLM data to line; instead, they put data to line at the same time that the TLM stream was first initialized.

Obtaining the Last Bit of Data

(1) The station did not initialize for the new bit rate until the telemetry stream dropped lock, or was requested to acquire the new bit rate by Network Operations Control (NOC).

(2) Even though the TLM stream was not initialized for the new TLM rate, there was always the danger that the Symbol Synchronizer Assembly (SSA) and Maximum Likelihood Convolutional Decoder (MCD) would false lock to the new rate. Therefore, the station and the Network Operations Control Team (NOCT) guarded against false locks in this mode of operation, although neither the NOCT Real-Time Monitor (RTM) or Test and Telemetry System (TTS) were able to obtain synchronization on the data if the station was false locked. The best solution found was to initialize for the correct bit rate immediately after losing lock on the present bit rate within the guidelines of the SOE.

1. Critical Periods. During the encounter phase, there were specific time periods when data collection was critical. These critical mission periods are defined in Table 1. However, the Project could and did declare as critical periods other than those listed below.

Analog recordings and redundant Telemetry Processor Assembly (TPA) DODRs were required during critical period support at the 64-m DSS's. The Project accepted the additional risks when a 34-m DSS (DSS 12) was used to support critical mission periods. When TLM data rates were above 44.8 kb/s, DSS 43 was not required to record redundant TPA DODRs, but analog recordings were required. During this time DSS 43 utilized the backup TPA for data replay as described below.

2. Data Replay Strategy. The primary concern during the encounter period was the timely receipt of the high rate telemetry and imaging data at JPL. Wide-band data lines were provided from all three of the 64-m stations. However, only the 230 kb/s capability from DSS 14 and the 168 kb/s capability from DSS 63 allowed transfer of the data rates above 44.8 kb/s in real-time. The 56 kb/s capability from DSS 43 required special consideration and strategy to provide the data in as near real-time as possible. To accomplish this requirement a special return procedure was instituted as follows:

3. Methods of Data Return from DSS 43. Two methods of telemetry return were employed; real-time and near real-time.

a. Real-Time Data Return. DSS 43 processed and returned in real-time (on the 56 kb/s WBDL) all high rate data with rates of 44.8 kb/s or lower.

PRECEDING PAGE BLANK-NOT FILMED

b. Near Real-Time Data. For data rates above 44.8 kb/s DSS 43 recorded real-time data on a DODR using one telemetry string and replayed the DODRs, using the second telemetry string, as soon as they were available. The data replays were done at the maximum line rate of the 56 kb/s wide-band data circuit. With the replays occurring at less than the real-time record rate a TLM return backlog existed until all DODRs had been replayed. Negotiations with other station users ensued to utilize their S/C track. All low rate data, 40 kb/s, were returned via the HSDL in real-time.

For DSS 43 passes containing data rates above 44.8 kb/s, but with no Optical Navigation (OPNAV) data, the replay strategy was:

(1) DSS 43 logged all HR data on DODR.

(2) As soon as the first DODR tape was completed, the station immediately started a replay of that tape over the 56 kb/s WBDL.

(3) When the first DODR tape replay was completed, the second tape was replayed and so forth until all data had been played in.

(4) DODR tapes were normally replayed in the same sequence as they were recorded.

(5) Some passes contained periods of HR data 44.8 kb/s or less between periods of higher rate data. During these periods, the station suspended replay, returned the high rate data in real-time and resumed replays when the WBDL was again available.

During some of the DSS 43 passes short periods of OPNAV data were contained in the high rate. It was a requirement of the Project Navigation Team that each period of this data be returned within a time not to exceed 4 hours after it was recorded on the spacecraft. To accommodate this requirement, the following replay strategy was used:

(1) Replay of the OPNAV data periods were specifically requested by the user. The requests were designated by data start and stop Earth received times.

(2) Due to the DODR replay backlog, the OPNAV replay requests in some cases required that DODRs be loaded for out of sequence replay. This was necessary to meet the OPNAV data return time requirement.

(3) In such cases the station completed the DODR tape replay already in process, mounted the tape containing the requested period, made the short replay and then resumed the normal replay sequence where it left off.

(4) During OPNAV replays, the data was processed by *Mission and Test Imaging System (MTIS) only.* TTS and Network Data Processing Terminal (NDPT) turned off the WB processors to prevent processing of non-sequential data.

During other specified periods requirement for near real-time DODR replay was for the latest data recorded. The station replayed the first completed DODR tape followed by the latest DODR tape to be completed, regardless of the order in which it was recorded. As each tape replay was finished, the next tape to be replayed was the most recent tape recorded. This out of order DODR replay continued until the end of the track at which time the skipped over tapes were replayed. The Project exercised the option of requesting the replay of any completed DODR tape during these periods of "Out of Order" replay. Such requests were made by the user through ACE to Operations Chief. The DSN honored these requests at the completion of the tape replay already in process and then resumed replay of the latest completed DODR.

c. DSS 43 Telemetry Back-up. During certain real-time data periods determined by the Project to require "hot back-up" TLM system with redundant DODR, the station configured both TLM strings for real-time data and suspended any data replays until the second TLM string was again available. For a data rate of 44.8 kb/s or less, the station was outputting data from the prime telemetry string, while at the same time recording a DODR on the back-up telemetry string. When the data rate was above 44.8 kb/s, the station recorded DODR on both TLM strings for subsequent replay.

When high rate data (real-time or replay) was not required from DSS 43 during the DSS 43/14 or DSS 43/63 overlaps the station was requested to halt the WB data output and record on DODR only.

d. Configuration – DSS 43. The telemetry configuration used by DSS 43 was dependent on two conditions of the downlink high rate data:

(1) HR TLM 44.8 kb/s or lower
For data rates of 44.8 kb/s or less, DSS 43 used the standard 64-m TLM configuration shown in Fig. 2.

(2) HR TLM above 44.8 kb/s
For data rates above 44.8 kb/s, DSS 43 used the record and replay configuration shown in Fig. 3.

III. Data Products

The Intermediate Data Record (IDR) is the primary data product provided to the Project by the DSN. Although telemetry data is provided in real-time or near real-time to the

PRECEDING PAGE BLANK NOT FILMED

Mission Control and Computing Center (MCCC) for the Project's use, the IDR is still required to provide the permanent record and gap filling of the data. In the case of radiometric data and tracking calibration data, the IDR is the only source of data to the Project. Monitor data is provided to the MCCC telemetry system (on the NOCC real-time monitor 5-8 data block) for inclusion with the telemetry data record. Command IDRs or fill tapes could be required by the Project to complete their system data record as required.

Stringent requirements are placed on all IDRs provided by the DSN. In the case of telemetry during cruise, the requirement is for 97.5% of the in-lock data blocks and during critical periods it is at least 99% of the in-lock data blocks. For radiometric data and tracking calibration data, the requirement is for the IDR to contain, at least 95% of the data required to be transmitted in real-time, by a DSS. As an indication of the impact of IDR production during this period, 367 telemetry IDRs were produced in January and 820 telemetry IDRs (with an additional 74 supplementary IDRs) in February. Even this later number increased in March during critical encounter activities. These IDRs were in addition to the optical navigation and radiometric data IDRs likewise produced.

IV. Occultation Data (Radio Science)

One Jupiter/Earth occultation was observed during the DSS 63 pass on 5 March 1979. To record this event, both closed loop and open loop receiver data and radiometric data were provided as the complete radio science package. New operational procedures were developed for the open loop receiver operation since the closed loop and radiometric data were already provided.

DSS 63 was provided with the radio science occultation subsystem during the later part of 1978. Testing and training were accomplished during January and February. Final preparation was completed just prior to the Jupiter encounter closest approach.

Figure 4 shows the Voyager occultation recording configuration. Figure 5 shows the Voyager open loop receiver configuration.

Prior to the Voyager mission, occultations were supported using an open-loop receiver with a fixed first local oscillator passing a bandwidth sufficient to encompass the event of interest, plus uncertainties, onto an analog recording. The analog recordings were shipped to JPL and digitized at CTA 21 and the resulting computer compatible tapes (CCT) were delivered to the experimenters. For Voyager, the total shift in frequency due to the Jupiter atmosphere was large and the existing system could not be used. A new subsystem was implemented; this new subsystem was called the DSS Radio Science Subsystem (DRS). This subsystem involved a computer-controlled programmable first local oscillator in the open-loop receiver that followed (using a series of linear ramps) the time-related frequency excursion of the expected signal of interest, thereby enabling the real-time bandwidth to be reduced to the point where real-time analog-to-digital conversion and production of a CCT recording was possible. This is the new system that was implemented at DSS 63, for the first Jupiter encounter.

In general terms, preparations for support of the occultation experiment began approximately two months prior to the event. The project experimenters supplied the DSN with the information necessary for the configuration and setup of the Occultation Data Assembly (ODA). The DSN then produced ODA predicts for the station supporting the pass. NAT Track transmitted the predict file to the DSS in advance of the pass to be supported and other occultation data information was datafaxed to the DSS prior to the encounter pass. The station supported the experiment, supplied pertinent information to the net controller, played back a portion of the recorded ODA CCT, duplicated the CCT and then shipped the tape to JPL. In addition to taking data using the Multimission Receiver (MMR)/ODA, the station used an Open Loop Receiver (OLR) (300 kHz output) and the Digital Recording Assembly (DRA) to record wide bandwidth data for backup purpose only. Upon special request these DRA recordings were shipped to CTA-21 where the bandwidth reduction equipment was used to produce a narrow bandwidth digital recording. The ODA CCTs shipped to JPL were delivered directly to the Project. The high speed portion of the recorded ODA data was processed by NDPT and an IDR provided to the Project, within 72 hours, for quick-look verification by spectrum analysis.

Operational and initialization instructions for the radio science subsystem were in the ODA Software Operations Manual (SOM) DMO-5123-OP and the operation procedures were documented in the Voyager Network Operations Plan 618-700, Rev. B. Special real-time messages were used to augment the operational and initialization instructions that were Voyager Project dependent. The open loop receiver Programmed Oscillator Control Assembly (POCA) predicts were generated at JPL and transmitted to the ODA, where the predicts were stored on disks. During Jupiter occultation, the predicts were used to drive the S/X-band open loop receiver POCA.

For the open loop recording, the DODR recording began prior to the start of Jupiter occultation. It was necessary to collect baseline data prior to and after occultation. The Project

Sequence of Events was the controlling document for the ODA recording on and off times. Open loop (S-band) backup recording was provided by the wide-band (300 kHz) OLR, and its DRA.

Voyager did not make use of the High Speed Data Line (HSDL) to get open loop ODA data to JPL, except for preliminary quick-look data, because the number of station hours required to replay data via HSDL was prohibitive. The prime method of getting data to JPL was to ship the open loop DODRs.

DODR recording for Voyager used six DODR tapes per hour, five DODRs per hour for the narrow-band MMR/ODA subsystem, and approximately one DODR per hour for the wide-band OLR/DRA subsystem. The DSS collecting the open loop data was required to ensure that adequate personnel were on board to handle the open loop recording task. Technical assistance was sent from JPL to DSS 63 to support the occultation period.

New or once used digital tape, at least 2300 feet in length for ODA and 12,500 feet in length for DRA, were required to be used for recording open loop data, to ensure optimum data return. DSS 63 required about 30 good digital tapes (24 for narrow-band recording, and 6 for wide-band recording) to meet this requirement.

Station personnel used the Spectral Signal Indicator (SSI) to verify that occultation data was actually being recorded onto the DODR. The SSI provided recording status for both the narrow-band and the wide-band recording subsystems. The narrow-band was used for the prime data and required more monitoring by the DSS operator than the wide-band subsystems. The Voyager Project planned to use the narrow-band data only, but in the event that the narrow-band data was not available, then CTA-21 would be requested to provide wide-band IDRs. The DSS was required to report signal status to the NOC at least every 15 minutes and more often when the signal disappeared or was marginal.

Table 1. Critical mission periods

Critical period	Duration	Remarks
1. Trajectory correction maneuvers	M-10h to M+3h	
2. Science calibrations (every 1/2 AU for each spacecraft)	24 hours	
3. Imaging movie	4 days each S/C for each planet	
4. Planetary closest approach	E-10d to E+1d	E-2d to E+2d for analog ODR retention requirement
5. Spacecraft emergencies	When declared for as long as declared	
6. Targets of opportunity (specified at least one month in advance)	No longer than 4 days	

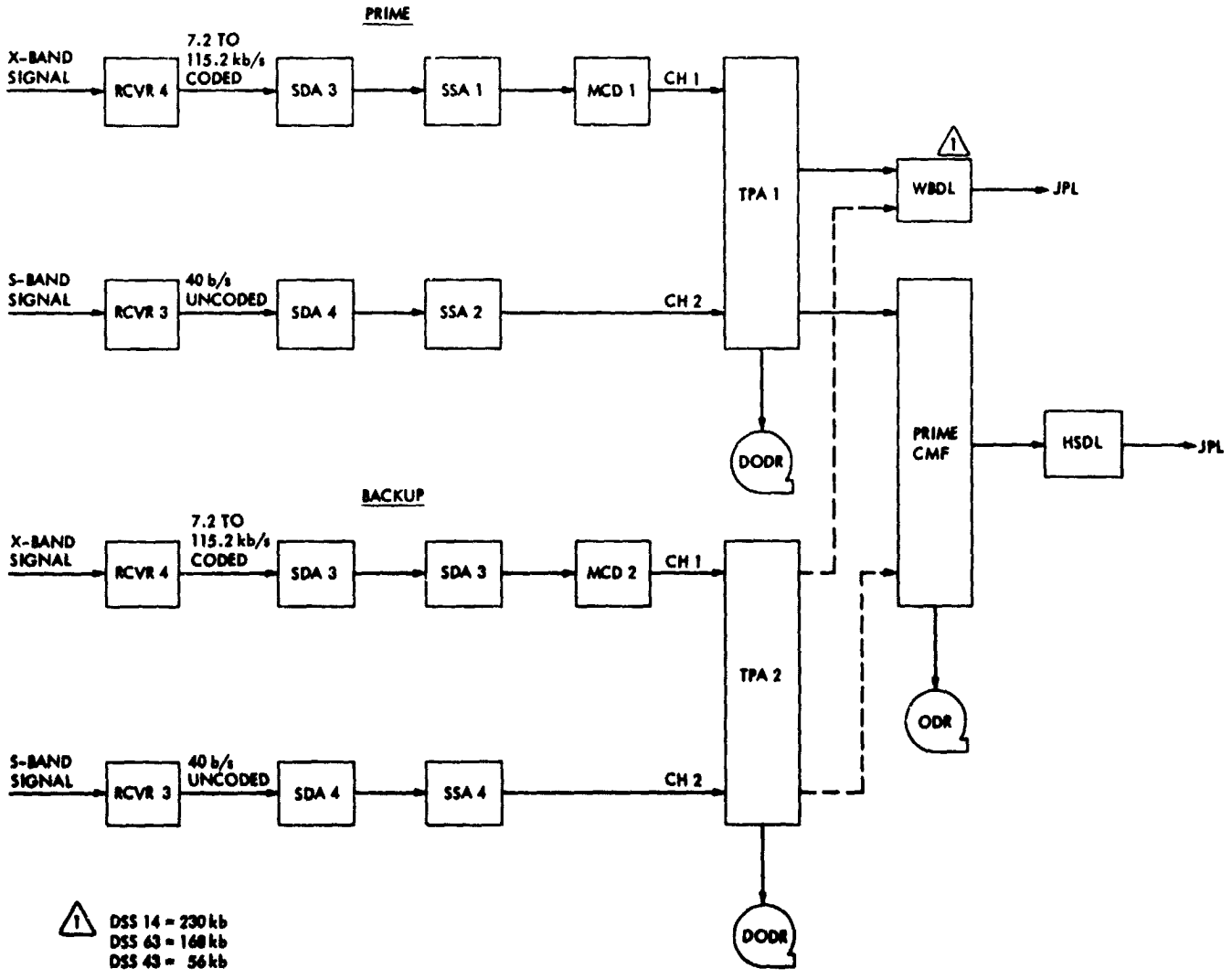

Fig. 1. 64-m standard telemetry configuration

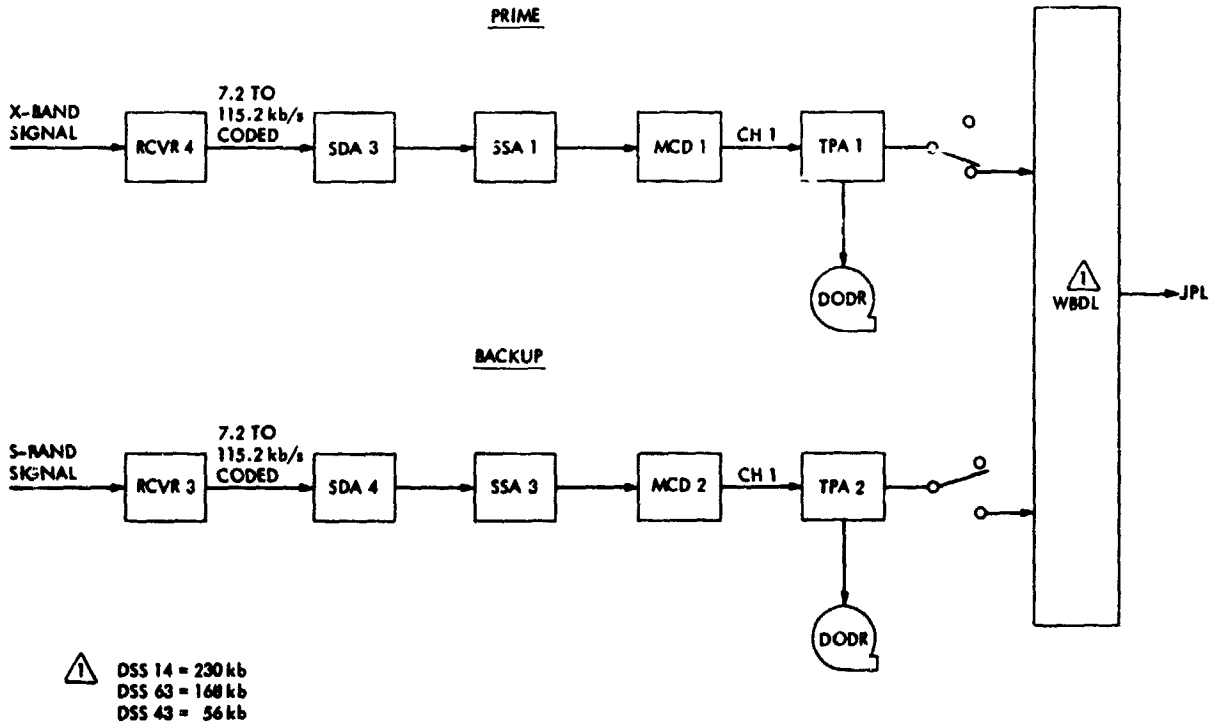

Fig. 2. 64-m S/X-band configuration (7.2 kb/s to 115.2 kb/s)

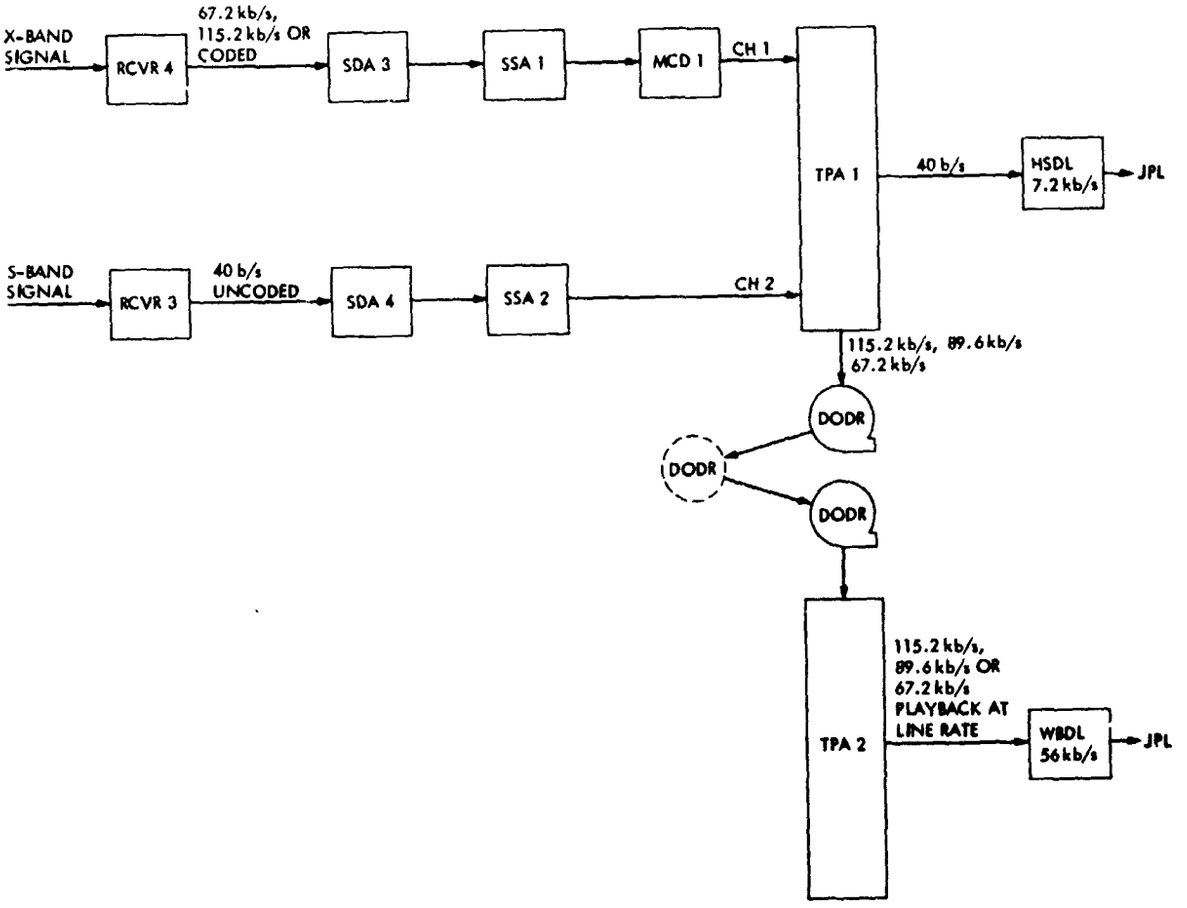

Fig. 3. 64-m recording and replay configuration (115.2 kb/s, 89.6 kb/s, or 67.2 kb/s)

ORIGINAL PAGE IS
OF POOR QUALITY

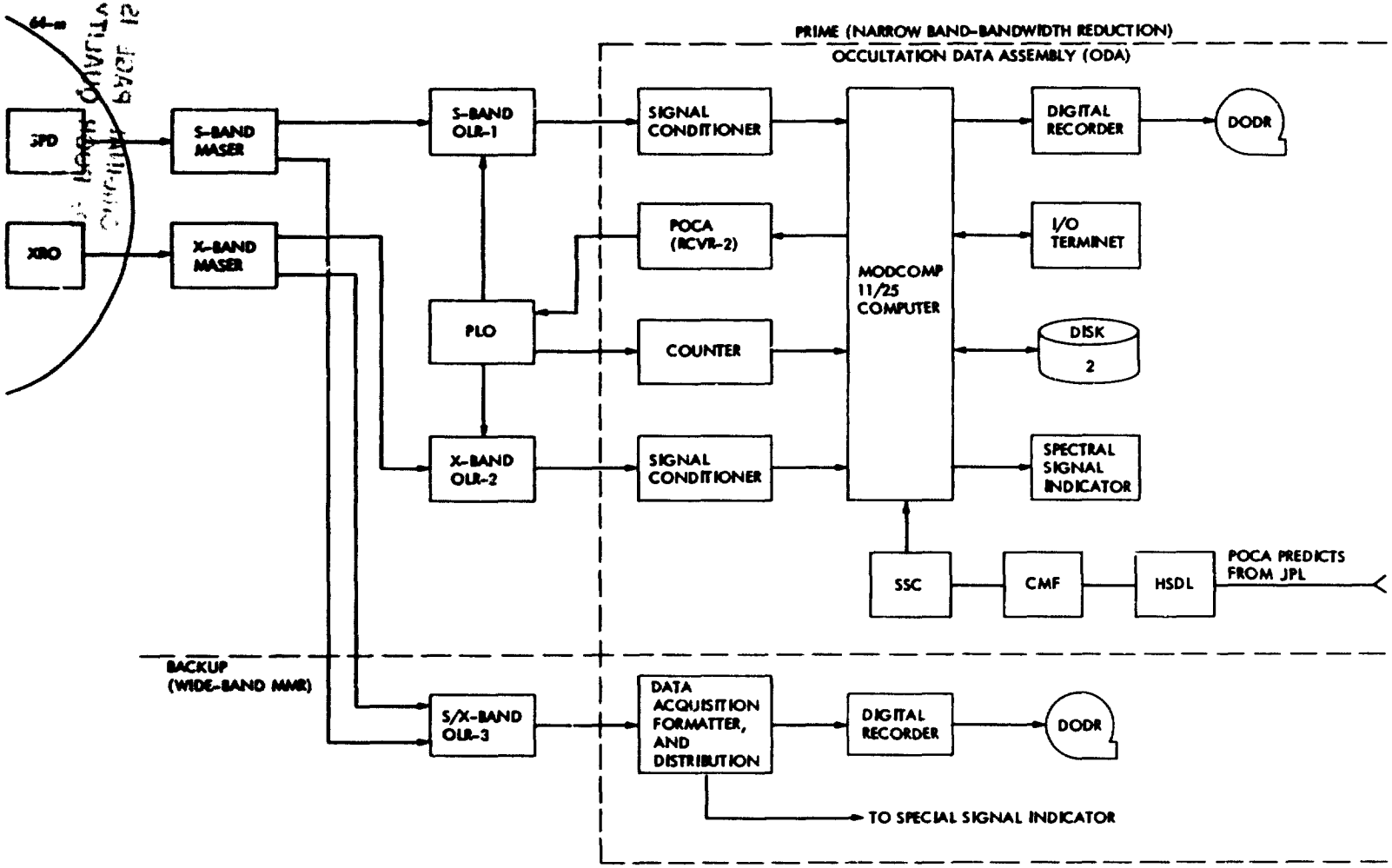

Fig. 4. 64-m open loop recording configuration

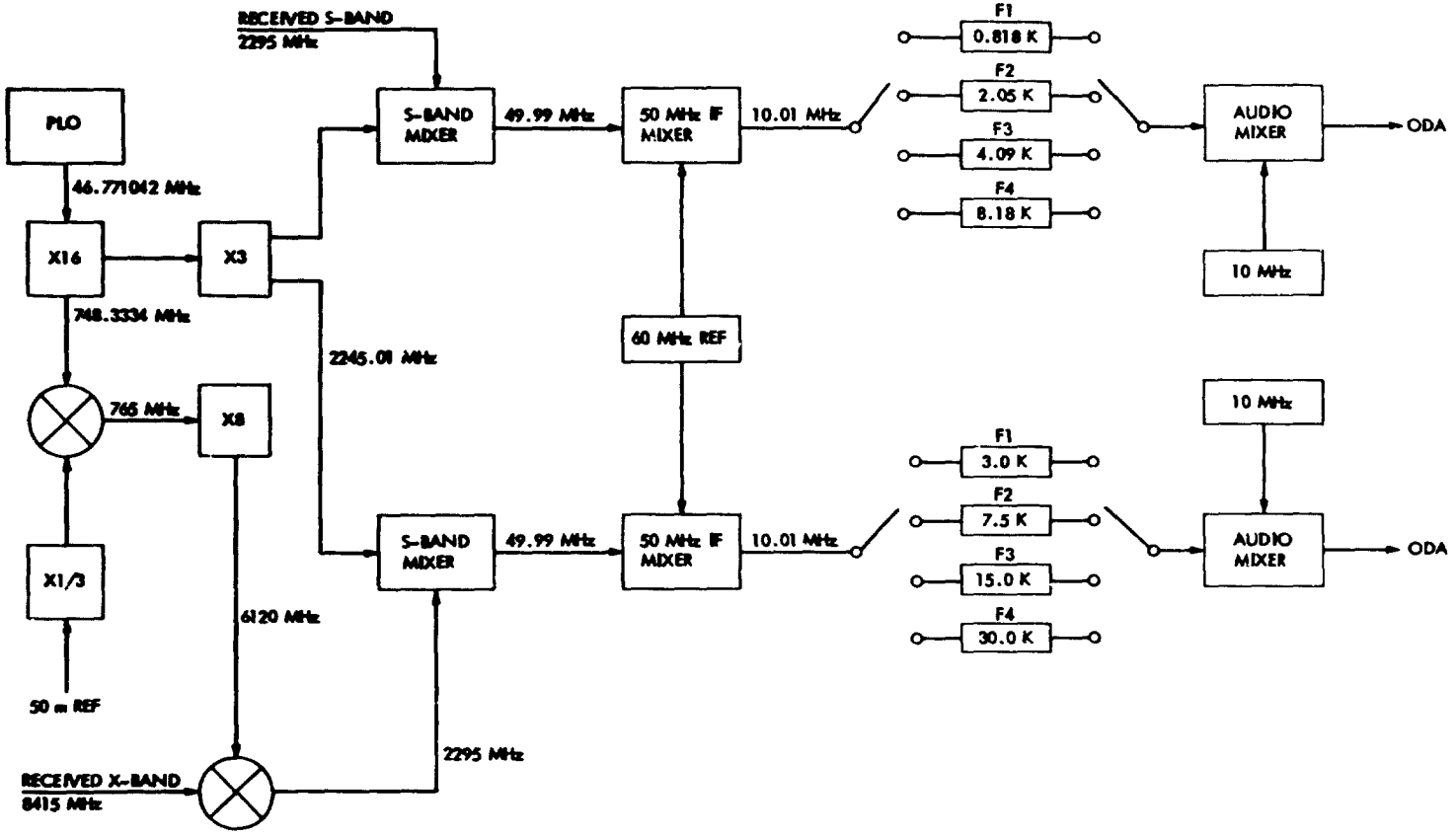

Fig. 5. 64-m open loop receiver configuration

N79-25091

Viking Continuation Mission Support

R. L. Gillette
Deep Space Network Operations Section

This report covers the period from 1 September 1978 through 31 March 1979. It reports on DSN support of Viking Spacecraft activities during the period and continues reporting on DSN Viking Command and Tracking support.

I. Viking Operations

A. Orbiters

The Viking Orbiter 1 (VO-1) spacecraft continued to operate normally during this reporting period as it collected and returned to Earth weather data and Mars photos as well as relaying to Earth data from the two Viking Landers. Viking Orbiter 2 (VO-2) ceased operation on 25 July 1978.

B. Landers

The Viking Landers also continued to operate as expected during this reporting period as they collected and relayed to Earth, via Orbiter 1, Mars weather information and photos.

On 25 October, an attempt was made to turn on Transmitter 2 on board Viking Lander 2. Transmitter 2 had only been operated from Lander touchdown through the first month of the primary mission and for a few weeks in the Extended Mission, at which time it ceased operation during a playback link. A decision was made not to attempt to power up the transmitter again until close to the solar conjunction period during the Viking Continuation Mission because of the limited life expectance after transmitter turn on. Because the attempt to turn-on transmitter 2 was unsuccessful, and because of the earlier failure of Transmitter 1, all data from VL-2 for the remainder of the continuation Mission will be via the Orbiter-1 relay transmission link.

On 19 February 1979, a command uplink to Viking Lander-1 (VL-1) terminated the Lander Continuation Automatic Mission (LCAM), and loaded a software sequence now referred to as Post-LCAM. The original LCAM sequence automatically transmitted data to Earth at preprogrammed times. The new Post-LCAM sequence requires a command uplink to the Lander-1 spacecraft to turn on the downlink transmitter. Commands transmitted to the Lander are now manually entered in the Command Processor Assembly (CPA) at a Deep Space Station (DSS) prior to the start of a Lander pass. Prior to the Post-LCAM, commands were remotely sent to the DSS CPA from the Mission Computer and Control Center (MCCC) at JPL. Figure 1 shows a typical Lander Pass in support of the Post-LCAM.

On 6 February 1979, a command uplink to Viking Lander-2 (VL-2) terminated the VL-2 LCAM sequence and loaded into the spacecraft computer memory the VL-2 Post-LCAM sequence. Since the downlink transmitters onboard VL-2 no longer function, data collected during the VL-2 Post-LCAM must be relayed to the VO-1 spacecraft for transmission to Earth.

During the Post-LCAM, both Lander spacecraft will collect meteorology and imaging data. The VL-1 spacecraft should be capable of returning Mars data up through 1990. VL-2 will be able to return data only as long as there is an Orbiter spacecraft.

II. Viking Survey Mission

The Survey Mission is the fourth phase of the Viking Mission, following the Primary Mission (terminated 31 May 1978), the Extended Mission (terminated 31 May 1978), and the Continuation Mission (terminated this reporting period, 25 March 1979). The Orbiter operations in the Survey Mission will terminate 31 October 1979, but the Lander operations could continue until 29 December 1990.

The objective of the Orbiter Survey Mission is to acquire high-resolution contiguous coverage with the Visual Imaging Subsystem (VIS) of a region on the planet that is likely to contain the landing sites for the next Mars mission. The Lander mission objectives are to take advantage of the unique capability of a transponder on a planet surface, to make frequent radio ranging measurements and to conduct a long-duration monitoring of weather conditions and surface changes at the Lander 1 site.

Throughout the Survey Mission, the landers will be in an automatic-mission mode, operating autonomously on the programs that have previously been stored in their on-board computers. Lander 1 will be repointing its high-gain antenna and acquiring and storing imaging, meteorology, and engineering data frequently, and will be ready to transmit these data to Earth every 7 or 8 days in response to a command. Lander 2 will be operating in a similar manner, but as it has no direct downlink capability, its data can be retrieved only through a relay to Orbiter 1 in May and possibly another in November.

Because of pressure from Voyager and Pioneer for Network support, Orbiter 1 was placed in a housekeeping mode with all science instruments powered off at the end of the Continuation Mission. New operating and safing sequences have been stored in the CCS to make the Orbiter as nearly self-sufficient as feasible so that neither uplinks nor downlinks will be required more often than every two weeks. This mode is expected to be continued until a date not yet determined, but probably after 15 July 1979. In the meantime, the only special Orbiter events that have been planned are a small number of telemetry passes with a 64-m station some time in April to retrieve about 70 VIS pictures still on the tape recorders and the receipt and relay of a data readout from Lander 2 in mid-May.

Science acquisition with Orbiter 1 is expected to resume in July when DSS availability will make a reasonable level of operation feasible. A fairly simple sequence of VIS observations will be carried out, probably daily, for approximately three months. Infrared Thermal Mapper (IRTM) and Mars Atmospheric Water Detector (MAWD) data will be acquired simultaneously with the VIS operations, but few if any special infrared sequences will be run. S- and X-band doppler and ranging may be scheduled simultaneously with Lander-1 direct links.

III. Radio Science

Viking Radio Science activities and experimentation continued during this reporting period. These activities include near-simultaneous Lander/Orbiter ranging, the General Relativity Experiment, and the Solar Corona Experiment. The General Relativity and Solar Corona experiments were conducted during the solar conjunction period of December 1978 through February 1979.

IV. Network Support

Table 1 shows the DSN tracking support for the Viking Continuation Mission from June 1978 through 25 March 1979. Tracking support continued to decrease throughout the continuation mission with a slight increase during the Solar conjunction Radio Science activity in December and January. This reduction in Viking operation activity was anticipated during the continuation mission. An even further reduction in tracking support will occur during the Viking Survey Mission.

Table 2 gives the total number of commands transmitted by the DSN during the Viking Continuation Mission.

References

1. Gillette, R. L., "Viking Extended Mission Support", in *The Deep Space Network Progress Report 42-46*, pp. 29-32, Jet Propulsion Laboratory, Pasadena, California, August 15, 1978.

2. Gillette, R. L., "Viking Extended Mission Support", in *The Deep Space Network Progress Report 42-47*, pp. 15-20, Jet Propulsion Laboratory, Pasadena, California, October 15, 1978.

3. Gillette, R. L., "Viking Continuation Mission Support", in *The Deep Space Network Progress Report 42-48*, pp. 7-11, Jet Propulsion Laboratory, Pasadena, California, December 15, 1978.

Table 1. DSN Viking Continuation Mission tracking support

DSS	1978 Jun.	Jul.	Aug	Sep.	Oct.	Nov.	Dec.	1979 Jan.	Feb.	Mar.
11	1[a]	2		1			1		8	5
	1[b]	13		3			2		32	14
12						4	2	7	20	8
						20	5	20	145	23
14	34	14	13	3	9	13	13	23	3	1
	242	89	85	12	48	51	29	45	4	8
42		2	1		4		6	6	8	4
		9	3		22		23	19	39	15
43	46	51	23	28	27	17	23	26	12	1
	346	449	135	188	181	116	188	122	49	8
44	3		3				1	1		1
	17		11				5	2		4
61			1				1	3	2	1
			5				8	19	7	3
62	3	1	1				1	3		2
	33	7	9				8	9		7
63	41	40	16	21	18	22	23	8	4	1
	343	291	130	157	114	130	130	53	7	7
Total	128	110	58	53	58	56	71	78	57	24
	982	858	378	360	365	317	398	289	283	89

[a]Number of tracks; the summation of all Viking spacecraft tracked.

[b]Track time: scheduled station support in hours.

Table 2. Number of commands transmitted during the Viking Continuation Mission

DSS	1978						1979			
	Jun.	Jul.	Aug.	Sep.	Oct.	Nov.	Dec.	Jan.	Feb.	Mar.
11	6	0		0	-		0	0	1111	3
12		-	-	-	-	1	0	17	531	3
14	1214	870	562	0	2	694	149	0	0	4
42	0	0	0	-	0	-	0	0	1006	458
43	1567	791	7	70	252	648	1914	1141	419	8
44	0	-	30	-	-	-	332	0	-	0
61	0	-	0	-	-	-	0	15	0	0
62	960	0	683	-	-	-	0	15	-	5
63	2451	2984	2073	4988	3376	2690	8	53	3	4
Total	6198	4645	3355	5058	3630	4032	2403	1241	3070	485

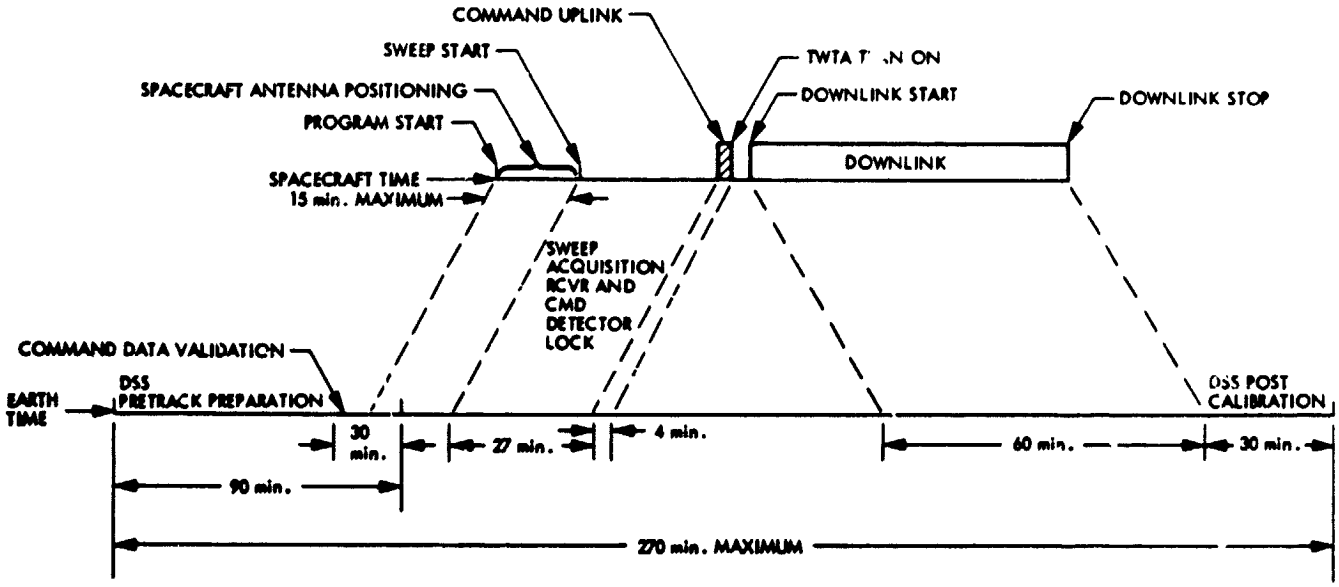

Fig. 1. Typical Lander pass

N79-25092

Pioneer Venus 1978 Mission Support

T. W. Howe
DSN Operations Section

This article reports on the Deep Space Network support of the Pioneer Venus Mission. It describes the Orbiter's Venus Orbit Insertion, Multiprobe Entry, and Orbiter Occultation Experiment support.

I. Venus Orbit Insertion (VOI)

A. Supporting Stations

DSSs 11 and 14 were the prime stations for support of VOI. DSS 43 provided support for the reorientation of the spacecraft into the orbit insertion attitude at approximately 45 hours prior to VOI. They also supported the loading of spacecraft Stored Command Logic (SCL) with the orbit insertion parameters.

The DSN Real-Time Telemetry System Analyst (NAT TEL) provided monitoring for spacecraft stored command load address pointers beginning at VOI minus 7 hours.

The Ground Communications Facility (GCF) provided critical support during the VOI period.

B. VOI Support Procedures

The VOI sequence was executed by the spacecraft by preprogrammed commands. To insure a successful VOI, a contingency plan was formulated. The plan included an uplink and downlink strategy for Pre-VOI, an uplink and downlink strategy for Post-VOI, and monitoring of SCL issued commands during Pre-VOI.

1. **Pre-VOI Strategies.** The Pioneer Venus Orbiter and Bus Spacecrafts had experienced random single bit changes in their SCLs during the entire transit phase of the mission. The bit changes occurred about once per week and were thought to be caused by cosmic rays passing through the solid state memories. Since the ignition of the Orbit Insertion Motor was to be initialized by the SCL, there was concern that a bit change could cause ignition to be earlier or later than the programmed time. To guard against such an occurrence, a plan was devised to provide for continuous monitoring of the address pointers in the redundant SCLs during the 7 hours prior to VOI. The DSN extracted these words from the telemetry data and made comparative counts with Ames Research Center (ARC).

In the event of a computer failure at ARC, the DSN would then have relayed the SCL count to ARC by voice until the computer could be restored. No ARC computer failure occurred, and this failure strategy was not required.

The Pre-VOI uplink strategy was essentially to maintain the uplink until approximately 10 minutes prior to occultation in order to retain a command capability. DSS 14 provided an uplink with the prime spacecraft receiver while DSS 11 acquired an uplink with the backup receiver. This configuration provided redundant command capabilities and, in the

event of a problem at the prime station, the other stations command modulation would be turned on and commanding continued.

Both stations turned off their transmitters at 10 minutes prior to occultation to insure a one-way doppler mode at entry.

Pre-VOI downlink strategy involved ramping the ground receiver during the hour prior to occultation in order to minimize the receiver phase error at entry and exit occultation.

2. Post-VOI Strategies. For Post-VOI, the desire was to obtain uplink lock as quickly as possible and transmit commands that would complete the VOI sequence in the event the preprogrammed sequence failed. It was estimated that a burn command reaching the spacecraft at the time of exit occultation would result in an orbit with a 48-hour duration instead of the desired 24-hour orbit for the nominal burn. For each minute's delay in the execution of the burn command, the orbit duration would increase by an estimated 5 hours.

The strategy for uplink acquisition was to use both DSS 11 and DSS 14 to simultaneously attempt to acquire the prime spacecraft receiver. The sweep was to cover a range of best lock frequency plus or minus 5 sigma or about 1700 Hz at S-band.

Following transmitter turn on for uplink acquisition sweep, command modulation was turned on and motor arm and fire commands were transmitted by both supporting stations.

Burn occurred at the nominal time and resulted in an orbit of slightly longer than the desired 24-hour duration.

The Post-VOI uplink with the spacecraft was missed by both stations. This was because the uplink tuning sweep strategy had been optimized for the anomalous no-burn case. Commanding for the no-burn case would have been mission critical. As a consequence, the uplink strategy was very conservative for the no-burn predicted doppler, but quite optimistic compared to the uncertainties for the burn case.

For Post-VOI downlink acquisition, a rapid lock was desired to determine the status of the orbit insertion and th health of the spacecraft.

DSS 14 used the Spectral Signal Indicator (SSI) in conjunction with an open loop receiver to detect downlink presence. A 300-kHz filter was used to detect signals in any of the possible modes (i.e., one-way, two-way, three-way, burn, no-burn).

DSS 11 concentrated on downlink acquisition for a nominal orbit insertion with their prime receiver used for two-way search and the backup used for one-way search

Following the failure to acquire uplink lock upon exit occultation, a second sweep was performed by DSS 14 and uplink established.

II. Occultation Experiment Support

The occultation experiment is divided into three major scientific objectives.

(1) *Radio Science Occultation I.* To determine refractivity profiles in the lower atmosphere of Venus, at different longitudes, from the analysis of phase perturbations of the S- and X-band telemetry carriers during occultation. The refractivity profiles are used to obtain temperatures, pressures, and densities in the neutral atmosphere above about 35 km. Also measurements of dispersive (S- and X-band) absorption by analysis of signal attenuation during occultation. These yield data on possible radio absorptive layers below about 50 km in the lower atmosphere of Venus, data used to measure electron-density height profiles by analysis of dispersive S- and X-band phase effects observed during occultations at a variety of solar illumination angles over the life of the mission, and data used to observe dynamics of the lower atmosphere as obtained from the horizontal pressure and temperature gradients, as well as pressure and density variations with respect to time. Dr. A. J. Kliore of JPL is principal investigator.

(2) *Radio Science Corona Turbulence.* To observe and interpret the small-scale turbulence characteristics of the Venus atmosphere above about 35 km, measuring the intensity variation of turbulence with altitude, planetary latitude and longitude, and the distribution of scale sizes in the atmosphere. A secondary objective is to determine the solar-corona turbulence and solar-wind velocity near the Sun. R. T. Woo of JPL is the principal investigator.

(3) *Radio Science Occultation II.* Determination of atmospheric and ionospheric structures from radio occultations; solar wind irregularity detection through S-X differential delay coupled with adjunct information; search for relationships between solar wind variations and Venus ionospheric reactions; comparison of orbiter scintillations to one another and to probe scintillations to deduce evidence of turbulence or layering, and possibly also a study of solar wind scintillations. T. A. Croft of Stanford Research Institute is principal investigator.

The DSN supports this experiment with four separate data taking configurations. The open loop receivers in conjunction with the Occultation Data Assembly (ODA) are used to produce digital tapes containing digital data decimated to a reduced bandwidth. The wide bandwidth Multimission Open Loop Receiver (MMR) together with the Digital Recording Assembly (DRA) is used to produce wide bandwidth recordings of S-band only as backup to the prime narrow bandwidth ODA recordings.

The closed loop receivers are used to produce S- and X-band doppler that is transmitted to JPL in real-time.

The closed loop receiver and Digital Instrumentation Subsystem produce high-rate sampling of X-band AGC for real-time transmission to JPL. The AGC data were not originally committed to the mission until concern over reliability of the new ODA made the taking of the AGC data prudent.

Figure 1 shows the Occultation Experiment (S/X) configuration.

Support of the Radio Science Experiments began on 5 December 1978. DSS 14 provided support on this date with good results, using the newly installed ODA. The S-band 10-kHz OLR bandwidth was used to allow for any uncertainties in predicts or ODA operation.

Support continued for the next two days with data taking suspended on 8 and 9 December for Multiprobe Entry Support. A spurious signal was detected during these first three occultation passes and was found to be caused by the OLR local oscillator mixer.

The S-band OLR bandwidth was reduced to 5 kHz during the third occultation pass as confidence in the system was gained. The bandwidth was further reduced on orbit 7 to 2 kHz.

The initial occultations occurred over DSS 14 only. The spacecraft periapsis passage was allowed to move later each day until it reached the mutual DSS 14 and 43 view period. Spacecraft maneuvers maintain the periapsis passage in the mutual view period.

DSS 43 support of the occultation experiment began during orbit 29 on 2 January 1979, in parallel with DSS 14.

Parallel support continued when possible through orbit 90 when the first occultation season ended. Table 1 illustrates the performance of the DSN and Pioneer Project in terms of total data taken and lost during the first occultation season.

During the first 36 occultations there were 144 data events. There were four events during each occultation, defined as entry S-band, entry X-band, exit S-band and exit X-band. Of these 144 events, 22 percent were lost due to various problems. Since a wide bandwidth recording of S-band data was taken by the MMR/DRA in parallel with the OLR/ODA data, the total percentage of data lost was reduced to 14 percent.

Table 1 shows that for the first 36 occultations, the majority of problems were associated with errors at the supporting Deep Space Stations (DSS). The second highest loss of data was due to hardware problems. These problems were mainly due to the operator unfamiliarity with the equipment, and problems uncovered through operational use of the equipment.

For the next 36 occultations, the total loss of data increased slightly, however DSS operator errors decreased to 21 percent, while Project errors increased to 31 percent. The Project experienced difficulties in maintaining spacecraft high-gain antenna pointing during the data taking periods.

During the final 18 occultations, data loss continued at a constant level. DSS operator errors were decreased still further to just 9 percent. Again, mainly due to high gain antenna pointing problems, the Project contributed to 72 percent of the total data lost. The second occultation season is scheduled to begin during May 1979.

III. Multiprobe Entry

A. Supporting Stations

DSSs 14 and 43 had the prime responsibilities of supporting probe entry real-time telemetry, radio metric data, precarrier analog recording, DLBI recording, and uplink to the large probe during the entry period of the four probes. DSSs 14 and 43 also supported the Bus after probe impact on the surface. DSSs 11 and 44 supported the Bus during the entry sequence.

DSS 11's prime responsibility was to support the uplink for the Bus for command and 2-way radio metric data and telemetry during the entry period.

DSS 44 acted as a backup to DSS 11 for Bus coverage.

DSS 42 equipment provided a radio metric data processing channel for small probe three.

Spaceflight Tracking and Data Network (STDN) stations at Santiago, Chile, and Guam supported the Differential Long Base Interferometry (DLBI) experiment.

B. Configurations

Figure 2 illustrates the telemetry and DLBI configuration used by DSS 14/43.

This configuration provided one closed loop receiver for each of the four probes and one open loop receiver for each of the probes. Receiver numbers 3 and 4 (Blk IV Receivers) were both used to support the large probe. One was tuned to the one-way downlink frequency, while the other was configured for either the two-way (DSS 14) or three-way (DSS 43) doppler mode. The Multi-Mission Open Loop Receiver (MMR) was used to support the DLBI experiment.

Figure 3 shows the DSS 14 Radio Metric Data configuration, while Fig 4 gives the DSS 42/43 radio metric data configuration. This configuration provided real-time doppler from each of the four probes.

C. DSN Multiprobe Entry Sequence

A preliminary DSN Multiprobe Entry Sequence was developed as early as March 1978 and remained basically unchanged for the actual event.

Development of this Sequence of Events (SOE) was described in Progress Report 42-46 while the actual SOE was shown in Progress Report 42-48.

Preparations for the entry event began on 8 December 1978 when DSS 14/43 commenced an entry countdown sequence. During this sequence the stations checked out all of their support equipment in the entry support configuration. A Configuration Verification Test (CVT) was then conducted with each station. Following successful completion of these tests, the stations were placed under configuration freeze. Following the implementation of a freeze, the stations were not allowed to alter their configuration or support any other flight project.

The entry sequence of events timing was related to entry (E) of the large probe with entry defined as an altitude of 200 kilometers.

At E - 3^h a check list was performed.

The Bus was acquired at E - 2^h49^m by DSS 14 and they began their large probe uplink acquisition sweep at E - 2^h30^m. At this time the large probe downlink had not yet been turned on. Table 2 shows the uplink tuning performed by DSS 14 for large probe acquisition. The sawtooth sweep pattern was used to insure a successful uplink acquisition.

At E - 1^h19^m DSS 43 acquired the Bus downlink.

Throughout this early period, both stations were using their Signal Spectrum Indicators to look for probe downlinks. This was done to see if any of the probes had accidentally turned on early. There was concern that the same SCL radiation effects described above for the Orbiter and Bus could cause the probe coast timers to time out prematurely and cause the downlinks to be turned on.

Another checklist was performed at E - 60^m by both DSS 14 and 43. At this time DSS 11 was providing an uplink to the Bus (S/C 13) and DSS 12 was supporting the Pioneer Venus Orbiter (S/C 12). At E - 21^m, the large probe downlink was detected and found to be in two-way lock with DSS 14. Each of the probes was to follow the same sequence of events. First, the RF downlink was turned on. This was followed by the subcarrier being turned on five minutes later. Entry into the atmosphere of Venus occurred some 16-1/2 minutes later. The time from entry until impact on the planet was approximately 56 minutes. Figure 5 illustrates the predicted timing of each of the probe events. Table 3 gives probe entry parameters while Table 4 gives the predicted event times versus actual times. Prior to ground observed entry of the large probe, a specially designed uplink acquisition sweep was performed to reacquire the large probe uplink following atmospheric entry blackout. This began at E - 3^m.

The criteria used for uplink acquisition were:

(1) Unperturbed large probe downlink for at least 190 seconds after the observed entry. This was required to allow time for the reverse telemetry playback data to lock up.

(2) Minimized sweep times.

(3) A good probability of uplink acquisition.

The final plan used both DSS 14 and 43 for the uplink acquisition. DSS 43 performed the primary acquisition sweep while DSS 14 performed a secondary sweep. The total sweep range covered 20 kHz centered at the predicted best lock frequency. Figure 6 shows the sweep range versus time for each station. It shows an overlap in coverage centered at best lock frequency, which insured the chance for an early acquisition.

The DSS 43 sweep began at the predicted atmospheric entry blackout time minus three minutes to preserve criterion (1) above.

DSS 14's sweep began one minute later causing a separation of 1000 Hz at S-band to minimize any uplink interference.

Once the determination of which station had actually acquired the uplink had been made, the three-way station was

to turn off their transmitter and tune to a frequency 460 Hz (S-band) away from the final frequency of the two-way station. This was done so that if a problem occurred at the two-way station, the other station could turn on their transmitter and have a good chance of capturing the uplink as the transponder drifted toward its rest frequency.

Due to a late exit from blackout, DSS 43 was unsuccessful in acquiring the uplink, and DSS 14 reacquired the uplink during the secondary sweep.

Table 5 gives the actual sweep message used by DSS 43 for large probe postentry uplink reacquisition. Table 6 shows the DSS 14 sweep.

All probes with the exception of Small Probe 2 impacted Venus on schedule and were presumed destroyed. Small Probe 2 survived the landing and continued to send data for some 67 minutes. The DLBI Principal Investigator reported later that from the DLBI data processing at M.I.T. he could detect the Small Probe 3 lasted about one second on the surface. This may not sound like much, but it meant that Probe 3 as well as 2 provided an anchor for the DLBI wind measurement. Last to enter the atmosphere was the Bus. It appeared to burn up some 2-1/2 minutes after entry when the signal was lost.

Support by all stations was excellent. Telemetry lock was obtained quickly after entry and data rate changes. The amount of real-time data returned was:

95 percent for the Large Probe,

95 percent for Small Probe 1,

84 percent for Small Probe 2,

88 percent for Small Probe 3.

Other than DSS 14 acquisition of the large probe uplink following blackout and the survival of Small Probe 2 following impact, everything went according to plan. The multiprobe entry planning and training described in Progress Report 42-48 had paid off.

Table 1. DSN occultation performance

Occultation number	Total data events	Data lost, %	Data lost after DRA recovery, %	Causes of data loss: DSS error, %	Hardware problem, %	Project error, %	NOCT error, %	S/W problem and unknown, %
1 - 36	144	22	14	63	20	7	5	5
37 72	256	25	14	21	25	31	23	
73 90	148	22	15		9	72	10	9

Table 2. DSS 14 large probe preentry uplink acquisition (Revision 1)

TXR on:	16:19:00	GMT
TXR power:	20	kW
Frequency:	43966874.51	Hz
Start tuning up (T0):	16:20:00	GMT
Tuning rate (R0):	+1.16	Hz/s
Tune to:	43967823.39	Hz
Start tuning down (T1):	16:33:38	GMT
Tuning rate (R1):	-1.13	Hz/s
Tune to:	43966899.05	Hz
Start tuning up (T2):	16:47:16	GMT
Tuning rate (R2):	+1.17	Hz/s
Tune to:	43967856.11	Hz
Start tuning down (T3):	17:00:54	GMT
Tuning rate (R3):	-1.13	Hz/s
Tune to:	43966932.77	Hz
Start tuning up (T0):	17:14:32	GMT
Tuning rate (R0):	+1.18	Hz/s
Tune to:	43967897.01	Hz
Start tuning down (T1):	17:28:10	GMT
Tuning rate (R1):	-1.11	Hz/s
Tune to:	43966989.03	Hz
Tune to TSF (T2):	17:41:48	GMT
Tuning rate (R2):	+1.19	Hz/s
TSF:	43968254.0	Hz
Stop tuning (R3/T3):	17:59:31	GMT

Table 3. Predicted probe entry parameters

Probe	Entry time[a], GMT	Entry angle, deg	Maximum g's	Descent time, min:s
Sounder Probe (LP)	18:48:44	-32.8	308	54:36
North Probe (SP-1)	18:53:08	-67.9	503	55:54
Day Probe (SP-2)	18:55:11	-25.3	241	56:18
Night Probe (SP-3)	18:58:45	-41.8	382	56:16
Bus	20:24:06	-9.0	[b]	[b]

[a]Earth receive time of entry at 200 kilometers altitude.

[b]Communication with the bus was lost at approximately 60 s at 120 km altitude when aerodynamic forces began to tumble and destroy the bus.

ORIGINAL PAGE IS
OF POOR QUALITY

Table 4. Predicted probe event time vs actual time

Probe	Event	Predicted Z, GMT	Actual Z, GMT	ΔT, s
LP	RF on	182724	182739	+15
SP1	RF on	183112	183110	− 2
SP2	RF on	183344	183340	− 1
SP3	RF on	183706	183721	+15
LP	TLM on	183224	183240	+16
SP1	TLM on	183612	183608	− 4
SP2	TLM on	183841	183840	− 1
SP3	TLM on	184206	184221	+15
LP	Entry	184844	184845	+ 1
SP1	Entry	185308	185253	−15
SP2	Entry	185511	185531	+20
SP3	Entry	185845	185926	+41
LP	Impact	194353	194306	−47
SP1	Impact	194906	184553	−193
SP2	Impact	195154	185112	−42
SP3	Impact	195502	185518	+16

Table 5. DSS 43 large probe postentry uplink acquisition (Revision 1)

TXR on:	18:45:44	GMT
TXR power:	20	kW
Frequency:	43966747.0	Hz
Start tuning (T0):	18:45:45	GMT
Tuning rate (R0):	−1.17	Hz/s
Tune to:	43966513.0	Hz
Stop tuning (T1/R1):	18:49:05	GMT
If confirmed three-way: turn TXR off and snap to:		
TSF:	43966926.0	Hz

Table 6. DSS 14 large probe postentry uplink acquisition (Revision 1)

Start tuning (T0):	**18:46:44**	**GMT**
Tuning rate (R0):	**−1476.0**	**Hz/s**
Tune to:	**43966778.0**	**Hz**
Tune to TSF (T1):	**18:46:45**	**GMT**
Tuning rate (R1):	**+1.125**	**Hz/s**
TSF:	**43967003.0**	**Hz**
Stop tuning (R2/T2):	**18:50:05**	**GMT**
If confirmed three-way by NOC, turn transmitter off and snap to		
TSF:	**43966590.0**	**Hz**

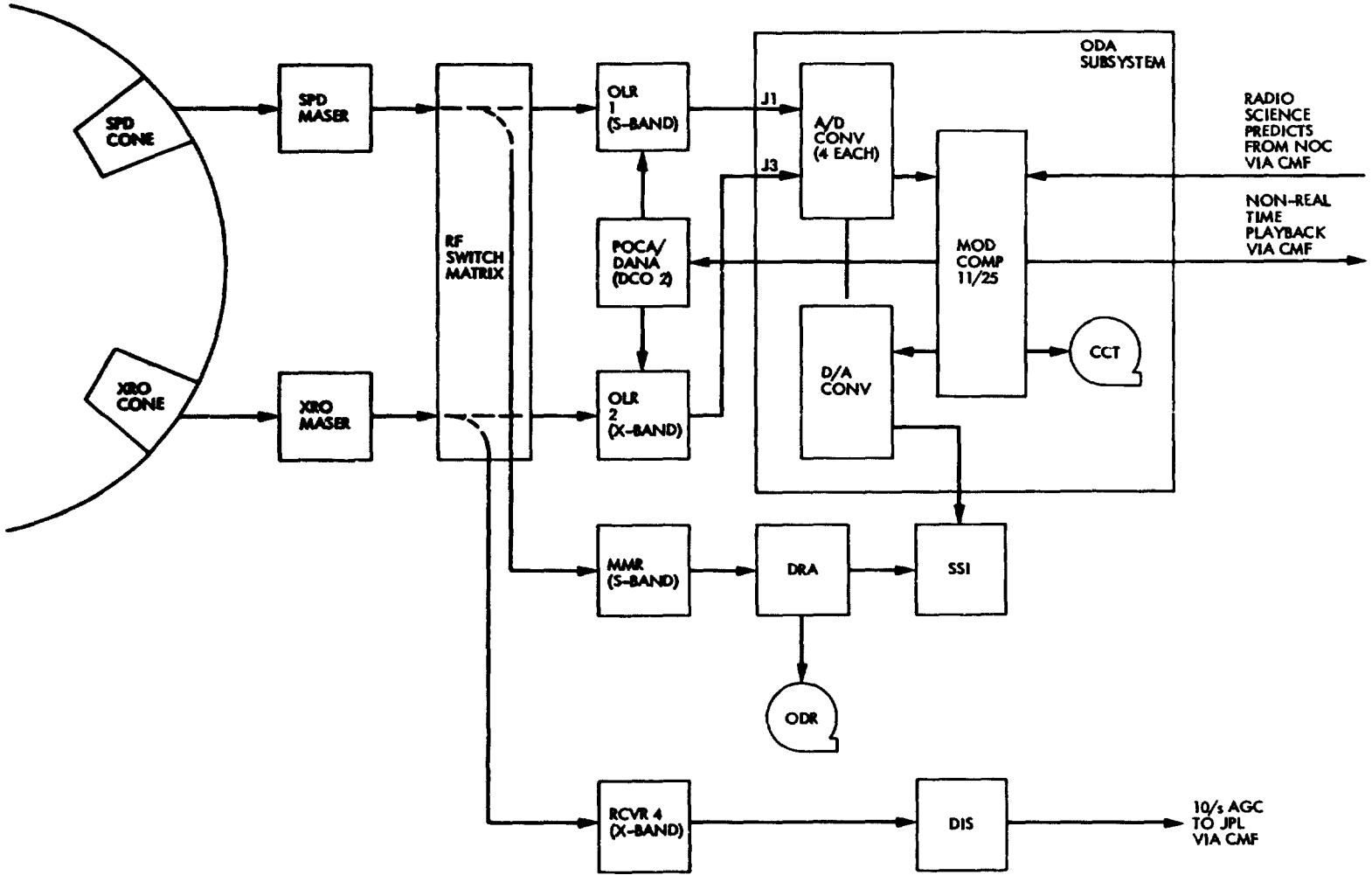

Fig. 1. Occultation experiment (S/X) configuration

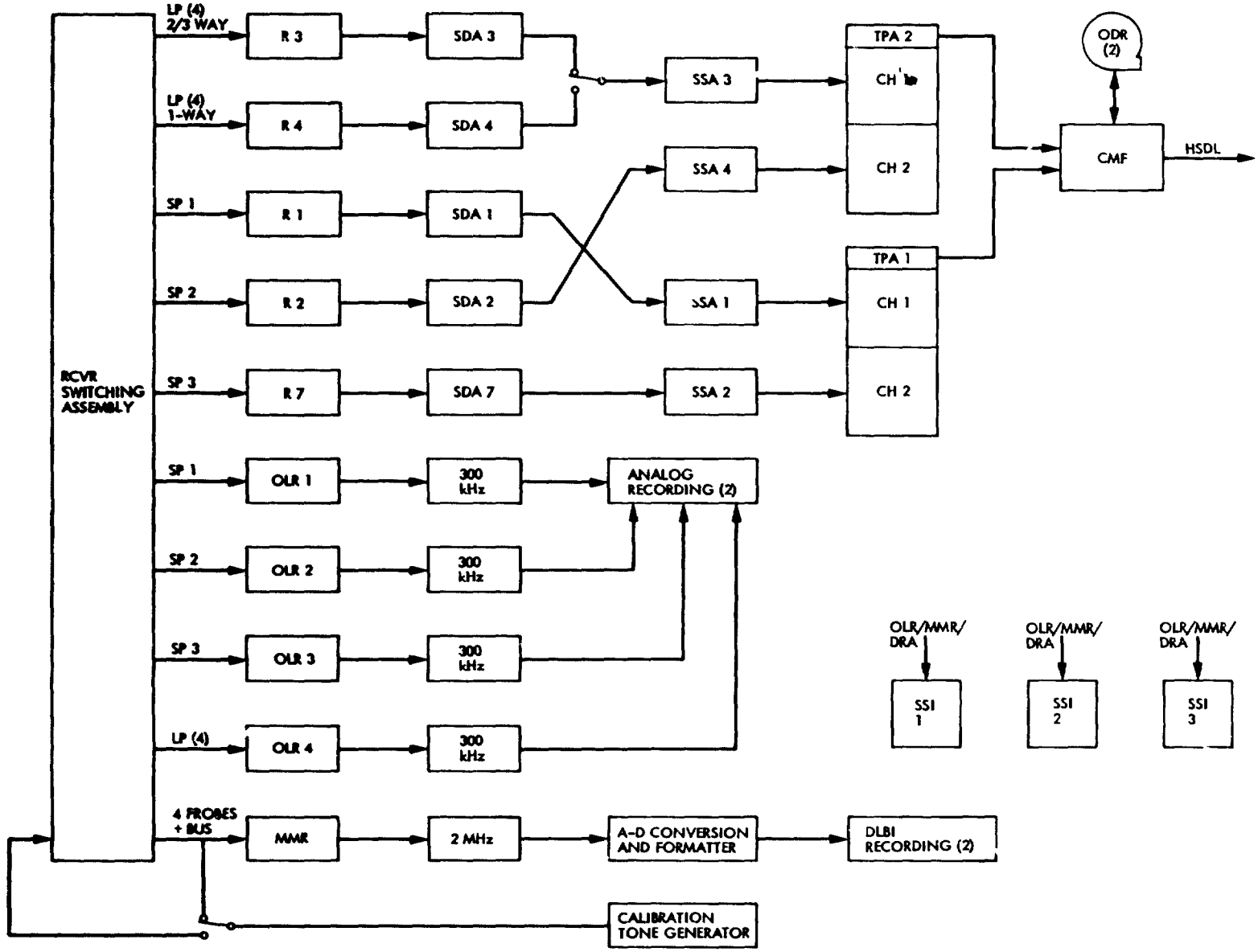

Fig. 2. DSS 14/43 telemetry and DLBI configuration for multiprobe entry

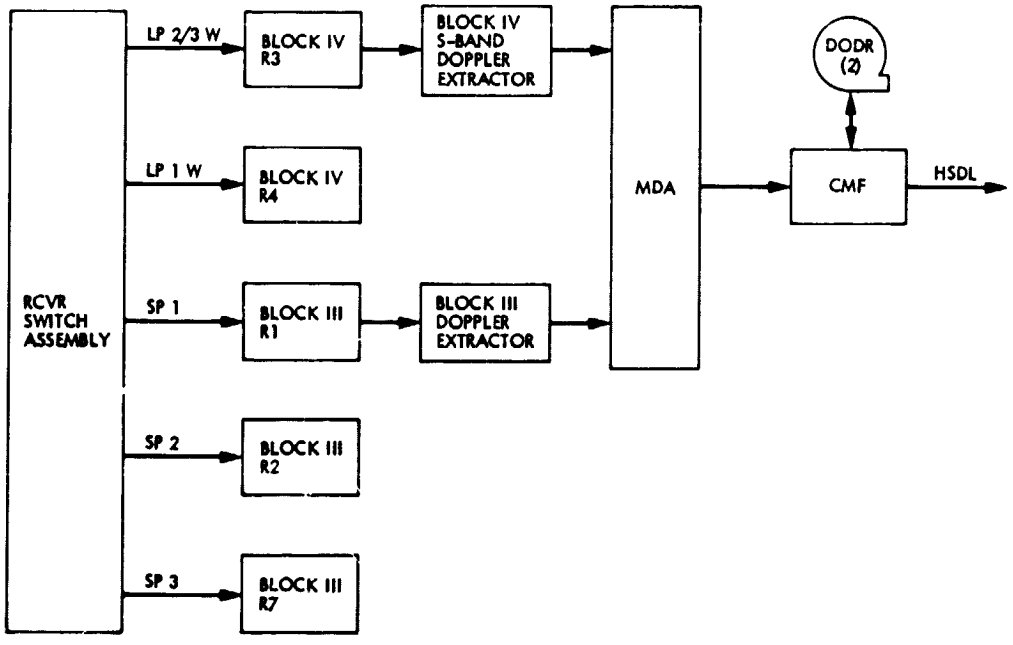

Fig. 3. DSS 14 radio metric data configuration for PV 78 multiprobe entry

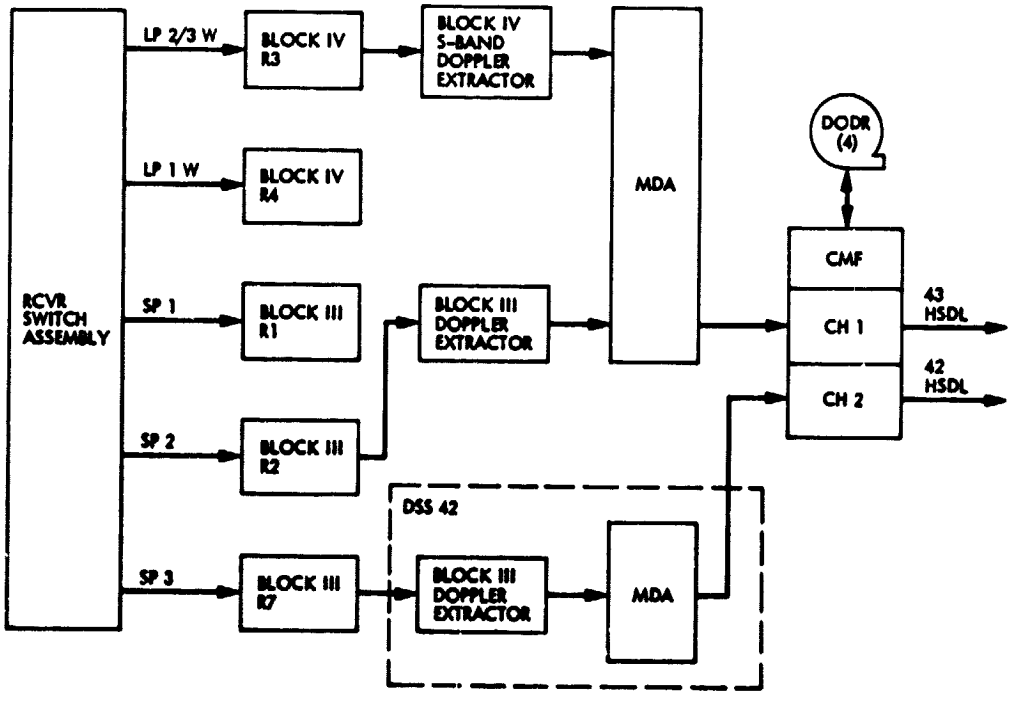

Fig. 4. DSS 43 radio metric data configuration for PV 78 multiprobe entry

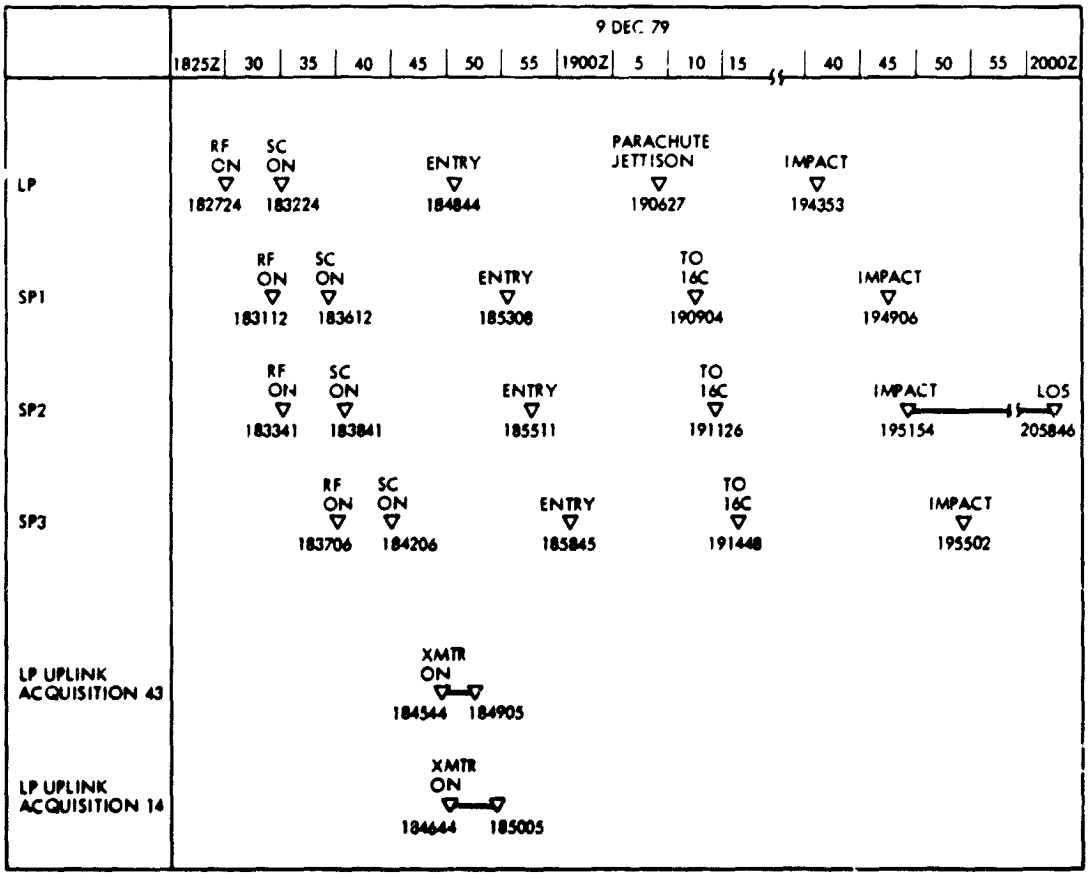

Fig. 5. Predicted probe event timing

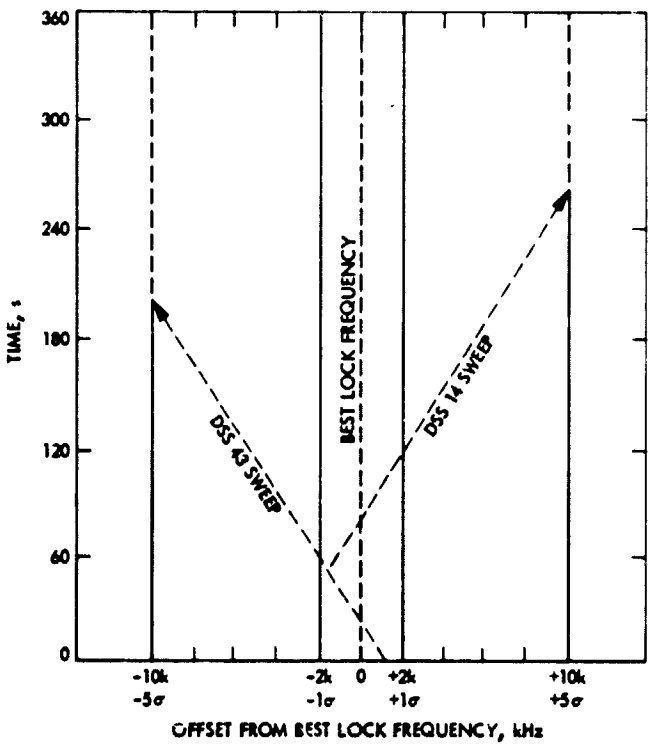

Fig. 6. Large probe uplink sweep strategy

N79-25093

Stability Analysis of the Multimegabit Telemetry Demodulator/Detector Design

J. K. Holmes
Communications Systems Research Section

Stability of the multimegabit telemetry digital Costas loop is considered. It is shown that the present design is stable with about 35.2 dB gain margin, and therefore is quite stable. This paper considers the bandpass filter implementation of the data filters.

I. Introduction

The purpose of this article is to demonstrate analytically that the multimegabit telemetry Costas loop demodulator is stable over the expected signal dynamic range. The gain margin is about 35.2 dB when $M = 4$ (see Fig. 1). It is well known that a digital Costas loop becomes more unstable as internal delays increase and this fact is verified by the analysis contained herein.

Two methods of stability analysis were employed. First, Jury's stability condition was used and secondly, a root locus was constructed for the digital loop. Both methods yield the same stability criteria.

II. Stability Analysis

First we develop the system loop equation expressed in z transforms. Consider Fig. 1, where the digital Costas loop under consideration is displayed. A portion of the phase detector is analog with the filtering accomplished digitally.

An equivalent loop model is shown in Fig. 2. Because the filtering is done digitally, the loop filter can be expressed directly in the Z variable where $Z = e^{ST_M}$ with S being the La Place transform variable. The internal updating duration into the loop filter is T_M where $T_M = MT_S$ with T_S being the data symbol[1] duration. At present, at all data rates, there are four samples per symbol out of the rate buffers (Fig. 1), so averaging over four samples is equivalent in terms of delays in sampling every symbol (at rate R_S). First we obtain $F(Z)$, the loop filter z-transform.

If the input of the summer branch of the loop filter is denoted as e_n and the output as U_n, then (see Fig. 1)

$$U_n = K_I \sum_{l=0}^{n} e_l \tag{1}$$

or by adding $K_I e_{n+1}$ to both sides we obtain

$$U_{n+1} = U_n + K_I e_{n+1} \tag{2}$$

[1]The parameter k is set so that this is true, and $M = 4$ in the present design (see Fig. 1).

Taking z-transforms we obtain the z-transform of $\{U_n\}$ in terms of the z-transform of $\{e_n\}$

$$U(Z) = \frac{E(Z)\,K_I}{1 - Z^{-1}} \tag{3}$$

where

$$E(Z) = z\{e_n\} = \sum_{n\ 0}^{\infty} e_n Z^{-n} \tag{4}$$

$$U(Z) = z\{U_n\} = \sum_{n=0}^{\infty} U_n Z^{-n} \tag{5}$$

The proportional term, when z-transformed, remains unaltered so that

$$F(Z) = K_L + \frac{K_I}{1 - Z^{-1}} \tag{6}$$

Next we need the z-transform of the product of the zero order hold ($H^o(S)$) and the $VCO(K_{VCO}/S)$ which we denote by

$$z\left\{H^o(S)\,\frac{K_{VCO}}{S}\right\} = B(Z)$$

Taking z-transforms we have

$$B(Z) = z\left\{\frac{1 - e^{-ST_M}}{S^2}\right\} K_{VCO} \tag{7}$$

or

$$B(Z) = \frac{K_{VCO}\,T_M}{Z - 1} \tag{8}$$

In order to get the closed loop transfer function (and letting $\theta(Z)$ be the transform of $\theta(t)$ etc.), we write the z transform of the oscillator output phase estimates as

$$\hat{\Theta}(Z) = \left(\frac{K_{VCO}T_M}{(Z - 1)}\right) GF(Z)\,\Phi(Z) \tag{9}$$

Since the phase error $\phi(t)$ has transform $\Phi(Z)$ and the phase estimate $\hat{\theta}(t)$ has transform $\hat{\Theta}$, we have

$$\Phi(Z) = \Theta(Z) - \hat{\Theta}(Z) \tag{10}$$

Now clearly

$$\hat{\Theta}(Z) = \frac{K_{VCO}\,T_M}{(Z - 1)} GF(Z)\,(\Theta(Z) - \hat{\Theta}(Z)) \tag{11}$$

where

$$\hat{\Theta}(Z) = z\{\hat{\theta}(t)\},\ \Phi(Z) = z\{\phi(t)\},\ \Theta(Z) = z\{\theta(t)\} \tag{12}$$

and where G is the signal gain of the Costas loop. Solving for $\hat{\Theta}(Z)$, we have

$$\hat{\Theta}(Z) = \left[\frac{GK_{VCO}\,T_M\,F(Z)}{(Z - 1) + K_{VCO}\,GT_M\,F(Z)}\right]\Theta(Z) \tag{13}$$

Therefore, the closed loop transfer function in the Z variable is

$$H(Z) = \frac{GK_{VCO}\,T_M\,F(Z)}{(Z - 1) + GK_{VCO}\,T_M\,F(Z)} \tag{14}$$

For our case of a hard-limited, in-phase channel Costas loop, the loop gain, G, is proportional to the signal gain through the limiter times the signal voltage itself. The limiter signal gain depends upon the SNR into the limiter.

Rearranging Eq. (14), we obtain

$$H(Z) = \frac{\dfrac{GK_{VCO}\,T_M}{(Z - 1)}\,F(Z)}{1 + \dfrac{GK_{VCO}\,T_M}{Z - 1}\,F(Z)} \tag{15}$$

Since the stability of the loop depends on the closed loop poles of $H(Z)$, we consider the denominator of $H(Z)$, which we denote by $DH(Z)$,

$$DH(Z) = 1 + \frac{GK_{VCO}\,T_M}{Z - 1}\,F(Z) \tag{16}$$

Using Eq. (6) in Eq. (16) we obtain

$$DH(Z) = 1 + \frac{GK_I K_{VCO} T_M}{Z-1} + \frac{GK_I I_M K_{VCO} Z}{(Z-1)^2} \quad (17)$$

Setting $DH(Z) = 0$ produces

$$Z^2 + (a+b-2)Z + (1-a) = 0 \quad (18)$$

where

$$a = GK_L K_{VCO} T_M \quad (19)$$

$$b = GK_I K_{VCO} T_M \quad (20)$$

We apply the Jury stability criterion (Ref. 1) to Eqs. (18) to (20) to determine if the loop is stable. The Jury stability criterion is based on the coefficients of $DH(Z)$. Specifically for digital first and second order loops, we have

(1) First order loop: if

$$DH(Z) = a_1 Z + a_0 = 0, a_1 > 0 \quad (21)$$

and

$$\left| \frac{a_0}{a_1} \right| < 1 \quad (22)$$

then the system is stable.

(2) Second order loop: If

$$DH(Z) = a_2 Z^2 + a_1 Z + a_0 = 0, a_2 > 0 \quad (23)$$

and

$$\text{(I)} \quad a_2 + a_1 + a_0 > 0$$

$$\text{(II)} \quad a_2 - a_1 + a_0 < 0$$

$$\text{(III)} \quad a_0 - a_2 < 0 \quad (24)$$

then the system is stable.

Use of condition (I) of (2) in Eq. (18) results in

$$1 + a + b - 2 + 1 - a = b > 0 \quad (25)$$

From condition II of (2) we have

$$1 + 2 - a - b + 1 - a = 4 - 2a - b > 0 \quad (26)$$

or

$$4 - GK_{VCO} T_M (2K_L + K_I) > 0 \quad (27)$$

The present design calls for

$$\frac{K_I}{K_L} = 2^{-8} = 0.00391 \quad (28)$$

so that for stability we must have

$$GK_{VCO} K_L T_M < 1.9961 \cong 2 \quad (29)$$

The third condition is met trivially, i.e.,

$$1 - a - 1 = -a < 0 \quad (30)$$

which is true since

$$-GK_L K_{VCO} T_M < 0 \quad (31)$$

We conclude from Jury's stability criterion that for loop stability we require $GK_{VCO}K_L T_M < 2$. At threshold conditions, it has been shown that $G_0 K_{VCO} K_L T_4 = 3.9046 \times 10^{-3}$ which is much less than 2.

As a double check on the stability result (Eq. 29) and also as a way of determining gain margin, we consider the root-locus plot for this system. To utilize the root locus we consider the open loop transfer function given by

$$OL(Z) = GF(Z) z \left\{ H^o(S) \frac{K_{VCO}}{S} \right\}$$

or

$$OL(Z) = \frac{GK_L K_{VCO} T_M}{(Z-1)} + \frac{GK_I T_M K_{VCO} Z}{(Z-1)^2} \quad (32)$$

Using the notation of Eqs. (19) and (20) we have

$$OL(Z) = \frac{a}{Z - 1} + \frac{bZ}{(Z-1)^2} \tag{33}$$

or

$$OL(Z) = \frac{(a+b)\left(Z - \frac{a}{(a+b)}\right)}{(Z-1)^2} \tag{34}$$

Using the methods of the root locus (Ref. 2), which apply to the Z plane as well as the S plane, we know that the locus starts at the poles of $OL(Z)$ with zero gain $(a + b = 0)$, and terminates on the zeros for unbounded gain $(a + b = \infty)$. Further, the locus exists at any point along the real axis where an odd number of poles plus zeros is found to the right of the point. Using the above facts and the remaining rules of root locus construction yields the root locus of our digital Costas loop, as shown in Fig. 3.

Since system instability occurs when the root locus goes onto or outside of the unit circle, it is necessary to find the value of "gain" $(a + b)$ such that the locus just crosses the unit circle at the point $Re(Z) = -1$ and $Im(Z) = 0$. Since the "gain" is given by zero and pole distances we obtain

$$a + b = \frac{|-2|^2}{\left|-1 - \frac{a}{(a+b)}\right|} \tag{35}$$

Equation (35) yields

$$2a + b = 4 \tag{36}$$

or

$$a + \frac{b}{2} = 2 \tag{37}$$

For stability, therefore, the locus must be inside the unit circle, so we require

$$\left(a + \frac{b}{2}\right) < 2 \tag{38}$$

This condition is precisely the same as that derived from Jury's stability criterion (Eq. (26)).

We conclude, then, that for stability

$$GK_L K_{VCO} T_M < 2 \tag{39}$$

III. Gain Margin

Now we shall determine the gain margin of the loop, that is, how many dB increase in signal level is needed to just make the system unstable. To determine the gain margin we must compute the range in G which is the product of the AGC output signal voltage A and the gain through the limiter α, which depends on the limiter input SNR (SNR_i), i.e.

$$G = \alpha A \ , \ \alpha = \alpha(SNR_i) \tag{40}$$

We do this by considering the widest pre-AGC filter case (53.4 MHz = B) in which data rates vary from 4 MSPS to 32 MSPS. First we determine the range of the signal component *rms* voltage A out of the AGC. Consider the noncoherent AGC model as shown in Fig. 4. Denote the input noise power by N_oB and the input signal power at threshold by S_0. Further, denote the gain of the AGC at threshold by g_0, and the total output power by P_T. Then we have

$$g_0 (N_oB + S_0) = P_T \tag{41}$$

or

$$g_0 = \left(\frac{P_T}{N_oB + S_0}\right) \tag{42}$$

At a higher input signal level, S_1, we have

$$g_1 (N_oB + S_1) = P_T \tag{43}$$

or

$$g_1 = \left(\frac{P_T}{N_oB + S_1}\right) \tag{44}$$

where g_1 is the AGC gain when the input signal power is S_1.

The output signal power component for each case is

$$P_0 = S_0 g_0 \tag{45}$$

$$P_1 = S_1 g_1 \tag{46}$$

Hence, the dynamic range of the output signal power is given by

$$\frac{P_1}{P_0} = \frac{g_1 S_1}{g_0 S_0} = \frac{N_o B + S_0}{N_0 B + S_1} \frac{S_1}{S_0} \tag{47}$$

or

$$\frac{P_1}{P_0} = \left[\frac{1}{\frac{N_o B}{S_1} + 1}\right]\left[1 + \frac{N_o B}{S_0}\right] \tag{48}$$

Then, when the final *SNR* is very large, Eq. (48) approaches

$$\frac{P_1}{P_0} = SNR_0^{-1} + 1 \tag{49}$$

where SNR_0 is the input *SNR* at threshold, i.e.,

$$SNR_0 = \frac{S_0}{N_o B} \tag{50}$$

Now the direct component loop gain $GK_V K_L T_M$ increases by the ratio $\alpha_1 r/\alpha_0$ where (α_1/α_0) is the ratio of limiter suppression factors. The suppression factor is given by

$$\alpha \cong \text{erf}\left(\sqrt{\frac{E_s}{N_o}}\right) \tag{51}$$

where

$$\text{erf}(x) = \frac{2}{\sqrt{\pi}} \int_o^x e^{-y^2} dy \tag{52}$$

The signal voltage ratio into the loop (out of the *AGC*) is given by

$$\frac{A_1}{A_0} = \frac{\sqrt{g_1 s_1}}{\sqrt{g_0 s_0}} = \frac{\sqrt{P_1}}{\sqrt{P_0}} = r \tag{53}$$

At the lowest data rates (4 MSPS) in which the 53.4 MHz bandpass filter is used and at the lowest value of E_s/N_o (-4 dB), we find that the *SNR*, in 53.4 MHz, is given by

$$SNR_o = \frac{E_s}{N_o} \frac{R_s}{B} = -15.1 \text{ dB} \tag{54}$$

The limiter suppression factor is equal to

$$\alpha_0 = \text{erf}(\sqrt{0.398}) = 0.627 \tag{55}$$

At the maximum data rate (32 MSPS) and the maximum value of E_s/N_o we find that the *SNR* in 53.4 MHz is

$$SNR_1 = \frac{E_s}{N_o} \frac{R_s}{B} = 9.8 \text{ dB} \tag{56}$$

and the corresponding limiter value is equal to

$$\alpha_1 = \text{erf}(\sqrt{15.8}) \cong 1.0 \tag{57}$$

Therefore the direct component loop gain at the maximum data rate and the maximum value of E_s/N_o, assuming that it is set to threshold at the lowest data rate (4 MSPS) and lowest value of E_s/N_o (-4 dB), is given by

$$r \frac{\alpha_1}{\alpha_0} G_0 K_L K_V T_4 = 3.48 \times 10^{-2} \tag{58}$$

where we have used Eqs. (48), (53), (55), (57) and the fact that $G_0 K_L K_V T_4 = 3.904 \times 10^{-3}$ at threshold. We conclude that the gain margin (*GM*) is

$$GM = 20 \log\left(\frac{2}{3.48 \times 10^{-2}}\right) = 35.2 \text{ dB} \tag{59}$$

when $M = 4$. It, therefore, is clear that the loop is quite stable.

IV. Conclusion

In the present digital Costas loop design with $M = 4$, there is about 35 dB of gain margin. Further refinement in the model will be discussed in a later report.

References

1. S. C. Gupta, *Transform and State Variable Methods in Linear Systems*, John Wiley & Sons, New York, 1966.
2. C. J. Savant, *Basic Feedlock Control System Design*, Chapter 4, McGraw-Hill Book Company Inc., New York, 1958.

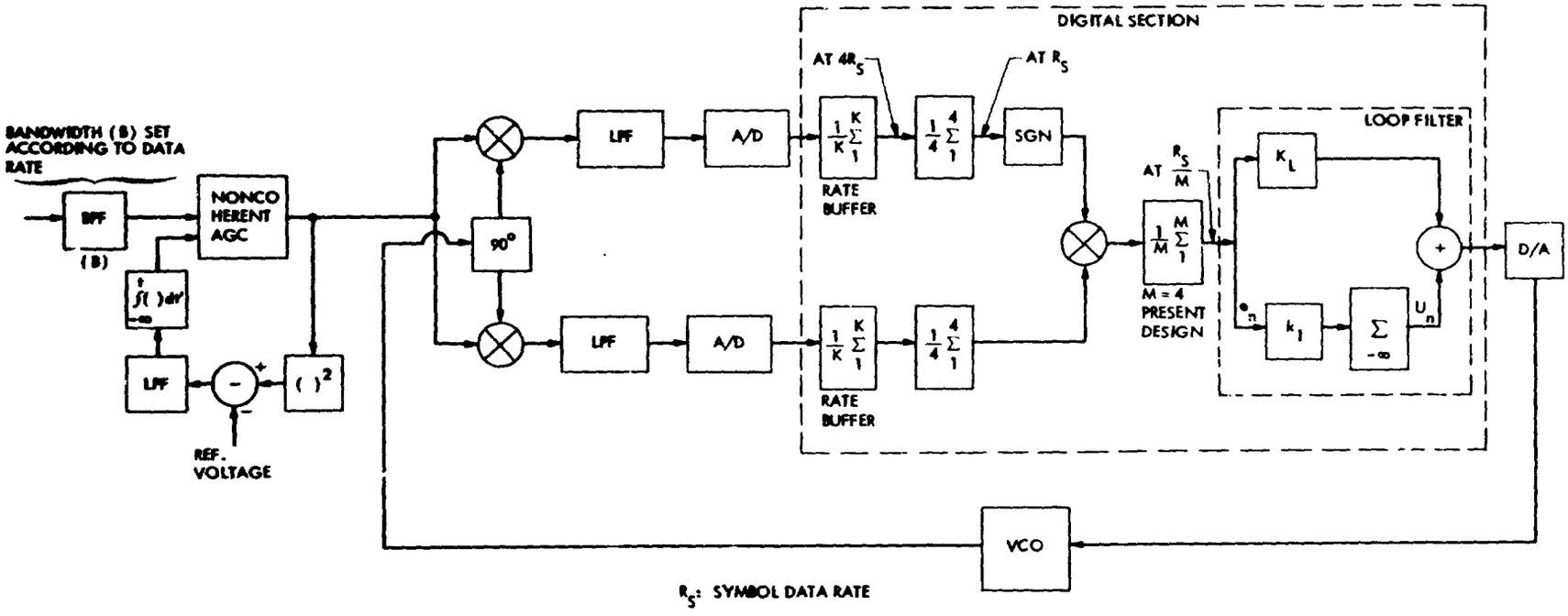

Fig. 1. Model of current multimegabit carrier mode (Costas loop) in tracking

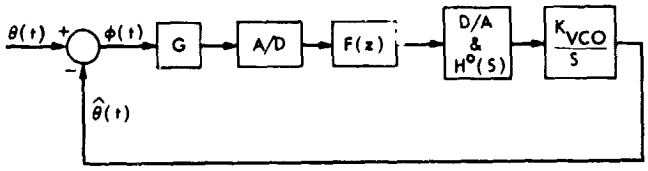

D/A: DIGITAL TO ANALOG CONVERTER

G: LOOP GAIN

$H^o(S)$: ZERO ORDER HOLD

Fig. 2. Equivalent linear phase lock loop model

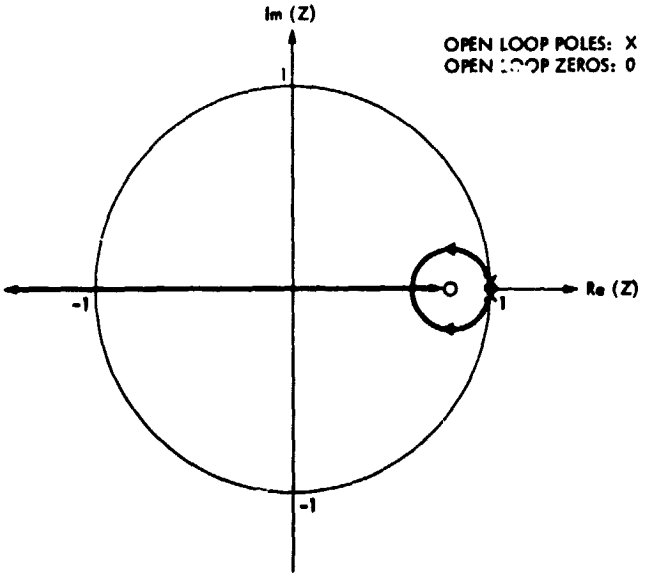

Fig. 3. Root locus of multimegabit digital Costas loop (second order)

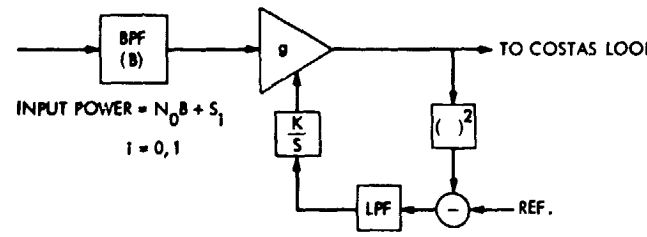

A = OUTPUT SIGNAL VOLTAGE = $\sqrt{P}$

$gS_i = P_i$ = OUTPUT SIGNAL POWER

P_T = TOTAL OUTPUT POWER

B = SELECTED ACCORDING TO DATA RATE

Fig. 4. Noncoherent AGC model for determining dynamic range

N79-25094

Pre-A/D Filter and AGC Requirements for Multimegabit Telemetry Data Detection

J. K. Holmes
Communications Systems Research Section

This article presents a candidate pre-A/D filter bandwidth versus data rate design for the Multimegabit Telemetry Demodulator/Detector, which is based on considerations of A/D bias, quantization errors, and automatic gain control (AGC) effects, as well as the deleterious effects of filtering.

Two methods of gain control of the input level to the A/D converter are considered. The first method uses a particular value of gain, according to which bandwidth is selected. The second method uses a second narrowband noncoherent AGC (in the LPF bandwidth) to attempt to keep the A/D input level constant. This second method reduces the BER degradation slightly but appears to be more difficult to implement.

I. Introduction

The purpose of this article is to develop a table of data rates vs the pre-A/D low-pass filter requirements for data detection (as an initial design) for the Multimegabit Telemetry Demodulator/Detector assembly, and to specify the types and the number of automatic gain controls (AGCs) needed. To do this task, it was required to consider the bit error rate (BER) degradation due to the effects of AGCs, A/D quantization, A/D bias, phase detector saturation, and the number of AGCs required. The system under consideration is shown, in a simplified form, in Fig. 1. Since data demodulation was the primary concern, the upper arm of Fig. 1 is the system under primary investigation.

The system philosophy is to arrange the sample rate, via the rate buffers, so that the internal sample rate out of the rate buffers is at four times the data symbol rate. Further, internal sample rates (data handling rates) are reduced to one fourth the symbol rate into the loop filter.

The noncoherent AGC is important also since the signal component variations out of the phase detectors (multipliers) can tolerate only so much dynamic variation before they are affected by dc offsets at weak signal conditions or, at the other end, limiting occurs at strong signal plus noise power conditions.

The narrowband noncoherent AGC, if used, can better control the signal and noise over the data rate extremes for a given filter bandwidth than can the gain set approach that fixes the gain for a particular bandwidth (see Fig. 1). However, the advantage in reduction of BER degradation is rather small and the implementation advantage of the filter-determined gain

select might well be the overriding factor favoring the latter approach.

Based on the functional requirement description the symbol error rate degradation is 0.5 dB from theoretical below 10 Msps and 1 dB from theoretical above 10 Msps, for symbol $SNR\ E_S/N_o \geq -4$ dB.

II. Dynamic Range Considerations

First we consider the dynamic range requirements of the wideband noncoherent AGC [see Fig. 1] having pre-AGC noise bandwidth B. From Ref. 1, the ratio of the signal power component out of a noncoherent AGC at an input SNR given by $SNR_0 = \alpha_0 S_0 / N_o B$, to the signal power component out of the AGC at an input SNR given by $SNR_1 = \alpha_1 S_1 / N_o B$ was shown to be (see Fig. 2).

$$\frac{P_1}{P_0} = \left[\frac{1}{\frac{N_o B}{\alpha_1 S_1} + 1}\right] \left[1 + \frac{N_o B}{\alpha_0 S_0}\right] \tag{1}$$

where N_o is the one-sided noise spectral density, B is the noise bandwidth of the BPF preceding the noncoherent AGC, α_i $(i = 0, 1)$ is the filter loss through the BPF, and S is the unfiltered input signal power. This result, Eq. (1), applies to both the wideband and narrowband noncoherent AGC's.

Now we shall determine the dynamic range of signal power out of the noncoherent AGC. First determine the minimum wideband noncoherent AGC input SNR. The minimum value of E_s/N_o is given by

$$\left(\frac{E_s}{N_o}\right)_{min} = -4 \text{ dB} \tag{2}$$

So that the minimum AGC input SNR is given by

$$\frac{\alpha_0 S_0}{N_o B} = \left(\frac{E_s}{N_o}\right)_{min} (\alpha_0) \left(\frac{R_s}{B}\right) = -31 \text{ dB} \tag{3}$$

where the bandpass filter has a bandwidth of $B = 60$ MHz, and the minimum symbol rate (R_s) of 125,000 sps through it, and $\alpha_0 \cong 1$.

The maximum value of E_s/N_o is given by:

$$\left(\frac{E_s}{N_o}\right)_{max} = +12 \text{ dB} \tag{4}$$

Therefore the maximum value of the AGC input SNR is given as

$$\frac{\alpha_1 S_1}{N_o B} = \left(\frac{E_s}{N_o}\right)_{max} (\alpha_1) \left(\frac{R_s}{B}\right) \sim 8.7 \text{ dB} \tag{5}$$

for the maximum E_s/N_o value and maximum symbol rate of 32 Msps and with $\alpha_1 = 0.87$. Therefore, the ratio of maximum-to-minimum wideband noncoherent signal power is, by Eq. 1,

$$\frac{P_1}{P_0} \sim 31.2 \text{ dB} \tag{6}$$

It follows that the dynamic range of the phase detectors (multipliers) must be 31.2 dB. If this dynamic range is too large, one option to reduce it would be to narrow the bandpass filter bandwidth at the lower data rates by, say, 10 dB so that the effective dynamic range would be only about 21 dB.

III. Approximate BER Degradation due to Quantization and dc Offsets

The Computer Labs MOD-4100 A/D converter was chosen for the multimegabit system. It has a dc accuracy of 10 MV ± 1/2 of the least significant bit. It has four-bit resolution so that we have four bits per sample. We consider the worst case data rate range[1] when the rate buffer sets $k = 1$, and therefore the statistic (a sample and dump filter), based on sampling four samples per bit on which bit decisions are made, is

$$e_o = \sum_{i=1}^{4} \left\{ g\left(\sqrt{\alpha}\, A_i + N_i\right) + b_i + \epsilon_i \right\} \tag{7}$$

where A_i is the sampled signal voltage, N_i is the sampled noise voltage, b_i is the sampled dc bias, α is now the power filtering loss through the low-pass filters (having bandwidth B_{LP}), g is the product of AGC voltage gains, and ϵ_i is the sampled quantization error. Based on this statistic, we will derive an expression for the matched filter output SNR in terms of the quantization spacing, ΔL, and the bias b. Since our analysis is

[1] See Table 1.

only meant to be approximate, we neglect intersymbol interference, which will be (approximately) accounted for by a separate calculation.

First note that (letting $E(\cdot)$ denote the ensemble average)

$$E\left[N_i^2\right] = N_o B_{LP} \tag{8}$$

with B_{LP} being the low-pass filter bandwidth preceding the A/D converter. Now the mean output signal of the sample and dump filter (just before dumping) is given by

$$E[e_o] = \sum_{i=1}^{4} \left(g\sqrt{\alpha}A_i + b_i\right) = 4g\sqrt{\alpha}A + 4b \tag{9}$$

assuming the voltages satisfy $A_i = A$ and $b_i = b$ with α being the power loss due to filtering of the LPF (see Fig. 1)[2]. The variance of the output statistic is given by

$$\text{Var}(e_o) = E\sum_{i=1}^{4} g^2 N_i^2 + E\sum_{i=1}^{4} \epsilon_i^2 \tag{10}$$

If ΔL is the quantizer spacing, then (assuming a uniform distribution)

$$E\left[\epsilon_i^2\right] = \frac{(\Delta L)^2}{12} \tag{11}$$

Therefore, the output SNR is given by

$$SNR_o \cong \frac{(4gA\sqrt{\alpha} + 4b)^2}{4g^2 N_o B_{LP} + \dfrac{(\Delta L)^2}{3}} \tag{12}$$

Rearranging, and using the fact that the symbol duration $T = 4T_s$, with T_s being the time between samples, we obtain

$$SNR_o \cong \frac{2E_s}{N_o}\left[\frac{\alpha\left(1 + \dfrac{b}{g\sqrt{\alpha}A}\right)^2}{1 + \dfrac{(\Delta L)^2}{12N_o B_{LP} g^2}}\right] \tag{13}$$

[2]This is a first-order correction for the effect due to filtering.

where we have used $2T_s \cong 1/B_{LP}$. The bracketed term is the degradation in terms of the quantizer spacing ΔL and the quantizer bias voltage b for a given bit and given bias.

The Computer Labs Mod-4100 A/D Converter has a 4-bit resolution and a maximum input range of ± 2.1 volts, so that

$$\Delta L = 0.2625 \text{ volts} \tag{14}$$

IV. Candidate Filter Bandwidth Versus Data Rate Design

As was mentioned in the introduction, the basic philosophy in the digital demodulator/detector design is to minimize the analog filter count and to set the internal sample rate (processing rate) at four times the data symbol rate out of the rate buffers (see Fig. 1). This way everything after the rate buffers can be scaled according to data rate.

The two basic requirements of operation into the A/D converter are, one, that the signal plus n_a times the rms noise be less than the one-sided A/D input voltage range, or

$$g_{WB}g_{NB}\sqrt{\alpha}A + n_a g_{WB}g_{NB}\sqrt{N_o B_{LP}} \leq V \tag{15}$$

The second requirement is that the signal voltage into the A/D converter shall always be bigger than b, or:

$$g_{WB}g_{NB}\sqrt{\alpha}A \geq b\,n_b \tag{16}$$

where g_{WB} is the noncoherent wideband voltage AGC gain, g_{NB} is the noncoherent narrowband voltage AGC gain, V is the one-sided quantizer input range, and n_a and n_b are confidence safety factors (numbers greater than one). To keep the BER degradation down to around 0.5 dB or less, below 10 Msps, $B_{LP}T$ should be greater than about 1.7 (Ref. 2). Above 10 Msps, $B_{LP}T$ should be greater than 0.8 to hold the BER degradation to about 1 dB (Ref. 2).

Table 1 illustrates a candidate filter design that requires six analog low-pass filter pairs (B_{LP}'s) and should keep the symbol BER just about within specifications.

V. Comparison of the Filter-Controlled Gain Approach With the Coherent AGC Approach

In this section we will compare the relative performance for the case that the signal plus noise into the A/D is controlled by

a fixed gain, set according to the low-pass filter bandwidth on one hand, and to the narrowband noncoherent AGC to control the signal plus noise into the A/D on the other hand. We will consider the 26.7-MHz filter data rate range since it operates over the largest data rate range.

Case I: filter bandwidth controlled gain

First we consider the case when the selection of a particular low-pass filter pair specifies a fixed gain into the A/D converter based on achieving acceptable bit error rate degradation.

At the highest data rate (32 Msps) and at an E_s/N_o (3 dB), which will provide a nominal maximum bit error rate of 1×10^{-5}, we require that Eq. (15) be satisfied as follows:

$$g_{WB_1} g_o \left[\sqrt{\alpha_1} A_1 + n_a \sqrt{N_o B_{LP}}\right] \leq V = 2.1 \text{ volts} \tag{17}$$

where g_o is the filter-controlled gain value fixed to the 26.7-MHz filter. This gain g_o is in lieu of the narrowband gain g_{NB}.

At the lowest data rate (4 Msps), for the same filter, and the same gain setting, g_o, and with the minimum E_s/N_o (-4 dB), we require that Eq. (16) satisfy:

$$g_{WB_2} g_o \sqrt{\alpha_2} A_2 = n_b b \tag{18}$$

where $b = 0.01$ volts and n_b should be at least 3 and preferably larger, and the subscript 2 denotes a different level of that variable. Now using $E_s/N_o = 2.0$ (3 dB) we conclude that the SNR into the AGC (see Fig. 1) satisfies

$$SNR_{LP} = \frac{\alpha_1 A_1^2}{N_o B_{LP}} = \frac{2.0}{\left(\frac{P_{LP} T}{\alpha_1}\right)} \tag{19}$$

Letting $n_a = 3.0$, which is equivalent to considering a 3σ noise amplitude, we obtain from Eqs. (17) and (19)

$$g_{WB_1} g_o \sqrt{N_o B_{LP}} \left[3 + \sqrt{\frac{2.0}{\frac{B_{LP} T}{\alpha_1}}}\right] = 2.1 \text{ volts} \tag{20}$$

Now since $B_{LP}T = 0.83$ at this maximum symbol rate (see Table 1) we can determine the filtering loss to be $\alpha_1 = 0.87$, assuming an ideal low-pass filter preceding the A/D converter. It follows from Eq. (20), with the fact that $B_{LP}T = 0.83$ and $\alpha_1 = 0.87$, that the rms noise voltage into the A/D converter is given by

$$g_{WB_1} g_o \sqrt{N_o B_{LP}} = 0.472 \text{ volts} \tag{21}$$

From Eq. (17), it follows that the signal voltage into the A/D converter is given by

$$g_{WB_1} g_o \sqrt{\alpha_1} A_1 = 0.684 \text{ volts} \tag{22}$$

Now it is easy to check to see if the condition of Eq. (18) has been satisfied. We have

$$n_b = \frac{g_{WB_1} g_o \sqrt{\alpha_1} A_1}{b} = \frac{0.684}{0.01} = 68.4 \tag{23}$$

which, as we shall see, causes a negligible degradation.

From Eqs. (13), (14), (21), and (23), the resulting degradation[3] due to bias and quantization only (the filtering losses will be considered below) is

$$DEGR(A_1) = \frac{\left(1 + \frac{b}{\sqrt{\alpha_1} A_1 g_o g_{WB_1}}\right)^2}{1 + \frac{(\Delta I)^2}{12 N_o B_{LP} g_o^2 g_{WB_1}^2}}$$

$$= \frac{\left(1 - \frac{1}{68.4}\right)^2}{1 + \frac{1}{12}\left[\frac{0.2625}{0.472}\right]^2} \tag{24}$$

or

$$DEGR(A_1) = 0.24 \text{ dB} \tag{25}$$

Now consider the degradation due to filtering, which includes power loss, distortion, and intersymbol interference effects.

[3] This equation is somewhat a worst case since it assumes the bias is always "bucking" the signal.

Since the baseline LPFs are 2-pole filters with $B_{LP}T = 0.83$, we have that the loss, from Ref. 2,[4] is about 0.6 dB. Therefore, the total degradation of about 0.84 dB is to be expected at the maximum data rate (32 Msps). Hence using B_{LP} = 26.7 MHz and a symbol rate of 4 Msps at E_s/N_o = 3 dB we have

$$DEGR_{TOT} = 0.84 \text{ dB} \tag{26}$$

This degradation does not include carrier loop or bit synchronization loop tracking inaccuracies. When E_s/N_o = −4 dB again at the highest data rate it can be shown that the degradation increases less than 0.1 dB so that the total degradation is about 0.9 dB.

Equations (21) and (22) apply to the case the highest data rate is in effect along with the assumption that the symbol-to-noise spectral density ratio is 3 dB and the gains, g_o and g_{WB_1} are set to satisfy Eq. (17) at E_s/N_o = 3 dB.

Now consider the case that the lowest admissible data rate (4 Msps) of the 26.7 megahertz filter is used (see Table 1) and the E_s/N_o ratio is minimum (−4 dB). Since the same LPF bandwidth is used, the gain g_o will be unchanged. However, the wideband noncoherent AGC will change gain since the signal power has been reduced. To compute the new gain level of the noncoherent AGC, we equate the noncoherent output power under strong and weak signal conditions so that

$$g_o^2 g_{WB_1}^2 \left[\alpha_1 A_1^2 + N_o B\right] = g_o^2 g_{WB_2}^2 \left[\alpha_2 A_2^2 + N_o B\right] \tag{27}$$

From Eq. (27) we can obtain the ratio of gains:

$$\frac{g_{WB_2}}{g_{WB_1}} = \sqrt{\frac{SNR_1 + 1}{SNR_2 + 1}} \tag{28}$$

where the SNRs out of the filter preceding the wideband AGC is given by

$$SNR_1 = \frac{\alpha_1 A_1^2}{N_o B} \tag{29}$$

$$SNR_2 = \frac{\alpha_2 A_2^2}{N_o B} \tag{30}$$

[4]The degradations computed here were at a BER = 10^{-5}, and were the only ones available.

We can now compute the SNRs in the bandwidth B:

$$SNR_1 = \left(\frac{E_s}{N_o}\right)_1 \alpha_1 \left(\frac{R_{s_1}}{B}\right) = 2(0.87)\left(\frac{32}{60}\right) = 0.9289 \tag{31}$$

$$SNR_2 = \left(\frac{E_s}{N_o}\right)_2 \alpha_2 \left(\frac{R_{s_2}}{B}\right) = 0.398(0.99)\left(\frac{4}{60}\right) = 0.0263 \tag{32}$$

It follows from Eqs. (28), (31), and (32) that

$$\frac{g_{WB_2}}{g_{WB_1}} = \sqrt{\frac{1 + 0.9289}{1 + 0.0263}} = 1.372 \tag{33}$$

We can now compute the new noise power associated with the lower symbol rate and lower E_s/N_o. From Eqs. (21) and (33), we obtain

$$g_o g_{WB_2} \sqrt{N_o B_{LP}} = g_o g_{WB_1} \sqrt{N_o B}\,(1.372) = 0.648 \text{ volts} \tag{34}$$

illustrating the fact that the noise level has increased from the strong signal result of Eq. (21).

From Eq. (22) we can compute the new signal voltage into the A/D converter

$$\left(g_o g_{WB_2} \sqrt{\alpha_2} A_2\right)^2 = \left(g_o g_{WB_1} \sqrt{\alpha_1} A_1\right)^2 \downarrow 7 \text{ dB} \downarrow 10 \log\left(\frac{32}{4}\right) \uparrow 10 \log\left(\frac{0.99}{0.87}\right) \uparrow 20 \log(1.372) \tag{35}$$

where, for example, ↓ 7 dB means reduce the previous quantity by 7 dB. We have

$$g_o g_{WB_2} \sqrt{\alpha_2} A_2 = 0.158 \text{ volts} \tag{36}$$

From Eqs. (13), (34), and (36) the resulting degradation (neglecting the filtering loss) is

$$DEGR\,(A_2) = \frac{\left(1 - \frac{0.01}{0.158}\right)^2}{1 + \frac{1}{12}\left[\frac{0.625}{0.648}\right]^2} = 0.63 \text{ dB} \quad (37)$$

Now the filtering losses with the low data rate corresponding to $B_{LP}T = 6.68$ obtained from Ref. 2 is 0.10 dB, so that the total degradation at $E_s/N_o = -4$ dB and at a symbol rate of 4 Msps is given by

$$DEGR_{TOT} = 0.73 \text{ dB} \quad (38)$$

By comparing Eqs. (26) and (38), it is clear that the high data rates suffer greater BER degradation.

Case II: narrowband noncoherent AGC controlled gain

Now we consider the case where a narrowband noncoherent AGC is used to control the signal-plus-noise level into the A/D converter, rather than a fixed gain in addition to the wideband noncoherent AGC. Using the same initial gain conditions at the high E_s/N_o (3 dB) as in the fixed gain method, we have from Eqs. (21) and (22),

$$g_{NB_1} g_{WB_1} \sqrt{N_o B_{LP}} = 0.472 \text{ volts} \quad (39)$$

and

$$g_{NB_1} g_{WB_1} \sqrt{\alpha_1} A_1 = 0.684 \text{ volts} \quad (40)$$

and, further the same degradations occur as before since the signal voltage and noise voltage are the same. Therefore, the total loss is as before (Eq. (26))

$$DEGR_{TOT} = 0.84 \text{ dB} \quad (41)$$

Now we consider the effect of both the wideband and narrowband noncoherent AGCs at the lowest symbol rate (4 Msps) and minimum E_s/N_o (-4 dB) for the 26.7-MHz filter. The wideband noncoherent AGC sets the gain as before, from Eq. (33), and increases with weaker input signal by the ratio

$$\frac{g_{WB_2}}{g_{WB_1}} = 1.372 \quad (42)$$

Notice that the narrowband AGC output power is determined by Eqs. (39) and 40), i.e.,

$$\left(g_{NB_1} g_{WB_1}\right)^2 \left(N_o B_{LP} + \alpha_1 A_1^2\right) = 0.831 \text{ volts}^2 \quad (43)$$

Now since the wideband noncoherent AGC gain has increased by the factor 1.372 (Eq. 42), we find that the new noise voltage and signal voltage into the narrowband AGC are given by

$$g_{WB_2} g_o \sqrt{N_o B_{LP}} = (1.372)(0.472) = 0.648 \text{ volts} \quad (44)$$

and

$$\left(g_{WB_2} g_o \sqrt{\alpha_2} A_2\right)^2 = (0.684)^2 \left(\downarrow 7 \text{ dB} \downarrow 10 \log \left(\frac{32}{4}\right) \uparrow 10 \log \left(\frac{0.99}{0.87}\right) \uparrow 20 \log (1.372)\right)$$

or

$$g_{WB_2} g_o \sqrt{\alpha_2} A_2 = 0.158 \text{ volts} \quad (45)$$

The result of Eq. (45) can be verified using Eq. (1) directly. Now the narrowband noncoherent AGC gain must be set so that the total power given by Eq. (43) is maintained at the output; therefore, it must be true, using Eqs. (43), (44), and (45), that

$$\left(\frac{g_{NB_2}}{g_{NB_1}}\right)^2 \left[(0.648)^2 + (0.158)^2\right] = 0.831 \quad (46)$$

or

$$\frac{g_{NB_2}}{g_{NB_1}} = 1.37 \quad (47)$$

Therefore, the signal voltage out of the narrowband noncoherent AGC is given by

$$g_{WB_2} g_{NB_2} g_o \sqrt{\alpha_2} A_2 = 0.158 \times 1.37 = 0.216 \text{ volts} \quad (48)$$

$$g_{WB_2} g_{NB_2} g_o \sqrt{N_o B_{LP}} = 0.648 \times 1.37 = 0.888 \text{ volts} \quad (49)$$

From the degradation result, Eq. (13), this new signal and noise level produce a degradation of

$$DEGR(A_2) = \frac{\left(1 - \frac{0.01}{0.216}\right)^2}{1 + \frac{1}{12}\left(\frac{0.2625}{0.888}\right)^2} = 0.44 \text{ dB} \quad (50)$$

The degradation due to filtering when $B_{IF}T = 6.68$ was already found to be 0.10 dB so that the total degradation is

$$DEGR_{TOT} = 0.54 \text{ dB}$$

VI. Conclusions

An initial low-pass pre-A/D converter filter bandwidth versus coded symbol rate table has been constructed and shown to meet the essential BER degradation specification while requiring only six low-pass filter pairs.

Further refinements in the BER degradation will be considered in a later DSN article.

References

1. J. K. Holmes, "Stability Analysis of the DSN Multimegabit Telemetry Demodulator/Detector Design," *DSN Progress Report* 42-51 (this issue).

2. J. J. Jones, "Filter Distortion and Intersymbol Interference Effects on PSK Signals," *IEEE Transactions on Communication Technology*, *Com-19*, No. 2, April 1971.

Table 1. Candidate filter BW vs symbol rate

Data rate R_S, Msps[a]	LPF BW B_{LP}, MHZ	Sampling rate 6_S, Msps[a]	Rate buffer divisor k	$6_S / B_{LP}$[a]	Samples per Symbol
16 → 32	26.7	64 → 128	1	2.4 → 4.8	4
8 → 16	26.7	64 → 128	2	2.4 → 4.8	8
4 → 8	26.7	64 → 128	4	2.4 → 4.8	16
2 → 4	13.35	32 → 64	4	2.4 → 4.8	16
1 → 2	6.68	16 → 32	4	2.4 → 4.8	16
0.5 → 1	3.34	8 → 16	4	2.4 → 4.8	16
0.25 → 0.5	1.67	4 → 8	4	2.4 → 4.8	16
0.125 → 0.25	0.83	2 → 4	4	2.4 → 4.8	16

[a]The notation 16 → 32 denotes the range of 16 to 32 Msps. For example, a data rate of 32 Msps corresponds to a sampling rate of 128 Msps and a ratio of data rate to low-pass filter BW of 4.8.

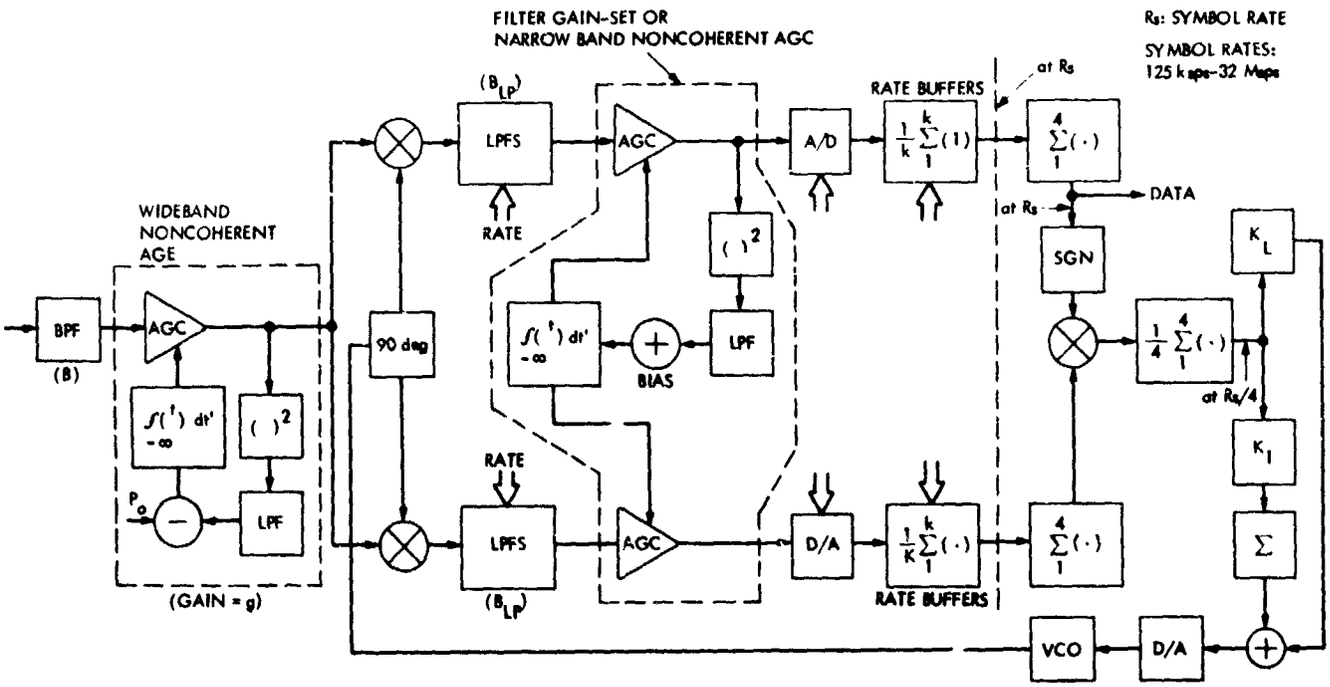

Fig. 1. Partial functional block diagram of the feasibility model, Multimegabit Demodulator/Detector Assembly

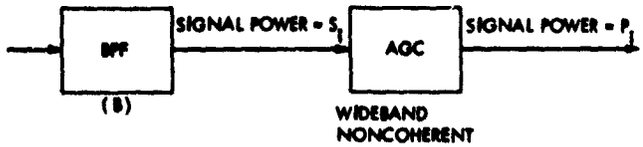

Fig. 2. Block diagram showing AGC input signal power, S_i, and its output signal power, P_i

N79-25095

Recovering the Spectrum of a Narrow-band Process From Syncopated Samples

P. H. Milenkovic
Communications Systems Research Section

Losslessly sampling a band-limited narrow-band process at an average rate equal to the Nyquist rate may require a nonuniform sampling strategy. One such strategy is phase quadrature sampling, in which a process of bandwidth B is sampled at rate B in each of two channels where the two channels are $\pi/2$ out of phase at frequency B. Phase quadrature sampling is a special case of syncopated sampling, where the phase between channels is fixed but arbitrary. A simple method for recovering the spectrum of the input process from syncopated samples is derived. The derivation indicates what values of phase between channels result in lossless sampling.

I. Introduction

Band-limited narrow-band processes can be losslessly sampled at rates which correspond to the Nyquist rate for the passband width rather than a rate of twice the highest frequency present. This is accomplished by sampling at periodic but nonuniform intervals (Refs. 1, 2 and 3). Time domain interpolation formulas are known for recovering the original process from such samples (Refs. 1 and 2). The general approach is based upon syncopated sampling, where a process of bandwidth B is sampled in two channels at a uniform rate B in each channel and a phase offset θ between channels. With phase quadrature sampling, θ is equal to $\pi/2$, or one-fourth, of a sample interval. A simple method for recovering the spectrum from two channels of samples is derived.

The current motivation for studying syncopated sampling is the Wide Band Data Acquisition System (WBDAS), which is used to collect data for Very Long Baseline Interferometry (VLBI) clock synchronization measurements (Ref. 3). The signal entering WBDAS from a station receiver is centered at 50 MHz and has been bandpass filtered so that most of its energy is in the range from 25 to 75 MHz. The WBDAS samples, quantizes, and records this signal.

In the WBDAS, phase quadrature sampling is employed. What this does to the signal is similar to what is done by single sideband demodulation, but without the side effect of signal group delay from an analog demodulator. The narrow-band signal $s(t)$ going into the sampler can be expressed in terms of cosine and sine components, $x(t)$ and $y(t)$, relative to the $\omega_o = 2\pi$ (50 MHz) center frequency:

$$s(t) = x(t)\cos(\omega_o t) + y(t)\sin(\omega_o t) \qquad (1)$$

Both $x(t)$ and $y(t)$ are baseband processes of bandwidth 25 MHz. The in-phase channel samples are taken at times nT

and the quadrature phase channel samples are taken at times $(n + 1/4)T$ where n is an integer and T is 20 nsec. The in-phase channel samples are:

$$\begin{aligned} s(nT) &= x(nT) \cdot 1 + y(nT) \cdot 0 \\ &= x(nT) \end{aligned} \tag{2}$$

and the quadrature channel samples are:

$$\begin{aligned} s\left[\left(n+\tfrac{1}{4}\right)T\right] &= x\left[\left(n+\tfrac{1}{4}\right)T\right] \cdot 0 + y\left[\left(n+\tfrac{1}{4}\right)T\right] \cdot 1 \\ &= y\left[\left(n+\tfrac{1}{4}\right)T\right] \end{aligned} \tag{3}$$

The two channels contain uniform samples at the Nyquist rate for $x(t)$ and $y(t)$, respectively. The quadrature sampling scheme can thus be intuitively viewed as a combination of demodulation and uniform sampling.

Uniformly sampling $s(t)$ at a rate equal to the average rate of the phase quadrature scheme will result in the loss of information. Sampling at times nT, where T is 10 nsec, gives the following result from Eq. (1):

$$s(nT) = x(nT)(-1)^n \tag{4}$$

The result is that while $x(t)$ has been sampled at a rate of 100 MHz or twice the Nyquist rate for a 25 MHz baseband signal, $y(t)$ has been completely lost.

II. Recovering the Spectrum

The spectrum of a band-limited narrow-band process of bandwidth B will be recovered from two channels of uniform samples taken at rate B where the two channels are offset by a phase θ. Being able to recover the spectrum indicates that the sampling is lossless as the process can be recovered by taking the inverse Fourier transform of its spectrum. This syncopated sampling scheme gives us the spectrum for any center frequency of the narrow-band process. One restriction is that given the center frequency, there are values of θ for which the method breaks down; these values are specified here.

The input signal $x(t)$ is sampled by two impulse trains $s_1(t)$ and $s_2(t)$ where:

$$s_1(t) = \sum_{m=-\infty}^{\infty} T\delta(t - mT) \tag{5}$$

$$s_2(t) = \sum_{m=-\infty}^{\infty} T\delta[t - (mT + T_o)] \tag{6}$$

T = sampling interval for both channels

T_o = time offset between the two channels

The resulting sampled signals on the two sampling channels are:

$$x_1(t) = s_1(t)x(t) \tag{7}$$

and

$$x_2(t) = s_2(t)x(t) \tag{8}$$

Next, the effect of sampling in the frequency domain is considered. Fourier transform pairs are denoted as follows, using capitals in the frequency domain:

$$X(f) \leftrightarrow x(t)$$

$$X_1(f) \leftrightarrow x_1(t)$$

$$X_2(f) \leftrightarrow x_2(t)$$

The sampling functions can be written in the time domain as a sum of exponentials:

$$s_1(t) = \sum_{m=-\infty}^{\infty} e^{2\pi jmt/T} \tag{9}$$

$$s_2(t) = \sum_{m=-\infty}^{\infty} e^{-jm\theta} e^{2\pi jmt/T} \tag{10}$$

where $\theta = 2\pi T_o/T$

The frequency translation theorem $X(f + f_o) \leftrightarrow x(t)e^{2\pi if_o t}$ results in:

$$X_1(f) = \sum_{m=-\infty}^{\infty} X\left(f + \frac{m}{T}\right) \tag{11}$$

$$X_2(f) = \sum_{m=-\infty}^{\infty} e^{-jm\theta} X\left(f + \frac{m}{T}\right) \tag{12}$$

The purpose of this discussion is to describe circumstances under which $X(f)$ can be recovered from $X_1(f)$ and $X_2(f)$. Suppose $x(t)$ is band-limited to the range $f_\ell < f < f_\ell + 1/T$ and

$-1/T - f_\ell < f < -f_\ell$. Then for $f_\ell < f < f_\ell + 1/T$, Eqs. (11) and (12) reduce to:

$$X_1(f) = X(f) + X\left(f + \frac{\hat{m}}{T}\right) \tag{13}$$

$$X_2(f) = X(f) + e^{-j\hat{m}\theta} X\left(f + \frac{\hat{m}}{T}\right) \tag{14}$$

where $\hat{m}$ in an integer function of f satisfying:

$$-f_\ell - \frac{1}{T} < f + \frac{\hat{m}}{T} < -f_\ell \tag{15}$$

It then follows that:

$$\begin{aligned} &\text{(i) } X(f) = \frac{X_1(f) - e^{j\hat{m}\theta} X_2(f)}{1 - e^{j\hat{m}\theta}} \text{ for } f_\ell < f < f_\ell + \frac{1}{T} \\ &\text{(ii) } X(f) = X^*(-f) \text{ for } -f_\ell - \frac{1}{T} < f < -f_\ell \\ &\text{(iii) } X(f) = 0 \text{ elsewhere} \end{aligned} \tag{16}$$

where * denotes complex conjugation. Property (ii) is a consequence of $x(t)$ being real valued.

III. Examples

In this section, the method for computing $X(f)$ is applied to specific cases. First $X_1(f)$ and $X_2(f)$ are expressed in terms of the samples:

$$\begin{aligned} X_1(f) &= \int_{-\infty}^{\infty} x_1(t)\, e^{-2\pi jft}\, dt \\ &= T \sum_{m=-\infty}^{\infty} x(mT)\, e^{-2\pi jfmt} \end{aligned} \tag{17}$$

$$\begin{aligned} X_2(f) &= \int_{-\infty}^{\infty} x_2(t)\, e^{-2\pi jft}\, dt \\ &= T e^{-j\theta fT} \sum_{m=-\infty}^{\infty} x(mT + T_o)\, e^{-2\pi jfmT} \end{aligned} \tag{18}$$

A. Uniform Sampling

The first case is uniform sampling on one channel of a baseband signal of bandwidth $1/T$. The sampling rate is $2/T$, the Nyquist rate. This system can be expressed as two channels of sampling run at rate $1/T$, offset in time by $T/2$. Equation (16) reduces to

$$X(f) = \frac{1}{2}\left[X_1(f) + X_2(f)\right] \tag{19}$$

which by Eq. (17) and (18) results in

$$X(f) = \frac{T}{2} \sum_{n=-\infty}^{\infty} x\left(n\frac{T}{2}\right) e^{-2\pi jfn\frac{T}{2}} \tag{20}$$

which, in fact, corresponds to uniform sampling at rate 2/T on one channel.

B. Quadrature Phase Sampling

The second special case is quadrature phase sampling. Here, the sampling period on each of two channels is T, and the sampling times on the two channels are offset by $T/4$. This type of sampling is applicable to narrow-band signals of bandwidth $1/T$ centered about frequency $1/T$ (or some integer multiple of $1/T$). Considering the signal to be centered about $1/T$:

$$f_\ell = \frac{T}{2} \quad \frac{T}{2} < f < \frac{3T}{2} \quad T_o = \frac{T}{4}$$

$$\hat{m} = -2 \quad \theta = 2\pi\frac{T_o}{T} = \frac{\pi}{2}$$

which by Eq. (16) results in

$$X(f) = \frac{1}{2}\left[X_1(f) + X_2(f)\right] \tag{21}$$

Employing Eqs. (17) and (18) to express $X_1(f)$ and $X_2(f)$ in terms of the samples gives:

$$\begin{aligned} X(f) = \frac{T}{2}\Bigg\{ &\sum_{-\infty}^{\infty} x(mT)\, e^{-2\pi jfmT} \\ &+ \sum_{-\infty}^{\infty} x\left[\left(m + \frac{1}{4}\right)T\right] e^{-2\pi jf\left(m+\frac{1}{4}\right)T}\Bigg\} \end{aligned}$$

$$\frac{T}{2} < f < \frac{3T}{2} \tag{22}$$

For the channel offset T_o differing from $T/4$, one can still formulate $X(f)$ in terms of $X_1(f)$ and $X_2(f)$ by way of Eq.

(16). The quantity θ will differ from $\pi/2$ and the formula will be more complicated than Eq. (21). When the sample offset is $T_0 = T/2$, then $\theta = \pi$ and Eq. (16) becomes singular as $1 - e^{jm\theta}$ becomes zero. Since this corresponds to uniform sampling on one channel, uniform sampling will not work for this passband at the average sample rate used for quadrature phase or syncopated sampling schemes near quadrature phase.

Finally, taking the inverse Fourier transform of Eq. (22) gives the sample reconstruction formula for quadrature phase sampling.

$$x(t) = \sum_{-\infty}^{\infty} x(mT) \frac{\sin\left(\frac{\pi}{T}(t - mT)\right)}{\frac{\pi}{T}(t - mT)} \cos\frac{2\pi t}{T} + \sum_{-\infty}^{\infty} x\left(mT + \frac{T}{4}\right) \frac{\sin\left\{\frac{\pi}{T}\left[t - \left(m + \frac{1}{4}\right)T\right]\right\}}{\frac{\pi}{T}\left[t - \left(m + \frac{1}{4}\right)T\right]} \sin\frac{2\pi t}{T} \tag{23}$$

This formula has been obtained before by working directly in the time domain (see Ref. 2).

References

1. Woodward, P. M., *Probability and Information Theory with Applications to Radar*, pp. 34-35, McGraw-Hill, New York, 1955.

2. Grace, O. D., and Pitt, S. P., "Quadrature Sampling of High-Frequency Waveforms," *Journal of the Acoustical Society of America*, Vol. 44, No. 5, pp. 1453-1454, 1968.

3. Hurd, W. J., "Preliminary Demonstration of Precision DSN Clock Synchronization by Radio Interferometry," *Deep Space Network Progress Report 42-37* pp. 57-68, Jet Propulsion Laboratory, Pasadena, California, February 15, 1977.

4. Ahmed, N., and Rao, K. R., *Orthogonal Transforms for Digital Signal Processing*, Springer-Verlag, Berlin, Heidelberg, New York, 1975.

5. Oppenheim, A. V., and Schafer, R. W., *Digital Signal Processing*, Prentice-Hall, Englewood Cliffs, New Jersey, 1975.

N79-25096

Installation of the Mu2 Ranging System in Australia

A. I. Zygielbaum
Communications Systems Research Section

The Mu2 Ranging System has been installed at DSS 42/43 in Australia. It was used to support the 1979 Viking Relativity Experiment and is currently supporting Voyager Navigation and the Advanced Systems Program. This article describes these tasks as well as Mu2 software and hardware modifications prior to installation.

I. Introduction

In October of 1978, the Mu2 Ranging System was installed at DSS 42/43 in Australia. The Mu2 is a research and development tool which has supported all range transponder-bearing spacecraft since Mariner Venus Mercury 1973. It has provided the data required by several Theory of Relativity experiments and investigations into the nature of the solar corona In the present case the Mu2 corroborated laboratory research by utilizing the Voyager 1 and 2 spacecraft and obtained data for the Viking Project Test of General Relativity. This article reports the rationale leading to the installation in Australia, the results of the effort, the engineering involved, and the intended future use of the Mu2.

Let us review, in a most cursory fashion, some of the features of the Mu2 (Ref. 1). All ranging systems measure the round trip time delay involved in transmitting a signal to some object and receiving a corresponding echo. The Mu2 is a binary sequentially-coded ranging machine. Its signal is a square wave whose period is regularly doubled. The signal is phase modulated onto a carrier, transmitted to a spacecraft which transponds it back to earth. The phase difference between the transmitted and received square waves is a direct measure of time delay (and an indirect measure of range). Detection and correlation of the received signal is accomplished digitally in the Mu2. This distinguishes it from the standard DSN ranging system, the Planetary Ranging Assembly (PRA), which uses analog techniques. Digital radio frequency signal processing allows the Mu2 to be fully automatic and exceptionally stable in performance.

Other distinguishing features include full two channel (usually S- and X-band) operation and square wave range codes up to 8 MHz in frequency. The PRA, on the other hand, is limited to having only a single code available on its second channel and a maximum code frequency of 500 kHz. The advanced software system, within the Mu2, facilitates radio science measurements under adverse signal conditions and also aids research into new ranging techniques.

This article is organized into four sections. First the rationale behind the reinstallation of the Mu2 into the DSN will be presented. Second the significant results of the effort are described. Third, we explain the hardware and software changes implemented in the Mu2. Finally, in the last section, the future of the Mu2 is proposed.

II. The Why

Installation of the Mu2 at DSS 42/43 was motivated by the Viking Radio Science Team, the ongoing advanced radiometric research program and the DSN commitments for Voyager Navigation. We discuss each in turn.

A. Viking Radio Science

During 1976, the Mu2 successfully supported both the solar corona and the Theory of Relativity experiments when Mars went through superior solar conjunction. Facilities available in the Mu2 software and hardware allowed it to reliably obtain range data when the radio ray-path was close to the solar disc. These include:

(1) Full dual channel operation which allows measurement of S-X differential delay to a maximum of 2 seconds. The PRA is limited to 2 μsec differentials.

(2) Full correlation voltages allow real-time assessment of range validity even when Doppler is unreliable as during solar conjunction.

(3) Extensive clean-up of noisy Doppler signals by a quadrature filtering technique enables the Mu2 to range during periods of great carrier phase jitter.

(4) Any of the range codes (8 MHz to 0.5 Hz) available on the Mu2 can be used as the initial or highest frequency code. Thus the precision of the range measurement can be matched to the modulation phase jitter in the range channel. Time is not wasted on integrating components whose period is a small multiple of the phase jitter thereby increasing data yield.

(5) Fully automatic operation removes error sources due to incorrect phasing of the range code demodulator 10 MHz station reference and inconsistent manual adjustment of analog front-end attenuators.

(6) The Mu2 uses "Tutorial Input" (Ref. 2) as an operator interface. This highly interactive system enables real-time modification to parameters in response to changing signal conditions.

Due to these capabilities, the Mu2 has ranged demonstrably closer to the Sun than the PRA. The results of the 1976 solar conjunction include a four-fold improvement in the confirmation of Einstein's Theory of General Relativity (Ref. 6). Reinstallation of the Mu2 into the DSN was requested by the Viking Radio Science Team for coverage of the January 1979 Mars superior solar conjunction.

B. Advanced Radiometric Research

An article by Layland, Zygielbaum and Hubbard (Ref. 3) described experiments which used frequency band-limiters to remove distortion from the received or "downlink" ranging signal. Recall that the Mu type ranging systems (Mu1, Mu2 and PRA) suffer from wave form distortion of the range code due to asymmetric amplitude and phase distortion of harmonics of the range code square wave. This problem is compounded by a mismatch between the actual correlation function produced by the ranging hardware and that assumed by the software. In essence, the software assumes that the returned signal is a square wave while limitations of the DSN transmitter, spacecraft transponder, and, to a lesser extent, the DSN receiver, reduce the signal to a badly distorted sine wave.

When using the normal 500-kHz high-frequency code, about 18.5 ns of peak- to-peak range error appear during ranging pre- and post-track calibrations through the test translator. Measurements when using the proof test MVM '73 transponder showed distortions of 7.4 ns. The transponder has less error because it is band-limiting at ±1.5 MHz, thereby removing the adverse effects of distorted fifth and higher-order harmonics. Unfortunately the third harmonic is still propagated and in fact is further corrupted by the transponder.

Ranging accuracy can be enhanced by simplifying the spectrum of the range code. One way to accomplish this is to utilize a 1-MHz initial code. The 1-MHz square wave is corrupted in transmission to the spacecraft. Fortuitously, however, the band-limited transponder will filter out the 3-MHz third harmonic as well as all higher harmonics prior to any nonlinear transponder elements. To remove any harmonics generated by the spacecraft transmitter or within the DSN receiver, a band-pass filter is installed in the receiver IF line connected to the Mu2. In this manner the Mu2 is presented with a well-scrubbed sine wave corresponding to the fundamental frequency of the range code. Using this technique, the laboratory measured peak-to-peak error was about 1 ns during station calibration and 0.6 ns with the MVM '73 transponder. The system configured to 1 MHz also exhibited less sensitivity, in terms of range error to different transmitter modulators

The logical continuation of these tests was to try the technique with a spacecraft. As discussed in the next subsection, the Voyager Project provided the spacecraft.

C. Voyager Navigation Requirements

During the summer of 1978 it became apparent that some difficulty was being experienced in meeting the $4.5\sqrt{2}$-meter interstation range accuracy requirement of the Voyager Project. Ranging of this precision was required to assure adequate navigation margins during the Voyager Saturn encounter. During the period immediately prior to the encounter, the spacecraft will be near zero declination where Doppler will not provide angle data of sufficient precision to navigate the encounter.

Accurate navigation is jeopardized by large range biases which had been observed between DSN stations. Even between conjoint, i.e., almost colocated, stations, biases were on the order of 4 meters. It was decided that the Mu2, with its higher

precision ranging and full dual channel capability, could be used to investigate the problem.

III. Preliminary Results

The results to date are encouraging, but far from complete. Upon completion of the experiments, a full report will be published in *The DSN Progress Report*.

A. Viking Radio Science

It was hoped that some definite results could be given at this time. Unfortunately, the solar corona was extremely noisy during the January, 1979, conjunction. This created a problem in that the DSN receivers could not maintain carrier phase lock with the spacecraft X-band signal when the spacecraft was "two-way". In this mode, the spacecraft downlink (spacecraft to Earth) signal frequencies are related by fixed multiples to the uplink (Earth to spacecraft) S-band signal frequency. For the S-band downlink, the multiple is 240/221 while for X-band it is 880/221.

The corrupting effects of a plasma upon a radio signal are inversely proportional to the square of the signal frequency (Ref. 4). At first glance, then, X-band should be better than S-band. However, in the multiplication of the S-band uplink frequency to X-band, the jitter induced by the solar plasma is increased by the same factor, resulting in a badly distorted signal.

While the S- and X-band range obtained by the Mu2 appears good, the S-band Doppler data is marginal and the X-band Doppler virtually unusable. We had planned to use the S-X two-way Doppler data to interconnect the S-X range data with earlier one-way Doppler data in a scheme to measure and track the solar corona charged particle density. Because of the poor signal conditions, we are forced to a less satisfactory and much more labor-intensive fall back.

Despite these problems, the recent data obtained by the Mu2 is expected to complement and improve the results of the 1976 experiment. A future article will discuss the data processing and tracking operations involved in this latest test of the Theory of General Relativity.

B. Advanced Radiometric Research

The data from the Mu2 at DSS 43 is corroborating the experiments reported by Layland, et al. (Ref. 3). Figure 1 is a graph of range residuals taken from observations of the Voyager 1 spacecraft at DSS 43. Less than a 30-minute gap separated PRA and Mu2 measurements. Not only is the Mu2 data less scattered but the PRA data seems to have a bimodality. Such a signature is possible due to wave form distortion.

Table 1 summarizes a representative sample of data drawn from the comparison plotted in Fig. 1 and from normal Voyager 1 tracking operations. The data are given as RMS scatter about a line fit to the range residuals. A linear fit is used since errors in the ephemeris or ionosphere model appear linear over a short span. While the Mu2 data appears "raw," the PRA residuals are shown both raw and corrected by the second point of "DRVID" (Difference Ranged Versus Integrated Doppler) measured after each range acquisition. Data from the Mu2 has about one-fifth of the scatter of the raw PRA data and one-third that of the DRVID-corrected PRA data.

Correcting the PRA data by DRVID involves extra computation and requires that temporal charged particle variation in the ray-path be small. It is difficult to distinguish the signature of a plasma event and the error imposed by wave-form distortion. On the basis of these findings, we have proposed that the DSN upgrade the PRA to utilize a 1-MHz high-frequency code.

C. Voyager Navigation Requirements

It is too soon to report any results from the investigation into the interstation range bias. The bias between DSS 42 and DSS 43 varied from 6 meters to 2.5 meters during the period April, 1978, through early January, 1979. During a Voyager navigation cycle, it was observed that no bias existed when the Mu2 was used at DSS 43 and the PRA at DSS 42. Other than pointing out the sensitivity of these biases to ground equipment variation, no further conclusions are justified at this time.

The Voyager navigation cycle consists of continuous tracking of a Voyager spacecraft for a period of about 48 hours. Ranging and Doppler data are taken in turn from each of the 64-meter stations in the DSN. As appropriate, some 26-meter stations are also sampled. Figure 2, which is taken from Ref. 5, shows the range residuals from a Voyager navigation cycle in late January 1979. The numbers in circles indicate the tracking station used. (DSS 42/43 are at Tidbinbilla, Australia; DSS 63 is at Robeledo, Spain; and DSS 12/14 are at Goldstone, California). The vertical lines indicate the bias between stations as determined from linear fits to the respective data sets. Note that the bias between Spain and California is smaller than that between the two Goldstone stations. Also, the lower scatter due to the use of the Mu2 at DSS 43 is readily apparent.

By the time this article is published, several experiments should have been performed testing various theories as to the cause of the interstation bias. These will involve both DSS 42 and DSS 43 in an interchange of equipment during Voyager tracking.

IV. Modifications to the Mu2

In this section, we present the modifications effected on the Mu2 software and hardware to accommodate installation at the conjoint Australian stations and to incorporate the filtered range code correlation algorithm into the operational software.

A. Hardware

When the Mu2 was last installed in the DSN (at DSS 14), the ranging interface with the High-Speed Data Line was via a computer known as the Tracking Data Handler (TDH). When the DSN was upgraded for the Voyager era, the TDH was replaced by the Metric Data Assembly (MDA). While the TDH was only one-way, processing output data, the MDA is two-way, also routing operator supplied parameters and commands from the so-called "host" computer to the ranging machine.

Because the Mu2 was installed in a conjoint station, two MDA interfaces were required. Each interface attached directly to the Mu2 data and control lines. The Mu2 uses a simple internal bus scheme which has five address lines, one enable line, two handshake lines and two sets of 16-bit unidirectional data lines. A control circuit board and two identical 14-line interface adapter boards, comprising a total of more than 100 integrated circuits, were installed in the Mu2 Interface Unit.

Besides the computer interfaces, two band-pass filters were required to shape the 10-MHz IF signal prior to detection within the Mu2. These filters are described in Ref. 2. They are ±1.5-MHz-wide with a 10-MHz center frequency. When the phase moduled IF signal is passed through the filters, all harmonics of the 1-MHz range code are greatly attenuated. In effect, a 1 MHz sine wave tone is then detected and correlated in the Mu2. This tone is largely devoid of the wave-form distortion plaguing lower frequency initial codes.

Installation at the conjoint DSS 42/43 required that the Mu2 interface to the Block III receiver at the DSS 42 26-meter station and the Block IV receiver at the DSS 43 64-meter station. The signals supplied by these receivers are compatible except that the Doppler tone which the Block III outputs is half the actual Doppler frequency. Provision for either receiver's Doppler was originally made by using movable straps on the Mu2 Doppler scaler circuit board. This board was modified so that the Mu2 computer could select the proper scaling.

Another change to the Doppler scaler was to allow the computer to configure for X-band or S-band Doppler scaling (they differ by a factor of 11/3). This allowed the DSS 42 ranging to be processed by Mu2 channel 2 which is normally used for X-band. The arrangement facilitates simultaneous processing of S-band ranging data from both stations.

B. Software

The software which orchestrates the Mu2 has been described in Ref. 1. Only those features salient to the DSS 42/43 installation will be discussed here. By far the most extensive modification to the software involved deleting the TDH software and adding software to support the MDA. In total, over 1800 changes were made in the Mu2 software to accommodate the DSS 42/43 installation.

One modification to the software involved transferring the sine-wave correlation algorithm from test software to the operational software. The modular construction of the Mu2 programming made this a very straightforward task. Modification was also made to the "mode" parameter to facilitate independently switching the two Mu2 channels between square-wave and sine-wave correlation routines.

A major change in Mu2 control philosophy accompanied the conversion to the MDA. Specifically Mu2 parameters and directives would normally be provided through the MDA rather than from the Mu2 console teletypewriter. The Mu2 uses an operator interface known as Tutorial Input (Ref. 2). Through the foresight of the MDA designers, free-form ASCII text can be transmitted from the MDA to attached devices. Therefore, all commanding could retain the Tutorial Input format. It was necessary only to place data blocks from the MDA into the Tutorial Input buffer.

Additional control capability had to be added to specify which MDA (i.e., which station) was in control. In either case, primary, or overriding, control remained with the console teletype. Three control commands were assigned only to the teletype. They are:

M/M1	Control from either teletype or MDA1 (DSS 43)
M/M2	Control from either teletype or MDA2 (DSS 42)
M/TTY	Control only from teletype

After program initialization, control may either be specified at the teletype or it will be assumed by the first MDA to "talk" to the Mu2. Control is returned to "unassigned" by using the release command M/REL.

The Viking era Mu2 had two interrupt buttons; one to start range acquisitions, the other to attract the computer's attention for commanding. Remote control of the Mu2 necessitated a new command, M/ACQ, to start acquisitions. In order to use the console teletype for commanding, the PDP-11 computer now monitors the teletype for a line-feed character. Upon

receipt of line-feed, teletype commanding is initiated. The two interrupt levels freed with these two changes were immediately absorbed by the MDA interface.

A workable control concept would be useless without a means for outputting data. The MDA provides the data pathway. Each second, the MDA expects a range data block of 35 words (Ref. 7). This block reports both parameters used to obtain the ranging and the range measurements including correlation voltages, DRVID, and power- to-noise estimates.

Within the block, the ranging system outputs Universal Time Coordinated (UTC). There is also a field for data validity. When this field indicates "new" data, the word containing UTC is interpreted as is a time tag for the data. In a break with the PRA philosophy, the Mu2 always sets the time tag to the appropriate data time. The MDA can then be late in sampling the block and still obtain the correct sample time.

As described in Ref. 1, the Mu2 software is modular. Three new modules were added to interface to the MDA and the TDH module was removed. Four thousand words of core memory were added to the PDP-11 to contain the new subroutines. The first module, the MDA data output module, is enabled by the system scheduler to output range data each second. This is done in background, as is all data handling, to prevent time conflicts. Upon completing the output sequence, the module enables MDA data input by initializing an appropriate time tag in the scheduler. The subsequent transfer from the MDA to the Mu2 contains either operator directives or a blank block.

After these two transfers are completed, the scheduler is again enabled to allow a second Mu2 to MDA transfer. This block contains information to be displayed on the station operator's CRT screen. The display can either be routine data, a list of operator supplied parameters, status messages, or alarm messages.

Three of the five available displays are associated with operator-supplied parameters. Display 1 shows the current default parameters. These are the parameters directly changed by operator input. At transmit time for a new range acquisition, the default parameters are copied into the transmit parameter buffer and also stored in the receive parameter circular buffer. The transmit parameters can be observed in display 2. After one round-trip-light-time (an operator-supplied parameter) has elapsed, receive parameters are transferred from the circular buffer to the receive parameter list. This list is presented in display 3.

It is because of the receive parameter circular buffer that each range acquisition done by the Mu2 is completely independent of any other acquisition. Hence, parameters can be changed at any time without affecting any acquisitions already in space.

Displays 4 and 5 are used to observe and analyze data quality. The ranging correlation voltages appear on display 4. As explained in the Mu2 technical report (Ref. 1), these voltages are a direct and immediate indicator of range quality. An indirect quality indicator, DRVID is presented on display 5. This display is mainly used during pre- and post-track range calibrations. The actual range measured and the epoch time (TO) appear on both displays.

Some problems arose in debugging the new software with the MDA. These were manifest as large numbers of parity errors in the transfers between the MDA and the Mu2. It appeared that there were timing conflicts within the MDA. The situation is aggrevated because most MDA activity occurs immediately after the station one second timing pulse. The problem was solved by delaying the transmission of the Mu2 range data block to 0.1 second, and the transmission of the display block to 0.5 seconds after the one-second pulse.

V. The Future

Several more experiments are planned for the near future into the interstation range bias problem. Other than these tests, the Mu2 will continue to be the prime ranging machine at DSS 43. At the present time, it is planned to remove the Mu2 on or about 1 October 1979. We hope to install it at DSS 13 for continuing experiments with Viking Lander 1 and research into automatic, "unattended," ranging.

Acknowledgements

The installation of the Mu2 in Australia was a five-month project which was approved and initiated only two months prior to the installation. The task was successfully completed through the efforts and long hours contributed by personnel throughout JPL, and in Australia.

The author regrets that it is impossible to list all of the names of people who contributed to the project. However, the following people at JPL deserve much of the credit: W. P. Hubbard, W. A. Lushbaugh, P. Herrin, R. Wells, C. Cripe, and R. Weber. At the Tidbinbilla complex in Australia, the whole station seemed to pitch in with incredible enthusiasm. In particular, the following people are recognized: A. Robinson, V. Koenig and P. Churchill. Also, the complex manager, T. Reid, provided much support.

Any effort, such as this one, is dependent on the skills and determination of many people. The success of this project pays tribute to all involved.

References

1. Martin, W. L., and A. I. Zygielbaum, Mu-II Ranging, JPL Technical Memorandum 33-768, Jet Propulsion Laboratory, Pasadena, CA, May,15, 1977.

2. Zygielbaum, A. I., "'Tutorial Input' -- Standardizing the Computer/Human Interface," *DSN Progress Report 42-43,* Jet Propulsion Laboratory, Pasadena, CA, Oct. 15, 1974.

3. Layland, J. W., A. I. Zygielbaum, and W. P. Hubbard, "On Improved Ranging," *DSN Progress Report 42-46,* Jet Propulsion Laboratory, Pasadena, CA, Aug. 15, 1978.

4. MacDo[illegible]l, P. F., "A First Principles Derivation of the Differenced Range Versus Integrated Doppler (DRVID) Charged Particle Calibration Method," *Space Programs Summary 37-62,* Vol. II, Jet Propulsion Laboratory, Pasadena, CA., March 31, 1970.

5. Koch, R. E., "Voyager Near Simultaneous Ranging Status Summary #2 " JPL Internal Memo, Voyager-NAV-79-057 March 13, 1979.

6. Shapiro, I. I., et al., "The Viking Relativity Experiment," *Journal of Geophysical Research,* Vol. 82, No. 28, Sept. 30, 1977.

7. Baugh, H. W., "Software Specification Document DSS Tracking Subsystem, Planetary Ranging Sun Earth Probe Operational Program," JPI #SSD DIR 5125 OP; JPL, Pasadena, California, Dec. 1, 1978 (JPL Internal Document).

Table 1. Mu2/PRA Comparison

Date	DSS-43 Mu2	DSS-43 PRA RAW/DRVID	DSS-14 PRA RAW/DRVID	DSS-63 PRA RAW/DRVID
5 Jan. 1979	7.8	4.25/3.96		
7 Feb. 1979	1.99			8.12/5.10
8 Feb. 1979	0.52		5.81/1.64	
17 Feb. 1979	1.36		4.24/2.60	4.82/3.00

Number indicates RMS scatter in Range Units about a linear fit to the range residuals.

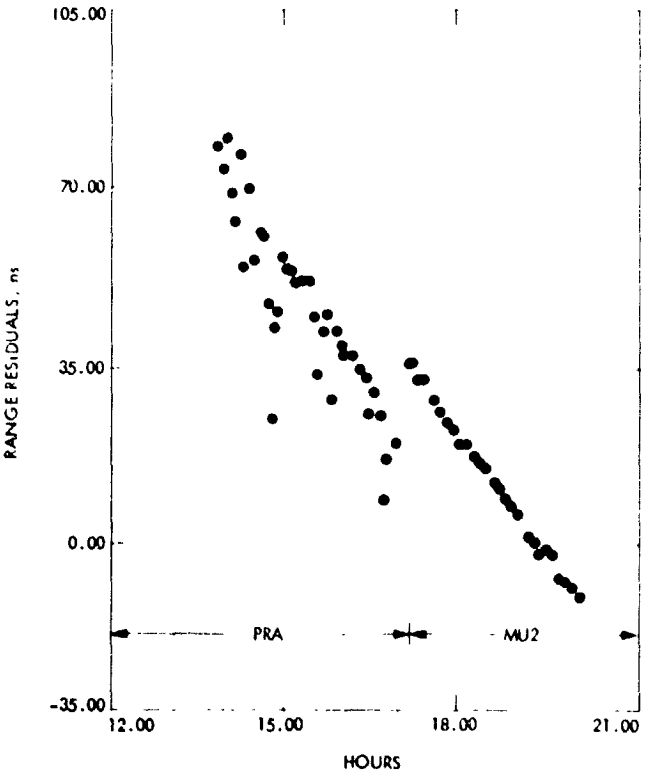

Fig. 1. Range residuals from the 5 January 1979 Mu2/PRA comparison test using Voyager 1

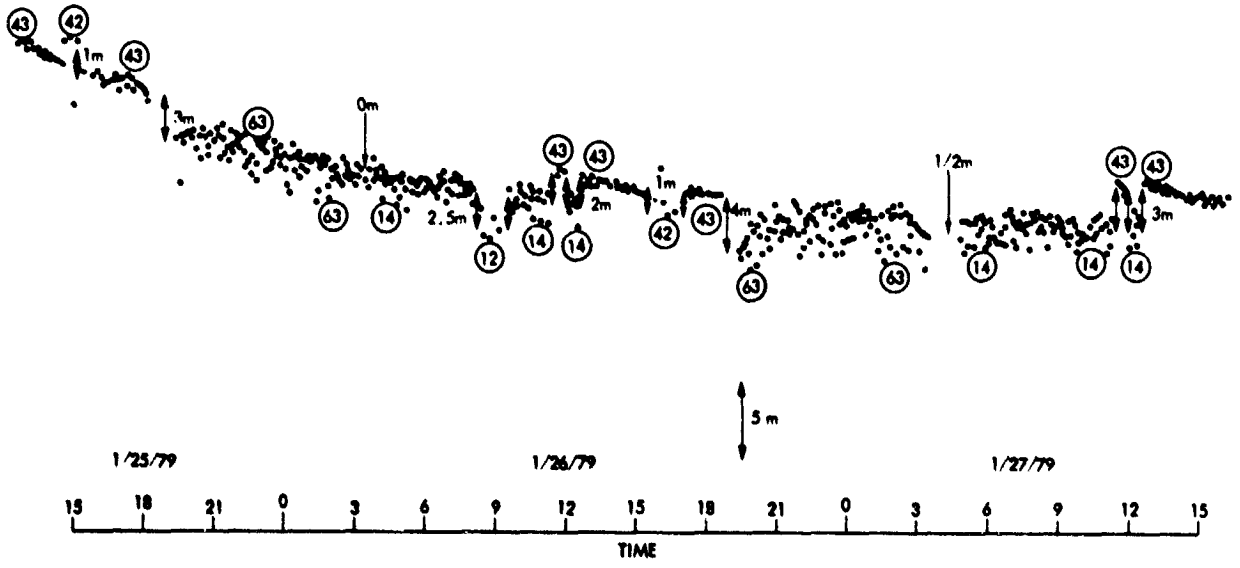

Fig. 2. Voyager 1 navigation cycle residuals

ORIGINAL PAGE IS
OF POOR QUALITY

N79-25097

Some Effects of Quantization on a Noiseless Phase-Locked Loop

C. A. Greenhall
Communications Systems Research Section

If the VCO of a phase-locked receiver is to be replaced by a digitally programmed synthesizer, the phase error signal must be sampled and quantized. We investigate effects of quantizing after the loop filter (frequency quantization) or before (phase error quantization). Constant Doppler or Doppler rate noiseless inputs are assumed. The main result gives the phase jitter due to frequency quantization for a Doppler-rate input. By itself, however, frequency quantization is impractical because it makes the loop dynamic range too small.

I. Introduction

This article contributes to the effort to develop a partly-digital receiver for the DSN. In this connection, it has been suggested that the voltage-controlled oscillator (VCO) of the carrier tracking loop be replaced by a number-controlled oscillator (NCO), an example of which is the Digiphase® Frequency Synthesizer. This synthesizer operates between 40 and 51 MHz; the frequency decades down to 10^{-6} Hz can be programmed synchronously during a specified portion of the 10 μs clock period. Thus, the filtered, digitized phase error signal, plus a bias derived from the Doppler prediction, would be used to program the synthesizer, whose output would be multiplied up to the local oscillator frequency (RF – 1st IF). Some effort (Ref. 1), later abandoned, has already been expended toward development of a third-order tracking loop with this synthesizer as NCO.

Two advantages of this arrangement are predicted to be: (1) the phase jitter produced by the synthesizer (and partly tracked out by the loop) should be less than that produced by an analog VCO because the synthesizer phase is controlled by a wideband loop that tends to track out slow phase variations; and (2) the synthesizer input, being a digital signal, would yield directly a convenient estimate of Doppler frequency. It would be unnecessary to extract Doppler data by mixing analog signals from the receiver and the exciter. The success of this approach depends on the truth of (1), for if the synthesizer exhibits slow, unbounded phase variations, then the integrated digital Doppler estimate might vary unacceptably from the true local oscillator phase. This question may be treated in a future article.

In order to program an NCO in the loop, the phase error must first be sampled and quantized. One might do this either before or after the loop filter. This article investigates both possibilities separately. Assumptions are (1) linearized second order loop, active form of loop filter, with special attention paid to the 1-Hz bandwidth setting of the DSN Block IV Receiver; (2) strong signal, at least 40 dB above margin; (3) all

noises absent, including oscillator jitter; (4) quadratic phase input $\theta = \theta_o + \omega_o t + 1/2\,\lambda t^2$; and (5) zero sampling interval: time is not quantized.

We show how the loop approaches lock from conditions close to lock, and we derive the steady state behavior of phase and frequency.

II. Loop Model

Figure 1 shows a block diagram of the mathematical model. The phase detector output is p and its quantized version is q. The unquantized oscillator frequency is y and its quantized version is z. The phase detector gain αK_d includes the limiter output signal amplitude of the real receiver (the limiter suppression factor α is 1 in a strong-signal situation). To simulate the Block IV 1-Hz loop at S-band with a 40-51 MHz oscillator, we set $\tau_2 = 1.5s$, $\tau_1 = 33919s$, $K_d = 5$ volt/rad, $g = 4$, $K_v/2\pi = 96$ Hz/volt, and $M = 40$. The loop gain is $\alpha K = \alpha K_d g K_v M = 4.83 \times 10^5\ s^{-1}$ and the loop parameter defined by

$$r = \frac{\alpha K \tau_2^2}{\tau_1}$$

equals 32. This value also holds for the 10 Hz and 100 Hz bandwidth settings. For the 3, 30, and 300 Hz settings, the value of r is 18.55. At threshold, $r = 2$ for all settings.

The quantizing function $Q_a(x)$ rounds x to the nearest odd multiple of a. The distance between quantizer levels is $2a$. The even multiples of a are "decision levels." To make mathematical sense out of this model, we assume a small "dead zone" of width 2ϵ around each decision level. For example, if $x(t)$ is a signal that starts at a and decreases, then $Q_a(x)$, initially at a, flips to $-a$ only when x reaches $-\epsilon$. Then $Q_a(x)$ does not return to $+a$ until x returns to $+\epsilon$. Results will be obtained by letting ϵ tend to 0.

III. Oscillator Frequency Quantization

Let the phase quantizer be removed from the loop, whose equations are then

$$y = \frac{\alpha K_d g K_v}{2\pi \tau_1}\left(\tau_2 \phi + \int \phi dt\right)$$

$$z = Q_{\Delta y}(y)$$

$$\phi = \theta - 2\pi M \int z dt$$

The effective quantization interval of the RF radian frequency $\omega = 2\pi M z$ is

$$2\Delta\omega = 4\pi M \Delta y$$

In terms of the dimensionless variables

$$t^* = \frac{t}{\tau_2},\quad \theta^* = \frac{r}{\tau_2 \Delta\omega}\theta,\quad \phi^* = \frac{r}{\tau_2 \Delta\omega}\phi$$

$$y^* = \frac{r}{\Delta y} y,\quad z^* = \frac{r}{\Delta y} z$$

the equations become

$$y^* = r\left(\phi^* + \int \phi^*\, dt^*\right) \tag{1}$$

$$z^* = Q_r(y^*) \tag{2}$$

$$\phi^* = \theta^* - \int z^*\, dt^* \tag{3}$$

At the risk of confusion, we shall drop the asterisks from the dimensionless variables for a while; when results are stated we shall make clear what variables we are talking about. Equations (1) and (3) really mean

$$y(t) - y(t_o) = r\left(\phi(t) - \phi(t_o) + \int_{t_o}^{t} \phi(s)\, ds\right)$$

$$\phi(t) - \phi(t_o) = \theta(t) - \theta(t_o) - \int_{t_o}^{t} z(s)\, ds$$

for any t_o and t. Initial conditions for Eqs. (1) – (3) are specified by $\phi(t_o)$ and $y(t_o)$.

We shall assume that the quantizer Q_r has a dead area $[-\epsilon, \epsilon]$.

A. Constant Doppler Input

Let $\theta = \theta_o + \omega_o t$, where $|\omega_o| < r$. We show the loop pull-in behavior for sufficiently small $\phi(0)$ and $y(0)$. Without loss of

generality we can assume $-\epsilon < y(0) < 2r$ and z is initially $+r$. For $t > 0$,

$$\phi(t) = \phi(0) + (\omega_o - r)t$$

$$y(t) = y(0) + r\left\{[\omega_o - r + \phi(0)]\ t + \frac{1}{2}(\omega_o - r)t^2\right\}$$

Let $\phi(0) < r - \omega_o$. Then y decreases until it reaches $-\epsilon$ at some time t_1. This makes z flip to $-r$. For $t > t_1$,

$$\phi(t) = \phi(t_1) + (\omega_o + r)(t - t_1)$$

$$y(t) = -\epsilon + r\left\{[\omega_o + r + \phi(t_1)]\ (t - t_1) + \frac{1}{2}(\omega_o + r)(t - t_1)^2\right\}$$

If $y(0)$ is small enough, then $\phi(t_1)$ is not too negative, so that we can assume $\omega_o + r + \phi(t_1) > 0$. Thus, y increases, and soon reaches $+\epsilon$. Then z flips back to $+r$, and so on. We see that y judders back and forth inside the dead zone $[-\epsilon, \epsilon]$, and z flips violently between $-r$ and $+r$. Meanwhile, what happens to the phase error ϕ? It satisfies the integral equation

$$\phi + \int \phi\, dt = \frac{y}{r} \tag{4}$$

For small ϵ, we can pretend $y = 0$ for $t > t_1$. Then the solution of Eq. (4) is $\phi(t) = \phi(t_1)\, e^{t_1 - t}$. We could, of course, compute the additional ϕ-disturbance due to the juddering of y.

If $\omega_o > r$ and $\phi(0)$, $y(0)$ are small, then whether $z(0)$ is r or $-r$, y floats upward, trying to make $\omega_o - z$ small. Eventually, the loop reaches a condition in which $y = 2kr$ (k is an integer), where $2kr$ is the nearest decision level to ω_o, and ϕ decays exponentially to 0. (We ignore the case where ω_o/r is an odd integer.)

We state this result in "real-world" units: *For a constant Doppler input $\theta = \theta_o + \omega_o t$ to the frequency-quantized loop, the unquantized frequency y eventually sticks at the nearest decision level $2k\Delta y$ to ω_o, the quantized frequency z flips rapidly between $(2k - 1)\Delta y$ and $(2k + 1)\Delta y$, and the phase error ϕ decays to 0 exponentially with time constant τ_2. The static phase error is 0.*

B. Constant Doppler Rate Input

We return to the use of dimensionless variables (unstarred). Let $\theta = \theta_o + \omega_o t + 1/2\ \lambda t^2$, $\lambda > 0$. The unquantized loop has a static phase error (SPE); the steady-state solution of Eqs. (1) and (3), with $z = y$, is $\phi = \lambda/r$, $y = \omega_o + \lambda t$. We are going to find a periodic solution of the quantized system; the period is necessarily $2r/\lambda$, the time it takes the Doppler to traverse one quantization interval. The idea is that for small λ the frequency y is normally stuck at a decision level of the quantizer and the phase error has decayed exponentially to 0. As $\dot{\theta} = \omega_o + \lambda t$ increases, though, there comes a time when y can no longer remain at that level; it must eventually float up to the next level in order to stay close to $\dot{\theta}$. During this *floating period*, ϕ is allowed to wander off. In fact, it exceeds the nominal SPE. During the subsequent *sticking period*, when y is stuck at the next decision level, ϕ again decays exponentially to 0. The sum of the lengths of the floating and sticking periods is $2r/\lambda$.

So, let us assume that at time 0, y is stuck at 0 (really, within $[-\epsilon, \epsilon]$). Let $\phi(0) = \phi_o$. For small $t > 0$, while z remains constant,

$$\phi(t) = \phi_o + (\omega_o - z)t + \frac{1}{2}\lambda t^2 \tag{5}$$

$$y(t) = r\left[(\omega_o + \phi_o - z)t + \frac{1}{2}(\lambda + \omega_o - z)t^2 + \frac{1}{6}\lambda t^3\right] \tag{6}$$

If $|\omega_o + \phi_o| < r$, then the coefficient of t in Eq. (6) has sign opposite to z, so y remains stuck at 0. In order to make the time origin the start of a floating period, we assume

$$\omega_o + \phi_o = r, \qquad \phi_o \leqslant \lambda \tag{7}$$

Then z immediately becomes $+r$ and stays there. For $t > 0$,

$$\phi(t) = \phi_o - \phi_o t + \frac{1}{2}\lambda t^2 \tag{8}$$

$$y(t) = r\left[\frac{1}{2}(\lambda - \phi_o)t^2 + \frac{1}{6}\lambda t^3\right] \tag{9}$$

The floating period ends when y reaches $2r$, the next decision level, where z must choose between r and $3r$. This happens at time t_1, the positive solution of

$$\frac{1}{6}\lambda t_1^3 + \frac{1}{2}(\lambda - \phi_o)\, t_1^2 - 2 = 0$$

For $t = t_1 + u$, u small and positive, while z is constant,

$$\phi(t_1 + u) = \phi(t_1) + (r - \phi_o + \lambda t_1 - z)\, u + \frac{1}{2}\lambda u^2 \tag{10}$$

$$y(t_1+u) = r\left\{2 + [\phi(t_1) - \phi_o + \lambda t_1 + r - z]\,u + O(u^2)\right\} \tag{11}$$

where $\phi(t_1)$ is computed from Eq. (8). Assume that

$$\phi(t_1) - \phi_o + \lambda t_1 < 2r \tag{12}$$

(The left side equals $(\lambda - \phi_o)t_1 + 1/2\ \lambda t_1^2$, and hence is positive.) Then the coefficient of u in Eq. (11) has opposite sign to $z - 2r$. Therefore, y is stuck at $2r$. For $t \geq t_1$, ϕ satisfies

$$\phi(t) = \phi(t_1)e^{t_1 - t}$$

and the "microscopic" behavior of the system near t is determined from

$$\phi(t+u) = \phi(t) + (\omega_o + \lambda t - z)\,u + \frac{1}{2}\lambda u^2$$

$$y(t+u) = r\left\{2 + [\omega_o + \phi(t) + \lambda t - z]\,u + \frac{1}{2}(\lambda + \omega_o + \lambda t - z)u^2 + \frac{1}{6}\lambda u^3\right\}$$

where $z = 2r \pm r$. The sticking period ends and a new floating period begins when $\omega_o + \phi(t) + \lambda t$ reaches $3r$. Comparing with Eqs. (5) and (6), we see that the situation is just like the one at time 0 (except that now $y = 2r$) provided $\lambda t = 2r$, $\phi(t) = \phi_o$, that is to say, $\phi(2r/\lambda) = \phi_o$. Of course, this makes sense only if $t_1 \leq 2r/\lambda$. We are led to the following system of equations:

$$\frac{1}{6}\lambda t_1^3 + \frac{1}{2}(\lambda - \phi_o)t_1^2 = 2 \tag{13}$$

$$\phi_1 = \phi_o(1 - t_1) + \frac{1}{2}\lambda t_1^2 \tag{14}$$

$$\phi_o = \phi_1 \exp\left(t_1 - \frac{2r}{\lambda}\right) \tag{15}$$

A solution ϕ_o, ϕ_1, t_1 is called *admissible* if

$$0 < \phi_o \leq \lambda \tag{16}$$

$$0 < t_1 \leq \frac{2}{\lambda} \tag{17}$$

$$\phi_1 - \phi_0 \leq 2r - \lambda t_1 \tag{18}$$

A special case should be exposed first. Equality in Eq. (17) for a solution is equivalent to equality in Eq. (18), and means that the sticking period has zero length. Working backwards by setting $t_1 = 2r/\lambda$ and $\phi_1 = \phi_o$, we solve Eq. (14) for ϕ_o and Eq. (13) for λ. We find that for $r \geq 4/3$ and $\lambda = \lambda_m$, where

$$\lambda_m = \frac{r^2}{2}\left[1 + \left(1 - \frac{4}{3r}\right)^{1/2}\right] \tag{19}$$

there is the admissible solution

$$\phi_o = r, \quad \phi_1 = r, \quad t_1 = 2r/\lambda_m$$

For other values of λ, Eqs. (13) – (15) can be solved numerically by iterating ϕ_o (Newton's method is used to solve Eq. (13) for t_1). Convergence is slow, but Steffensen's acceleration method (Ref. 2) yields the solution within about 8 decimal places using only 6 iterations of Eqs. (13) – (15).[1] For $\lambda < r/10$ we can take $\phi_o \approx 0$ and solve for t_1, ϕ_1 immediately. We have not proved existence or uniqueness of the admissible solution; indeed, some of the results are empirical.

Eqs. (13) – (15) were solved for $r = 32$, 18.55, 10, 5, and 2, and for $10^{-3}r \leq \lambda \leq r^2$. For $\lambda > \lambda_m$, λ_m given by Eq. (19), the solution became inadmissible. Evidently, for $\lambda \geq \lambda_m$ we enter a situation in which there is no sticking period. We have not looked at this yet.

For any admissible solution, the time average of $\phi(t)$ over a period $2r/\lambda$ is exactly the SPE λ/r. The maximum of ϕ is ϕ_1, and the minimum is

$$\phi_{min} = \phi_o - \frac{\phi_o^2}{2\lambda} > 0$$

obtained by minimizing Eq. (8). Thus ϕ does fluctuate about the nominal SPE of λ/r. The peak-to-peak variation

$$V_\phi = \phi_1 - \phi_{min}$$

is plotted vs. λ/r in Fig. 2 with r as a parameter (the variables are starred). These curves show that V_ϕ is an insensitive function of r and λ/r. For $r = 32$,

$$\max V_\phi = 1.72$$

[1] If one iterates t_1 instead of ϕ_o, then it is not necessary to solve a cubic equation. Unfortunately, this iteration is violently unstable at the admissible solution.

achieved for $\lambda/r = 0.6$ approximately. Figure 3 sketches $\phi(t)$ vs. t for $r = 32$, $\lambda/r = 0.5$ (the variables are starred). As λ decreases, V_ϕ decreases slowly. The width of the ϕ-pulse, however, gets narrow relative to the period $2r/\lambda$, so that the RMS phase jitter decreases faster than the peak-to-peak phase jitter.

We have actually been working with dimensionless variables. Here are some of the results in real-world units.

Let the loop with RF frequency quantization $2\Delta\omega$ have the input $\theta = \theta_o + \omega_o t + 1/2\ \lambda t^2$ where the Doppler rate λ satisfies

$$0 \leqslant \lambda \leqslant \frac{\Delta\omega}{\tau_2}\frac{r}{2}\left[1 + \left(1 - \frac{4}{3r}\right)^{1/2}\right] \qquad (20)$$

The steady-state phase error fluctuates about the static phase error

$$\text{SPE} = \frac{\tau_2^2\lambda}{r} \qquad (21)$$

periodically with period $2\Delta\omega/\lambda$. The peak-to-peak amplitude V_ϕ of this fluctuation satisfies

$$V_\phi \leqslant 0.86\frac{\tau_2}{r}2\Delta\omega \qquad (r = 32) \qquad (22)$$

$$V_\phi \leqslant 0.83\frac{\tau_2}{r}2\Delta\omega \qquad (r = 18.55) \qquad (23)$$

the maximum being achieved when

$$\lambda = 0.6\frac{\Delta\omega}{\tau_2} \qquad (24)$$

approximately.

Assume a 1-Hz loop with a synthesizer programmed down to the 10^{-3} Hz decade. Then

$$2\Delta y = 0.001 \text{ Hz}$$

$$\frac{2\Delta\omega}{2\pi} = 0.04 \text{ Hz at S-band}$$

$$\max V_\phi = 0.0101 \text{ rad} = 0.58 \text{ deg}$$

achieved when

$$\lambda = 0.05 \text{ rad/s}^2 = 0.008 \text{ Hz/s}$$

$$\text{SPE} = 0.2 \text{ deg}$$

The maximum Doppler rate and SPE for which the present analysis is valid is obtained from Eqs. (20) and (21) as

$$\lambda_{max} = 0.422 \text{ Hz/s}$$

$$\text{SPE}_{max} = 10.7 \text{ deg}$$

The phase jitter V_ϕ is only 0.17 deg, a small ripple on the SPE.

At this point it appears that digitizing the phase error signal at the oscillator input is not practical. To achieve a 10^{-3} Hz quantization with a 12-bit A-D converter would mean a loop-controllable oscillator frequency range of only 4 Hz, whereas the Block IV VCO, in narrow mode, has a range of 960 Hz. It is probably necessary to digitize the phase error in front of the loop filter or even earlier.

IV. Phase Error Quantization

Returning to Fig. 1, we remove the frequency quantizer and install the phase quantizer. The loop equations are

$$p = \alpha K_d \phi, \qquad q = Q_{\Delta p}(p)$$

$$y = \frac{gK_v}{2\pi\tau_1}\left(\tau_2 q + \int q dt\right)$$

$$\phi = \theta - 2\pi M \int y dt$$

The effective quantization interval for ϕ is

$$2\Delta\phi = \frac{2\Delta p}{\alpha K_d}. \qquad (25)$$

Appropriate dimensionless variables are now

$$t^* = \frac{t}{\tau_2}, \qquad \theta^* = \frac{\theta}{\Delta\phi}, \qquad \phi^* = \frac{\phi}{\Delta\phi}$$

$$q^* = \frac{q}{\Delta p}, \qquad y^* = \frac{2\pi M\tau_2}{\Delta\phi}y$$

in terms of which the loop equations become

$$q^* = Q_1(\phi^*), \tag{26}$$

$$y^* = r\left(q^* + \int q^*\, dt^*\right) \tag{27}$$

$$\phi^* = \theta^* - \int y^*\, dt^* \tag{28}$$

As before, we shall drop the asterisks from these variables during the analysis.

The quantization interval of q is 2. As before, we assume that Q_1 has a dead zone of width 2ϵ about each decision level $2k$. Implicit in this model is the decision to make 0 a decision level, not a quantization level. Eq. (27) says that if q jumps by ± 2 then y jumps by $\pm 2r$. If q is a constant, say $2k+1$, on the interval $[t_1, t_2]$, then

$$y(t_2) - y(t_1) = r(t_2 - t_1)(2k+1).$$

Let $\theta = \theta_o + \omega_o t + 1/2\,\lambda t^2$, where we now allow λ to be 0. The unquantized loop has a SPE $\phi = \lambda/r$. In order for the quantized phase error q to be λ/r in some average sense, it must happen that ϕ gets stuck at the closest decision level $2k$ to λ/r, while q jumps between $2k+1$ and $2k-1$, bracketing λ/r. To show how this happens, it is convenient to define some more variables

$$\phi' = \phi - \frac{\lambda}{r}, \qquad q' = q - \frac{\lambda}{r},$$

$$y' = y - \omega_o - \lambda t$$

(we shall *not* drop the primes from these variables). They satisfy

$$q' = Q'(\phi') \tag{29}$$

$$y' = r\left(q' + \int q'dt\right) \tag{30}$$

$$\phi' = -\int y'dt \tag{31}$$

where[2]

$$Q'(\phi') = Q_1\left(\phi' + \frac{\lambda}{r}\right) - \frac{\lambda}{r}$$

[2] Because of the indefinite integrals, additive constants in Eqs. (30) and (31) can be deleted.

is just an offset quantizer whose decision level m lying closest to the origin satisfies

$$-1 \leqslant m \leqslant 1, \qquad m = -\frac{\lambda}{r} \pmod 2.$$

Assume that λ/r is not an odd integer, so that m is unique and $-1 < m < 1$. We shall show merely that if $\phi'(0) - m$ and $y'(0)$ are small enough, then ϕ' eventually sticks at m. Without loss of generality we can assume $\phi'(0) > m - \epsilon$ and $q'(0) = m + 1$ (rather than $m - 1$). For $t > 0$,

$$y'(t) = y'(0) + r(m+1)t \tag{32}$$

$$\phi'(t) = \phi'(0) - y'(0)t - \frac{1}{2}r(m+1)t^2 \tag{33}$$

Let $y'(0) \geqslant 0$. Then ϕ' decreases, reaching m at time

$$t_1 = \frac{-y'(0) + \sqrt{D}}{r(m+1)}$$

where

$$D = y'(0)^2 + 2r(m+1)[\phi'(0) - m]$$

(we neglect ϵ). Now, q' flips to $m-1$ and y' flips to

$$y'(0) + r(m+1)t_1 - 2r = \sqrt{D} - 2r$$

If

$$D < 4r^2 \tag{34}$$

Then ϕ' immediately starts to increase again, so q' flips back to $m+1$, and so on. Thus ϕ' is stuck at m.

If $y'(0) < 0$ then ϕ' initially increases. We can make sure that ϕ', given in Eq. (33), never reaches the next decision level $m+2$ by requiring

$$D < 4r(m+1) \tag{35}$$

In fact, Eq. (35) implies Eq. (34) if $r \geqslant 2$. Then ϕ' reaches m at time t_1 as before.

When ϕ' sticks at m, y' starts flipping between $\sqrt{D}$ and $\sqrt{D} - 2r$. By examining the microscopic behavior of ϕ' in the

2ε-dead zone, one can show, using an analysis not given here, that the upper and lower limits y'_+, y'_- of y' change with time, and in fact

$$y'_+ \to (m+1)r, \quad y'_- \to (m-1)r$$

exponentially with time constant 1. This result, though intuitively attractive, is on shakier ground than the other results here because it depends on the detailed behavior of the quantizer in its dead zones, which, after all, are but mathematical artifices introduced to make sense of the loop equations.

If λ/r happens to be an odd integer, then it appears that ϕ' wanders irresolutely between the two nearest decision points $\lambda/r - 1$ and $\lambda/r + 1$.

Returning through two changes of variables to real-world units, we state results: *Consider the input* $\theta = \theta_o + \omega_o t + 1/2\,\lambda t^2$ *to the loop with detector output quantization, where* 0 *is a decision level of the quantizer and* $2\Delta\phi$, *defined by Eq. (25), is the effective phase error quantization interval. Then the error* ϕ *sticks at the decision level* $2k\Delta\phi$ *that is nearest to the SPE of* $\tau_2^2\lambda/r$. *The RF frequency* ω *of the local oscillator flips rapidly between the two values*

$$\frac{d\theta}{dt} + \frac{r}{\tau_2}\left(2k\Delta\phi - \frac{\tau_2^2\lambda}{r}\right) \pm \frac{r\Delta\phi}{\tau_2}. \tag{36}$$

Thus, the peak-to-peak jitter in ω *is*

$$V_\omega = \frac{r}{\tau_2}\,2\Delta\phi. \tag{37}$$

Evidently, Eq. (37) is the counterpart of Eq. (22) or (23).

In the 1-Hz loop let the maximum range $\pm K_d$ of the phase detector be quantized by an 8-bit A-D converter. Then for strong signals ($\alpha = 1$), we have

$$2\Delta\phi = 2^{-7}\ \text{rad} = 0.45\ \text{deg.},$$

$$V_y = \frac{V_\omega}{2\pi M} = 6.6 \times 10^{-4}\ \text{Hz}.$$

We have been assuming in this section that the oscillator frequency y is not quantized. Since an NCO is being used, its frequency is necessarily quantized. If, however, we make its quantization $2\,\Delta y$ small compared to its peak-to-peak jitter V_y, then the results of this section still hold. In the 1-Hz loop example, we must assume that the synthesizer is programmed at least as far down as the 10^{-4} Hz decade; this is feasible because the signal has been digitized earlier. Then the phase jitter caused by frequency quantization (Section III B) will be small compared to the phase error quantization $2\,\Delta\phi$. If the synthesizer is programmed down only to 10^{-3} Hz, then one must examine a more complicated model that includes both frequency and phase error quantization.

V. Conclusions

There is a rough rule-of-thumb relationship

$$\Delta\phi \approx \frac{\tau_2}{r}\,\Delta\omega \tag{38}$$

which holds when either the phase error ϕ or the RF frequency ω is quantized. If ω is quantized into pieces of width $2\Delta\omega$, then $2\Delta\phi$ from Eq. (38) gives an upper bound for the peak-to-peak phase jitter. Conversely, if ϕ is quantized into pieces of width $2\Delta\phi$ then $2\Delta\omega$ from Eq. (38) is the peak-to-peak frequency jitter. In either case, the variable being quantized tends to stick at a decision level of the quantizer, which acts as a bang-bang control element in the loop.

It is not practical to digitize the error signal at the input to the loop oscillator (frequency quantization), because the oscillator frequency range would be too small. The digitizing must be done earlier, in which case Eq. (38) still tells us how fine the programming of the digitally-controlled oscillator must be to maintain phase jitter below a certain level.

References

1. Johns, C. E., *Block IV Receiver Development*, JPL Technical Report 32-1526, Vol. X, Jet Propulsion Laboratory, Pasadena, Calif., 1972, pp. 175-178.
2. Henrici, P., *Elements of Numerical Analysis*, New York, 1964, pp. 90-96.

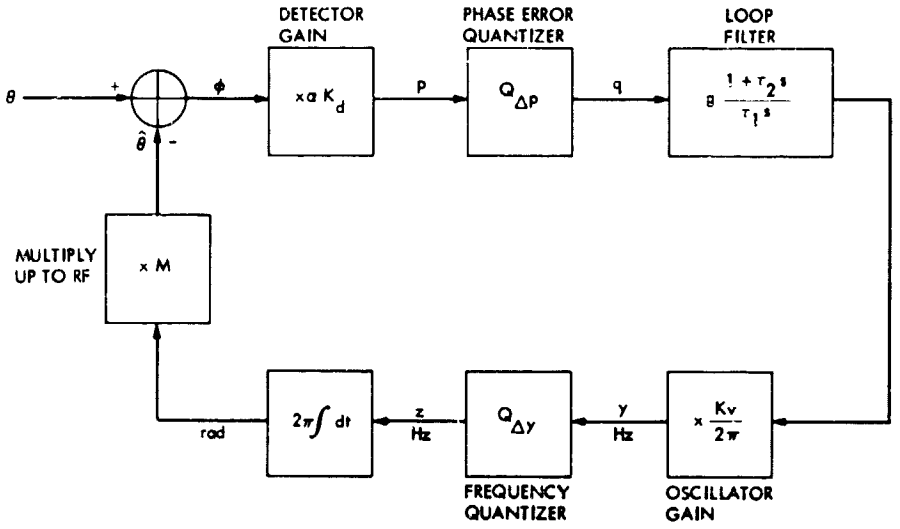

Fig. 1. Loop mathematical model

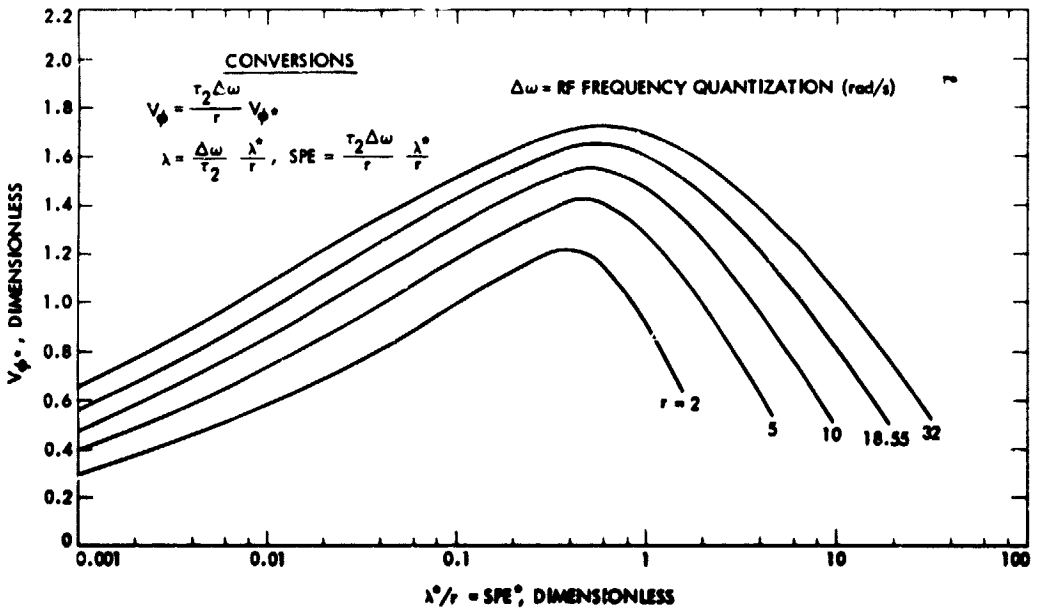

Fig. 2. Peak-to-peak phase variation for Doppler-rate input $\theta = 1/2\ \lambda t^2$ to a loop with frequency quantization

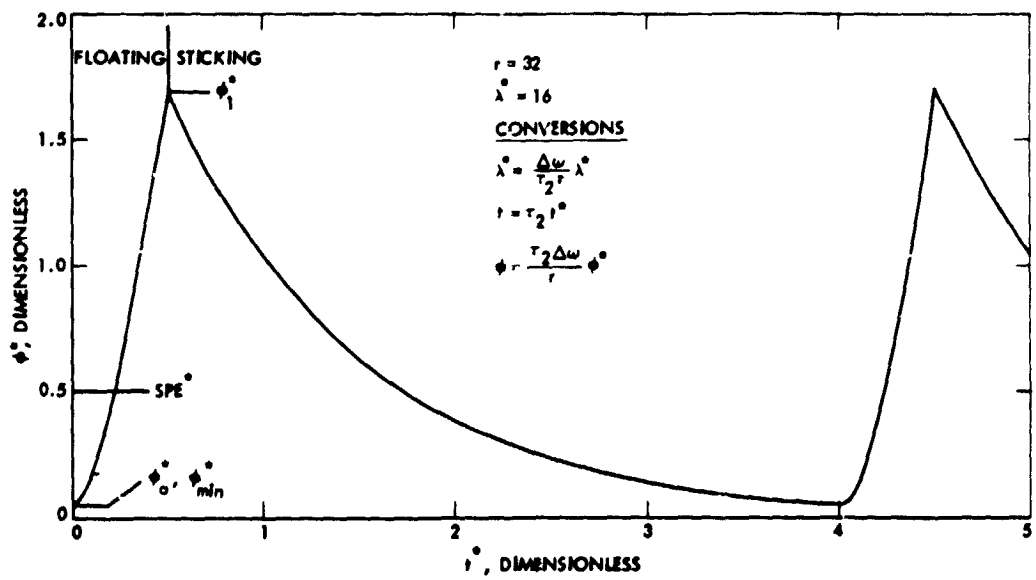

Fig. 3. Phase error vs. time for a Doppler-rate input to a loop with frequency quantization

N79-25098

A Transmission Line Phase Stabilizer

G. Lutes
Communications Systems Research Section

To meet the phase stability requirements of certain experiments performed with the Deep Space Network, transmission lines carrying reference signals must be stabilized to reduce changes in their electrical length due to mechanical movement or changes in ambient temperature. A transmission line phase stabilizer being developed at JPL to perform this function is described in this article.

I. Introduction

Reference signals that are stable to parts in 10^{14} are supplied within the Deep Space Net (DSN) stations by a station reference such as a Hydrogen Maser Frequency Standard.

The stability of these reference signals, as received by the user, is degraded by changes in the propagation lengths of the transmission lines used to distribute them. These changes are due to thermal expansion, generally >60 parts in 10^7 per °C, and mechanical movement of the lines.

These transmission line instabilities are greater than can be tolerated in some critical applications, such as Very Long Baseline Interferometry (VLBI), and interstation clock synchronization, so it is necessary to stabilize the transmission lines carrying these critical reference signals.

A transmission line phase stabilizer to perform this function is being developed at JPL and is described in this article.

II. Basic Considerations

A model for a transmission line distribution system without stabilization is shown in Fig. 1.

The relationship between the reference signal (E_R) and the distributed signal (E_3) is a function of the Voltage Standing Wave Ratio (VSWR) on the line and the propagation delay of the line, and can be found as described below.

For simplicity we will solve for the relationship between E_1 and E_3 and assume that the relationship between E_R and E_1 is constant, as it will be if the load on the reference port is constant.

From Ref. 1,

$$\frac{E_3}{E_1} = \frac{Z_R + Z_0}{2Z_R}\left(e^{\gamma d} + Ke^{-\gamma d}\right) \qquad (1)$$

where

$$K = \frac{Z_R - Z_0}{Z_R + Z_0}$$

d = The length of the line

Z_0 = The characteristic impedance of the line

$\gamma = \alpha + j\beta$ = The complex propagation constant

α = The loss factor (nepers/meter)

β = The delay factor (radians/meter)

and from the model

$$\frac{E_1}{E_2} = \frac{Z_s + Z_0}{Z_s} \tag{2}$$

Where, from Ref. 1,

$$Z_s = Z_0 \frac{e^{\gamma d} + Ke^{-\gamma d}}{e^{\gamma d} - Ke^{-\gamma d}} \tag{3}$$

Then substituting Eq. (3) into Eq. (2) and simplifying:

$$\frac{E_1}{E_2} = \frac{2e^{\gamma d}}{e^{\gamma d} + Ke^{-\gamma d}} \tag{4}$$

and multiplying Eq. (4) and Eq. (1) we get:

$$\frac{E_1}{E_3} = \frac{Z_R + Z_0}{Z_R} e^{\gamma d}$$

$$= \frac{Z_R + Z_0}{Z_R} e^{d(\alpha + j\beta)}$$

$$= \frac{Z_R + Z_0}{Z_R} e^{d\alpha} (\cos d\beta + j \sin d\beta)$$

$$\frac{E_1}{E_3} = \frac{Z_R + Z_0}{Z_R} e^{d\alpha} \angle d\beta \tag{5}$$

It can be seen from Eq. (5) that the relationship between the phase of E_1 and E_3 is a function of the length of the cable only, and is not affected by VSWR. The amplitude relationship is a function of VSWR and line length.

The purpose of the line stabilizer is to set and hold the phase relationship between E_R and E_3 constant under all conditions likely to be encountered in the field.

III. Description

The transmission line stabilizer consists of two basic parts: a transmitter and a receiver.

The transmitter is located near the station reference at one end of the transmission line to be stabilized. It transmits a reference signal up the line and receives a return signal coming down the same line from the receiver. These two signals are compared in phase, and an error voltage is generated that is used to reduce the error by controlling a voltage controlled phase shifter in series with the line.

The receiver is located at the far end of the stabilized transmission line near the user's equipment. It receives the reference signal from the transmitter, processes it so it can be separated from the reference signal, and sends the processed signal back down the line to the transmitter. It also supplies a stable reference signal to the user.

IV. Analysis

As shown in Fig. 2, a reference signal ($A_1 \sin wt$) from the station standard is split into three equal signals ($A_2 \sin wt$) by three-way power splitter HY-1.

Two of these signals are used as local references in the transmitter and are applied to the LO ports of mixers A2 and A3.

The third signal is sent through a hybrid, a voltage controlled phase shifter, a manual phase shifter and then to the receiver through the transmission line being stabilized.

At the receiver, the received signal goes through another hybrid and then through a narrow (100-Hz) tracking filter that greatly reduces leakages of the control signal to the output reference and restores the amplitude of the reference signal.

The signal out of the tracking filter is split by power splitter HY-2 into three equal signals [$A_2 \sin (wt + \phi)$] where ϕ is phase delay from the input reference to the output.

One signal is used as the stabilized output and provides a reference to the user.

Another signal drives the frequency divider, which divides the reference frequency by 1000.

The third signal goes through mixer A1 where it is modulated by the output of the frequency divider, which is

$$A_3 \sin \left(\frac{wt + \phi + \theta}{1000} \right) \tag{6}$$

where $\theta/1000$ = phase delay through the divider.

The signal out of mixer A1 consists of two spectral lines around a suppressed carrier.

$$A_4 \left[\cos\left(\frac{999\,(wt+\phi)-\theta}{1000}\right) - \cos\left(\frac{1001\,(wt+\phi)+\theta}{1000}\right)\right] \quad (7)$$

The signal is sent through the hybrid down the transmission line back to the transmitter.

At the transmitter, the return signal goes through the manual phase shifter, the voltage controlled phase shifter, and the hybrid, to a quadrature hybrid where it is split into two equal signals in quadrature. The outputs of the quadrature hybrid are

$$A_5 \left[\cos\left(\frac{999\,(wt+\phi+\xi)-\theta}{1000}\right) - \cos\left(\frac{1001\,(wt+\phi+\xi)+\theta}{1000}\right)\right] \quad (8)$$

$$A_5 \left[\sin\left(\frac{1001\,(wt+\phi+\xi)+\theta}{1000}\right) - \sin\left(\frac{999\,(wt+\phi+\xi)-\theta}{1000}\right)\right] \quad (9)$$

where ξ = the return delay down the transmission line.

These signals are mixed with the reference signals (sin wt) in mixers A2 and A3.

The outputs of mixers A2 and A3 after low-pass filtering are respectively

$$A \left[\sin\left(\frac{wt+\phi+\xi+\theta}{1000}\right) \sin(\phi+\xi)\right] \quad (10)$$

$$A_7 \left[\sin\left(\frac{wt+\phi+\xi+\theta}{1000}\right) \cos(\phi+\xi)\right] \quad (11)$$

and are applied to the final mixer (A4).

The filtered signal out of mixer A4 is

$$A_8 \sin 2(\phi+\xi) \quad (12)$$

a dc voltage equal to the product of Eqs. (10) and (11). This signal is applied to the voltage controlled phase shifter to reduce the phase error.

V. Stable Operating Area

Adjustment of the manual phase shifter, which acts like a narrowband line stretcher, is required to set the operating point of the system near the center of a stable operating area.

Two conditions on the slope of the control voltage versus line length curve must be met for stable operation.

(1) The slope does not equal zero or change sign.

(2) The slope has the opposite sign to the slope of the voltage controlled phase shifter (phase versus control voltage).

The stable operating points can be found by plotting the control signal Eq. (12) versus line length (ϕ). See Fig. 3.

Since $\phi \approx \xi$, then Eq. (12) becomes

$$A_8 \sin 2(\phi+\xi) \approx A_8 \sin 4\phi \quad (13)$$

It can be seen from Fig. 3 that the stable operating areas are

$$(n-1)\frac{\pi}{8} < \phi < (n+1)\frac{\pi}{8} \quad (14)$$

where

$$n = 0, 4, 8, 12, \cdots \quad (15)$$

It can also be seen that a stable operating point occurs every $\pi/2$ radians of line length.

VI. Correction Factor

The correction factor for a perfectly matched system can be found by setting

$$\epsilon_0 - G \sin 2(\phi+\xi) = \epsilon_c \quad (16)$$

where

ϵ_0 = the open loop error

ϵ_c = the closed loop error

$G = AK_D K_\phi$

AK_D = total voltage gain in the signal path from mixer A1 output to the voltage control phase shifter input times the phase factor (volts/radian)

$= A_8 \sin 2(\phi+\xi)$ (12)

K_D = the detector gain (not solved for explicitly in this analysis)

K_φ = gain of the phase shifter (radians/volt)

A stable operating point, assuming the phase shifter has the proper slope, is where $\phi \approx \pi/2$, and since $\phi \approx \xi$,

$$(\phi + \xi) \approx (\pi/2 + \pi/2 + \epsilon_c) = (\pi + \epsilon_c) \tag{17}$$

Substituting Eq. (17) into Eq. (12) and simplifying,

$$\sin 2(\phi + \xi) = \sin 2\epsilon_c \tag{18}$$

substituting Eq. (18) into Eq. (16),

$$\epsilon_0 - G \sin 2\epsilon_c = \epsilon_c \tag{19}$$

for small ϵ_c, Eq. (19) becomes

$$\approx \epsilon_0 - 2G\epsilon_c = \epsilon_c$$

Therefore, the correction factor is:

$$\frac{\epsilon_c}{\epsilon_0} = \frac{1}{1 + 2G} \tag{20}$$

VII. Problems

The dominant remaining problem with the present system is the detector sensitivity to changes in amplitude of the signal returned from the stabilizer's receiver. These changes are due primarily to changes in VSWR on the transmission line as pointed out previously in Eq. (5). This problem can be reduced by redesigning the detector or by adding an automatic level control circuit to the present system.

Another source of error is the contamination of the reference signals by leakage, such as that which occurs between the ports of the hybrids. Since hybrid isolation is a function of VSWR on the line, this problem can be reduced by controlling the quality of the transmission line as much as practical, as well as improving the shielding and power supply decoupling.

In some applications, the leakage of the 5-kHz sidebands into the signal supplied to the user must be reduced to extremely low levels. In the present system, these sidebands are approximately 100 dB below the output signal. With extreme care in shielding and grounding, it may be possible to improve this.

Thermal stability of the system is degraded because of the numerous cables that must be used to get signals in and out of the ovens. An improved thermal design would improve the long-term stability.

Miscellaneous problems related to testing, measuring, and monitoring the system have not yet been addressed.

VIII. Test Results

Preliminary short-term tests have been run, and proper operation of the system has been verified.

A line stretcher, placed in series with a 1-km length of coaxial cable (RG 223), was used to change the line length by 25 cm (883 ps). This change was reduced by the transmission line stabilizer to a worse-case change of < 0.3 cm (10 ps), a correction of > 83 times.

Preliminary tests indicate that the phase noise of the system should not appreciably degrade the distributed signal from the station reference.

IX. Conclusion

Preliminary tests indicate that the basic design of the system is sound, but there are several problems that still need attention.

Work is underway to reduce the sensitivity to changes in VSWR on the transmission line so that system performance can be guaranteed.

A new packaging design should be considered to improve long-term stability and accuracy.

Test and monitoring methods and equipment must be developed if line stabilizers are to be used in the DSN on a regular basis.

Transmission line stabilizers will be required if reference signals are to be distributed with phase stabilities in the order of 10 ps or less since there are no other transmission media available at the present time that are this stable without compensation.

Reference

1. John D. Ryder, *Network Lines and Fields*, Prentice Hall, 1949, Chapters 5 and 6.

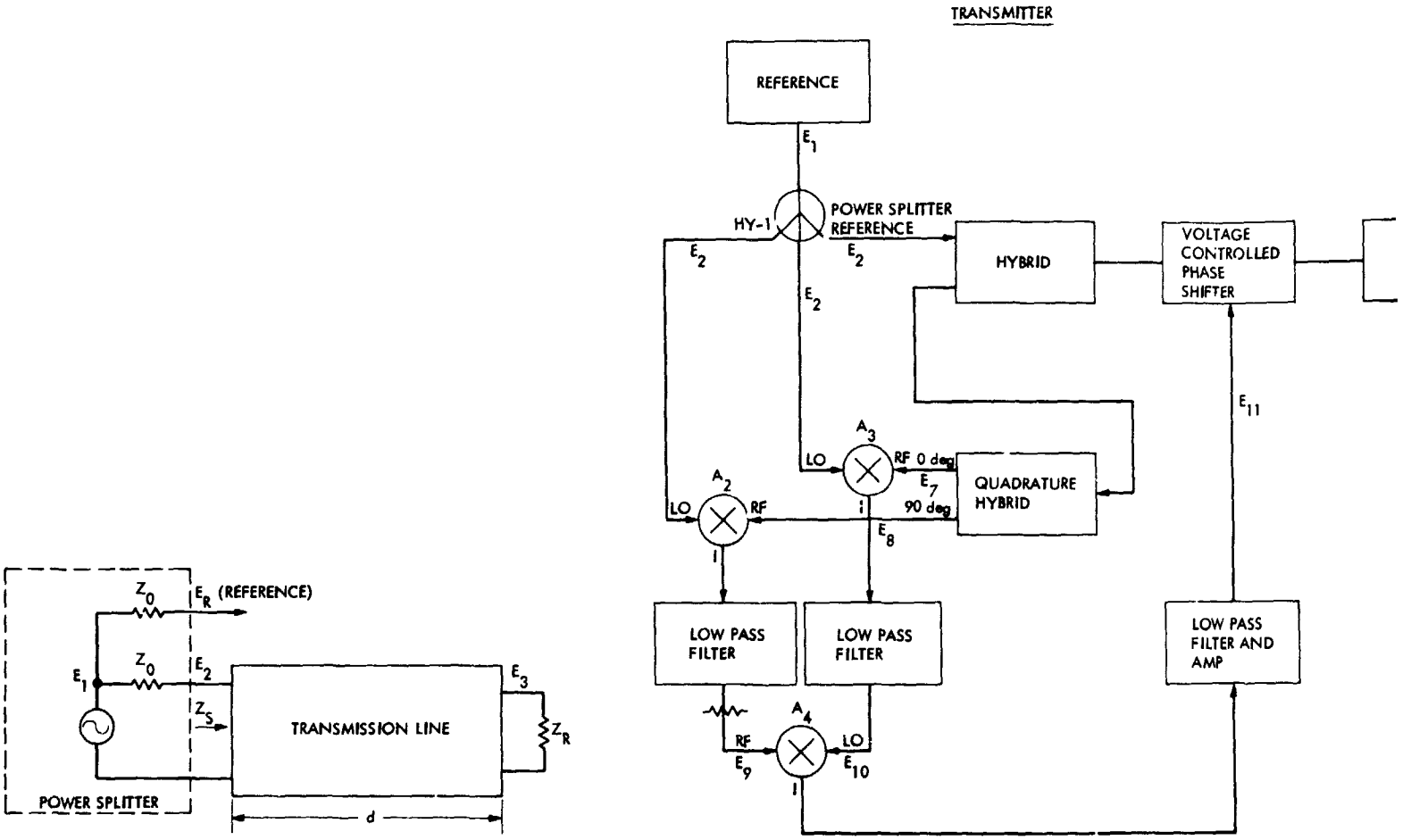

Fig. 1. Transmission line distribution system model

FOLDOUT FRAME

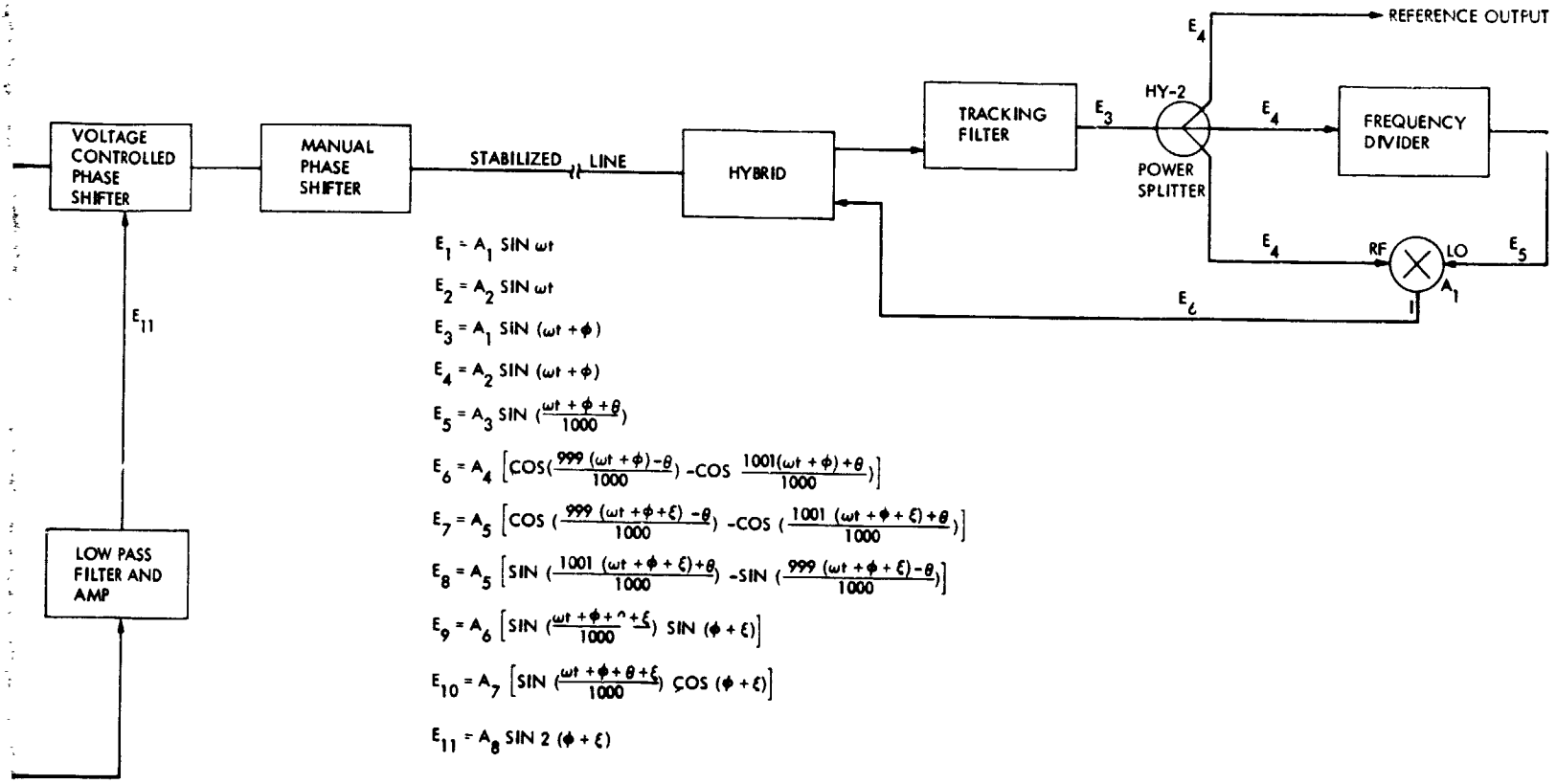

$E_1 = A_1 \sin \omega t$

$E_2 = A_2 \sin \omega t$

$E_3 = A_1 \sin (\omega t + \phi)$

$E_4 = A_2 \sin (\omega t + \phi)$

$E_5 = A_3 \sin \left(\frac{\omega t + \phi + \theta}{1000}\right)$

$E_6 = A_4 \left[\cos\left(\frac{999(\omega t + \phi) - \theta}{1000}\right) - \cos\left(\frac{1001(\omega t + \phi) + \theta}{1000}\right)\right]$

$E_7 = A_5 \left[\cos\left(\frac{999(\omega t + \phi + \xi) - \theta}{1000}\right) - \cos\left(\frac{1001(\omega t + \phi + \xi) + \theta}{1000}\right)\right]$

$E_8 = A_5 \left[\sin\left(\frac{1001(\omega t + \phi + \xi) + \theta}{1000}\right) - \sin\left(\frac{999(\omega t + \phi + \xi) - \theta}{1000}\right)\right]$

$E_9 = A_6 \left[\sin\left(\frac{\omega t + \phi + \theta + \xi}{1000}\right) \sin(\phi + \xi)\right]$

$E_{10} = A_7 \left[\sin\left(\frac{\omega t + \phi + \theta + \xi}{1000}\right) \cos(\phi + \xi)\right]$

$E_{11} = A_8 \sin 2(\phi + \xi)$

Fig. 2. Simplified block diagram of transmission line stabilizer

FOLDOUT FRAME 2

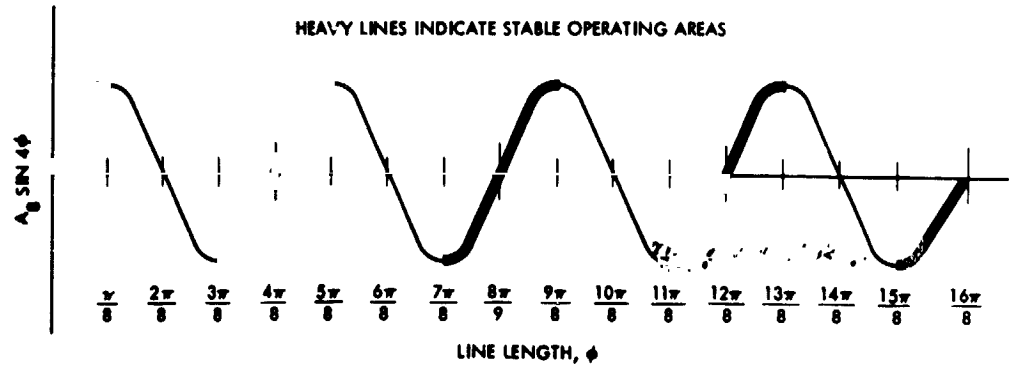

Fig. 3. Open loop error voltage in transmission line stabilizer

PAGE 72 INTENTIONALLY BLANK

N79-25099

Antenna Feedhorn Software Upgrade

P. D. Potter
Radio Frequency and Microwave Subsystems Section

The HYBRIDHORN computer program was developed in 1973 to serve as an item of general purpose antenna feedhorn design and analysis software, and has been utilized extensively since that time for this purpose. The 1973 formulation contains a small flare angle approximation which is subject to question for designs such as the Williams S- and X-band feedhorn. Additionally, the original formulation did not allow azimuthal variation indices other than unity. The HYBRIDHORN program has been recently upgraded to correct both of these deficiencies. A new large flare angle formulation has been found which appears to have escaped the attention of others. In the upgrade, all of the major program elements have been converted to Univac 1108 compatible structured Fortran (SFTRAN) for ease of software maintenance. This article describes the small and large angle formulations and presents some sample numerical results.

I. Small Flare Angle Formulation

The small flare angle approximation is discussed in Ref. 1. The formulation is based on the fact that the fields on a spherical cap in the horn aperture are well approximated by the standard cylindrical (Bessel function) fields (Ref. 2).

Figure 1 shows the horn geometry. Clarricoats (Ref. 3) derived the cylindrical fields for the case of arbitrary index, m, of azimuthal variation. For linear polarization, the following field expressions apply in the horn flare:

$$E_{rmn} = +E_{mn} \cdot J_m(x) \sin(m\phi) \tag{1a}$$

$$H_{rmn} = -\left(\frac{E_{mn}}{Z_0}\right) \cdot \mathrm{BAL}_{mn} \cdot J_m(x) \cos(m\phi) \tag{1b}$$

$$E_{\theta mn} = -jE_{mn} \cdot \left(\frac{k}{K_{mn}}\right) \cdot \left[\frac{J_m(x)}{x}\right] \cdot \left[\bar{\beta}_{mn} F_m(x) + m\,\mathrm{BAL}_{mn}\right] \sin(m\phi) \tag{1c}$$

PAGE 74 INTENTIONALLY BLANK

$$E_{\phi mn} = -jE_{mn} \cdot \left(\frac{k}{K_{mn}}\right) \cdot \left[\frac{J_m(x)}{x}\right] \cdot \left[m \cdot \bar{\beta}_{mn} + \mathrm{BAL}_{mn} \cdot F_m(x)\right] \cos(m\phi) \tag{1d}$$

$$H_{\theta mn} = +j\left(\frac{E_{mn}}{Z_0}\right) \cdot \left(\frac{k}{K_{mn}}\right) \cdot \left[\frac{J_m(x)}{x}\right] \cdot \left[m + \bar{\beta}_{mn} \cdot \mathrm{BAL}_{mn} \cdot F_m(x)\right] \cos(m\phi) \tag{1e}$$

$$H_{\phi mn} = -j\left(\frac{E_{mn}}{Z_0}\right) \cdot \left(\frac{k}{K_{mn}}\right) \cdot \left[\frac{J_m(x)}{x}\right] \cdot \left[F_m(x) + m \cdot \bar{\beta}_{mn} \cdot \mathrm{BAL}_{mn}\right] \sin(m\phi) \tag{1f}$$

where

$$F_m(x) \equiv x \cdot \left[\frac{J'_m(x)}{J_m(x)}\right] \tag{2}$$

$J_m(x)$ = Bessel function of the first kind and order m

$J'_m(x)$ = derivative of $J_m(x)$ with respect to x

k = free-space propagation constant

Z_0 = free-space characteristic impedance

$$x \equiv K_{mn} \cdot r \cdot \theta \tag{3}$$

$$\bar{\beta}_{mn} \equiv \left(1 - \frac{K_{mn}^2}{k^2}\right)^{1/2} = \text{normalized propagation constant} \tag{4}$$

The assumed circumferential grooves in the horn wall require that the azimuthal electric field components be zero at the wall surface. Thus, from Eq. (1d),

$$\mathrm{BAL}_{mn} = -m \cdot \frac{\bar{\beta}_{mn}}{F_m(x_1)} \tag{5}$$

where

$$x_1 = K_{mn} \cdot r \cdot \theta_1 \tag{6}$$

BAL_{mn} is the mode balance; at the balance frequency it is +1 for the normally-used HE_{mn} modes and -1 for the EH_{mn} modes. At the balance frequency, the horn wall presents infinite longitudinal reactance (E_{rmn} divided by $H_{\phi mn}$) and radiation patterns result which have essentially equal E- and H-plane patterns.

By consideration of the boundary conditions, the characteristic equation, which may be solved for K_{mn}, is obtained as:

$$F_m^2(x_1) - m^2\bar{\beta}_{mn}^2 - \left(\frac{K_{mn}}{k}\right)^2 \cdot F_m(x_1) \cdot S_m(x'_1, x'_0) = 0 \tag{7}$$

where

$$S_m(x'_1, x'_0) = \text{radial line admittance function} \equiv x'_1 \cdot \left[\frac{J'_m(x'_1) \cdot Y_m(x'_0) - J_m(x'_0) \cdot Y'_m(x'_1)}{J_m(x'_1) \cdot Y_m(x'_0) - J_m(x'_0) \cdot Y_m(x'_1)}\right] \tag{8}$$

$Y_m(x)$ = Bessel function of the second kind and order m

$Y'_m(x)$ = derivative of Y_m with respect to x

$$x'_1 = k \cdot r \cdot \theta_1 \tag{9}$$

$$x'_0 = x'_1 + k \cdot \text{GROOVE} \tag{10}$$

GROOVE = groove depth

An important special case of the above equations is that in which the groove depth approaches zero, i.e., the horn has smooth walls. For this case BAL_{mn} either approaches a positive zero, and HE_{mn} modes become TM_{mn} modes, or BAL_{mn} approaches a negative infinity and EH_{mn} modes become TE_{mn} modes. The smooth wall case is thus easily accommodated by the above equations.

The final desired outputs of the HYBRIDHORN program are the E- and H-plane polar radiation patterns, given the frequency of operation, horn geometrical parameters and mode excitation amplitudes and phases. By circular symmetry and resulting orthogonality, the azimuthal radiation pattern dependence is given by the selected order, m, of the sinusoidal/cosinusoidal variation. The following steps are performed to compute the radiation patterns:

(1) Given the throat region mode phases, the aperture mode phases are determined by numerical solution of (7) at points in the horn flare and numerical integration of $\bar{\beta}_{mn}$.

(2) The aperture cap fields are determined from Eq. (1c) and Eq. (1d).

(3) The radiated far-fields are determined by a near-field spherical wave expansion (SWE) about the horn vertex of the aperture cap fields (external fields assumed zero).

(4) The SWE fields are normalized and phase-translated to a specified reference point on the horn axis.

Equations (1a-1f) are formal solutions to Maxwell's equations in *cylindrical* coordinates with the assumed anisotropic wall boundary condition; for this cylindrical solution, x is the radial coordinate times K_{mn}. In 1963 Ludwig (Ref. 4) showed that for a spherical geometry such as the horn flare, Eqs. (1a-1f) closely approximate the true fields if the radial cylindrical coordinate is replaced by the arc length (see Eq. (3), (6) and (9) above). This approximation, valid for small flare angles such as those typically utilized in a Cassegrain antenna feedhorn, was discussed in detail by Narasimhan and Rao (Ref. 2). This approximation was used in the original HYBRIDHORN formulation (Ref. 1) and has shown good agreement with experimental data for small (less than 20 degrees) flare angle horns. One of the purposes of the HYBRIDHORN upgrade was to provide the capability of accurate large flare angle calculations. This more rigorous formulation is described in the following section.

II. Large Flare Angle Formulation

The allowable fields in an infinite conical waveguide follow directly from Maxwell's equations. In a source-free isotropic region and assuming $e^{+j\omega t}$ time dependence, Maxwell's equations are:

$$\mathbf{E} = \frac{1}{j\omega\epsilon} \cdot (\nabla \times \mathbf{H}) \tag{11a}$$

$$\mathbf{H} = \frac{1}{j\omega\mu} \cdot (\nabla \times \mathbf{E}) \tag{11b}$$

$$\nabla \cdot (\mu \mathbf{H}) = 0 \tag{11c}$$

$$\nabla \cdot (\epsilon \mathbf{E}) = 0 \tag{11d}$$

Since divergence (curl) is identically zero, from Eq. (11c) **H** may be expressed as the curl of a vector (known as the vector potential), $\mathbf{A}_E$:

$$\mathbf{H}_E \equiv \left(\frac{1}{\mu}\right) \cdot (\nabla \times \mathbf{A}_E) \tag{12a}$$

Equating (11b) and (12a), and recognizing that curl (grad) is identically zero, the result is:

$$\mathbf{E}_E \equiv -\nabla \phi_E - j\omega \cdot \mathbf{A}_E \tag{12b}$$

where ϕ_E is known as the scalar potential.

Similarly, using Eq. (11a) and (11d),

$$\mathbf{E}_H \equiv -\left(\frac{1}{\epsilon}\right) \cdot (\nabla \times \mathbf{A}_H) \tag{13a}$$

$$\mathbf{H}_H \equiv -\nabla \phi_H - j\omega \mathbf{A}_H \tag{13b}$$

By combining Eq. (12a) and (12b) with (11a), and Eq. (13a) and (13b) with (11b), the two vector wave equations are obtained:

$$\nabla \times \nabla \times \mathbf{A}_E + j\omega\mu\epsilon \nabla \phi_E - k^2 \cdot \mathbf{A}_E = 0 \tag{14a}$$

$$\nabla \times \nabla \times \mathbf{A}_H + j\omega\mu\epsilon \nabla \phi_. - k^2 \cdot \mathbf{A}_H = 0 \tag{14b}$$

As particular solutions of (14a) and (14b), consider *E* - (*TM*) and *H* - (*TE*) waves:

$$\mathbf{A}_E \equiv A_E \, \mathbf{a}_r \tag{15a}$$

$$\mathbf{A}_H \equiv A_H \, \mathbf{a}_r \tag{15b}$$

From Eqs. (12a) and (13a) it is clear that Eqs. (15a) and (15b) result in waves with only transverse magnetic and transverse electric fields, respectively.

The scalar potentials, ϕ_E and ϕ_H, are not independent of the vector potentials $\mathbf{A}_E$ and $\mathbf{A}_H$ and may be selected arbitrarily. The following selections lead to convenient results:

$$\phi_E \equiv -\frac{1}{j\omega\mu\epsilon} \cdot \frac{\partial A_E}{\partial r} \tag{16a}$$

$$\phi_H \equiv -\frac{1}{j\omega\mu\epsilon} \cdot \frac{\partial A_H}{\partial r} \tag{16b}$$

Expressing Eqs. (14a) and (14b) in spherical coordinates and using (16a) and (16b), the following scalar wave equations are obtained:

$$\nabla^2 \left(\frac{A_E}{r}\right) + k^2 \cdot \left(\frac{A_E}{r}\right) = 0 \tag{17a}$$

$$\nabla^2 \left(\frac{A_H}{r}\right) + k^2 \cdot \left(\frac{A_H}{r}\right) = 0 \tag{17b}$$

Equations (17a) and (17b) are readily solved by the method of separation of variables. For outward traveling waves with the polar axis included in the region,

$$\left(\frac{A_H}{r}\right) = a_{m\nu} \cdot h_\nu^{(2)}(kr) \cdot P_\nu^m(\cos\theta) \cdot \begin{bmatrix}\cos(m\phi)\\ \sin(m\phi)\end{bmatrix} \tag{18a}$$

$$\left(\frac{A_E}{r}\right) = b_{m\nu} \cdot h_\nu^{(2)}(kr) \cdot P_\nu^m(\cos\theta) \cdot \begin{bmatrix}\sin(m\phi)\\ \cos(m\phi)\end{bmatrix} \tag{18b}$$

where $a_{m\nu}$, $b_{m\nu}$ are *TM* and *TE* wave amplitudes

$h_\nu^{(2)}(kr)$ = the fractional order, outward spherical Hankel function (Refs. 5 and 6)

$P_\nu^m(\cos\theta)$ = fractional degree associated Legendre function of the first kind (Refs. 5, 7)

Equations (18b), (12a) and (11a) can be used to find the expressions for the *TM* field components, and Eqs. (18a), (13a) and (11b) can be used to obtain the *TE* field components. The resulting expressions, previously published by Borgnis and Papas (Ref. 8) are the appropriate expressions for the fields in an infinite, smooth wall conical waveguide. For anisotropic impedance walls, as in a hybridmode horn, hybrid modes may be defined which are combinations of *TM* and *TE* modes. Thus, the HYBRIDHORN fields are expressed as:

$$E_{rmn} = +E_{mn} \cdot \nu_n \cdot (\nu_n + 1) \cdot \frac{h_\nu^{(2)}(kr)}{kr} \cdot P_\nu^m(\cos\theta) \cdot \sin(m\phi) \tag{19a}$$

$$H_{rmn} = -\left(\frac{E_{mn}}{Z_0}\right) \cdot \mathrm{BAL}_{mn} \cdot \nu_n \cdot (\nu_n + 1) \cdot \frac{h_\nu^{(2)}(kr)}{kr} \cdot P_\nu^m(\cos\theta) \cdot \cos(m\phi) \tag{19b}$$

$$E_{\theta mn} = -jE_{mn} \cdot \left\{\frac{j}{kr} \cdot \frac{\partial}{\partial r}\left[rh_\nu^{(2)}(kr)\right] \cdot \frac{\partial P_\nu^m(\cos\theta)}{\partial\theta} + \mathrm{BAL}_{mn} \cdot m \cdot h_\nu^{(2)}(kr) \cdot \frac{P_\nu^m(\cos\theta)}{\sin\theta}\right\} \cdot \sin(m\phi) \tag{19c}$$

$$E_{\phi mn} = -jE_{mn} \cdot \left\{\frac{jm}{kr} \cdot \frac{\partial}{\partial r}\left[rh_\nu^{(2)}(kr)\right] \cdot \frac{P_\nu^m(\cos\theta)}{\sin\theta} + \mathrm{BAL}_{mn} \cdot h_\nu^{(2)}(kr) \cdot \frac{\partial P_\nu^m(\cos\theta)}{\partial\theta}\right\} \cdot \cos(m\phi) \tag{19d}$$

$$H_{\theta mn} = +j\left(\frac{E_{mn}}{Z_0}\right) \cdot \left\{m \cdot h_\nu^{(2)}(kr) \cdot \frac{P_\nu^m(\cos\theta)}{\sin\theta} + \frac{j\mathrm{BAL}_{mn}}{kr} \cdot \frac{\partial}{\partial r}\left[rh_\nu^{(2)}(kr)\right] \frac{\partial P_\nu^m(\cos\theta)}{\partial\theta}\right\} \cdot \cos(m\phi) \tag{19e}$$

$$H_{\phi mn} = -j\left(\frac{E_{mn}}{Z_0}\right)\cdot\left\{h_\nu^{(2)}(kr)\cdot\frac{\partial P_\nu^m(\cos\theta)}{\partial\theta} + jBAL_{mn}\cdot\frac{m}{kr}\cdot\frac{\partial}{\partial r}\left[rh_\nu^{(2)}(kr)\right]\cdot\frac{P_\nu^m(\cos\theta)}{\sin\theta}\right\}\cdot\sin(m\phi) \quad (19f)$$

With the assumed circumferential grooves, the boundary conditions are:

$$E_\phi\Big|_{\theta=\theta_1} = 0 \quad (20)$$

$$\frac{H_\phi}{E_r}\Big|_{\theta=\theta_1} = \text{longitudinal wall admittance} \equiv Y_m(kr) \quad (21)$$

which results in,

$$\sum_{n=1}^{n=\infty} E_{mn}\cdot\left\{\frac{jm}{kr}\cdot\frac{\partial}{\partial r}\left[rh_\nu^{(2)}(kr)\right]\cdot\frac{P_\nu^m(\cos\theta_1)}{\sin\theta_1} + BAL_{mn}\cdot h_\nu^{(2)}(kr)\cdot\frac{\partial P_\nu^m(\cos\theta)}{\partial\theta}\Big|_{\theta=\theta_1}\right\} = 0 \quad (22)$$

and

$$Y_m(kr) = -\frac{j}{Z_0}\,\frac{\sum_{n=1}^{n=\infty} E_{mn}\cdot\left\{h_\nu^{(2)}(kr)\cdot\frac{\partial P_\nu^m(\cos\theta)}{\partial\theta}\Big|_{\theta=\theta_1} + jBAL_{mn}\cdot\frac{m}{kr}\cdot\frac{\partial}{\partial r}\left[rh_\nu^{(2)}(kr)\right]\cdot\frac{P_\nu^m(\cos\theta_1)}{\sin\theta_1}\right\}}{\sum_{n=1}^{n=\infty} E_{mn}\cdot\nu_n\cdot(\nu_n+1)\cdot\frac{h_\nu^{(2)}(kr)}{kr}\cdot P_\nu^m(\cos\theta_1)} \quad (23)$$

The technique of separating variables, which allowed expression of Eqs. (17a) and (17b) as two sets of three total differential equations with solutions as Eqs. (18a) and (18b), requires that Eqs. (22) and (23) be satisfied for all values of kr in the horn. The spherical Hankel function $h_\nu^{(2)}(kr)$ and the radial derivative function, $\partial/\partial r\,[rh_\nu^{(2)}(kr)]$ are both complex and bear a differing relationship to each other as a function of kr. It is thus clear that Eq. (22) cannot be satisfied by a single HE_{mn} or EH_{mn} mode, but rather a summation of modes must be used, as shown. The literature contains an extensive discussion of this problem (Refs. and 10). Clearly, some approximation must be invoked to arrive at the single mode characteristic equation analogous to (7) and the balance condition analogous to (5). The approximations appearing in the literature are both numerically unjustified and lead to equations which cannot be directly compared to the small flare angle formulation discussed in the previous section.

A neat solution to the above dilemma is obtained by using a result derived by Ludwig (Ref. 4). Ludwig showed that if

$$h_\nu^{(2)}(kr) \equiv |h_\nu^{(2)}(kr)|\,e^{-j\alpha_\nu(kr)} \quad (24)$$

then

$$\bar{\beta}_{mn} = \frac{\partial\alpha_\nu(kr)}{\partial(kr)} = \frac{1}{|(kr)\cdot h_\nu^{(2)}(kr)|^2} \quad \text{(exact)} \quad (25)$$

Using Eq. (25), it is easily shown that,

$$\frac{1}{kr}\cdot\frac{\partial}{\partial r}\left[rh_\nu^{(2)}(kr)\right] = h_\nu^{(2)}(kr)\cdot(-j\bar{\beta}_{mn} - \text{ERROR}) \quad (26)$$

where

$$\text{ERROR} \equiv \frac{1}{2} \cdot \frac{1}{\bar{\beta}_{mn}} \cdot \frac{\partial \bar{\beta}_{mn}}{\partial (kr)} \tag{27}$$

The normalized propagation constant $\bar{\beta}_{mn}$ differs significantly from unity for typical horn geometries, but the change of β_{mn} with kr is slow, leading to a small value for the error term. Figure 2 is a plot of $(1 - \beta_{mn})$, |ERROR| and |ERROR|/$(1 - \beta_{mn})$ for kr from 1 to 100 and ν from 1 to 20. The approximation of retaining the nonunity value for β_{mn}, but neglecting the error term, is seen to be excellent; the relative magnitudes of the error and $(1 - \beta_{mn})$ terms are seen to decay as approximately $1/(kr)$. Thus, the approximation is made that,

$$\frac{1}{kr} \cdot \frac{\partial}{\partial r} \left[r h_\nu^{(2)} (kr) \right] \approx - j \beta_{mn} \cdot h_\nu^{(2)} (kr) \tag{28}$$

Combining Eq. (28) with (19a) and (19b),

$$E_{rmn} = + E_{mn} \cdot \nu_n \cdot (\nu_n + 1) \cdot \frac{h_\nu^{(2)} (kr)}{kr} \cdot P_\nu^m (\cos \theta) \cdot \sin (m\phi) \tag{29a}$$

$$H_{rmn} = - \left(\frac{E_{mn}}{Z_0} \right) \cdot \text{BAL}_{mn} \cdot \nu_n \cdot (\nu_n + 1) \cdot \frac{h_\nu^2 (kr)}{kr} \cdot P_\nu^m (\cos \theta) \cdot \cos (m\phi) \tag{29b}$$

$$E_{\theta mn} = - j E_{mn} \cdot h_\nu^{(2)} (kr) \cdot \frac{P_\nu^m (\cos \theta)}{\sin \theta} \cdot \left[\bar{\beta}_{mn} \cdot F_{m\nu} (\cos \theta) + m \cdot \text{BAL}_{mn} \right] \cdot \sin (m\phi) \tag{29c}$$

$$E_{\phi mn} = - j E_{mn} \cdot h_\nu^{(2)} (kr) \cdot \frac{P_\nu^m (\cos \theta)}{\sin \theta} \cdot \left[m \cdot \bar{\beta}_{mn} + \text{BAL}_{mn} \cdot F_{m\nu} (\cos \theta) \right] \cdot \cos (m\phi) \tag{29d}$$

$$H_{\theta mn} = + j \left(\frac{E_{mn}}{Z_0} \right) \cdot h_\nu^{(2)} (kr) \cdot \frac{P_\nu^m (\cos \theta)}{\sin \theta} \cdot \left[m + \bar{\beta}_{mn} \cdot \text{BAL}_{mn} \cdot F_{m\nu} (\cos \theta) \right] \cdot \cos (m\phi) \tag{29e}$$

$$H_{\phi mn} = - j \left(\frac{E_{mn}}{Z_0} \right) \cdot h_\nu^{(2)} (kr) \cdot \frac{P_\nu^m (\cos \theta)}{\sin \theta} \cdot \left[F_{m\nu} (\cos \theta) + m \cdot \bar{\beta}_{mn} \cdot \text{BAL}_{mn} \right] \cdot \sin (m\phi) \tag{29f}$$

where

$$F_{m\nu} (\cos \theta) \equiv \frac{\dfrac{\partial P_\nu^m (\cos \theta)}{\partial \theta}}{\dfrac{P_\nu^m (\cos \theta)}{\sin \theta}} \tag{30}$$

A comparison of Eqs. (29a) to (29f) with Eqs. (1a) to (1f) shows that the approximation in Eq. (28) yields expressions for the fields in a large flare angle horn which are identical in form to those for the small flare angle (Bessel) formulation. The mathematical equivalence between the associated Legendre function and the Bessel function is covered by Ludwig (Ref. 4). Direct numerical comparisons between the two formulations will be discussed in the following section.

With the approximation in Eq. (28), the horn boundary conditions may now be satisfied individually by each mode, and result in the following relationships:

$$\mathrm{BAL}_{mn} = -\frac{m \cdot \bar{\beta}_{mn}}{F_{m\nu}(\cos\theta_1)} \tag{31}$$

$$Y_m(kr) = -\left(\frac{j}{Z_0}\right) \cdot \frac{1}{\nu_n(\nu_n+1)} \cdot \frac{kr}{\sin\theta_1} \cdot \left[F_{m\nu}(\cos\theta_1) + m \cdot \bar{\beta}_{mn} \cdot \mathrm{BAL}_{mn}\right] \tag{32}$$

Equation (32) implies that the wall admittance must be a specified function of kr. The amount of mode conversion which would occur with constant depth grooves in the horn flare has not been investigated but, based on previous experimental results, is expected to be small. In the HYBRIDHORN program, a constant groove depth and the radial line impedance formula (Eq. 8) are assumed. With the relationship

$$Y_m(kr) = -\left(\frac{j}{Z_0}\right) \cdot \frac{S_m(x_1', x_0')}{(kr)\theta_1} \tag{33}$$

The characteristic equation is obtained from (31) and (32) as:

$$F_{m\nu}^2(\cos\theta_1) - m^2 \cdot \bar{\beta}_{mn}^2 - \frac{\nu_n \cdot (\nu_n+1)}{(kr)^2} \cdot \left(\frac{\sin\theta_1}{\theta_1}\right) \cdot F_{m\nu}(\cos\theta_1) \cdot S_m(x_1', x_0') = 0 \tag{34}$$

The upgraded HYBRIDHORN program allows computations to be performed using either the small flare angle (Bessel) formulation, given in Section I above, or the large flare angle (Legendre) formulation, given in this section. The following section discusses numerical results.

III. Numerical Results and Conclusions

The upgraded HYBRIDHORN program allows user selection of either small flare angle (Bessel) or large flare angle (Legendre) computations. The former involve less machine time and are thus normally preferable. For the dominant HE_{11} mode, direct comparisons were made as a function of flare angle. Table 1 gives the horn geometrical parameters and the results of this comparison. The general conclusion is that the Bessel (small flare angle) option may be safely used for horn flare angles less than 20 degrees. Numerical experiments for a 20 degree flare angle were also performed for higher-order modes, azimuthal variations from $m = 0$ to $m = 3$, and for both smooth and corrugated horn walls; a similar conclusion was obtained from these experiments.

The relative pattern insensitivity to formulation selection is a somewhat negative and surprising result, but does lend great confidence to the correctness of both formulations, and also settles the question of whether the Bessel (old) formulation is sufficiently accurate for typical DSN feedhorn configurations.

In the process of upgrading the HYBRIDHORN program to handle both formulations and the case of $m \neq 1$, the coding was generally improved, including conversion of all major program elements to structured Fortran (SFTRAN, version 2). This coding improvement should facilitate future program maintenance.

C-2

References

1. P. D. Potter, "Efficient Antenna Systems: A New Computer Program for the Design and Analysis of High-Performance Conical Feedhorns," *JPL Technical Report 32-1526*, Vol. XIII, pp. 92-107, Jet Propulsion Laboratory, Pasadena, Calif., February 15, 1973.

2. M. S. Narasimhan and B. V Rao, "Hybrid Modes in Corrugated Conical Horns," *Electronic Letters*, Vol. 6, No. 2, pp. 32-34, Jan. 22, 1970.

3. P. J. B. Clarricoats and P. K. Saha, "Propagation and Radiation Behavior of Corrugated Feeds - Part 1: Corrugated Waveguide Feed," *Proc. IEE* (British), Vol. 118, No. 9, pp. 1167-1176, Sept. 1971.

4. A. Ludwig, "Antennas for Space Communications: Antenna Feed Research," in *Supporting Research and Advanced Development*, Space Programs Summary 37-22, Vol. IV, pp. 184-189, Jet Propulsion Laboratory, Pasadena, Calif., Aug. 31, 1963.

5. J. A. Stratton, *Electromagnetic Theory*, Chapter 7. McGraw-Hill Book Company, Inc., New York, 1941.

6. *Handbook of Mathematical Functions*, Chapter 10, Milton Abramowitz and Irene A. Stegun, Eds., National Bureau of Standards, GPO, Washington, D.C., June, 1964.

7. *Ibid.*, Chapter 8.

8. F. E. Borgnis and C. H. Papas, "Electromagnetic Waveguides," in S. Flugge, *Handbuch der Physik*, Vol. XVI, pp. 352-358, Springer-Verlag, Berlin, 1958.

9. P. J. B. Clarricoats and P. K. Saha, "Progagation and Radiation Behavior of Corrugated Feeds – Part 2: Corrugated-Conical-Horn Feed," *Proc. IEE* (British), Vol. 118, No. 9, pp. 1177-1186, Sept. 1971.

10. M. E. J. Jeuken and C. W. Lambrechtse, "Small Corrugated Conical-Horn Antenna with Wide Flare Angle," *Electronic Letters*, Vol. 5, pp. 489-490, October 2, 1969.

Table 1. HE_{11} mode flare angle comparisons[a]

Flare Angle	β_{11} (Aperture cap)		BAL_{11} (Aperture cap)		$P_m(\theta_1), P_{m1}(\cos\theta_1)$ (Aperture cap)		K_{11} (Aperture cap)		Bessel pattern error relative to Legendre at −40 dB level, dB
	Bessel	Legendre	Bessel	Legendre	Bessel	Legendre	Bessel	Legendre	
20°	.99969	.99969	1.06386	1.06347	−.93968	−.94003	.11102	.11191	0.1
40°	.99973	.99971	1.05999	1.05848	−.94315	−.94448	.10439	.10748	0.3
60°	.99978	.99975	1.05386	1.05072	−.94869	−.95149	.09385	.10024	0.7
70°	.99981	.99977	1.05008	1.04602	−.95213	−.95579	.08734	.09559	1.0

[a]Frequency = 8.415 GHz
Aperture diameter = 106.68 cm (42 in.)
Groove depth = 5.0927 cm (2.005 in.)

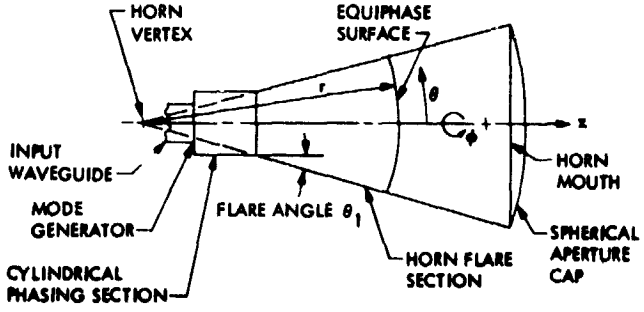

Fig. 1. Horn geometry

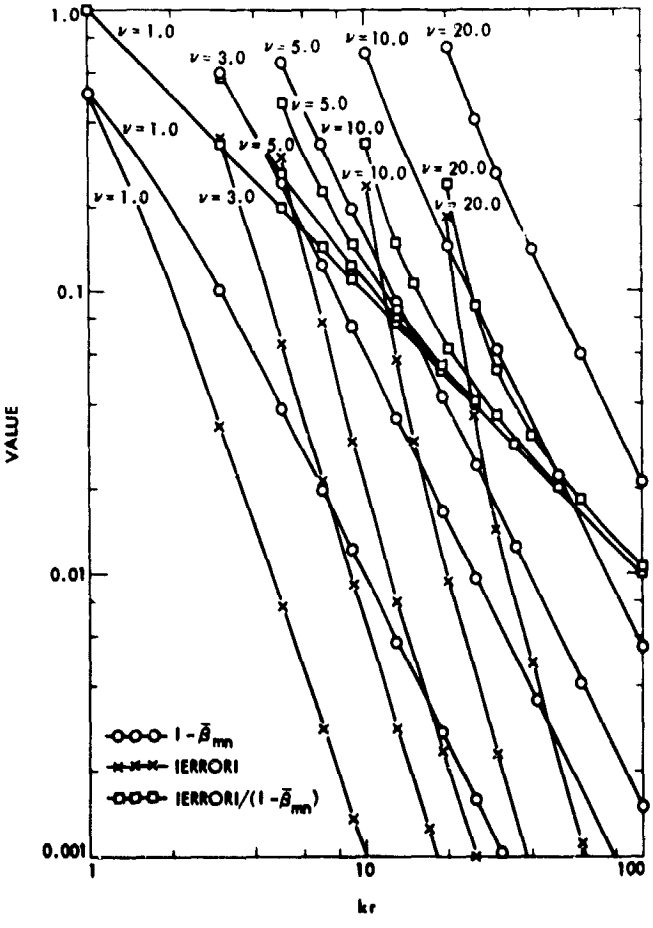

Fig. 2. Large flare angle approximation errors

D/3

N79-25100

Feasibility of Inertialess Conscan Utilizing Modified DSN Feedsystems

P. D. Potter
Radio Frequency and Microwave Subsystems

The closed-loop conical-scan (conscan) technique has proven to be a useful method for pointing the DSN antennas more accurately than is possible by open-loop methods. As presently implemented, the antenna beam is scanned about the received signal direction by physical movement of the antenna. While straightforward, this approach has at least two disadvantages. Firstly, because of structural distortions, finite angle encoder resolution, and drive servo response, the actual antenna beam direction only approximates the commanded beam direction. Secondly, because of the large mass moved during scan, the rate of scan is severely restricted. If there are significant gain or signal level variations during a scan period, the conscan system interprets these variations as antenna pointing error. Both of these disadvantages would be alleviated in an inertialess conscan system in which the beam scanning was performed electronically. Recently, standard JPL antenna feedhorn software was upgraded (described separately in this report) to calculate, among other things, asymmetric corrugated horn radiation patterns of the type that would be needed for electronic beam scan. A brief look has been taken at the required horn excitation. The results, described in this article, are highly promising.

I. Introduction

The basic conscan technique utilized with the DSN antennas has been described in detail by Ohlsen and Reid (Ref. 1). Basically, the beam is continuously precessed at a specified scan radius about the expected signal arrival direction, and variations of signal are cross-correlated with the beam position. To a first approximation, any error between the precession cone axis and the signal direction results in a sinusoidal variation of the received signal level. This variation may then be processed and utilized to effect a pointing correction. A limitation of conscan is that spacecraft signal level variations and receiver gain fluctuations that occur during one scan period are interpreted as pointing errors; thus it would be desirable to scan very rapidly and integrate over many scan periods, as the spectrum of signal fluctuations tends to decay rapidly with increasing frequency. This objective could be achieved with electronic, rather than mechanical, beam scanning. A second important consideration is that mechanical scanning is inherently limited in accuracy by drive servo response, finite encoder resolution, and structural distortions. To be useful, an electronic beam scanning system would have to be designed such that antenna aperture efficiency and system noise temperature are not significantly degraded by introduction of the beam scanning capability. These prob-

lems are only addressed conceptually in this article, but do not appear serious.

II. Method of Beam Scan

A good way of visualizing the inertialess conscan system is in terms of the more familiar monopulse technique. In the monopulse technique, the feed system produces a "reference" beam (symmetrical with respect to the antenna axis) and a pair of spatially-orthogonal "error" beams (asymmetrical with respect to the antenna axis). For small pointing errors, the error beam signal is directly proportional to pointing error. Each of the two error beams has a plane (containing the antenna axis) of zero output called the "null plane." The two null planes are designed to be as orthogonal as possible, thus providing pointing errors in two perpendicular coordinates.

It can readily be seen from symmetry considerations that if the three outputs from a monopulse feed were combined in such a way that controlled small amounts of the error outputs were added to the reference output, the resultant beam would be scanned off axis by an amount directly related to the amount of error output added to the reference output. Moreover, if the total amount of error signal added to both channels was held constant, but varied sinusoidally and consinusoidally, respectively, with time between the two channels, the result would be a precessing beam; i.e., a conscan. This is the basic concept discussed here. Although we are discussing conical scan and not monopulse, it is convenient to retain the "reference" and "error" nomenclature to identify symmetry properties of feedhorn modes and beams.

Conceptually, the inertialess conscan feed discussed here consists of a corrugated conical horn similar to those presently in use in the DSN, except that capability is introduced in the throat region of the horn for generating a controllable amount of error (asymmetric) mode for beam scan. This generation could be accomplished, for example, by a system of probes driven by semiconductor devices The feedhorn propagation characteristics of these error modes and their radiation characteristics can be calculated to high accuracy with recently upgraded JPL software (Ref. 2). It turns out that these error modes have very fortunate properties, which appear to have gone unnoticed in previous work; these properties are discussed in the following section.

III. Asymmetric Feedhorn Modes for Beam Scan

The fields inside a corrugated conical feedhorn may be expanded in a series of orthogonal modes (Clarricoats, Ref. 3, has an excellent discussion of this technique), each of which takes the form of a complicated polar (θ) dependence multiplied by sinusoidal/cosinusoidal azimuthal (ϕ) dependence. Additionally, there are two general classes of these "hybrid" modes, designated HE_{mn} and EH_{mn}. Thus the polar and azimuthal electric fields for these modes are given respectively by,

$$E_{\theta_{mn}} = A_n(\theta) \begin{bmatrix} \sin(m\phi) \\ \cos(m\phi) \end{bmatrix} \quad (1a)$$

$$E_{\phi_{mn}} = B_n(\theta) \begin{bmatrix} \cos(m\phi) \\ \sin(m\phi) \end{bmatrix} \quad (1b)$$

The subscript n refers to the order of the Eigenvalue solution to fields in the horn. For the reference beam (as presently used in the DSN feedhorns), the HE_{11} mode is normally used, sometimes in conjunction with the HE_{12} mode for beamshaping purposes. The index m is selected to be 1 for pattern symmetry, and $A_n(\theta)$ is made as nearly equal to $B_n(\theta)$ as possible for polarization purity and high aperture efficiency (see Ludwig, Ref. 4).

Because the corrugated feedhorn has circumferential grooves, it can also support smooth wall modes that have only circumferential wall currents (the TE_{on} modes). Figure 1 shows the minimum three modes necessary to construct circularly-polarized error patterns; namely TE_{01} EH_{01}/HE_{01}, and HE_{21}.[1] At the horn balance frequency (infinite groove reactance) all three of these error modes have the same Eigenvalue solution and hence propagate with the same velocity (Ref. 3). Additionally, the polar field variation is identical for each. Near the balance frequency, these desirable properties are approximately maintained. Thus, the circularly polarized error beams are inherently broadband. The reference mode does, however, propagate with a different velocity. Thus for the inertialess conscan system described here, the phase of the beam scan is frequency sensitive and must be taken into account.

Using the upgraded hybridhorn program (Ref. 2), HE_{11} (reference), EH_{01}, TE_{01}, and HE_{21} feedhorn 8.415-GHz patterns were computed for the standard DSN horn developed by Brunstein (Ref. 5); these are shown in Figs. 2 through 5. Similar 8.415-GHz patterns were computed for the multifrequency feedhorn recently developed by Williams (Ref. 6); these are shown in Figs. 6 through 9. In all cases, the three

[1] Ludwig's (Ref. 4) proposed definition of normal and cross-polarization is used in Fig. 1.

error mode patterns have essentially coincident phase centers and nearly equal phase delay in travelling from horn throat to aperture. As can be seen in Figs. 2 through 9, all of the error patterns are essentially identical (for a given horn), thus insuring high polarization purity.

IV. Error Mode Excitation and Control

For the standard Brunstein horn, the computed 8.415-GHz mode cutoff horn throat diameter is shown in Table 1 for the lowest modes.

As shown in Table 1, the four required modes have the lowest cutoff diameters, thus allowing rejection of undesired higher order modes.

Figure 10 shows conceptual designs for standard and multifrequency horns with electronic scan.

V. Conclusion

This brief study of beamscan by use of corrugated conical horn modes was performed as a part of the hybrid horn software (Ref. 2) verification process. The results are highly encouraging and indicate that inertialess conscan is feasible with modified versions of present DSN feedhorns. Mode excitation devices have not, however, been investigated.

Acknowledgement

Inertialess conscan and this general method of achieving it was originally suggested by D. A. Bathker of Section 333.

References

1. J. E. Ohlson and M. S. Reid, *Conical-Scan Tracking with the 64-m Diameter Antenna at Goldstone*, Technical Report 32-1605, Jet Propulsion Laboratory, Pasadena, Calif., October 1, 1976.

2. P. D. Potter, "Antenna Feedhorn Software Upgrade," *The Deep Space Network Progress Report 42-51* (this issue).

3. P. J. B. Clarricoats and P. K. Saha, "Propagation and Radiation Behavior of Corrugated Feeds – Part 1. Corrugated Waveguide Feed," *Proc. IEE* (British), Vol. 118, No. 9, Sept. 1971, pp. 1167-1176.

4. A. C. Ludwig, "The Definition of Cross-Polarization," *IEEE Transactions on Antennas and Propagation*, Vol. AP-21, pp. 116-119, January, 1973.

5. S. A. Brunstein, "A New Wideband Feed Horn with Equal E- and H-Plane Beamwidths and Suppressed Sidelobes," in *The Deep Space Network, Space Programs Summary 37-58*, Vol. II, pp. 61-64, Jet Propulsion Laboratory, Pasadena, Calif., July 31, 1969.

6. W. F. Williams, "A Prototype DSN X-S Band Feed: DSS 13 First Application Status," *The Deep Space Network Progress Report 42-44*, Jet Propulsion Laboratory, Pasadena, Calif., pp. 98-103, January and February, 1978.

Table 1. Mode cutoff diameters

Mode	Cutoff diameter, cm (in.)	Comments
HE_{11}	2.29 (0.90)	Normally-used (reference) mode
HE_{21}	3.81 (1.50)	Desired error mode
EH_{01}	4.06 (1.60)	Desired error mode
TE_{01}	4.34 (1.71)	Desired error mode
EH_{11}	5.51 (2.17)	Undesired mode
HE_{12}	5.97 (2.35)	Beamshaping mode

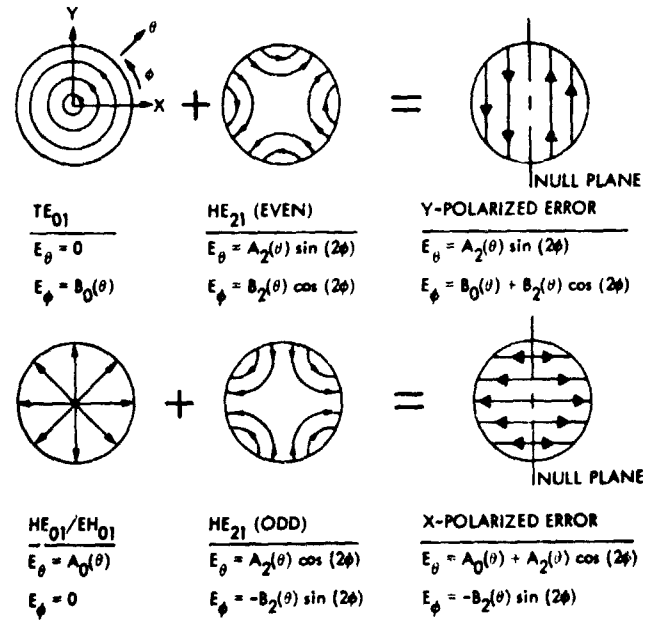

TE_{01}: $E_\theta = 0$, $E_\phi = B_0(\theta)$

HE_{21} (EVEN): $E_\theta = A_2(\theta) \sin(2\phi)$, $E_\phi = B_2(\theta) \cos(2\phi)$

Y-POLARIZED ERROR: $E_\theta = A_2(\theta) \sin(2\phi)$, $E_\phi = B_0(\theta) + B_2(\theta) \cos(2\phi)$

HE_{01}/EH_{01}: $E_\theta = A_0(\theta)$, $E_\phi = 0$

HE_{21} (ODD): $E_\theta = A_2(\theta) \cos(2\phi)$, $E_\phi = -B_2(\theta) \sin(2\phi)$

X-POLARIZED ERROR: $E_\theta = A_0(\theta) + A_2(\theta) \cos(2\phi)$, $E_\phi = -B_2(\theta) \sin(2\phi)$

Y-POLARIZED ERROR:

$$E_N = \left\{ [B_0(\theta) + B_2(\theta)] + [A_2(\theta) - B_2(\theta)] \sin(2\phi) \right\} \cos\phi$$

FOR $B_0(\theta) = A_2(\theta) = B_2(\theta)$, $E_N = 2B_0(\theta) \cos\phi$ (DESIRED POLARIZATION)

$E_C = 0$ (CROSS POLARIZATION)

X-POLARIZED ERROR:

$$E_N = [A_0(\theta) + A_2(\theta)] \cos\phi + [B_2(\theta) - A_2(\theta)] \sin(2\phi) \sin\phi$$

FOR $A_0(\theta) = A_2(\theta) = B_2(\theta)$, $E_N = 2A_0(\theta) \cos\phi$ (DESIRED POLARIZATION)

$E_C = 0$ (CROSS POLARIZATION)

Fig. 1. Error channel modes in corrugated horns

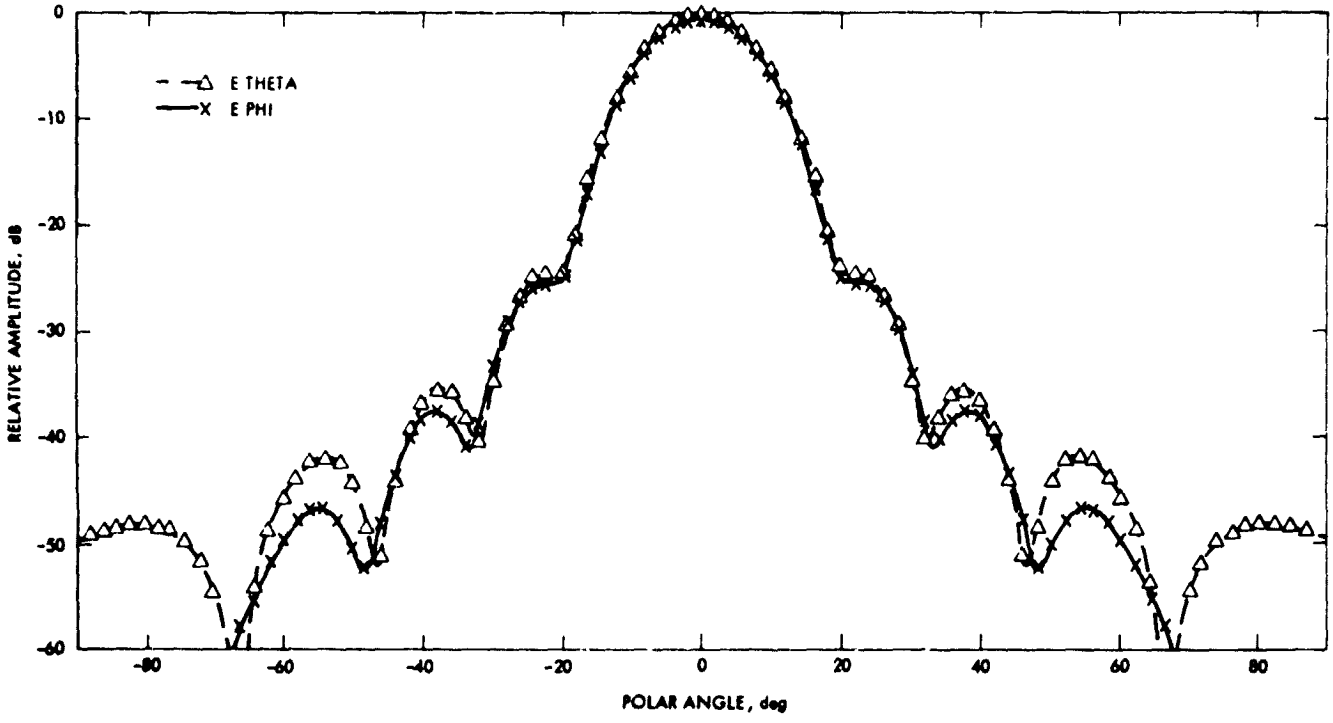

Fig. 2. Brunstein horn, HE_{11} Mode, 8.415 GHz

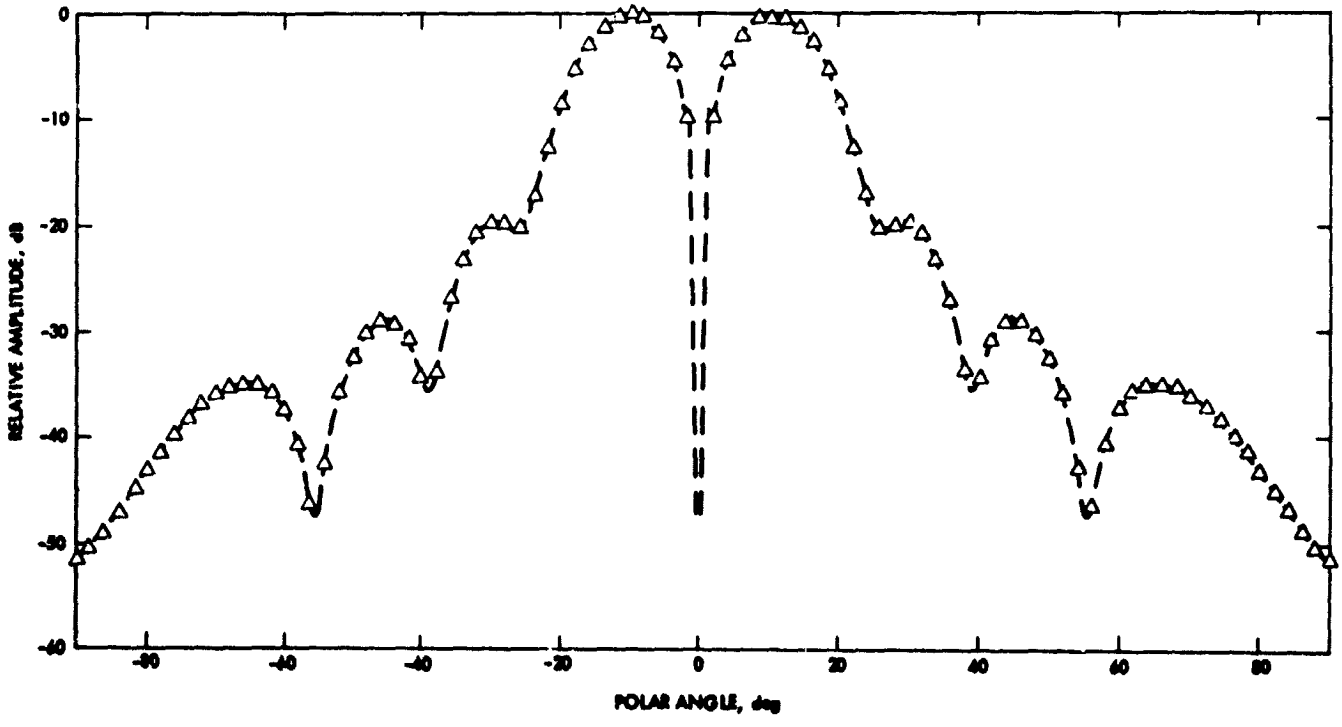

Fig. 3. Brunstein horn, EH_{01} Mode, 8.415 GHz, E theta

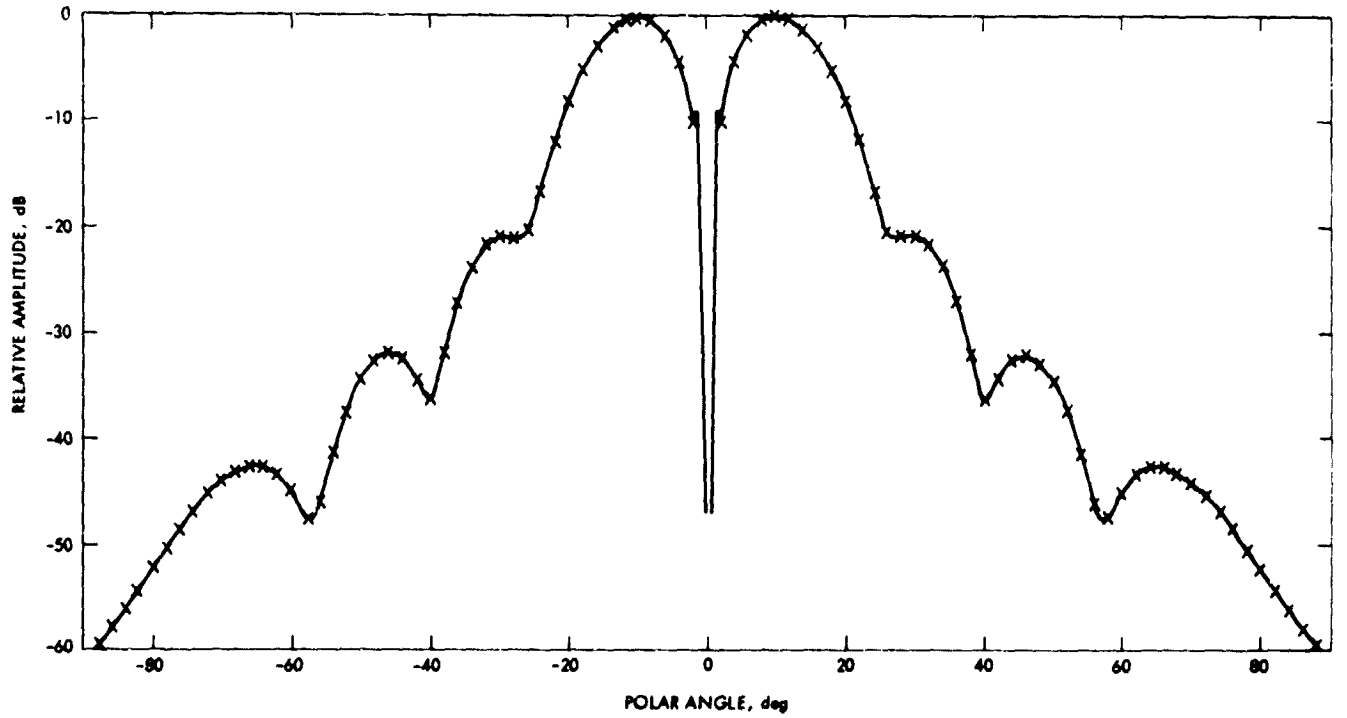

Fig. 4. Brunstein horn, TE_{01} Mode, 8.415 GHz, E phi

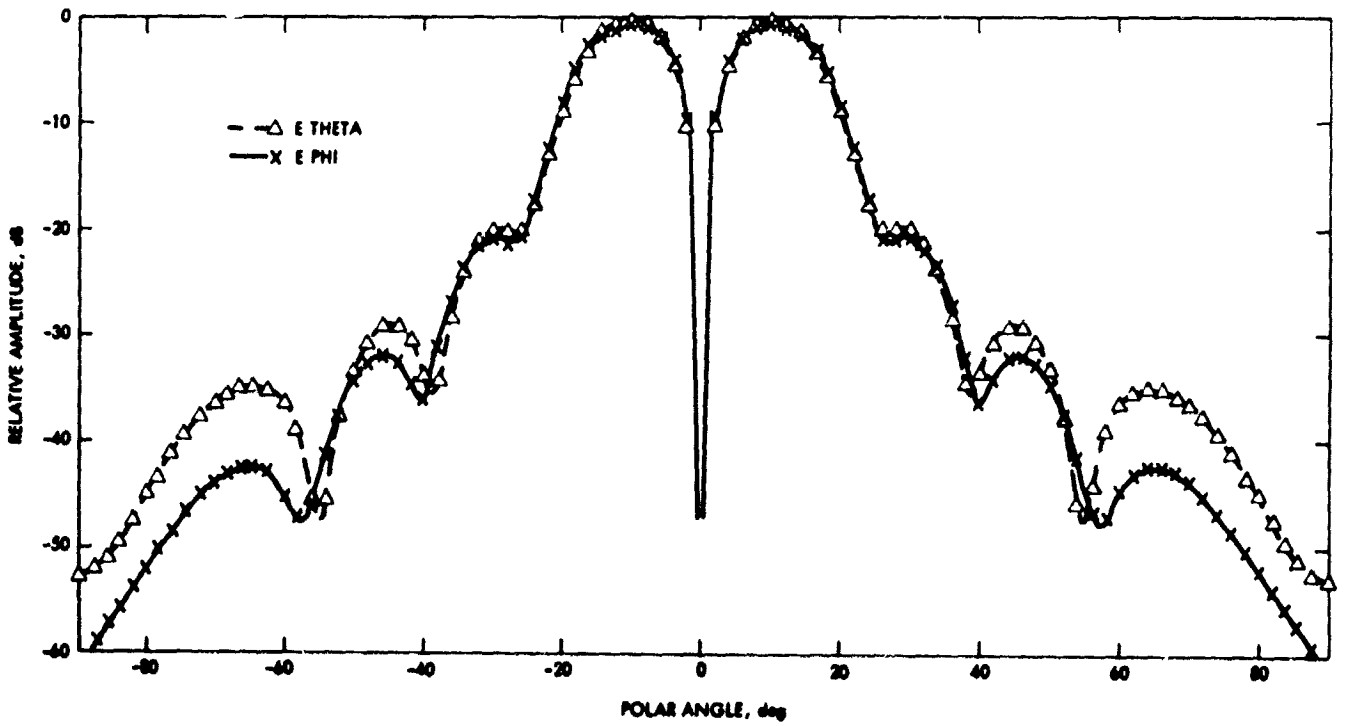

Fig. 5. Brunstein horn, HE_{21} Mode, 8.415 GHz

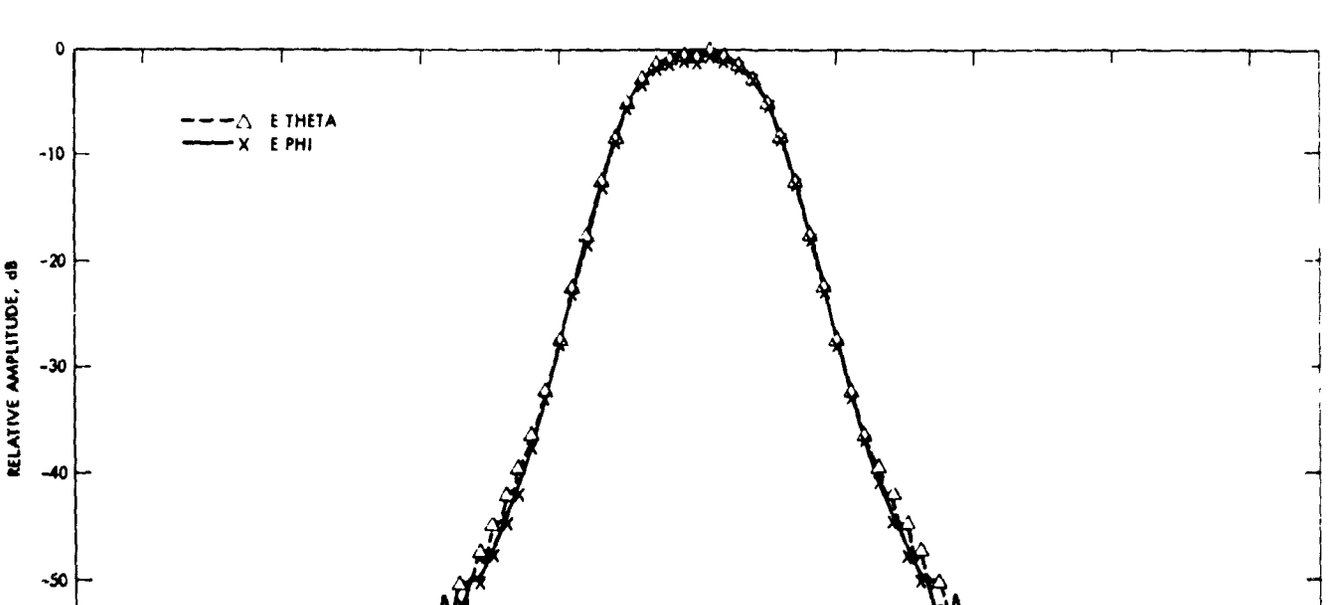

Fig. 6. Williams horn, HE_{11} Mode, 8.415 GHz

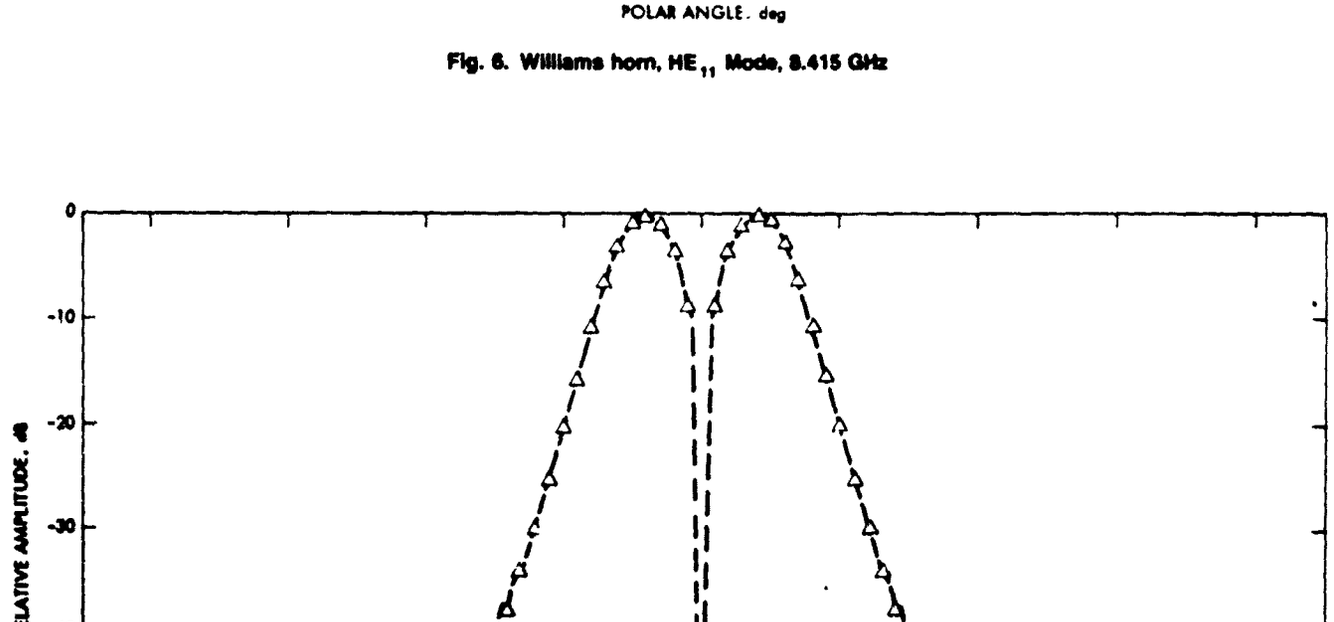

Fig. 7. Williams horn, EH_{01} Mode, 8.415 GHz, E theta

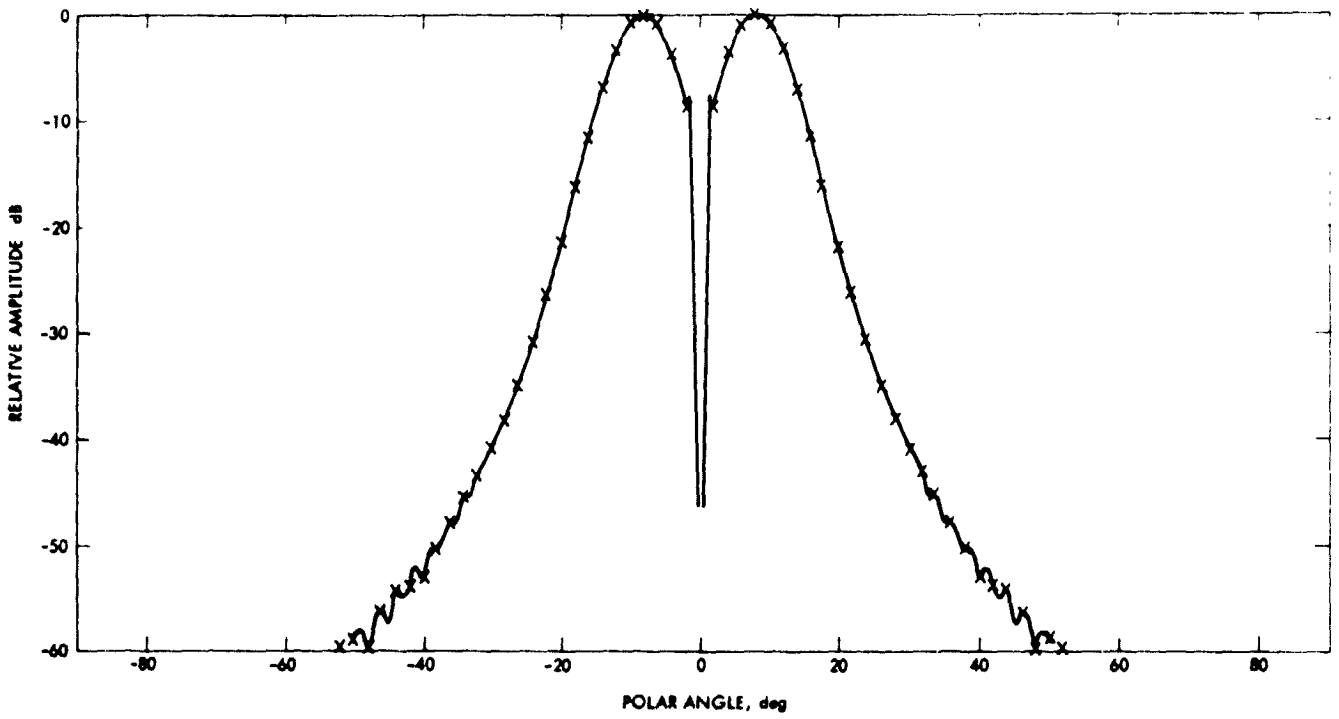

Fig. 8. Williams horn, TE_{01} Mode, 8.415 GHz, E phi

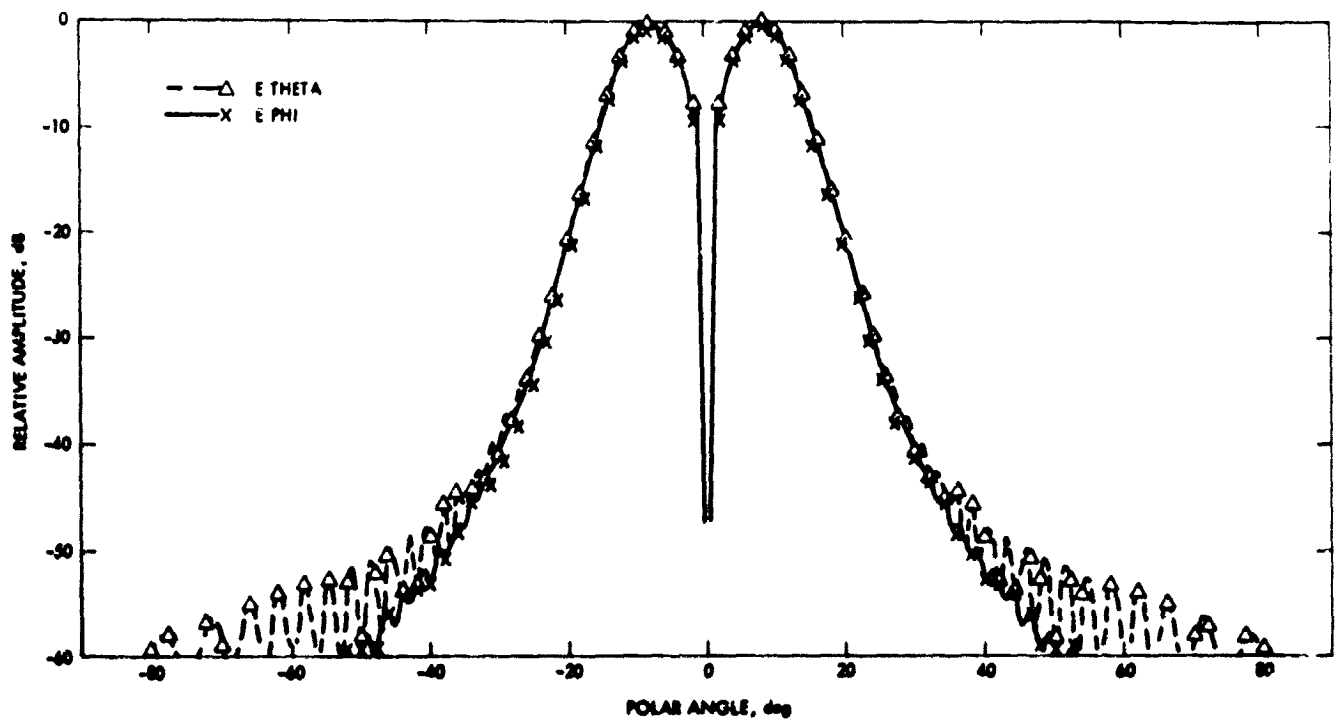

Fig. 9. Williams horn, HE_{21} Mode, 8.415 GHz

ORIGINAL PAGE IS
OF POOR QUALITY

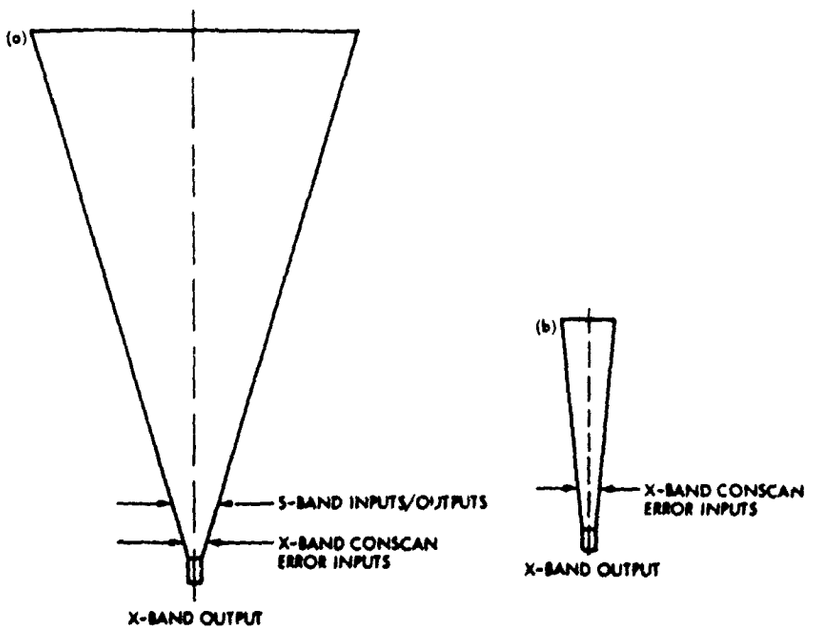

Fig. 10. Conceptual electronic beam scan configurations. (a) multi-frequency horn with electronic X-band beam scan; (b) single-frequency horn with electronic X-band beam scan

N79-25101

Costas Loop Demodulation of Suppressed Carrier BPSK Signals in the DSN Environment—Experimental Results Obtained at TDL

R. Reasoner
DSN Data Systems Section

G. Stevens and K. T. Woo
Communications Systems Research Section

Suppressed carrier binary phase-shift keyed (BPSK) signalling is currently being considered as a design alternative for future DSN telemetry in the multimegabit range. Carrier tracking of such signals is usually achieved by a Costas loop, as opposed to the ordinary phase lock loop. A Costas loop capable of demodulating BPSK signals with data rates up to 1 Msps has been designed and constructed and its Doppler tracking performance with respect to a Block III receiver has been tested at the Telecommunications Development Laboratory (TDL). The purpose of these experiments is to investigate the compatibility of suppressed carrier signalling with the current radio metric system; specifically Doppler tracking and ranging. This article documents the experimental results obtained to-date with respect to Doppler tracking.

I. Introduction

In future imagery missions such as VOIR, the symbol rates of the returned telemetry data are expected to be in the multimegabit per second region. In this range of data rates, it is pointed out in Ref. 1 that, from the telemetry systems point of view, suppressed carrier binary phase-shift keyed (BPSK) signalling with Costas loop carrier recovery will offer advantages both in bandwidth savings and improved tracking performance over the residual carrier format. However, the compatibility of this approach with the existing radio metric system has not been verified. The basic concerns here are the Doppler tracking and ranging accuracies, and their sensitivities to data rates, data patterns, temperature variations, and Doppler conditions. Also, when the Costas loop is used in conjunction with one of the DSN receivers, the effects of hardware constraints peculiar to these receivers such as passband characteristics, mixer nonlinearities, and oscillator phase instabilities on this new type of signal format are also of concern in the overall system performance.

To investigate these effects on system performance it is felt that, aside from detailed analyses, which are only as accurate as the models assumed, actual testing of a Costas loop performing carrier recovery for suppressed carrier signals in the DSN environment is most beneficial.

A scaled-down version of the Costas loop that will be implemented in the multimegabit telemetry demodulator/detector (MTDD) has been designed and constructed. The symbol rates of the MTDD range from 100 kilosymbols per second (ksps) to 30 megasymbols per second (Msps) (Ref. 2). The Costas loop described here is capable of demodulating BPSK signals with data rates up to 1 Msps only. A detail description of this Costas loop is documented in Ref. 3. This loop has been tested with respect to the Block III receiver at TDL. So far, the tests performed concern only Doppler tracking. Four categories of tests have been performed. The first category consists of design verifications of the Costas demodulator. This consisted of measuring the loop's rms phase jitter and steady-state phase error at assumed Doppler conditions and various symbol SNRs (ST/N_0). Their sensitivities with respect to data pattern and data rate variations were investigated as were the loop's frequency pull-in time and pull-in range. The pull-in time and range tests serve only to verify the design, since sweep acquisition is planned in the MTDD unit.

The second category of tests consists of long-term stability tests of the Costas loop in the TDL environment, which closely approximates that of the DSN stations. The third category of tests was designed to test the variations in the phase of the Costas loop's reconstructed carrier due to Doppler offsets and the effects of asymmetric passband filtering in the receiver front end (e.g., the maser amplifier). The fourth category of tests was designed to investigate the performance of the Costas loop when used for carrier recovery of residual carrier signals with an 80-deg modulation angle and with data on a square-wave subcarrier. The Voyager spacecraft transmits signals of this type.

The test results obtained at the TDL with respect to these tests are documented in this paper. These preliminary results indicate that there is no noticeable incompatibility between the current radio metric system and Costas loop demodulation of suppressed carrier BPSK signalling, as far as Doppler tracking is concerned. Of course, further testing has to be performed with respect to ranging accuracies.

II. Description of Test Configurations

The Telecommunications Development Laboratory (TDL) was employed to test the performance of this Costas demodulator. The TDL contains the equipment necessary to generate BPSK signals at S- and X-band, Block III and Block IV receivers, Doppler extractors, and the capability to perform automated phase data gathering and analysis. The Block III receiver was selected over the Block IV receiver for our measurements due to hardware problems in the Block IV during the test period.

Figure 1 indicates the configuration used to generate BPSK S-band signals. The Data Rate Synthesizer and Subcarrier Generator are locked to the Frequency and Timing Subsystem (FTS) that provides reference tones for the TDL. The Data Rate Synthesizer and Subcarrier Generator are manually programmed to the desired data rate and subcarrier frequency, respectively. The Data Pattern Generator is manually set to either a PN sequence or a switch selected data pattern. Either the modulated subcarrier or the data pattern itself may be selected to modulate the carrier.

The Block III Exciter is also shown in Fig. 1. The exciter output is monitored by a frequency counter to provide equivalent Doppler information (frequency counted X 96 = carrier frequency at S band). The signal level to the modulator is varied to adjust for the desired carrier suppression. The output from the translator circuit is the S-band downlink signal.

Figure 2 depicts the receiver end of the configuration. The S-band signal is attenuated to a desired level based on Y factor measurements at the 50 MHz IF output. The output from the 10-MHz IF is fed to a narrowband measurement system to measure the carrier suppression by testing the power at the carrier frequency with and without modulation. The 10-MHz IF output drives the Block III receiver control loop and the Costas control loop. The Block III receiver VCO is driven by either loop by connecting the appropriate cables.

Detail descriptions of the Costas loop design can be found in Ref. 3. For the particular loop that was intended only for testing purposes at TDL, no automatic gain control circuit was provided. The manual gain control (MGC) in the Block III was therefore used in testing this Costas loop.

Figure 3 shows the data acquisition hardware. The Doppler extractor is fed by the exciter and receiver oscillator outputs (each tripled). The extractor simulates the up and down conversions as well as the spacecraft transponder. The signals are mixed to 50 MHz (in lock), divided by 4, and complex mixed against 12.5 MHz to provide a phase error/4 signal and a phase error/4 + 90 deg signal. These signals are fed to two analog-to-digital converters (A/D) that are controlled by an Altair 8800 microcomputer. The 8800 is initialized by, and transmits digital information to, a Modcomp II minicomputer.

The software available at TDL has the capability to provide mean phase (for long-term stability) and phase jitter (for rms) analyses.

III. Performance Verification Tests

The first set of tests performed was intended to verify the predicted performance of the Costas loop design.

Before installing the Costas loop in the TDL, the hardware was tested with simulated, noise-free signals. A 10-MHz biphase modulated suppressed carrier signal was generated with the equipment shown in Fig. 4. The frequency and phase of the 10-MHz carrier oscillator was controlled by the Costas loop hardware. In particular, pull-in time of the Costas loop was measured by stepping the carrier frequency oscillator in known increments. Results of these tests are shown in Table 1. Also shown in Table 1 are the theoretical predictions on these pull-in times, which are derived in Ref. 3. The particular loop design with a received data rate of 100 ksps (Ref. 3) was used in obtaining the test data shown here.

As shown in Table 1, reasonable agreement in the pull-in time performance between predictions and measurements were obtained. Also measured was the pull-in range of the loop. The measured pull-in range was around 1000 Hz. The predicted pull-in range is 894 Hz (Ref. 3).

After the Costas loop was installed at TDL, interfacing with the 10-MHz IF of the Block III receiver, its performance was tested in the presence of thermal noise and oscillator phase instabilities. To verify its performance, the rms phase jitter and steady-state phase errors of the loop were first tested as functions of the following variables:

(1) Data patterns (PN or square wave)

(2) Data rates (100 ksps to 1 Msps)

(3) Symbol SNRs (from −4 dB to +4 dB)

The rms phase jitter of the Costas loop was tested with the configurations shown in Figs 1, 2, and 3. Figure 5 shows the rms phase jitter of the loop as ST/N_0 increases from −4 to +4 dB. The loop was designed for the 100 ksps data rate. Test results for both PN and square wave data are shown. The results shown in Fig. 5 demonstrated good agreement between predicted and measured performance. They also demonstrated that the loop's performance is practically insensitive to whether the data pattern is PN or square wave. Agreement between predictions and measurements are better at high ST/N_0s than at low ST/N_0s. This can be attributed to the effects of oscillator phase instabilities, since, at low ST/N_0s signal suppression due to the hard-limiter in the in-phase channel (Ref. 3) of the Costas loop is more severe, resulting in narrower loop bandwidths and larger phase jitter due to oscillator phase instabilities. The performance predictions given in Ref. 3 treated the effects of thermal noise only, while the oscillator phase noise effects were neglected.

Figure 6 shows the rms phase jitter of the three loops designed for data rates at 100 ksps, 250 ksps, and 1 Msps respectively, as functions of ST/N_0. By design, the theoretical performance of these loops should be identical. However, measured results show that the phase jitters of the loops at higher data rates are larger than those of the lower data rate cases. This is due largely to the inherent bandlimiting of the complex mixer (Ref. 3). In addition, this may also be due, though much less significantly, to the data generator that generates less perfect waveforms at higher data rates. Neither of these effects was included in the analysis reported in Ref. 3. Nevertheless, fair agreement still exists between measurements and predictions.

In addition to rms phase jitter, the steady-state phase error of the Costas loop in the presence of a 2-kHz Doppler offset was also measured for ST/N_0s ranging from −4 to +4 dB. Figure 7 shows the steady-state phase errors of the loops designed for 100 ksps and 250 ksps respectively, with a Doppler offset of 2 kHz. It is observed from Fig. 7 that the measured steady-state phase error of the loop receiving 100 ksps data is in better agreement with theory than that of the loop receiving 250 ksps. This is again due to additional bandlimiting in the complex mixer, which is not accounted for in the analyses, and which introduces additional signal suppression in the loop error signal.

In the actual design of the Costas loop in the Multimegabit Telemetry Demodulator/Detector, the mixer bandwidth will be selected much wider than the data rate to minimize this effect.

IV. Long-Term Stability Tests

To quantify the effects of temperature variations and oscillator long-term instabilities on the reconstructed carrier phase, a long-term stability test in excess of 16 hours has been performed on the Costas loop. The test configuration was the same as that described in Section I. The Costas loop tracks a suppressed carrier BPSK signal with PN data at 100 ksps, and at a ST/N_0 of 4 dB. The loop bandwidth was 110 Hz in this case. The values of the reconstructed carrier phase were recorded and are illustrated in Fig. 8. Each recorded value of the reconstructed carrier phase corresponds to an average of 10,000 samples of the Doppler extractor output, sampling at a rate of 55 ms per sample. Over the 16 hours of observation, the reconstructed carrier phase of the Costas loop was observed to vary not more than 17 deg. This is well within its error budget. In terms of transport delay, a 17-deg phase shift corresponds only to a distance movement of 7 mm at S-Band, and corresponds to an even smaller movement at X-Band.

At another test, the current Block III receiver's residual carrier loop was used to track a residual carrier signal with

modulation angle θ = 80 deg and 100 ksps data on a 360-kHz square-wave subcarrier, at a ST/N_0 of +4 dB. A long-term stability test over a 60-hour period was performed. The reconstructed phase of the residual carrier loop was again recorded and these data are illustrated in Fig. 9. The threshold loop bandwidth setting was 12 Hz in this case. It was observed that the reconstructed phase of the carrier varies over a range 50 deg in this period.

Since these phase variations depend upon the room temperature, no definite conclusion can really be drawn in the above mentioned sample-of-one tests. More tests are planned in the future. Nevertheless it can be said that the phase-shift variation of the Costas loop's reconstructed carrier on a long-term basis is not any worse than that of the current residual carrier loop in Block III, when both loops are operated in the TDL environment.

V. Tracking of Residual Carrier Signals With Data Modulation On a Square Wave Subcarrier

Residual carrier signals are commonly used in the DSN. For example, the Voyager return telemetry uses a modulation angle of 80 deg and data is modulated on a square-wave subcarrier at 360 kHz. To track this type of signal, the arm filters of the Costa loop have to be bandpass filters around the subcarrier frequency to achieve optimum tracking performance. The predicted performance of the Costas loop and the bandpass arm filter design for tracking this type of signal are known.

The test results of the RMS phase jitter of the Costas loop when used to track a residual carrier signal with a modulation angle of θ of 80 deg and a subcarrier at 3.6 times the data rate of 100 ksps are shown in Fig. 10. The arm filters used in this case are RLC bandpass filters centered at the subcarrier frequency. The low-pass equivalents of these filters have a one-pole RC characteristic, and the one-sided bandwidth of this low-pass characteristic is chosen to be at twice the data rate. Also shown in Fig. 10 are the rms jitter measurements of the Costas loop used to track a suppressed carrier signal (θ = 90 deg) with 100 ksps data on the carrier. Comparing these two results, it is observed that the rms phase jitter of the Costas loop tracking of the residual carrier case is about 1-dB worse than those of the suppressed carrier case. This is in fair agreement with the analysis.

Also shown in Fig. 10 is the corresponding rms jitter of the residual carrier loop in the Block III receiver. The loop bandwidth was set to 12 Hz at threshold. The Costas loop tracking is seen to be better than the existing residual carrier tracking over the entire range of ST/N_0 from −4 to +4 dB.

VI. Tests on Asymmetric Bandpass Filtering Effects

In the presence of Doppler offsets, the received signal spectrum will not be centered with respect to the maser amplifier bandpass characteristics. The reconstructed carrier phase of the Costas loop will then depend upon the Doppler offset as well as the maser phase delay characteristics. The same is true for the residual carrier loop. This effect has been analyzed in Ref. 4.

To receive telemetry signals with data rates up to 30 Msps, it is necessary for the X-band maser to have a 1-dB bandwidth around 100 MHz. Since the characteristic of this maser is not yet available we can only make some approximate tests here. In our tests at TDL, a tunable two-pole Tchebycheff bandpass filter with a 0.5-dB ripple in the passband was used to simulate the maser passband characteristic. This filter was placed between the Costas loop and the 10-MHz IF output of the Block III receiver, as shown in Fig. 11. This amounts to an IF simulation of the X-Band maser. The bandpass filter was first designed to be centered at the 10-MHz IF and to have a 1-dB bandwidth of 350 kHz, which is about 3.3 times larger than the received data rate of 100 ksps. After the Costas loop acquired lock, the phase of the reconstructed carrier was recorded from the Doppler extractor output. The filter was then perturbed by adjusting the variable inductor and capacitor elements until the phase of the reconstructed carrier experienced a 37-deg shift. The filter was then recalibrated and the center frequency was determined. Figure 12 plots the amplitude responses of this two-pole Tchebycheff bandpass filter before and after it was perturbed. It was centered at the 10-MHz IF before perturbing. After perturbing, the center frequency was changed to 9.95 MHz. This corresponds to a shift of 50 kHz, which is equal to one half of the 100 ksps data rate that the loop was tracking. According to the analytical result reported in Ref. 4, this frequency shift of the signal carrier with respect to the passband center frequency should have produced a phase shift of 12.5 deg in the Costas loop's reconstructed carrier. However, perturbing the components of the bandpass filter also alter the filter's bandpass characteristic in addition to changing its center frequency. This explains the fact that the measured phase shift is more than the analytical predictions, since the latter assumes no change in the filter bandpass characteristic except for the change in the signal's carrier with respect to the filter's center frequency. Nevertheless, they do indicate a fair agreement. The (future) X-band maser is assumed to have a 1-dB bandwidth of 100 MHz, which is about 3.3 times the

maximum data rate of 30 MHz. In this case, the Doppler offset of half the data rate will amount to 15 MHz. In other words, it will take a Doppler offset of around 15 MHz to introduce a 37-deg shift in the reconstructed carrier of the Costas loop if the maser passband characteristic can indeed be approximated by this two-pole Tchebycheff characteristic. Since realistic Doppler offsets are not greater than 1 MHz, this will imply that the phase shifts in the reconstructed carrier are not a severe problem if we have a wide bandwidth maser.

VII. Conclusions

A Costas loop has been designed, constructed, and installed in the Block III receiver at TDL. Its purpose was to investigate the compatibility of Costas loop demodulation of suppressed carrier BPSK telemetry with the current radio metric system in the DSN. Initial tests with respect to Doppler tracking indicate no noticeable incompatibilities. More tests are planned with respect to ranging compatibility.

References

1. Lesh, J., "Tracking Loop and Modulation Format Considerations for High Rate Telemetry," DSN Progress Report, Vol. 42-44, Jet Propulsion Laboratory, Pasadena, Calif., Jan.-Feb., 1978.

2. Lesh, J., "Functional Requirements Document For Feasibility Model-Multimegabit Telemetry Demodulator/Detector Assembly (MTDD-F)," Memorandum No. 331-79-02, Jet Propulsion Laboratory, Pasadena, Calif., Dec. 29, 1978. (JPL internal document.)

3. Stevens, G., and Woo, K. T., "Design of A Costas Loop to Operate with the Block III Receiver and Its Predicted Performances," this issue of the DSN Progress Report.

4. Woo, K. T., "Effects of Asymmetric Passband Filtering on the Phase of the Costas Loop's Reconstructed Carrier," this issue of the DSN Progress Report.

Table 1. Results of pull-in time tests

Frequency offset, Hz	Predicted values of pull-in time, s	Experimental results of pull-in time, s
100	2.83	3
200	11.3	10
300	25.47	22
400	45.25	39

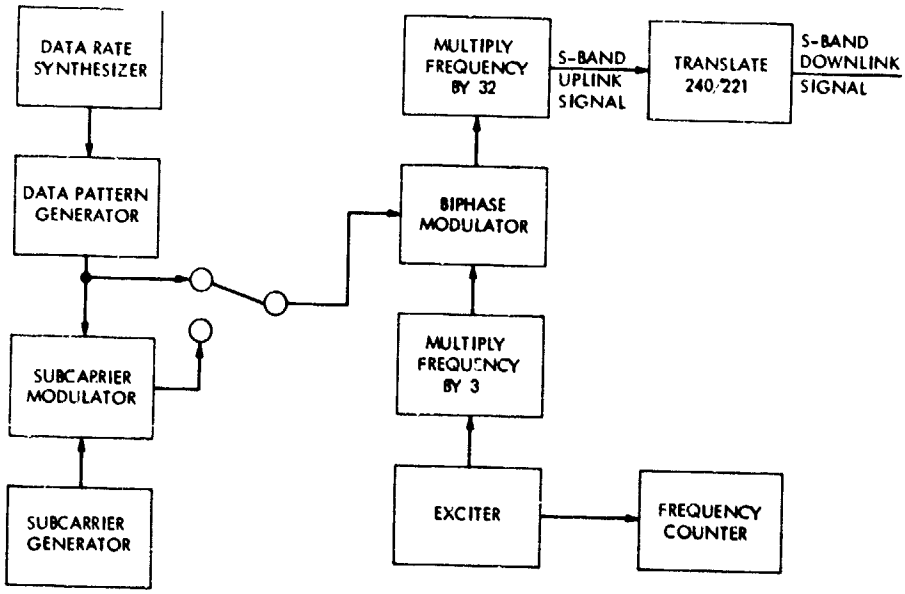

Fig. 1. Transmitter hardware configuration

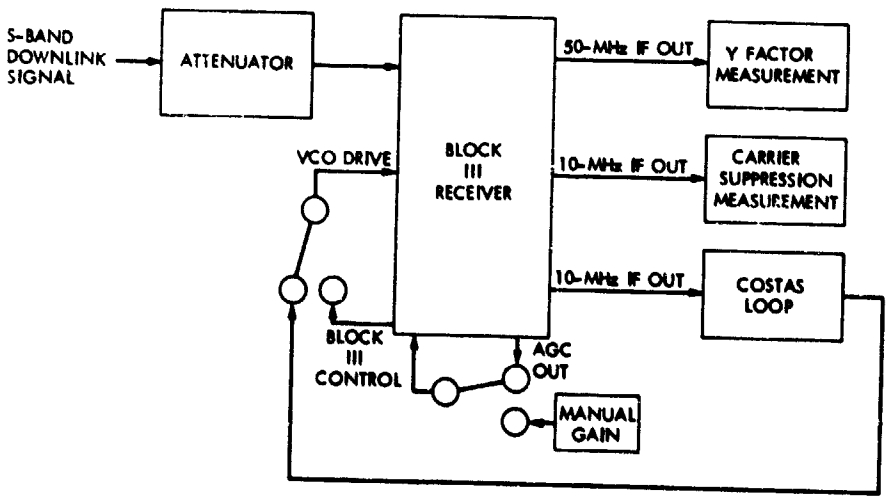

Fig. 2. Receiver hardware configuration

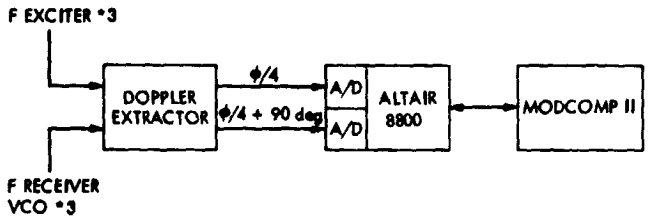

Fig. 3. Data acquisition hardware

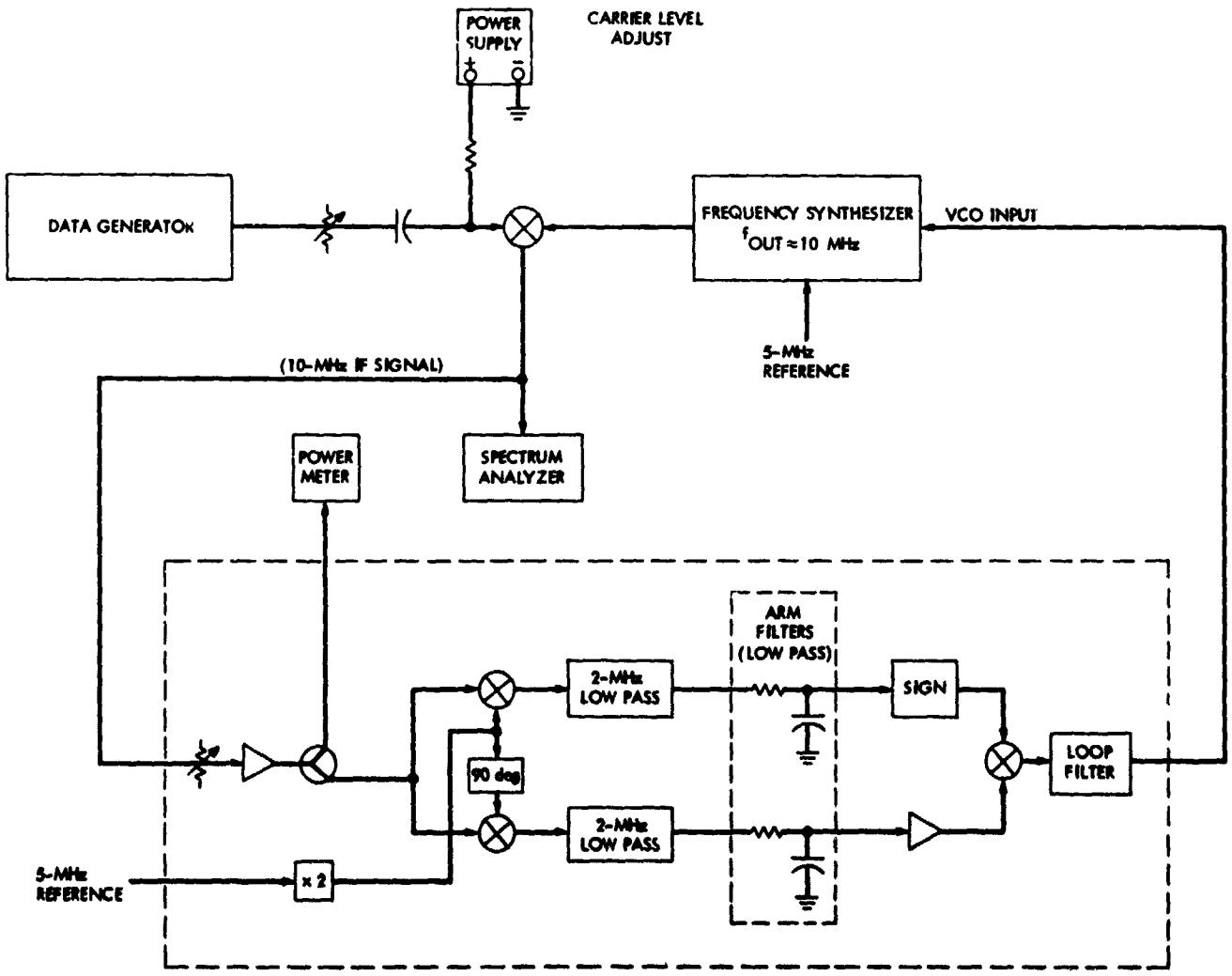

Fig. 4. Costas loop test setup to generate BPSK modulated IF signal

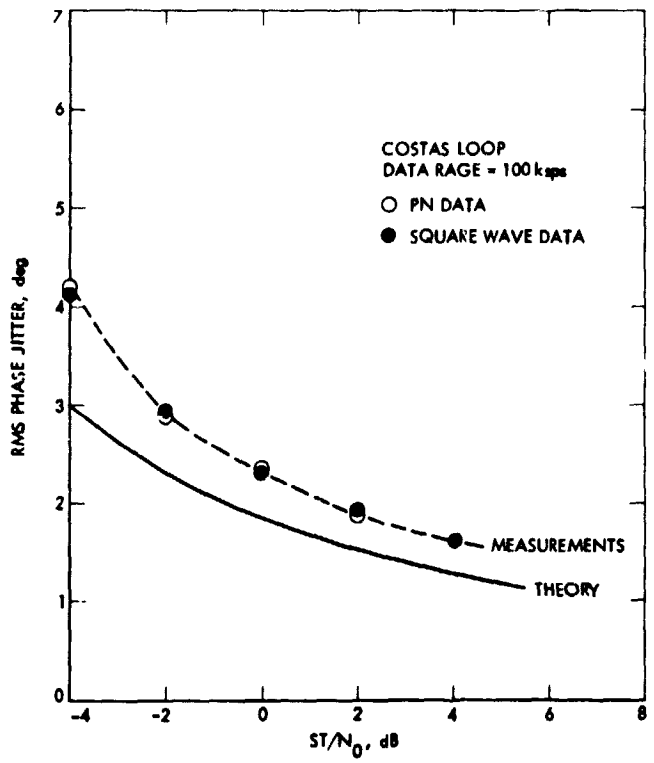

Fig. 5. Rms phase jitter measurements for 100 kaps

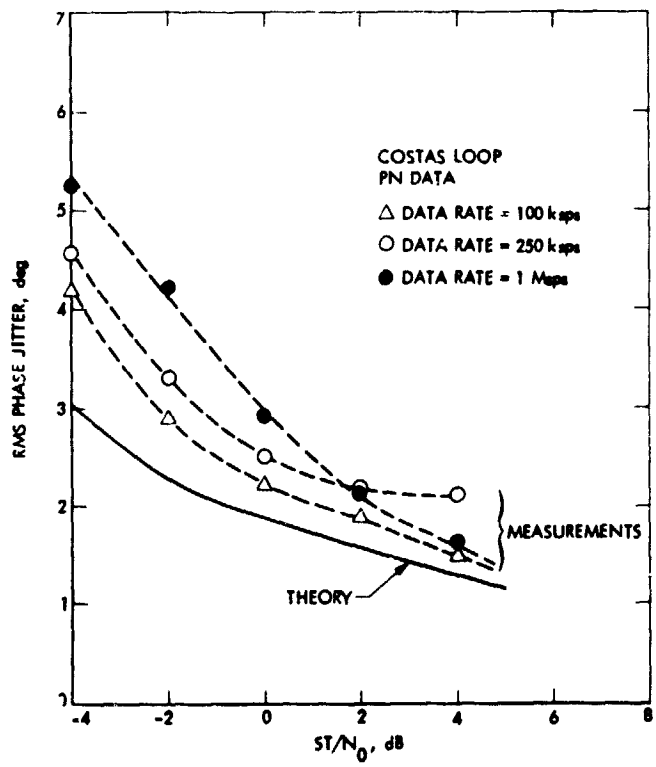

Fig. 6. Rms phase jitter measurements for 100 kaps to 50 kaps, and 1 Msps

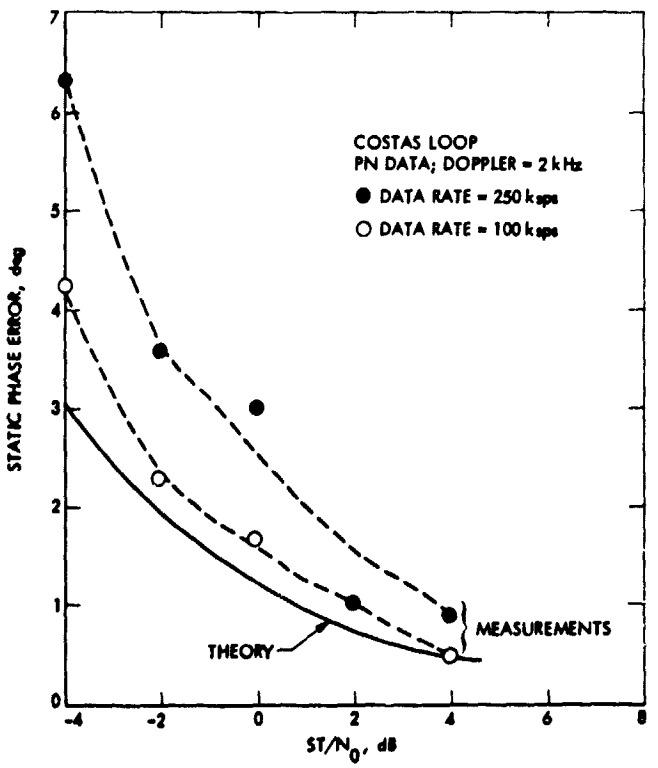

Fig. 7. Steady-state phase error measurements

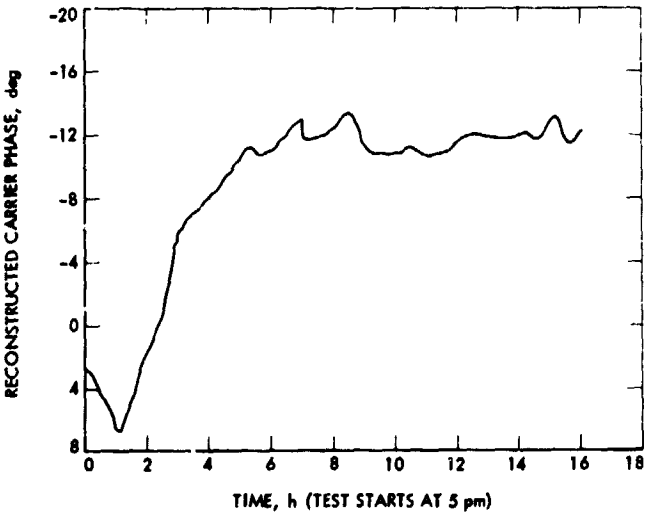

Fig. 8. Long-term stability test results on the Costas loop's reconstructed carrier phase (data rate = 10 ksps, ST/N_0 = 4 dB, suppressed carrier, PN data)

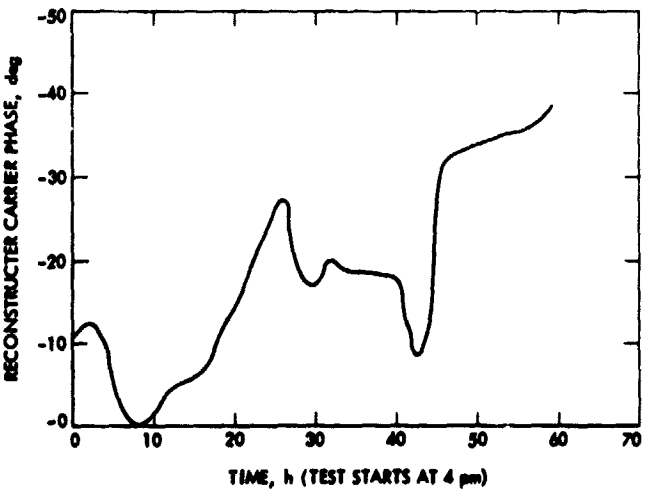

Fig. 9. Long-term stability test results on the Block III residual carrier loop's reconstructed carrier (modulation angle θ = 80 deg, PN data, 100 ksps, data on 360 kHz square wave subcarrier, ST/N_0 = 4 dB

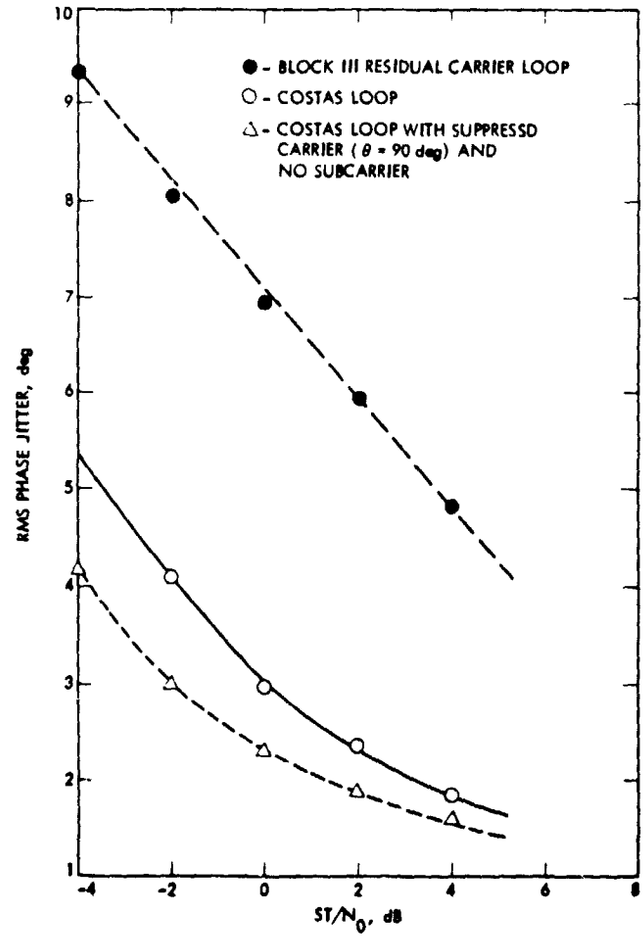

Fig. 10. Residual carrier signalling phase jitter measurements (data rate = 100 kspe, modulation angle θ = 80 deg, subcarrier frequency = 360 kHz)

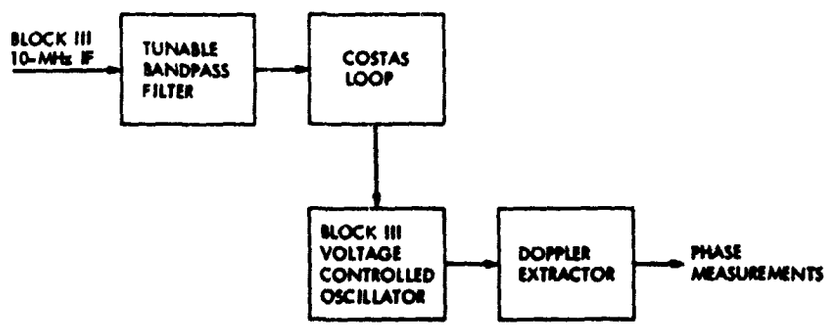

Fig. 11. Test configuration to simulate the effect of receiver front end asymmetric filtering on the phase shifts of the reconstructed carrier in the presence of Doppler shifts

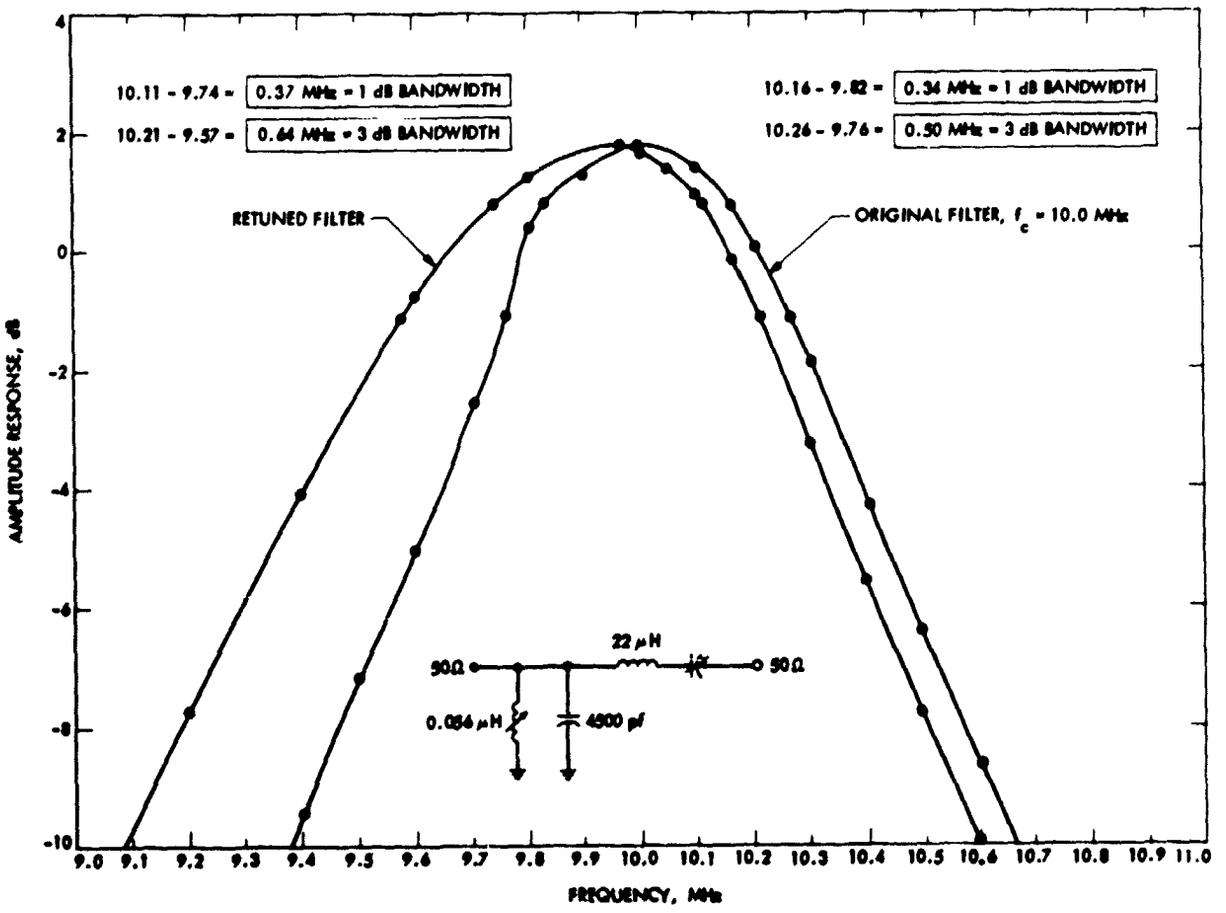

Fig. 12. Amplitude responses of bandpass filter before and after returning

N79-25102

Effects of Asymmetric Passband Filtering on the Phase of the Costas Loop's Reconstructed Carrier

K. T. Woo
Communications Systems Research Section

The reconstructed carrier of a telemetry return signal is used in deriving the Doppler and range information in the radiometric systems. When suppressed carrier BPSK signalling with Costas loop demodulation is used, there are concerns on the amount of shift in the reconstructed carrier phase, when the received signal suffers asymmetric bandpass filtering through the various stages of the receiver. This paper quantifies this effect and concludes that the phase shifts due to asymmetric bandpass filtering on the Costas loop's reconstructed carrier can be slightly worse than those suffered by the residual carrier loop's reconstructed carrier. However, they are well within the error budgets of the radiometric system.

I. Introduction

Figure 1 illustrates the various stages of a Block IV receiver. Various bandpass filtering occurs in the chain of IF stages in the receiver before the signal is demodulated, either with a phase lock loop, when residual carrier signals are received, or with a Costas loop, when suppressed carrier signals are received. In either case, there will be asymmetric bandpass filtering on the received signal spectrum. The bandpass filters following the first mixer-amplifier will always have their center frequencies line up with the proper IF frequencies, when carrier tracking is achieved so that the VCO is in frequency lock with the received carrier. Nevertheless, filtering on the signal spectrum is still not exactly symmetrical with respect to the center frequency, due to limitations in bandpass filter designs. The dominant asymmetric filtering effect, however, comes from the maser amplifier, which precedes the first mixer-amplifier in the receiver IF chain. Since the maser amplifier is in front of the first mixer-amplifier, the received carrier does not necessarily line up with the center frequency of the maser when there are Doppler offsets. Because of these effects there will be phase shifts on the reconstructed carrier, and the exact amount will be Doppler and maser-characteristic dependent. It is true, however, that these phase shifts will occur on the residual carrier loop's reconstructed carrier, as well as on that of the Costas loop.

The reconstructed carrier phase is used in the radiometric system in deriving range and Doppler information. Consequently it is necessary that these phase shifts be maintained at reasonably small values over the range of Doppler offsets of interest. For the residual carrier loop in the existing Block III or Block IV receiver, the phase shifts on the reconstructed carrier due to Doppler shifts and passband filtering are well calibrated and are known to be well within the error budgets of the existing radiometric systems. When a Costas loop is used to demodulate suppressed carrier BPSK telemetry (Ref. 1), however, no known data are available. Further, since the

Costas loop utilizes the whole signal spectrum in reconstructing its carrier phase, it is unclear how severe the effect of asymmetric bandpass filtering will be on the phase shift of the reconstructed carrier in the presence of Doppler offsets.

An analytical approach is attempted in order to answer this question quantitatively in this paper. Measured results are also obtained (Ref. 2) which are in fair agreement with these analysis results. In our analyses, the dominant bandpass filtering is assumed to be the maser, which is approximated by a two-pole Tchebycheff characteristic with a 1-dB bandwidth approximately equal to 3.5 times the data spectrum. It is found that, in the case of the Costas loop, the Doppler offset has to be approximately on the order of one-third the filter bandwidth in order to create phase shifts on the order of 25 degrees. For a 30 MSPS data rate, this implies Doppler offsets of 30 MHz or more, which is much larger than the realistic Doppler offsets of practical interest. For realistic values of Doppler offsets around 1 MHz, the phase shift will be on the order of 1 degree.

II. Analysis

In the presence of Doppler offsets, the phase of the reconstructed carrier of a residual carrier tracking loop is basically determined by the phase delay characteristic of the maser amplifier at the detuned carrier frequency, relative to the center frequency of the maser. In the case of the Costas loop, since the entirety of the signal spectrum is used to reconstruct the carrier phase, this phase will depend upon the maser delay characteristics at the detuned carrier frequency as well as at all the harmonics in the data spectrum.

Square-wave data has the highest number of transitions of any data stream, and thus will suffer the most phase distortion due to filtering. Thus if the received signal is assumed to be square-wave modulated, the results obtained will be the worst case bound. Since a square-wave can be represented by the Fourier series,

$$d_{SQ}(t) = \sum_{k=0}^{\infty} a_{2k+1} \cos\left[\frac{2\pi(2k+1)t}{T}\right] \tag{1}$$

where the coefficients a_{2k+1} are given by

$$a_{2k+1} = \frac{4}{\pi}\frac{(-1)^k}{2k+1} \tag{2}$$

The received RF signal at carrier frequency ω_c can be written as:

$$S(t) = d_{SQ}(t)\cos(\omega_c t + \theta)$$

$$= \frac{1}{2}\sum_{k=0}^{\infty} a_{2k+1}\left\{\cos\left[\left(\omega_c - \frac{2\pi(2k+1)}{T}\right)t + \theta\right]\right.$$

$$\left. + \cos\left[\left(\omega_c + \frac{2\pi(2k+1)}{T}\right)t + \theta\right]\right\} \tag{3}$$

where T is the symbol duration, and where θ is the carrier phase, to be tracked by the Costas loop. Let $G(\omega)$ be the transfer function of the maser characteristic. The filtered output with input $S(t)$ will be given by

$$\hat{S}(t) = \frac{1}{2}\sum_{k=0}^{\infty} a_{2k+1}\left\{\alpha_{-(2k+1)}\cos\left[\left(\omega_c - \frac{2\pi(2k+1)}{T}\right)t\right.\right.$$

$$\left. + \theta + \beta_{-(2k+1)}\right] \tag{4}$$

$$\left. + \alpha_{(2k+1)}\cos\left[\left(\omega_c + \frac{2\pi(2k+1)}{T}\right)t + \theta + \beta_{2k+1}\right]\right\}$$

where in Eq. (4) α_n and β_n denote the amplitude and phase responses of the bandpass characteristic $G(\omega)$, at $\omega = \omega_c + n2\pi/T$, respectively. In other words,

$$\alpha_n \equiv G\left(\omega_c + \frac{2\pi n}{T}\right)$$

$$\beta_n \equiv \arg\left[G\left(\omega_c + \frac{2\pi n}{T}\right)\right] \tag{5}$$

and where arg(z) stands for the argument of the complex function z.

The operation of the Costas loop is identical in performance to that of the squaring loop, which squares the filtered signal $\hat{S}(t)$ and tracks the $2\omega_c$ component. Defining

$$A_n \equiv \begin{cases} a_n \alpha_n & \text{if } n > 0 \\ a_{-n}\alpha_n & \text{if } n < 0 \end{cases} \tag{6}$$

the signal $\hat{S}(t)$ can be written, from (4), as

$$\hat{S}(t) = \frac{1}{2} \sum_{\substack{n=-\infty \\ n=\text{odd}}}^{\infty} A_n \cos \left[\left(\omega_c + \frac{2\pi n}{T} \right) t + \theta + \beta_n \right] \quad (7)$$

The squared signal $[\hat{S}(t)]^2$ is equal to

$$[\hat{S}(t)]^2 = \frac{1}{8} \sum_{\substack{\ell=-\infty \\ \ell,m=\text{odd}}}^{\infty} \sum_{m=-\infty}^{\infty} A_\ell A_m \left\{ \cos \left[\left(2\omega_c + \frac{2\pi(\ell+m)}{T} \right) t + 2\theta + \beta_\ell + \beta_m \right] + \cos \left[\frac{2\pi(\ell-m)}{T} t + \beta_\ell - \beta_m \right] \right\} \quad (8)$$

The component at $2\omega_c$ in $[\hat{S}(t)]^2$, which will be tracked by the squaring loop, is observed from Eq. (8) to be:

$$y(t) = \frac{1}{4} \sum_{\ell=1}^{\infty} A_\ell A_{-\ell} \cos [2\omega_c t + 2\theta + \beta_\ell + \beta_{-\ell}] \quad (9)$$

which, after some simple algebra, can also be written in the following form:

$$y(t) = \frac{1}{4} v \cos [2(\omega_c t + \theta) + 2\psi] \quad (10)$$

where

$$v = \sqrt{\left(\sum_{k=0}^{\infty} C_{2k+1} \cos [\beta_{2k+1} + \beta_{-(2k+1)}] \right)^2 + \left(\sum_{k=0}^{\infty} C_{2k+1} \sin [\beta_{2k+1} + \beta_{-(2k+1)}] \right)^2} \quad (11)$$

$$\psi = \frac{1}{2} \tan^{-1} \left\{ \frac{\sum_{k=0}^{\infty} C_{2k+1} \sin [\beta_{2k+1} + \beta_{-(2k+1)}]}{\sum_{k=0}^{\infty} C_{2k+1} \cos [\beta_{2k+1} + \beta_{-(2k+1)}]} \right\} \quad (12)$$

and where for $k = 0, 1, 2, \ldots$

$$C_{2k+1} = A_{2k+1} A_{-(2k+1)} = (a_{2k+1})^2 \alpha_{2k+1} \alpha_{-(2k+1)} \quad (13)$$

The phase shift in the Costas loop's reconstructed carrier for square-wave modulating signals undergoing bandpass filtering is then equal to Ψ, as given in Eq. (12).[1]

It is instructive to notice that, when bandpass filtering is absent, i.e., when $\alpha_n = 1$ and $\beta_n = 0$, v in Eq. (11) becomes

$$v = \sum_{k=0}^{\infty} \left(\frac{4}{\pi} \frac{1}{2k+1} \right)^2 = 2 \quad (14)$$

and $\Psi = 0$. Hence the error signal $y(t)$ becomes

$$y(t) = \frac{1}{2} \cos 2(\omega_c t + \theta) \quad (15)$$

which is clearly the $2\omega_c$ component in the squared signal $[\hat{S}(t)]^2$ when the filtering effect is negligible.

In general, when the filter phase response is odd symmetric with respect to the center frequency, so that

$$\beta_{2k+1} = -\beta_{-2k+1} \quad (16)$$

then it is clearly true from Eq. (12) that $\Psi = 0$, i.e., there will be no phase shift. For a general bandpass characteristic such that Eq. (16) does not necessarily hold, the phase shift Ψ is given by Eq. (12).

[1] The value ψ was used rather than 2ψ since the Doppler system tracks the carrier at ω_c rather than $2\omega_c$.

III. Numerical Results

Currently the X-band maser passband 1 dB bandwidth in the Block III or Block IV receivers is about 40 MHz. To receive multimegabit telemetry with data rates up to 30 MBPS at the DSN in the 1980's it is imperative to increase the maser bandwidth. It is assumed here that the future maser will have an equivalent baseband bandwidth of about 100 MHz, in order to receive data rates up to 30 MBPS. Without available data on the future maser, the best one can do at the present is to assume a certain bandpass characteristic for it and evaluate the phase shift effect on the reconstructed carrier, in the presence of Doppler offsets. This has been performed experimentally (Ref. 2). The experiment was actually performed at IF, but was intended to simulate the effect of maser filtering. A two-pole Tchebycheff bandpass characteristic was used to simulate the maser bandpass characteristic. The circuit diagram of this bandpass filter is illustrated in Fig. 2. It has center frequency at the 10 MHz IF and a 1-dB bandwidth of 350 KHz. This has then a bandwidth roughly equal to three times the data rate of 100 KBPS, which is one of the data rates used in the tests reported in Ref. 2. The amplitude and phase responses of this bandpass characteristic are plotted in Figs. 3 and 4 respectively. The phase shift in the reconstructed carrier in the residual carrier loop case, in the presence of Doppler, is basically equal to the phase response of this filter at the detuned frequency. For the case of Costas loop demodulation, the phase shift Ψ can be computed from Eq. (12), with the information available in Figs. 3 and 4. The computed result is illustrated in Fig. 5. It is observed that a Doppler offset of 100 kHz can only produce a phase shift of 25 degrees. The Doppler offset of 100 kHz corresponds to an offset of one data rate, which corresponds to one-third of the maser 1-dB bandwidth assumed. When these results are translated to the future maser with a 1-dB bandwidth of 100 MHz (i.e., 3 times the maximum data rate of 30 MSPS), it can be predicted that a phase shift of 25 degrees in the Costas loop's reconstructed carrier will result when there is a Doppler offset of 30 MHz. This, of course, assumes that the two-pole Tchebycheff characteristic is a good approximation to the maser passband. Also shown in Fig. 5 is the phase shift that the residual carrier loop will suffer in the presence of Doppler offsets, for the same passband characteristics assumed. It can be seen from Fig. 5 that the phase shift in the Costas loop's reconstructed carrier is only slightly worse than that of the residual carrier loop.

A 30 MHz Doppler offset is much larger than most realistic values. For a realistic Doppler offset of 1 MHz, which equals 1/30 of the maximum data rate and therefore is equal to about 1/100 of the (future) maser 2-dB bandwidth, the phase shift in the reconstructed carrier of the Costas (or residual carrier) loop is on the order of 1 degree (see Fig. 5). This is much smaller than that which is allowed by the radiometric system's error budget.

IV. Conclusions

Assuming the maser characteristic to be approximately equal to that of a two pole Tchebycheff bandpass characteristic, with a 1-dB bandwidth at 3-5 times the data rate, the phase shifts suffered by the Costas loop's reconstructed carrier have been quantified, as functions of Doppler offsets. These offsets are then compared with the corresponding ones of the residual carrier loop's reconstructed carrier. It is concluded that, even though the corresponding phase shifts of the Costas loop are slightly worse than that of the residual carrier loop, they are both well within the error budgets of the radiometric system.

References

1. Lesh, J., "Tracking Loop and Modulation Format Considerations for High Rate Telemetry", *DSN Progress Report 42-44*, Jet Propulsion Laboratory, Pasadena, Calif., Jan. – Feb., 1978.

2. Reasoner, R., Stevens, G., and Woo, K. T., "Costas Loop Demodulation of Suppressed Carrier BPSK Signals in the DSN Environment – Experimental Results Obtained at TDL" (this issue of the *DSN Progress Report*).

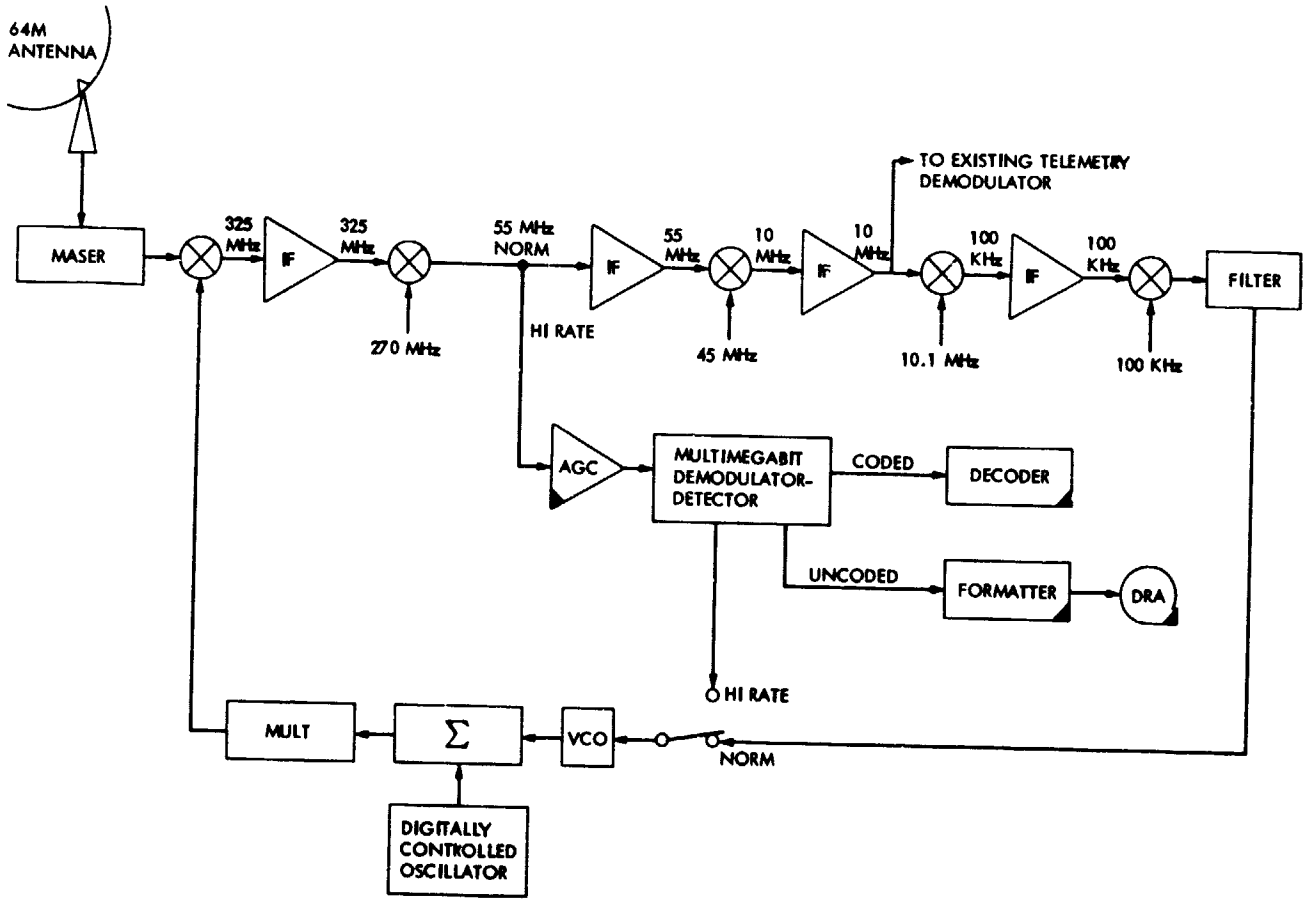

Fig. 1. Block diagram of the system under consideration

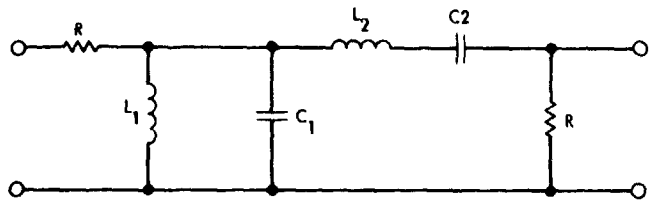

$R = 50\Omega$, $C_1 = 4500$ pf, $C_2 = 11.5$ pf

$L_1 = 0.056\ \mu H$, $L_2 = 22\ \mu H$

$f_0 = 10$ MHz, 3-dB BW = 0.5 MHz

Fig. 2. Block diagram of the two-pole Tchebycheff filter used to simulate the maser characteristic

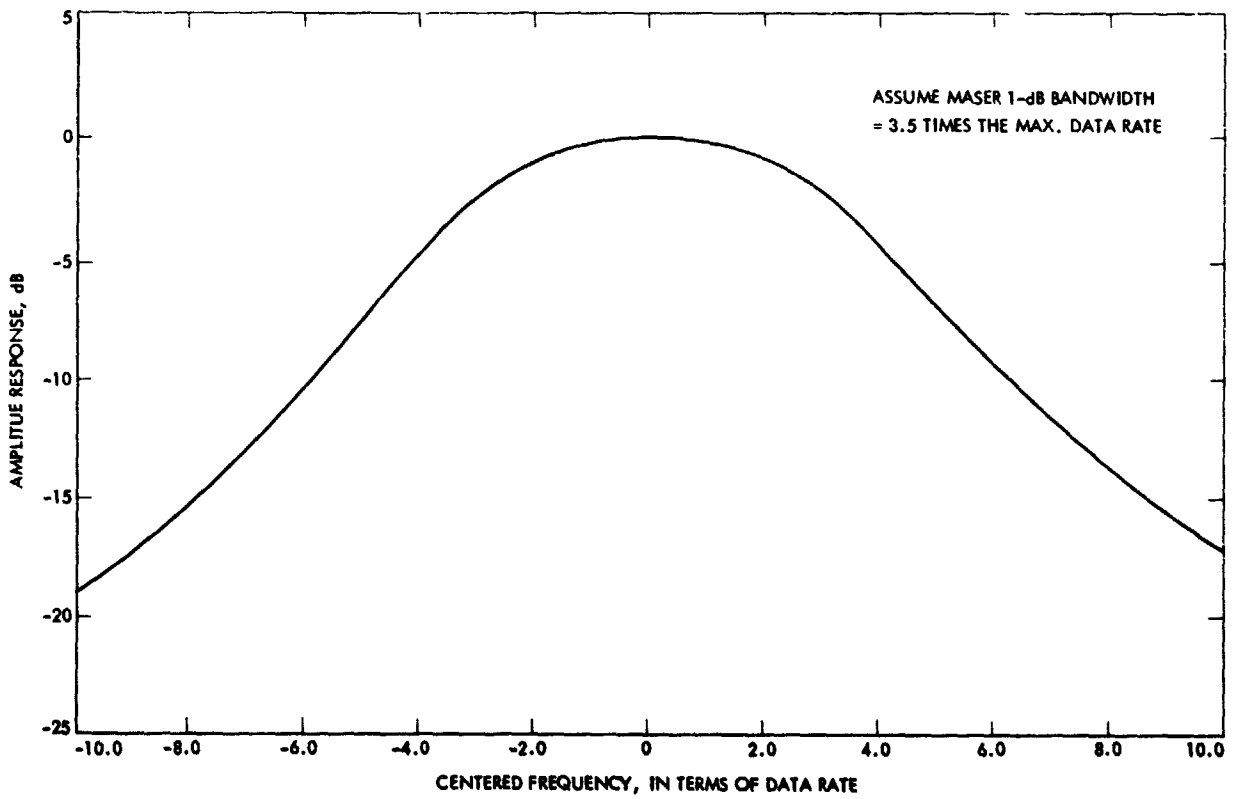

Fig. 3. Amplitude response of the BPF used to simulate the maser characteristic

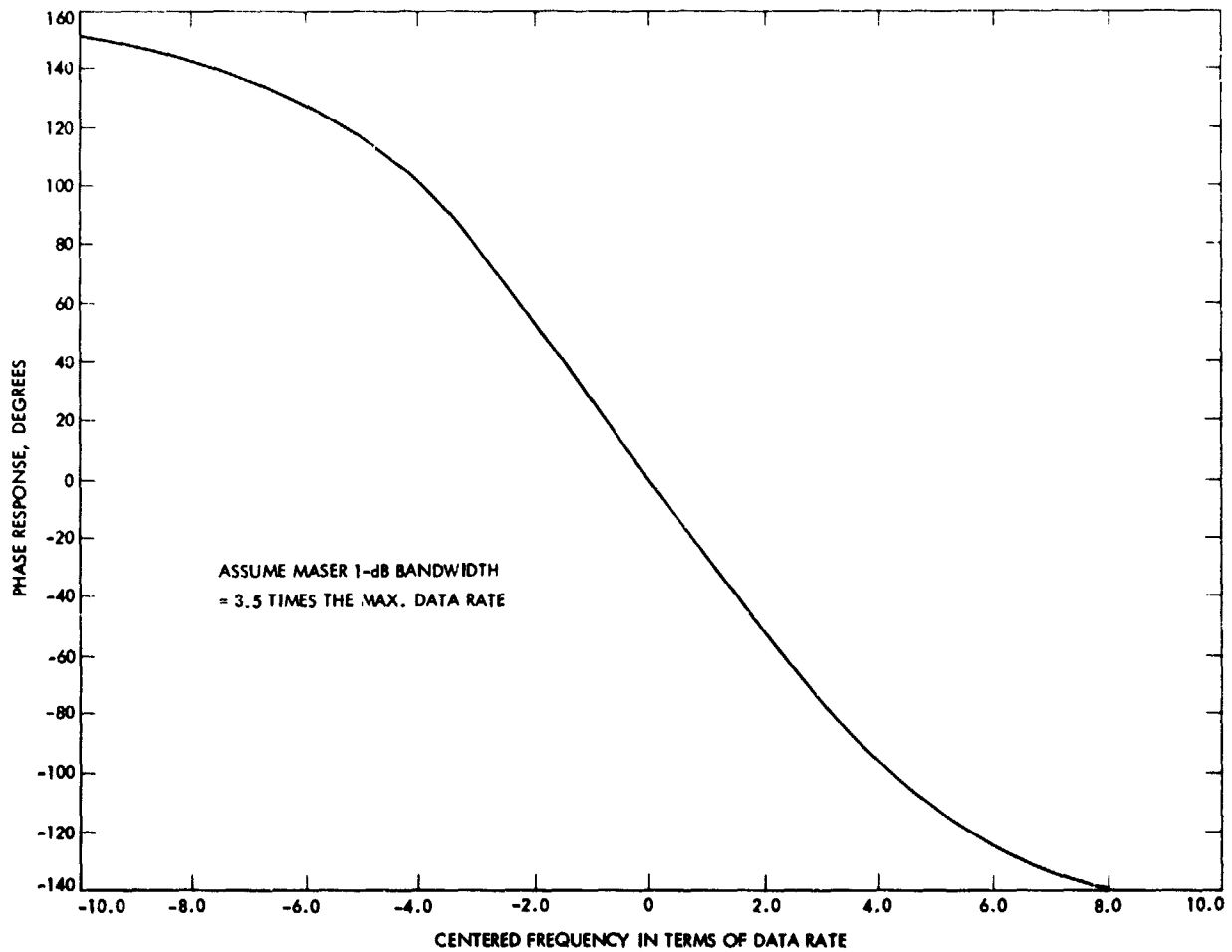

Fig. 4. Phase response of the BPF used to simulate the maser characteristic

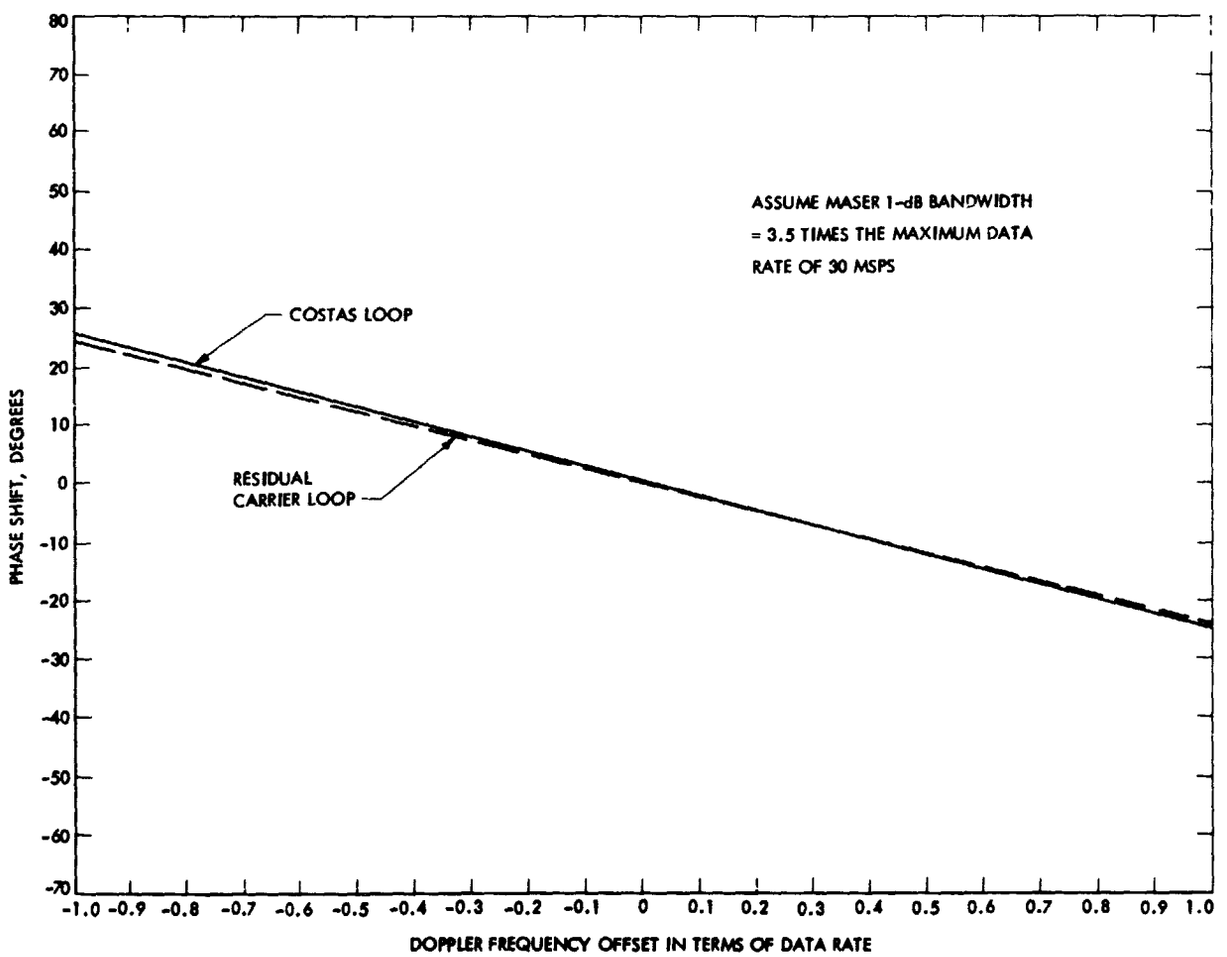

Fig. 5. Phase shift in reconstructed carrier due to Doppler offsets and the assumed receiver front end phase delay characteristic

N79-25103

Design of a Costas Loop to Operate With the Block III Receiver and Its Predicted Performance

G. Stevens and K. T. Woo
Communications Systems Research Section

A Costas loop has been designed and constructed to operate with the Block III receiver. It is a scaled-down version of the carrier tracking loop design in the Multimegabit Telemetry Demodulator and Detector (MTDD) unit under development. The constructed loop has been tested with the Block III Receiver at the Telecommunications Development Laboratory (TDL). This article describes its system design, hardware construction, and predicted performance.

I. Introduction

In order to test the compatibility of the current radiometric system in a DSN environment with suppressed carrier binary phase-shift keyed (BPSK) signalling and Costas loop carrier recovery, a Costas loop has been designed and constructed to operate with the Block III receiver. It has been tested with the Block III receiver at the Telecommunications Development Laboratory (TDL) and its measured performance, with respect to Doppler tracking, has been reported in Ref. 1. This article describes its design considerations. Its expected performance regarding steady state phase error under assumed Doppler conditions, rms phase jitter, and their respective sensitivities with respect to variations in signal-to-noise ratios are discussed. The loop's expected pull-in time is also given. System design considerations will first be discussed in Section II. Descriptions of hardware design and construction will be given in Section III. Predicted performance will be discussed in Sections IV, V, and VI.

II. System Design Considerations

The Costas loop is designed to be operated with the Block III Receiver in the long loop mode, controlling the VCO input, the output of which is multiplied to S-band for use in the first mixer. The system configuration is illustrated in Fig. 1. This loop will provide the Block III receiver with the option of tracking suppressed carrier signals, in addition to the existing capability of tracking residual carrier signals. In order to carry out the desired tests, as mentioned in Ref. 1, at the earliest time possible, the Costas loop modification is a scaled down version of the carrier tracking loop to be used in the Multimegabit Telemetry Demodulator and Detector (MTDD) now under development. In particular, this current Costas loop design utilizes a complex mixer which was developed in earlier projects (Refs. 2 and 3) and has a bandwidth of less than 2 MHz. Because of this inherent bandwidth limitation the designed Costas loop can only track signals having data rates up to 1 megasymbol per second (MSPS).

The Costas loop constructed has a hard limited inphase channel, so that the third multiplier which derives the loop error signal is a chopper-type device. This is illustrated in Fig. 2. The inphase (I) and quadrature (Q) arm filters are one-pole RC filters, which are scaled to the data rates received. The loop filter has transfer function of the form

$$F(s) = \frac{1 + \tau_2 s}{1 + \tau_1 s} \tag{1}$$

so that the loop is a second order loop.

The design goal of this loop is to be able to track suppressed carrier BPSK signals with symbol SNR's (ST/N_o) as low as -4 dB with an rms phase jitter less than or equal to 3 degrees. In addition, the steady state phase error is to be less than or equal to 3 degrees with Doppler offsets less than 2 kHz and Doppler rates of 2 Hz/s or less. The design parameters to be determined in a Costas loop are the arm filter bandwidths and the loop filter time constants, or equivalently, the squaring losses (Ref. 4), loop bandwidths (B_L) and damping factor (ζ), in addition to the open loop gain. In order to meet the steady state phase error requirements it is shown in Section V that the total loop gain has to satisfy

$$K_T \geq 2.4 \times 10^5 \tag{2}$$

The loop bandwidth constraint, in order to meet the jitter requirement, is found to be

$$B_L T \leq 2.4 \times 10^{-4} \tag{3}$$

where $1/T$ is the data rate received. For the four data rates of concern in Ref. 1, the loop bandwidths are, at the design point with $ST/N_0 = -4$ dB, selected from Table 1. These loop bandwidths are design point values and they increase with ST/N_0. The arm filter noise bandwidths are chosen to equal twice the data rate, so that squaring losses are acceptable.

With the desired damping factor set to be $\zeta = 0.707$ at design point values, and with the loop gain K_T satisfying Eq. (2), and B_L's given in Table 1, the time constants τ_1, τ_2 in the loop filter can be determined. They are given in Table 2.

Further discussions on performance evaluations are given in Sections IV, V, and VI. In the next section we first describe the hardware design of the Costas loop.

III. Description of Hardware Design

A block diagram of the Costas loop phase detector and loop filter assembly hardware is shown in Fig. 3. The 10 MHz IF signal is amplified and applied to the input of a 2-way power splitter. One output drives a true rms voltmeter which is used as a signal level monitor when adjusting the IF signal level. The other power splitter output drives a 10 MHz quadrature IF mixer (complex mixer). Inphase and quadrature (I&Q) baseband signals are generated by the complex mixer by splitting the IF signal into two paths and mixing with 10 MHz LO signals which are in phase quadrature. The resulting baseband mixer products are then bandlimited to 2 MHz by 2-section elliptic low pass filters. A detailed description of the complex mixer is given in Refs. 2 and 3.

The inphase and quadrature baseband signals generated by the complex mixer are next passed through identical arm filters. Simple resistance-capacitance (RC) low pass filters are used when processing signals in which the carrier is biphase modulated directly by the data symbols. When the data is modulated onto a square wave subcarrier, the low pass arm filters are replaced by resistance-inductance-capacitance (RLC) bandpass filters, whose passbands are centered at the subcarrier fundamental frequency. Inphase and quadrature baseband signals generated by the complex mixer are also buffered and supplied to test points to facilitate wave form inspection with an oscilloscope.

A hard limiter follows the inphase channel's arm filter. The output of the quadrature channel's arm filter is linearly amplified. These two signals are then multiplied together in a double balanced mixer whose output drives an active lead/lag loop filter. The loop filter's output is supplied to the receiver's voltage-controlled crystal oscillator in its LO chain. Variable gain control and an inverted output are provided in the loop filter and amplifier. A built-in voltmeter monitors the VCO control voltage. Offset currents generated within the Costas loop's phase detector are cancelled by an offset adjustment potentiometer.

In this Costas loop design the bandwidths of the RC-arm filters are chosen to be twice the received data rate. The arm filter design is illustrated in Fig. 4, while the respective parametric values of the filter components are described in Table 3.

The loop filter design, corresponding to the time constants described in Table 2, is illustrated in Fig. 5, with its component values given in Table 4.

IV. Tracking Analysis of the Costas Loop

The tracking performance of a Costas loop with hard limited in phase channel has been analyzed in detail in Ref. 4. Basically, the steady state phase error and the rms phase jitter of the loop are dependent upon the signal suppression factor $\mathfrak{F}$ and the squaring loss factor S_L, in addition to other design parameters such as loop filter time constants and the gains of the phase detector and the VCO.

Signal suppression on the loop error signal is due to the arm filters and the hard limiter, and varies with ST/N_o and the choice of arm filter bandwidth relative to the data rate. When the arm filters are one-pole RC filters, this signal suppression factor $\mathfrak{F}$ has been evaluated in Ref. 4. The results are shown here in Fig. 6. The total loop gain in the Costas loop design as described in Section III is dependent upon $\mathfrak{F}$ through the following relationship:

$$K_T = \mathfrak{F}\sqrt{S}\ K_p K_v K_{LF} \tag{4}$$

where S is the average signal power at the output of the manual gain control (MGC) unit, K_p is the phase detector gain, K_v is the VCO gain, and K_{LF} is the variable loop filter gain as described in Section III. Both loop bandwidth and damping varies with loop gain, and they are thus also SNR dependent. The same is thus also true for the steady state phase error and the rms phase jitter of the loop. These dependences are further discussed in Section V.

The rms phase jitter of the loop for a given loop bandwidth B_L is given by Ref. 4.

$$\sigma_\phi^2 = \left[\left(\frac{ST}{N_o}\right)\left(\frac{1}{B_L T}\right) S_L\right]^{-1} \tag{5}$$

where S_L is the squaring loss factor, which is less than unity, and is also dependent upon ST/N_o and the arm filter bandwidth. The squaring loss of the Costas loop with a hard limited in phase channel and one pole low pass RC arm filters has been evaluated in Ref. 4, and the results are included in Fig. 7 for reference.

With $\mathfrak{F}$ and S_L known from Figs. 6 and 7 it is then straight forward to determine the parameters in the loop design and to predict the performance of loop as ST/N_o varies. These are discussed in the next section.

V. Determination of Design Parameters and Performance Predictions

The basic parameters to be determined in the loop design are: the arm filter bandwidth, the total loop gain K_T, and the time constants τ_1 and τ_2 in the loop filter. The values of K_T, τ_1 and τ_2 also determine the loop bandwidth B_L and the damping factor ζ.

The selection of arm filter bandwidth affects the squaring loss S_L of the Costas loop, as illustrated in Fig. 7. It is observed from Fig. 7 that S_L varies from -5 to -9 dB for choices of arm filter bandwidths from 0.75 to 4.5 times the data rate, at the design point ST/N_o of -4 dB. Even though not shown on Fig. 7, the squaring loss S_L decreases rapidly when the arm filter bandwidth decreases below $0.75/T$, where $1/T$ is the symbol rate. Squaring loss is least when the arm filter bandwidth B is around $1/T$. And as B increases above $1/T$, S_L decreases monotonically again. Nevertheless, S_L is relatively constant for BT values ranging from 0.75 to 2.5. In this particular design the one pole RC arm filters are chosen to have a BT product of 2. The squaring losses with the arm filter bandwidth selected in this way will be less than 6.6 dB for all $ST/N_o > -4$ dB.

With a squaring loss of 6.6 dB or less the required loop bandwidth B_L at the design point ST/N_o of -4 dB can be chosen, in order to have rms phase jitter below 3 degrees, according to Eq. (5) as follows:

$$B_L T \leq \left(\frac{ST}{N_o} S_L\right)\left(\frac{\pi}{60}\right)^2 = 2.4 \times 10^{-4} \tag{6}$$

This resulted in the design point loop bandwidths listed in Table 1.

Next we consider the total open loop gain K_T. The steady state phase errors due to a radian Doppler offset Ω_0 and a Doppler rate Ω_1 are Ω_0/K_T and Ω_1/ω_n^2 respectively, for a second order loop (Ref. 5), where ω_n is the natural frequency of the loop. Assuming we choose a damping factor of ζ of 0.707 at the design point, the values of ω_n for the selections of B_L shown in Table 1 will be ≥ 45. The steady state phase error due to a Ω_1 of 2 Hz/s will then be ≤ 0.35 degrees. The combined steady state phase error ϕ_{ss} due to both Ω_0 and Ω_1 can be modeled as

$$\phi_{ss} = \sqrt{\left(\frac{\Omega_0}{K_T}\right)^2 + \left(\frac{\Omega_1}{\omega_n^2}\right)^2} \tag{7}$$

In order for ϕ_{ss} to be ≤ 3 degrees for a Doppler offset of 2 kHz and a Doppler rate of 2 Hz/s it follows from Eq. (7) that the total loop gain K_T must satisfy

$$K_T \geq \frac{\Omega_0}{\sqrt{\phi_{ss}^2 - (\Omega_1/\omega_n^2)^2}} \geq 2.4 \times 10^5 \qquad (8)$$

With K_T determined as above it is straightforward to determine the variable loop filter gain K_{LF} from Eq. (4), given the signal power S, the VCO gain K_v, and the phase detector gain K_p. The VCO gain K_v in block III is equal to $2\pi \times 96 \times 400$ radians/volt. The phase detector gain K_p is measured to be 0.646 volts/radians. However, the signal level $\sqrt{S}$ is SNR dependent, since it is controlled by a manual gain control (MGC) which holds the signal plus noise power constant in the IF bandwidth (B_{IF}) of 7.92 MHz. It can be derived that the signal level $\sqrt{2S}$ after MGC is given by

$$\sqrt{2S} = \frac{\sqrt{2}\,\lambda}{\sqrt{1 + \dfrac{B_{IF}T}{(ST/N_o)}}} \qquad (9)$$

where $\lambda = 0.15$ volt is the desired average signal plus noise power in the MGC output and is determined by the appropriate input level to the complex mixer as described in Section II. Since $\tilde{\alpha}$ equals 0.298 at $ST/N_o = -4$ dB with arm filter $BT = 2$, the loop filter gain K_{LF} is then determined from Eqs. (4), (8), and (9) to be:

$$K_{LF} = \frac{K_T}{\tilde{\alpha} K_p K_v \sqrt{S}} = \frac{2.4 \times 10^5}{(0.298)(0.646)(2\pi \times 96 \times 400)\dfrac{\sqrt{2} \times 0.15}{\sqrt{1 + \dfrac{B_{IF}T}{ST/N_o}}}} \qquad (10)$$

At the design point $ST/N_o = -4$ dB, with $B_{IF} = 7.29$ MHz, these required values of K_{LF}'s are determined to be the following:

Variable Loop Filter Gain Settings K_{LF}

Data Rates	K_{LF}
100 KSPS	331
250	210.5
500	149.6
1000	107

With B_L requirements given in Table 1 and total open loop gain K_T requirements given in Eq. (7), it is straightforward to determine the loop filter time constants τ_1 and τ_2 from the following well-known relationships (Ref. 5) of second order loops with loop filters of the forms given in Eq. (1):

$$\tau_1 = \frac{K_T}{\omega_n^2} \qquad (11)$$

$$\tau_2 = \frac{2\omega_n \tau_1 \zeta - 1}{K_T} \qquad (12)$$

Requiring ζ_o (design point value) to be 0.707, so that $\omega_n = 1.89\,B_L$, the respective values of τ_1 and τ_2 are determined from Eqs. (11) and (12) to be those given in Table 2.

Next we consider the performance of this loop design as ST/N_o increases above -4 dB. Both $\tilde{\alpha}$, K_T, S_L and B_L are dependent upon ST/N_o. The dependences on ST/N_o of $\tilde{\alpha}$ and S_L have already been given in Figs. 6 and 7. The dependence of K_T on ST/N_o comes from $\tilde{\alpha}$ as well as the signal $\sqrt{S}$ level after MGC, as given in Eq. (10). From K_T and τ_1 the natural frequency ω_n of the loop can be determined from Eq. (11), and from which ζ can be determined from Eq. (12). Given ω_n and ζ, B_L can be determined by the following well known relationship (Ref. 5) of second order loops:

$$B_L = \frac{\omega_n}{2}\left(\zeta + \frac{1}{4\zeta}\right) \qquad (13)$$

The dependences of B_L and ζ on ST/N_o are plotted in Figs. 8 and 9 for this Costas loop design. Given B_L, S_L, the rms jitter can be determined from Eq. (5). Also, the steady state phase error, given K_T and ω_n, can be determined from Eq. (7). Their respective dependencies upon ST/N_o are plotted in Figs. 10 and 11.

VI. Pull-in Time Considerations

In the absence of noise, the dynamic loop error signal in Fig. 2 has the form

$$e(t) = K_p \operatorname{sgn}\left[\sqrt{S}\,\widehat{d(t)\cos\phi(t)}\right]\left[\sqrt{S}\,\widehat{d(t)\sin\phi(t)}\right] \qquad (14)$$

where $\phi(t)$ is the phase error process, $d(t)$ is the baseband data waveform, and the notation "$\widehat{\ }$" is used to denote the

operation of the arm filters. Suppose we assume the filtering operation is negligible, which will be seen to be justifiable for pull-in time considerations, then the differential equation that governs the dynamics of the Costas loop is given by

$$\frac{d\phi}{dt} = \frac{d\theta}{dt} - KF(p)\ \{\text{sgn}\ [\cos\phi(t)]\ \sin\phi(t)\} \qquad (15)$$

where θ is the received carrier phase, F is the loop filter transfer function, p is the Heaviside operator d/dt, and K is a constant proportional to the signal level, the VCO gain, and the phase detector gain. Strictly speaking, K depends also upon the frequency offset between the local VCO and the incoming carrier. The function sgn $[\cos\phi(t)]$ can be expressed in a Fourier series.

$$\text{sgn}\ [\cos\phi(t)] = \frac{4}{\pi}\sum_{k=0}^{\infty}\frac{(-1)^k}{2k+1}\cos\ [(2k+1)\phi(t)] \qquad (16)$$

which consists only of odd harmonics of $\phi(t)$. During the acquisition phase the term corresponding to $k = 0$ has the dominant effect on the loop, since all terms in Eq. (16) pass through the loop filter. Thus, to a good approximation, the behavior of the Costas loop, neglecting the arm filters and ignoring higher-order Doppler derivatives, is governed by:

$$\frac{d\tilde{\phi}}{dt} = \tilde{\Omega}_0 - 2K'F(p)\sin\tilde{\phi} \qquad (17)$$

where $\tilde{\phi} = 2\phi$, $K' = (2/\pi)K$, and $\tilde{\Omega}_0 = 2\Omega_0$, where Ω_0 is the initial frequency offset in radians per second. The $\tilde{\phi}$ process then satisfies the same well-known differential equation (Ref. 5) that is satisfied by an ordinary phase lock loop. The effective Doppler offset is now $2\Omega_0$, and the effective gain is $2K'$.

During tracking $\tilde{\phi} \approx 0$ and Eq. (17) can be linearized to be

$$\frac{d\tilde{\phi}}{dt} = \tilde{\Omega}_0 - 2K'F(p)\tilde{\phi} \qquad (18)$$

Let $\tilde{\zeta}$ and $\tilde{\omega}_n$ denote the damping factor and natural frequency, respectively, of the linearized model Eq. (18). Then $\tilde{\zeta}$ and $\tilde{\omega}_n$ are equal to $\sqrt{2}\,\zeta$ and $\sqrt{2}\,\omega_n$ respectively, where ζ and ω_n are those given in Eqs. (11) and (12) which correspond to the linearized differential equation governing ϕ rather than $\tilde{\phi}$. This is because the gain in Eq. (18) is $2K'$ rather than K'. The pull-in range of the Costas loop model (17) can then be given in the same way as that of a phase lock loop (Ref. 5):

$$|\tilde{\Omega}_0| = |2\Omega_0| \leq 2\sqrt{(2K')\tilde{\zeta}\tilde{\omega}_n}$$

$$= 4\sqrt{K'\zeta\omega_n} \qquad (19)$$

This implies $|\Omega_0| \leq 2\sqrt{K'\zeta\omega_n}$. Suppose the initial frequency offset is small compared to the arm filter bandwidth; then K' here should be very close to K_T, the total loop gain design parameter discussed in Section V. For the design at 100 KSPS discussed in Section V with $K_T = 2.4 \times 10^5$, $\tau_1 = 112.5$ s, and $\tau_2 = 0.03124$ sec, ζ is 0.707 and ω_n is 46.2. When these values are substituted in Eq. (19), the pull-in range is computed to be

$$\left|\frac{\Omega_0}{2\pi}\right| < 894\ \text{Hz}$$

This pull-in range is much narrower than the arm filter bandwidth, which equals 200 kHz when the received data rate is 100 KSPS, so we are justified in neglecting arm filter effects for this computation.

The pull-in time of the loop model governed by Eq. (17) can now be computed in the same way as that of the phase lock loop (Ref. 5):

$$T_{acq} = \frac{\tilde{\Omega}_0^2}{2\tilde{\zeta}\tilde{\omega}_n^3} = \frac{(2\Omega_0)^2}{2\sqrt{2}\,\zeta(\sqrt{2}\,\omega_n)^3} = \frac{\Omega_0^2}{2\zeta\omega_n^3} \qquad (20)$$

For the loop design at 100 KSPS mentioned previously the pull-in times for various initial frequency offsets are given in Table 5. These predictions agree closely with measurements reported in Ref. 1.

VII. Conclusions

The design and performance prediction of the Costas loop tested with the Block III receiver at TDL as reported in Ref. 1 is documented in this paper. The test results reported in Ref. 1 are found to be in good agreement with these performance predictions.

References

1. Reasoner, R., Stevens, G., and Woo, K. T., "Costas Loop Demodulation of Suppressed Carrier BPSK Signals in the DSN Environment – Experimental Results Obtained at TDL", this issue of *The DSN Progress Report*.

2. Constenla, L. C., "Complex Mixer System," Technical Report 32-1526, Jet Propulsion Laboratory, Pasadena, California, Dec. 15, 1972.

3. Stevens, G. L., "Complex Mixer System Modifications," *The DSN Progress Report 42-42*, Jet Propulsion Laboratory, Pasadena, California, Sept. and Oct., 1977, pp. 88-91.

4. Simon, M. K., "Tracking Performance of Costas Loops With Hard-Limited In-Phase Channel," *IEEE Trans. on Comm.*, Vol. COM-26, No. 4, Apr. 1978, pp. 420-432.

5. Viterbi, A., *Principles of Coherent Communications*, McGraw Hill Book Co., New York, NY, 1966.

Table 1. Loop bandwidths

Data rates	Design point Loop bandwidth at ST/N_0 = -4 dB
100 KSPS	24.04 Hz
250 KSPS	60.1 Hz
500 KSPS	122.2 Hz
1000 KSPS	244.4 Hz

Table 2. Loop filters

Data rates	Loop filter time constants	
	τ_1	τ_2
100 KSPS	112.50 s	0.03124 s
250 KSPS	18.00 s	0.01246 s
500 KSPS	4.500 s	0.006117 s
1000 KSPS	1.125 s	0.00306 s

Table 3. Arm filter designs

Data rates	$2\pi \times f_c$	R	C
100 KSPS	8×10^5 rad/s	510 Ω	2451 pf
250 KSPS	2×10^6 rad/s	510 Ω	980 pf
500 KSPS	4×10^6 rad/s	510 Ω	490 pf
1000 KSPS	8×10^6 rad/s	510 Ω	245 pf

(f_c = 3 dB corner frequency)

Table 4. Loop filter designs

Data rates	R_1	R_2	R_3	C
100 KSPS	50K	3.08K	10M	9.92 μf
250 KSPS	50K	6.68K	10M	1.866 μf
500 KSPS	50K	13.6K	10M	0.4498 μf
1000 KSPS	50K	27.2K	10M	0.1125 μf

Table 5. Pull-in times of the Costas loop design receiving data rate at 100 KSPS

Initial frequency offset	Pull-in time
100 Hz	2.83 s
200 Hz	11.3 s
300 Hz	25.47 s
400 Hz	45.25 s

ORIGINAL PAGE IS
OF POOR QUALITY

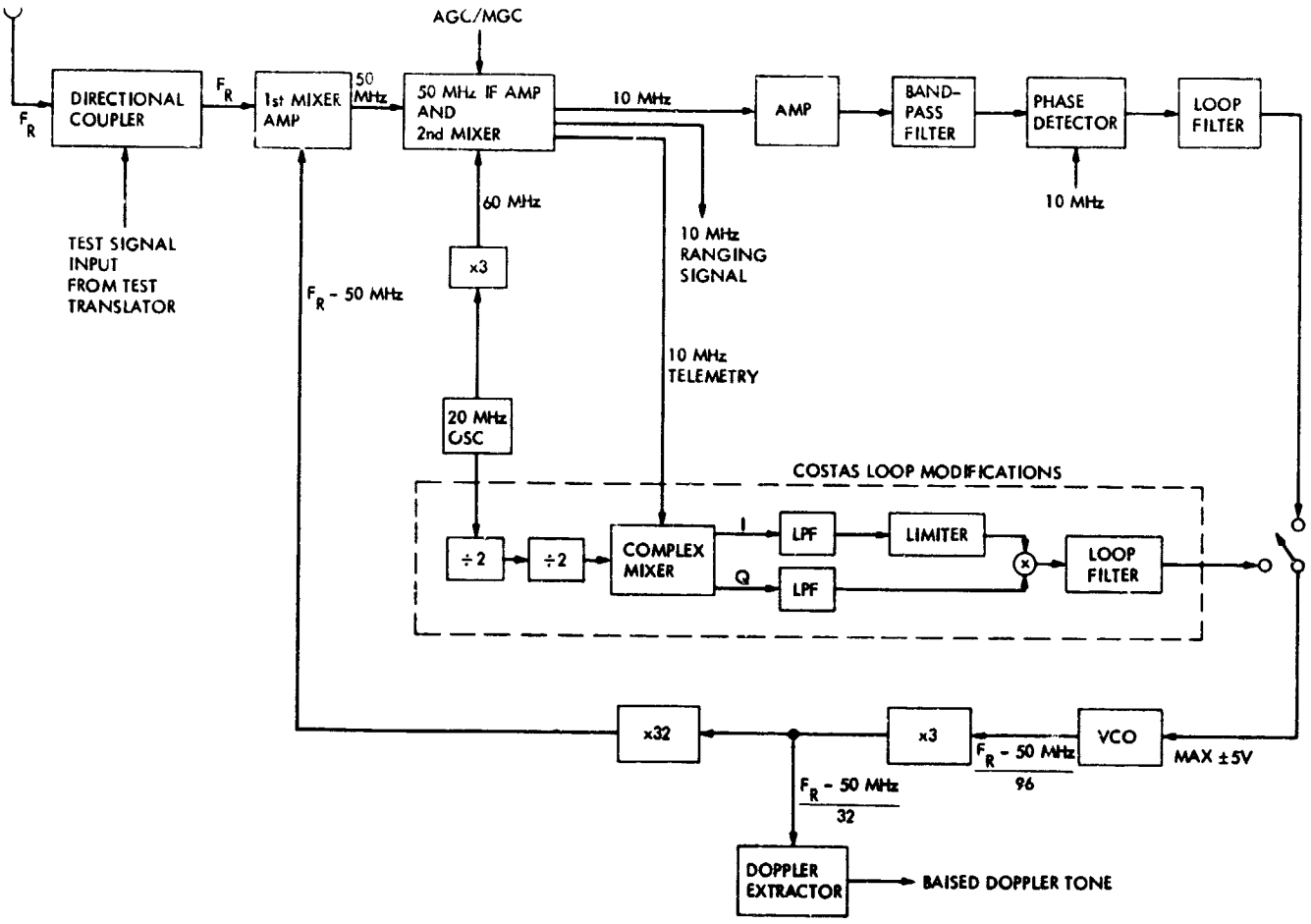

Fig. 1. Modification of block III receiver to include Costas loop

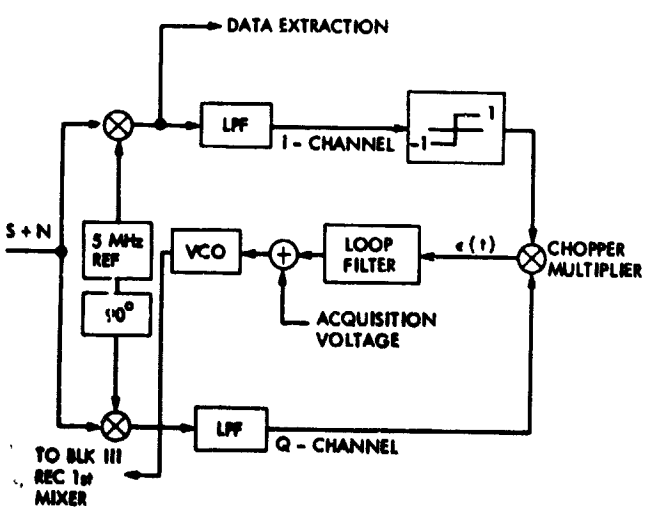

Fig. 2. Functional block diagram of a Costas loop with hard limited inphase channel

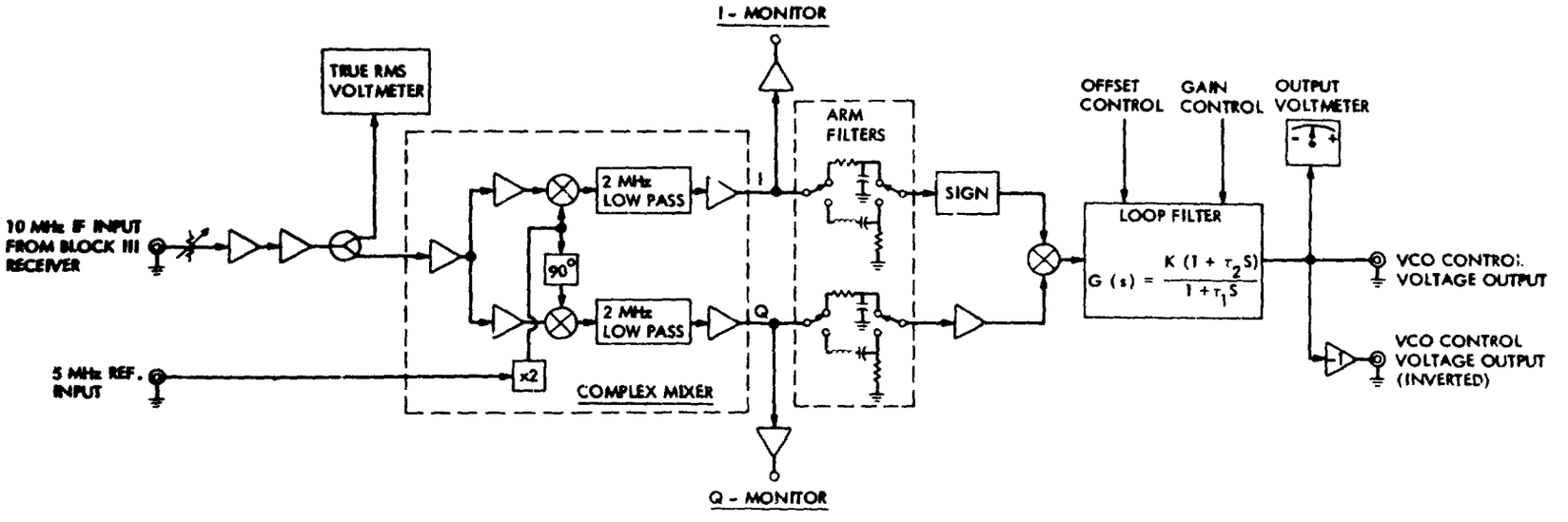

Fig. 3. Block diagram of analog Costas loop hardware

ORIGINAL PAGE IS OF POOR QUALITY

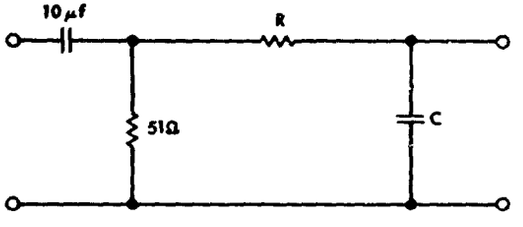

Fig. 4. Block diagram of A-C coupled low pass arm filters

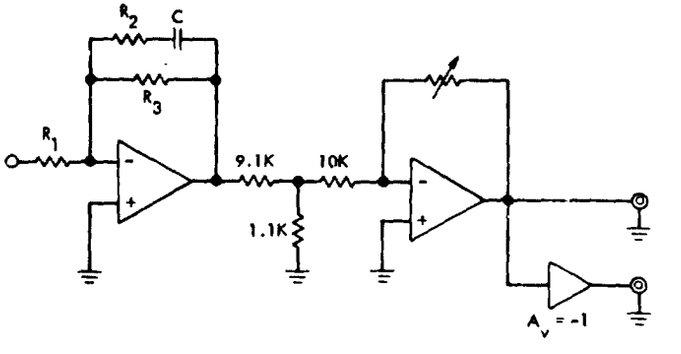

Fig. 5. Block diagram of loop filter design

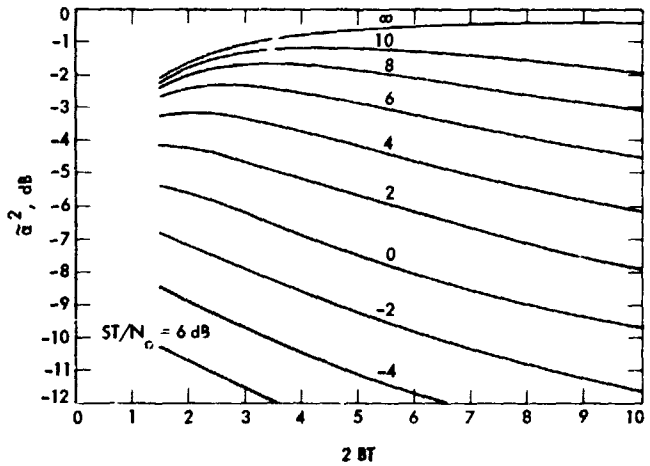

Fig. 6. Signal power suppression factor vs the ratio of two-sided arm filter bandwidth to data rate with signal-to-noise ratio as parameter.

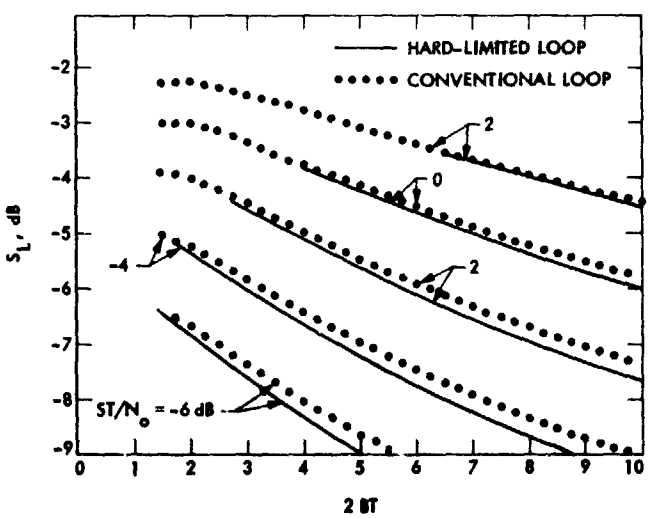

Fig. 7. Squaring loss variations vs 2*BT*, with *ST*/N_0 as a parameter; small SNR approximation; RC filter, NRZ data.

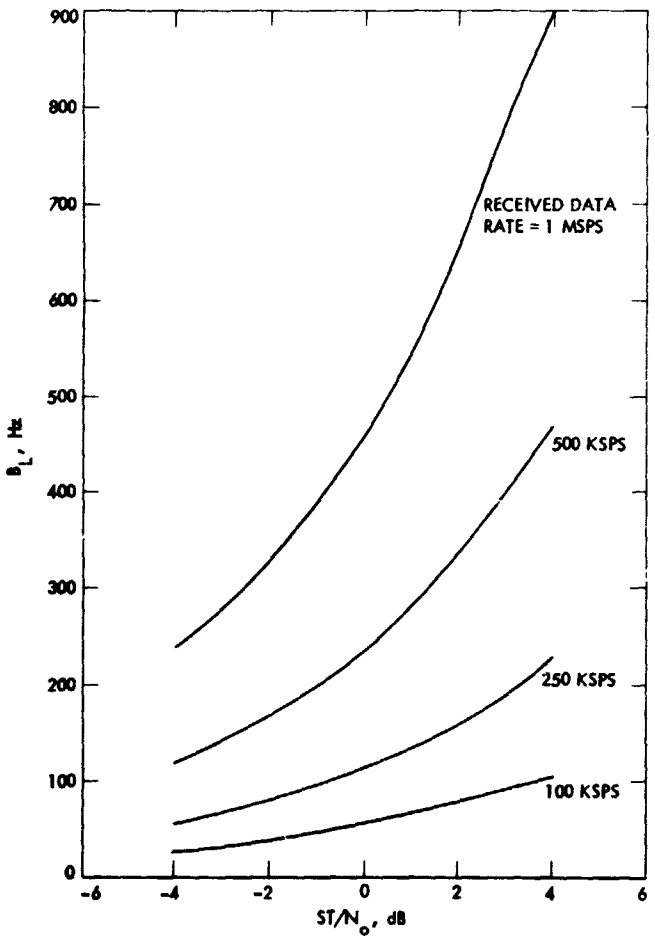

Fig. 8. Design values of Costas loop noise bandwidth as functions of *ST*/N_0

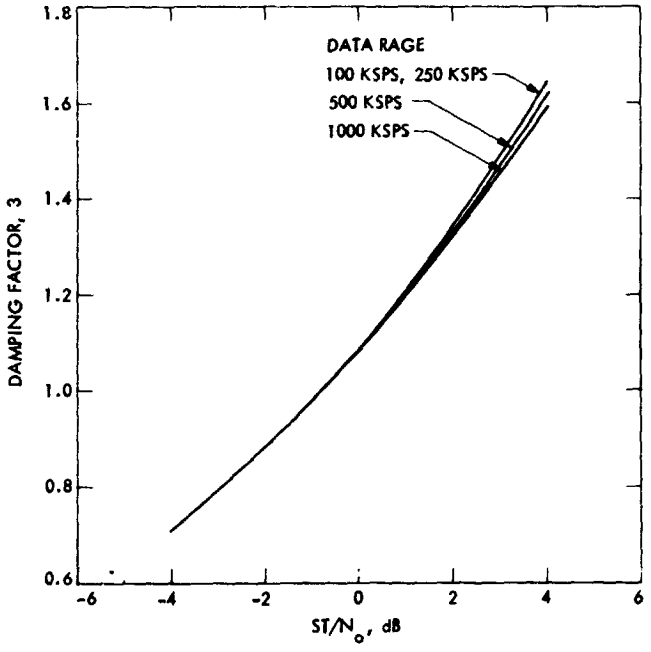

Fig. 9. Design values of Costas loop damping factor as functions of ST/N_0

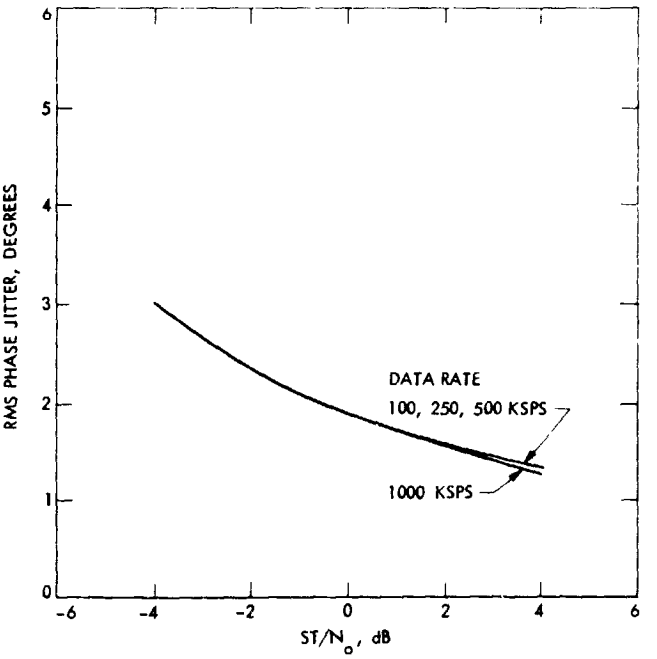

Fig. 10. Design values of Costas loop rms phase jitters as functions of ST/N_0

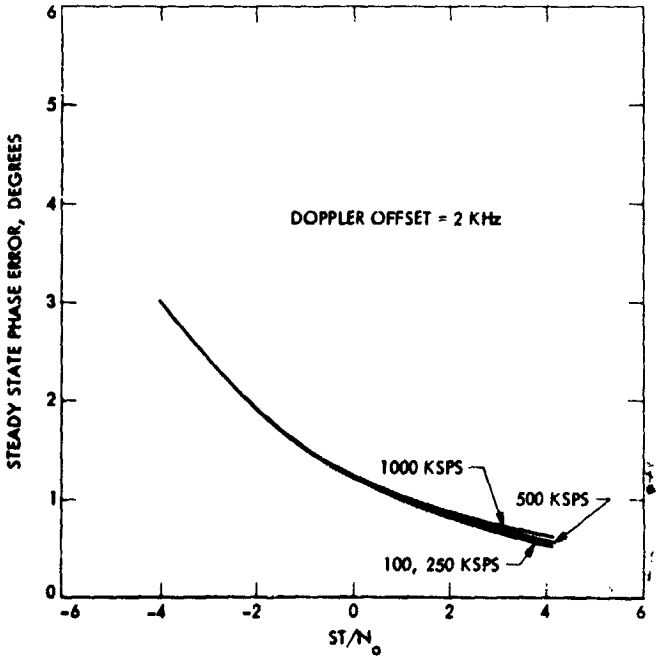

Fig. 11. Design values of Costas loop steady state phase errors as functions of ST/N_0

N79-25104

The Constantin-Rao Construction for Binary Asymmetric Error-Correcting Codes

R. J. McEliece
Consultant

E. R. Rodemich
Communications Systems Research Section

Recently Constantin and Rao gave an ingenious construction for a class of binary codes capable of correcting a single asymmetric error. In this article we shall give a complete analysis of the size of these codes.

I. Introduction

Most known classes of binary error-correcting codes have been designed for use on symmetric channels, i.e., channels for which the error probabilities $1 \to 0$ and $0 \to 1$ are equal. However, in certain applications (e.g., LSI memory protection (Ref. 1), optical communication (Ref. 6)), the observed errors are highly asymmetric, and the appropriate channel model may in fact be the Z-channel, in which the transition $0 \to 1$ is impossible. Of course any code capable of correcting t errors on a symmetric channel will also be capable of correcting t Z-channel errors; but at present there is no entirely satisfactory technique for dealing directly with asymmetric errors, comparable say to the BCH-Goppa construction (Ref. 5) for symmetric errors. Recently, however, Constantin and Rao (Ref. 1) gave an ingenious construction for a class of binary codes capable of correcting a single asymmetric error. Since our article is based on theirs, we begin with a description of the C.-R. codes.

Let V_n denote the set of binary n-tuples, and let G be any Abelian group of order $n + 1$. We suppose the nonzero elements of G are indexed $g^{(1)}, g^{(2)}, \cdots, g^{(n)}$. For each $\mathbf{x} = (x_1, \cdots, x_n) \in V_n$, we define

$$\gamma(\mathbf{x}) := \sum_{i=1}^{n} x_i g^{(i)} \tag{1}$$

the addition in Eq. (1) taking place in G. For each $g \in G$, define

$$V_n(g) := \{\mathbf{x} \in V_n : \gamma(\mathbf{x}) = g\} \tag{2}$$

Constantin and Rao showed that each of the subsets $V_n(g)$ is (qua code) capable of correcting one asymmetric error. They observed that since there are $n + 1$ sets $V_n(g)$, and since each of the 2^n elements of V_n belongs to exactly one of them, then

$$|V_n(g)| \geq \frac{2^n}{n+1}, \text{ for some } g \in G \tag{3}$$

Since $2^n/(n+1)$ is an *upper bound* on the cardinality of a single symmetric error-correcting code of length n, the simple bound of Eq. (3) already indicates that something interesting is afoot,[1] and one naturally wishes to know more about the numbers $|V_n(g)|$. As a step in this direction, Constantin and Rao showed that

$$|V_n(0)| \geq |V_n(g)|, \text{ all } g \in G \tag{4}$$

in effect Eq. (4) eliminates the need to consider $V_n(g)$ for $g \neq 0$. However, this is as far as Constantin and Rao went; they were unable to find an exact formula for $|V_n(0)|$ except for certain special groups, and they did not identify the group or groups of order $n+1$ yielding the largest value of $|V_n(0)|$. We have been able to fill in these gaps using finite Fourier analysis. The details of our work appear in Sections II and III, but here we sketch our main conclusions.

First, we have obtained an explicit formula for $|V_n(g)|$ in general. The formula depends on the characters of G, and is given (with the change in notation noted below) in Theorem 1 of Section III. For $g = 0$, the case of primary interest, however, the formula simplifies to

$$|V_n(0)| = \frac{1}{n+1} \sum_{h \text{ odd}} 2^{(n+1)/o(h)} - 1 \tag{5}$$

the summation in Eq. (5) being extended over all elements $h \in G$ whose order $o(h)$ is odd. We can also show (Corollary 1, Section III) that the maximum of $|V_n(g)|$ is often not attained uniquely:

$$|V_n(g)| \leq |V_n(0)|, \text{ with equality if and only if } o(g) \text{ is a power of 2.}$$

In particular, if $n+1$ is a power of 2, all CR codes of length n have exactly $2^n/(n+1)$ codewords. Since this is also the number of words in the Hamming single (symmetric) error correcting code of the same length, we conclude that the CR construction is uninteresting for these lengths. However, it will follow from our results that for all other lengths, the CR construction produces codes that are strictly larger than the best single symmetric error correcting code.

[1] Indeed, if n is even, the maximum size for a single symmetric error-correcting code is $\leq 2^n/(n+2)$, and if $n \equiv 1 \pmod 4$, it is $\leq 2^n/(n+3)$. (See Ref. 4, Chapter 17.) Hence (3) shows that the best CR code of lengths $\equiv 0, 1, 2 \pmod 4$ has more codewords than any code designed to correct one symmetric error.

We will also show (Corollary 2, Section III):

$$|V_n(0)| \leq \frac{1}{n+1}\left(2^n + n2^{\frac{n-2}{3}}\right)$$

with equality if and only if $n+1$ is a power of 3 and G is an elementary Abelian 3-group. And finally, we will show (Corollary 3, Section III) that among all Abelian groups of order $n+1$, $|V_n(0)|$ is maximized only by those groups whose odd Sylow subgroups are elementary Abelian.

Change in notation:

In what follows, the order of G will be denoted by n rather than $n+1$. Furthermore, in Section III we shall index the elements of G, *zero included*, as $G = \{g^{(0)}, g^{(1)}, \cdots, g^{(n-1)}\}$, and redefine the mapping γ: $V_n \to G$ by

$$\gamma(\mathbf{x}) := \sum_{i=0}^{n-1} x_i g^{(i)}$$

We shall then study the numbers

$$f(g) := |\{\mathbf{x} \in V_n : \gamma(\mathbf{x}) = g\}|$$

The effect of this is that to translate our formulas for $f(g)$ into formulas for $|V_n(g)|$, one must:

(1) Replace n by $(n+1)$.

(2) Divide the $f(g)$'s by 2.

Thus, for example, Corollary 1 in Section III reads $f(0) \leq 1/n \sum 2^{n/o(h)}$; using (1) and (2), we obtain $|V_n(0)| \leq 1/(n+1) \sum 2^{(n+1)/o(h)-1}$, as claimed in Eq. (5).

II. Some Fourier Analysis

Let G be a finite Abelian group of order n, which we write additively. Then G is a direct sum of cyclic subgroups. This means that there exist elements $\gamma_1, \gamma_2, \cdots, \gamma_m$ in G of orders $n_1, n_2, \cdots, n_m$ with $n = n_1 n_2 \cdots n_m$, such that every element in G has a unique expansion of the form $g = g_1\gamma_1 + \cdots + g_m\gamma_m$, with $0 \leq g_i < n_i$, $i = 1, 2, \cdots, m$. For brevity, we write $g = (g_1, \cdots, g_m)$.

For each $i \in \{1, 2, \cdots, m\}$, let ζ_i be a complex primitive n_ith root of unity. We define a mapping $\langle g, h \rangle$ of $G \times G$ into

the complex numbers as follows. Let $g = (g_1, \cdots, g_m)$, $h = (h_1, \cdots, h_m)$.

$$\langle g, h\rangle := \prod_{i=1}^{m} \zeta_i^{g_i h_i} \tag{6}$$

This mapping enjoys the following easily-checked properties.

$$\langle g, h\rangle = \langle h, g\rangle \tag{7}$$

$$\langle g, h\rangle\langle g, h'\rangle = \langle g, h + h'\rangle \tag{8}$$

$$\langle g, jh\rangle = \langle jg, h\rangle = \langle g, h\rangle^j \tag{9}$$

$$\sum_{g \in G} \langle g, h\rangle = \begin{cases} 0 \text{ if } h \neq 0 \\ n \text{ if } h = 0 \end{cases} \tag{10}$$

Now let $f(g)$ be any function mapping G into the complex numbers. The Fourier transform $\hat{f}$ of f is defined as follows:

$$\hat{f}(h) := \sum_{g \in G} \langle h, -g\rangle f(g) \tag{11}$$

Using the properties of Eqs. (7), (8), and (10), it is easy to verify the Fourier inversion formula:

$$f(g) = \frac{1}{n} \sum_{h \in G} \langle h, g\rangle \hat{f}(h) \tag{12}$$

This is well-known and can be found, at least implicitly, in any good algebra text, e.g., Ref. 3, Chapter 1. We now derive an alternate version of Eq. (12), which is not as well-known, but which is often useful.

Let us call two elements h and h' of G *equivalent*, and write $h \sim h'$, if h and h' both generate the same cyclic subgroup of G. *From now on we shall assume that the Fourier transform $\hat{f}$ of f has the property that $\hat{f}(h) = \hat{f}(h')$ whenever $h \sim h'$.*

If $G = G_1 \cup G_2 \cup \cdots \cup G_r$ is the decomposition of G into "$\sim$" equivalence classes, and if $h_1, \cdots, h_r$ are arbitrary representatives of these classes, then Eq. (12) can be written as

$$f(g) = \frac{1}{n} \sum_{i=1}^{r} \hat{f}(h_i) \sum_{h \in G_i} \langle h, g\rangle \tag{13}$$

If h_i has order d_i, then every element $h \in G_i$ has the form $h = jh_i$ for some integer $1 \leqslant j \leqslant d_i$ with $(j, d_i) = 1$. Thus by Eq. (9) the inner sum in Eq. (13) is

$$\sum_{\substack{1 \leqslant j \leqslant d_i \\ (j, d_i) = 1}} \langle jh_i, g\rangle = \sum_{\substack{1 \leqslant j \leqslant d_i \\ (j, d_i) = 1}} \langle h_i, g\rangle^j \tag{14}$$

Now by Eq. (9), $\langle h_i, g\rangle$ is a complex e_i-th root of unity for a divisor e_i of d_i, and it follows from a theorem of Ramanujan (see Ref. 2, Theorem 272) that the sum (Eq. (14)) is equal to $\phi(d_i)\mu(e_i)/\phi(e_i)$, where ϕ is Euler's ϕ-function and μ is Mobius' function. Hence Eq. (13) becomes

$$f(g) = \frac{1}{n} \sum_{i=1}^{r} \phi(d_i) \frac{\mu(e_i)}{\phi(e_i)} \hat{f}(h_i) \tag{15}$$

Notice that if we define the product of $g = (g_1, \cdots, g_m)$ and $h = (h_1, \cdots, h_m)$ by

$$gh := (g_1 h_1, \cdots, g_m h_m) \tag{16}$$

then the integer e_i appearing in Eq. (15) is just the order of the element gh_i. Thus if for $g \in G$ we define

$$[g] = \frac{\mu(e)}{\phi(e)}, \quad e = \text{order}(g) \tag{17}$$

Eq. (15) can be written as

$$f(g) = \frac{1}{n} \sum_{i=1}^{r} \phi(d_i) [gh_i] \hat{f}(h_i) \tag{18}$$

Finally we note that $[gh] = [gh_i]$ for all $h \in G_i$, and that $|G_i| = \phi(d_i)$, and so Eq. (18) can be written in either of the following ways:

$$f(g) = \frac{1}{n} \sum_{i=1}^{r} \phi(d_i) [h_j h_i] \hat{f}(h_i), \text{ if } g \sim h_j \tag{19}$$

$$f(g) = \frac{1}{n} \sum_{h \in G} [gh] \hat{f}(h) \tag{20}$$

III. Main Results

Let $G = \{g^{(0)}, g^{(1)}, \cdots, g^{(n-1)}\}$ be a finite Abelian group (we assume $g^{(0)} = 0$), and let V_n denote the set of n-tuples of 0's and 1's. For $\mathbf{x} = (x_0, x_1, \cdots, x_n) \in V_n$, define the mapping $\gamma: V_n \to G$ by

$$\gamma(\mathbf{x}) := \sum_{i=0}^{n-1} x_i g^{(i)} \tag{21}$$

Our problem is to count the number of times each element in G is covered in this mapping, i.e., to find the numbers

$$f(g) := |\{\mathbf{x} \in V_n : \gamma(\mathbf{x}) = g\}| \tag{22}$$

We will solve this problem by using the results of Section II. Here is the result:

Theorem 1:

For each $g \in G$,

$$f(g) = \frac{1}{n} \sum_{h \text{ odd}} \langle h, g \rangle 2^{n/o(h)} \tag{23}$$

In particular,

$$f(0) = \frac{1}{n} \sum_{h \text{ odd}} 2^{n/o(h)} \tag{24}$$

(In Eqs. (23) and (24), the symbol $o(h)$ denotes the order of the element $h \in G$, and the summation is extended over all elements in G of odd order.)

Proof:

This will follow from Eq. (12), once we compute $\hat{f}(h)$. From Eq. (11),

$$\hat{f}(h) = \sum_{g \in G} \langle h, -g \rangle f(g)$$

$$= \sum_{g \in G} \langle -h, g \rangle f(g) \qquad \text{(from Eq. (9))}$$

$$= \sum_{\mathbf{x} \in V_n} \langle -h, x_0 g^{(0)} + \cdots + x_{n-1} g^{(n-1)} \rangle$$

(from Eq. (22))

$$= \prod_{i=0}^{n-1} (1 + \langle -h, g^{(i)} \rangle) \qquad \text{(from Eq. (8))}$$

One can easily see from Eq. (6) that for a fixed value of h, with $o(h) = d$, the mapping $g \to \langle -h, g \rangle$ is a homomorphism of G onto the complex d-th roots of unity. Thus if K denotes the product $\prod_{t=0}^{d-1} (1 + \zeta^t)$, ζ being an appropriate primitive complex d-th root of unity, $\hat{f}(g) = K^{n/d}$. But the d complex numbers $\{1 + \zeta^t\}_{t=0}^{d-1}$ are roots of the equation $(z-1)^d - 1 = 0$, and so their product is $1 - (-1)^d$, hence $K = 2$ if d is odd, $K = 0$ if d is even. Hence

$$\hat{f}(h) = 0 \quad \text{if } o(h) \text{ is even}$$

$$= 2^{n/o(h)} \quad \text{if } o(h) \text{ is odd} \tag{25}$$

and theorem 1 follows.

Corollary 1:

$$f(g) \leqslant f(0) = \frac{1}{n} \sum_{h \text{ odd}} 2^{n/o(h)}$$

with equality if and only if $o(g)$ is a power of 2.

Proof:

From Theorem 1,

$$f(g) = |f(g)| \leqslant \frac{1}{n} \sum_{h \text{ odd}} |\langle h, g \rangle| \, 2^{n/o(h)} \tag{26}$$

But $\langle h, g \rangle$, being a complex root of unity, has absolute value 1, and so

$$f(g) \leqslant \frac{1}{n} \sum_{h \text{ odd}} 2^{n/o(h)} = f(0) \tag{27}$$

This inequality will be equality, if and only if $\langle h, g \rangle = 1$ for all elements h of odd order. Now from Eq. (9) $\langle h, g \rangle$ will in general have an order which divides g.c.d. $(o(h), o(g))$. Hence if $o(g)$ is a power of 2, then $\langle h, g \rangle = 1$ for all h of odd order, and equality holds in Eqs. (26) and (27). Conversely if $o(g)$ is not a power of 2, then in the expansion $g = g_1\gamma_1 + \cdots + g_m\gamma_m$, there will exist an index i such that $g_i \neq 0$, and $o(g_i\gamma_i)$ is not a power of 2. If $o(\gamma_i) = n_i = 2^a q$ with q odd, let $d = $ g.c.d. $(2^a g_i, n_i)$. Then $d \not\equiv 0 \pmod{n_i}$ since $g_i\gamma_i$'s order is not a power of 2.

If the integer h_i is chosen so that $0 \leq h_i \leq n_i - 1$ and $(2^a g_i)h_i \equiv d \pmod{n_i}$, it follows that $h = 2^a h_i \gamma_i$ has odd order, and that

$$\langle h, g \rangle = \zeta_i^{2^a g_i h_i} = \zeta_i^d \neq 1. \qquad \text{QED.}$$

Corollary 2:

$f(0) \leq 1/n\,(2^n + (n-1)2^{n/3})$, with equality if and only if n is a power of 3, and G is an elementary Abelian 3-group.

Proof:

From Corollary 1,

$$f(0) = \frac{1}{n} \sum_{h \text{ odd}} 2^{n/o(h)}$$

$$= \frac{1}{n} \left(2^n + \sum_{\substack{h \text{ odd} \\ h \neq 0}} 2^{n/o(h)}\right)$$

If $h = 0$, but $o(h)$ is odd, then $o(h) \geq 3$. Hence $2^{n/o(h)} \leq 2^{n/3}$, and so

$$f(0) \leq \frac{1}{n} (2^n + (n-1)2^{n/3}) \qquad (28)$$

Equality clearly holds in Eq. (29) if and only if every element in G (except 0) has order 3, i.e., iff G is an elementary Abelian 3-group. QED.

To state our final corollary, we need to introduce some number-theoretic notation. Let the prime-power decomposition of n be

$$n = \prod_{p|n} p^{e_p(n)} \qquad (29)$$

and let P_1 be the set of odd primes dividing n. If π is a subset of P_1, we define

$$\alpha_\pi(n) := \prod_{p \in \pi} \left(p^{e_p(n)} - 1\right) \qquad (30)$$

$$[\pi] := \prod_{p \in \pi} p \qquad (31)$$

Corollary 3:

If G is a group of order n, then

$$f(0) \leq \frac{1}{n} \sum_{\pi \subseteq P_1(n)} \alpha_\pi(n) 2^{n/[\pi]} \qquad (32)$$

with equality iff for all odd p, the Sylow p-subgroups of G are elementary Abelian.

Proof:

Let

$$G = \sum_{p|n} G_p$$

be the decomposition of G as the direct sum of its Sylow subgroups. If π is a subset of $P_1(n)$ let S_π be the subset of G consisting of these elements whose orders involve exactly the primes in π. Then clearly $|S_\pi| = \alpha_\pi(n)$, and every element in S_π has order at least $[\pi]$. The inequality of Eq. (32) follows. Furthermore, equality holds in Eq. (32) iff each element in each S_π has order exactly $[\pi]$, and this will happen iff each odd G_p is elementary. QED.

We conclude with one illustration of how Theorem 1 can be used to compute the values $f(g)$, for all $g \in G$. Suppose, then, that $G = Z_p \oplus Z_q$ is a direct sum of a cyclic p-group and a cyclic q-group, p and q being odd primes. We represent the elements of G as pairs (x, y), $0 \leq x < p$, $0 \leq y < q$. There are just four equivalence classes of elements in G, and we can choose as representatives of these classes $(0, 0)$, $(0, 1)$, $(1, 0)$, $(1, 1)$. The following table will prove useful:

i	h_i	d_i	$\phi(d_i)$	$\hat{f}(h_i)$
0	(0, 0)	1	1	2^{pq}
1	(0, 1)	q	$q-1$	2^p
2	(1, 0)	p	$p-1$	2^q
3	(1, 1)	pq	$(p-1)(q-1)$	2

Now what Eq. (19) says, in essence, is that the value $f(h_j)$ is the j-th component of the vector $\mathbf{f} = 1/n\, H \hat{\mathbf{f}}$, where H is the $r \times r$ matrix defined by

$$H_{ij} := \phi(d_i)\,[h_i h_j] \qquad (33)$$

and $\hat{\mathbf{f}}$ is the column vector whose i-th component is $\hat{f}(h_i)$. In the present case, clearly

$$\mathbf{f}^T = (2^{pq}, 2^p, 2^q, 2)$$

and from the above table we compute

$$H = \begin{bmatrix} 1 & (q-1) & (p-1) & (p-1)(q-1) \\ 1 & 1 & (p-1) & -(p-1) \\ 1 & (q-1) & -1 & -(q-1) \\ 1 & -1 & -1 & +1 \end{bmatrix}$$

Hence

$$f(h_0) = \frac{1}{pq}\{2^{pq} + (q-1)2^p + (p-1)2^q + (p-1)(q-1)2\}$$

$$f(h_1) = \frac{1}{pq}\{2^{pq} - \quad 2^p + (p-1)2^q - \quad (p-1)2\}$$

$$f(h_2) = \frac{1}{pq}\{2^{pq} + (q-1)2^p - \quad 2^q - \quad (q-1)2\}$$

$$f(h_3) = \frac{1}{pq}\{2^{pq} - \quad 2^p - \quad 2^q + \quad 2\}$$

For example with $p = 3$, $q = 5$, we get $f(h_0) = 2192$, $f(h_1) = 2188$, $f(h_2) = 2184$, $f(h_3) = 2182$. This means that the CR codes of length 14 defined by this group have

$$|V_{14}(g)| = \begin{cases} 1096 \text{ if } g \sim h_0 \\ 1094 \text{ if } g \sim h_1 \\ 1092 \text{ if } g \sim h_2 \\ 1091 \text{ if } g \sim h_3 \end{cases}$$

The best possible single symmetric error-correcting code of length 14 has only 1024 words (see Ref. 4, Appendix A).

References

1. Constantin, S. D. and T. R. N. Rao. "On the Theory of Binary Asymmetric Error-Correcting Codes," *Information and Control*, in press.
2. Hardy, G. M. and E. M. Wright, *An Introduction to the Theory of Numbers*, (4th ed.) London: Oxford University Press, 1960.
3. Lang, S. *Algebra*. Reading, Mass: Addison-Wesley, 1965.
4. MacWilliams, F. J. and N. J. A. Sloane, *The Theory of Error Correcting Codes*. Amsterdam: North-Holland Publishing Co., 1977.
5. McEliece, R. J. *The Theory of Information and Coding*. Reading, Mass: Addison-Wesley, 1976.
6. Pierce, J. R., "Optical Channels: Practical Limits with Photon Counting," *IEEE Trans. Communications COM-26* (1978), pp. 1819-1821.

N79-25105

Carrier Tracking Loop Performance in the Presence of Strong CW Interference

B. K. Levitt
Communications Systems Research Section

In a coherent data link, narrow-band radio frequency interference (RFI) near the carrier frequency can degrade the link performance by impacting the carrier tracking loop behavior and producing a partial or complete loss of coherence. If the RFI is strong enough, this effect can occur even though the frequency of the interference lies well beyond the carrier tracking loop bandwidth. In 1973, F. Bruno and A. Blanchard independently performed similar analyses of the response of a phase-locked loop (PLL) to a continuous wave (CW) interferer, and derived conditions under which the loop dropped carrier lock and tracked the interference instead. This paper compares the contributions of these two analysts, and extends Bruno's closed form approximation for the loop phase error. This result is applied in a subsequent article to the general problem of coherent detection of residual and suppressed carrier telemetry in the presence of strong CW interference.

I. Introduction

Because of increasing competition for the available RF spectrum, the DSN has become concerned about the disruptive potential of RFI on network operations. In an effort to define the RFI threat, the DSN is currently developing a sensitive wide-band RFI monitoring capability to detect and identify sources of RFI at the Goldstone complex (Ref. 1). This surveillance system will characterize the RF environment in which the DSN functions, but a parallel activity is needed to investigate the effects of different classes of RFI on components of a DSN receiver, and ultimately to determine the resulting degradation in link performance. One recent example of this is Low's simulation work at DSS 11 to measure the increase in telemetry error rate due to CW interference at odd harmonics of the data subcarrier (Ref. 2). As a further contribution to this effort, this paper reviews and extends some earlier analyses of the impact of a CW interferer on the performance of a carrier tracking loop.

One of the first investigations of this problem was the experimental study conducted in 1966 by Britt and Palmer at Langley Research Center on second-order PLL's (Ref. 3). They measured the loop phase error as a function of the interference-to-carrier power ratio (P_I/P_C), and determined limiting values of P_I/P_C for which carrier lock was lost, for CW interference within the loop passband. In 1972, Ziemer, at the University of Missouri, reported on a perturbation analysis of weak CW interference in Costas loops (Ref. 4). He restricted the interference levels to be small enough to allow the degraded carrier tracking loop to remain in its linear operating range. In their independent analytical treatment of PLL's, in 1973, Bruno (Ref. 5) of Hazeltine Corporation and Blanchard (Ref. 6) of Centre Spatial de Toulouse (France) eliminated this

constraint, permitting P_I/P_C to become large enough for the loop to produce a steady-state static phase error well outside the linear region. Using the same mathematical approach, they solved for the loop phase error and derived loss of lock conditions that are principally valid for strong CW interference beyond the loop passband. However, whereas Blanchard left his solutions in implicit form, Bruno derived explicit approximations for the degraded loop phase error that are accurate over a small part of the lock region. In the rest of this paper, we will examine the contributions of these two analysts in some detail, and extend Bruno's closed form approximate phase error results to the entire lock region.

II. Analysis

Consider a PLL which is initially locked to a carrier with amplitude A and frequency ω_o. In the presence of a CW interferer at offset frequency $\Delta\omega$, with $\alpha^2 \equiv P_I/P_C$, the PLL input is

$$r(t) = \sqrt{2}A\,[\sin \omega_o t + \alpha \sin (\omega_o + \Delta\omega)\, t]\,. \qquad (1)$$

Neglecting the $2\omega_o$ term, the loop error signal is

$$\begin{aligned}\epsilon(t) &= \sqrt{2}\, r(t) \cos\,[\omega_o t - \phi(t)] \\ &= A\,[(1 + \alpha \cos \Delta\omega t) \sin \phi(t) + \alpha \sin \Delta\omega t \cos \phi(t)]\end{aligned} \qquad (2)$$

Using the operator $p = d/dt$, the loop phase error is constrained by

$$\phi(t) = -K_{VCO}\left[\frac{F(p)}{p}\right]\epsilon(t)\,, \qquad (3)$$

where $F(s)$ is the loop filter and K_{VCO} is the gain of the voltage-controlled oscillator (VCO).

Equations (2) and (3) cannot be solved analytically for $\phi(t)$ for all values of α and $\Delta\omega$. However, based on their experimental observations, Bruno and Blanchard both adopted the steady-state trial solution

$$\phi(t) = \lambda + \sigma \sin (\Delta\omega t - \nu)\,, \qquad (4)$$

where the static phase error $\lambda[\epsilon - \pi/2, \pi/2]$. Note that Eq. (4) implies that the average VCO frequency is ω_o, reflecting the assumption that the loop remains locked to the carrier with an RFI-induced oscillation at the beat frequency $\Delta\omega$. Substituting this trial solution for $\phi(t)$ into Eqs. (2) and (3), and equating the *dc*, cos $\Delta\omega t$, and sin $\Delta\omega t$ coefficients on both sides of the resulting equation, Bruno derived the lock constraints

$$\sin \lambda = -\frac{\sigma^2 \delta \cos \psi}{2J_0(\sigma)}\,, \qquad (5)$$

$$\sin (\lambda - \nu) = -\frac{\sigma^2 \delta \cos \psi}{2\alpha J_1(\sigma)}\,, \qquad (6)$$

$$\left[\frac{\sigma\delta \sin \psi + 2J_1(\sigma)\cos \lambda}{J_0(\sigma) - J_2(\sigma)}\right]^2 + \left[\frac{\sigma^2 \delta \cos \psi}{2J_1(\sigma)}\right]^2 = \alpha^2\,, \qquad (7)$$

where ψ is the phase angle of $F(j\Delta\omega)$, δ is the normalized offset frequency

$$\delta \equiv \frac{\Delta\omega}{A\,K_{VCO}\,|F(j\Delta\omega)|}\,, \qquad (8)$$

and ψ and δ are implicit functions of $\Delta\omega$ in Eqs. (5)-(7). The Bessel functions above result from expansions of sin $[\sigma \sin (\Delta\omega t + \nu)]$ and cos $[\sigma \sin (\Delta\omega t + \nu)]$. This trial solution is valid if components at $2\,\Delta\omega$ and higher can be ignored, which requires that σ be on the order of 1 rad or less so that terms of the form $J_n(\sigma)$ for $n > 2$ are negligible relative to their lower order counterparts. This does not severely limit the usefulness of these results since larger values of σ correspond to peak phase errors on the order of $\pi/2$ or higher, at which point it becomes questionable whether the loop can properly be characterized as being locked to the carrier. Since σ increases monotonically with α, the implication is that as the interference power rises, there is a brief transition region in which the loop is not locked to the carrier or the CW interferer, and the form of the phase error differs from Eq. (4) for large σ.

Blanchard adopted the same trial solution and again considered only components at *dc* and $\Delta\omega$, but he made several simplifying assumptions. He neglected $J_n(\sigma)$ for $n > 1$, restricted himself to second order loop filters of the form

$$F(s) = \frac{1 + \tau_2 s}{1 + \tau_1 s} \qquad (9)$$

or

$$F(s) = \frac{1 + \tau_2 s}{\tau_1 s} \qquad (10)$$

where $\tau_1 \gg \tau_2$, and assumed that $\Delta\omega \gg 1/\tau_2$ so that

$$|F(j\Delta\omega)| \approx \frac{\tau_2}{\tau_1} \tag{11}$$

$$\psi \approx 0.$$

Then Eq. (7) reduces to

$$\alpha^2 = \left[\frac{\sigma^2\delta}{2J_1(\sigma)}\right]^2 \left\{1 - 4\left[\frac{J_1(\sigma)}{J_0(\sigma)}\right]^4\right\} + \left[\frac{2J_1(\sigma)}{J_0(\sigma)}\right]^2. \tag{12}$$

Actually, Blanchard's restrictions are not unreasonable. Most PLL's are currently implemented with second order filters, and for a given α, a large $\Delta\omega$ is consistent with a small σ, which is a necessary condition for the analysis above to be valid. What Bruno's results can accommodate that Blanchard's preclude are situations in which $\Delta\omega$ is too small for Eq. (11) to hold, yet α is low enough to yield an acceptably small value of σ.

Note that Eq. (5) is meaningless when the magnitude of the right-hand side exceeds 1. Consequently, Bruno and Blanchard both adopted $|\lambda| = \pi/2$ to be the limiting condition for the loop to be locked to the carrier. They later confirmed this result experimentally. So, for a given $\Delta\omega$, the loop remains in lock for $|\lambda| \leq \pi/2$, which translates into $\sigma \leq \sigma_o$ or $\alpha \leq \alpha_o$. Equation (5) defines σ_o as a function of δ:

$$\frac{\sigma_o^2}{J_0(\sigma_o)} = \frac{2}{|\delta \cos\psi|}, \tag{13}$$

and, using $\sigma = \sigma_o$ with $|\lambda| = \pi/2$ in Eq. (7) yields α_o:

$$\alpha_o^2 = \left[\frac{J_0(\sigma_o)}{J_1(\sigma_o)}\right]^2 \left\{1 + \left(\frac{2\tan\psi}{\sigma_o}\right)^2 \left[\frac{J_1(\sigma_o)}{J_0(\sigma_o) - J_2(\sigma_o)}\right]^2\right\} \tag{14}$$

In Appendix A, it is shown that the implicit dependence of α_o on δ in Eqs. (13) and (14) can be replaced by the simple explicit relationship

$$\alpha_o^2 \cong 2\left|\frac{\delta}{\cos\psi}\right| \tag{15}$$

provided

$$\frac{\sigma_o^2}{2}\left|\sin^2\psi - \frac{\sigma_o^2}{48}\right| \ll 1^1 \tag{16}$$

In particular, when $\Delta\omega$ is much larger than the PLL bandwidth so that $\psi \approx 0$, Eq. (15) is accurate for $\sigma_o^4 \ll 96$, which is everywhere Eqs. (13) and (14) are valid.

For given loop parameters and values of δ and $\alpha \leq \alpha_o$, it is difficult to compute σ using Eqs. (7) or (12). While Blanchard left his solution in this implicit form, Bruno simplified the computation by substituting

$$J_0(\sigma) - J_2(\sigma) \cong 1 - \frac{3}{8}\sigma^2 \text{ and } 2J_1\frac{(\sigma)}{\sigma} \cong 1$$

in Eq. (7), resulting in the perturbation expressions,

$$\sigma^2 \cong \frac{\alpha^2}{\delta^2 + 2\delta\sin\psi\cos\lambda + \cos^2\lambda + \frac{3}{4}\alpha^2} \tag{17}$$

for small σ. However, Eq. (17) is still complicated by the dependence of $\cos\lambda$ on σ via Eq. (5). To circumvent this, Bruno restricted his approximation to the region $\sigma \ll \sigma_o$ or $|\sin\lambda| \ll 1$, allowing Eq. (17) to trivially simplify to

$$\sigma^2 \cong \frac{\alpha^2}{\delta^2 + 2\delta\sin\psi + 1 + \frac{3}{4}\alpha^2}. \tag{18}$$

In Appendix B, it will be proved that for $\sigma^2 \ll \sqrt{2}$ and any value of $|\lambda| \leq \pi/2$, σ^2 can be accurately computed from the explicit approximation

$$\sigma^2 \cong \frac{\alpha^2}{\delta^2 + 2\delta\sin\psi + 1} \tag{19}$$

In particular, if $\sigma_o^2 < \sqrt{2}$, Eq. (19) is valid over the entire PLL lock region. Completing the solution for λ and ν for small σ, Eqs. (5) and (6) reduce to

$$\sin\lambda \cong -\frac{\sigma^2\delta\cos\psi}{2}, \tag{20}$$

$$\sin(\lambda - \nu) \cong -\frac{\sigma\delta\cos\psi}{\alpha}. \tag{21}$$

[1] **Bruno derived Eq. (15) (as did Blanchard with $\psi = 0$) for small σ_o (or large α_o); however, the constraint of Eq. (16) under which Eq. 15 is valid, is our contribution.**

III. Example

To illustrate these results, consider a loop filter of the form of Eq. (9), representative of a PLL in a DSN receiver. For example, suppose

$$\tau_1 = 2 \text{ sec}$$

$$\tau_2 = \frac{1}{8} \text{ sec}$$

$$A K_{VCO} = 1000 \text{ sec}^{-1} \tag{22}$$

for which the loop noise bandwidth at threshold and at the specified operating point are given by

$$2B_{LO} \cong \frac{3}{2\tau_2} = 12 \text{ Hz},$$

$$B_L \cong \frac{1 + \dfrac{A K_{VCO} \tau_2^2}{\tau_1}}{4\tau_2} = 17.6 \text{ Hz}. \tag{23}$$

Applying Eq. (13) to the given loop parameters, we find that $\sigma_o \leqslant 1$ rad for $\Delta\omega/2\pi \geqslant B_L$: this is the region for which the analysis above is valid. Also, for this range of $\Delta\omega$, the constraint of Eq. (16) is satisfied, indicating that Eq (15) can be used to compute α_o^2, the limiting interference-to-carrier power for which the PLL maintains carrier lock. The loop lock region is illustrated in Figs. 1 and 2. Using Eqs. (5) and (7) for $\Delta\omega/2\pi$ near B_L, and the simpler approximations of Eqs. (19) and (20) for $\Delta\omega/2\pi \gg B_L$, profiles of α^2 and σ were also computed for $|\lambda| < \pi/2$ and presented in these figures. As expected, the farther the interference lies outside the loop bandwidth, the larger the value of P_I/P_C required to pull the loop out of lock, and the smaller its effect on the loop behavior as measured by σ_o. Also, $\alpha_o^2 \gg 1$ over much of the lock region for which the analysis applies, which supports the strong CW interference restriction in the title of this paper. Of course, as mentioned earlier, for offset frequencies within the loop bandwidth corresponding to $\sigma_o \geqslant 1$ rad, the loop can be pulled out of lock for $P_I \sim P_C$, and Eq. (4) simply does not represent the form of the phase error in this region.

Figure 1 shows that for a given value of $\Delta\omega$, the loop phase error is not significantly degraded until α^2 approaches the limit α_o^2. This behavior is illustrated in more detail in Fig. 3 for $\Delta\omega/2\pi = 1000$ Hz, using Eqs. (19) and (20).

References

1. Levitt, B. K., "Analysis of a Discrete Spectrum Analyzer for the Detection of Radio Frequency Interference," in *The Deep Space Network Progress Report 42-38*, Jet Propulsion Laboratory, Pasadena, California, pp. 83-98, April 15, 1977.

2. Low, P. W., "Radio Frequency Interference Effects of Continuous Sinewave Signals on Telemetry Data," in *The Deep Space Network Progress Report 42-40*, Jet Propulsion Laboratory, Pasadena, California, pp. 174-193, August 15, 1977.

3. Britt, C. L., and Palmer, D. F., "Effects of CW Interference on Narrow-Band Second-Order Phase-Lock Loops," *IEEE Trans. Aerospace and Electronic Systems*, Vol. AES-3, pp. 123-135, January 1967.

4. Ziemer, R. E., "Perturbation Analysis of the Effect of CW Interference in Costas Loops," in the *Record of the 1972 National Telecommunications Conference*, Houston, Texas, December 4-6, 1972, pp. 20G-1 to 20G-6.

5. Bruno, F., "Tracking Performance and Loss of Lock of a Carrier Loop Due to the Presence of a Spoofed Spread Spectrum Signal," in the *Proceedings of the 1973 Symposium on Spread Spectrum Communications, Vol. I*, edited by M. L. Schiff, Naval Electronics Laboratory Center, San Diego, California, pp. 71-75, March 13-16, 1973.

6. Blanchard, A., "Interferences in Phase-Locked Loops," *IEEE Trans. Aerospace and Electronic Systems*, Vol. AES-10, pp. 686-697, September 1974.

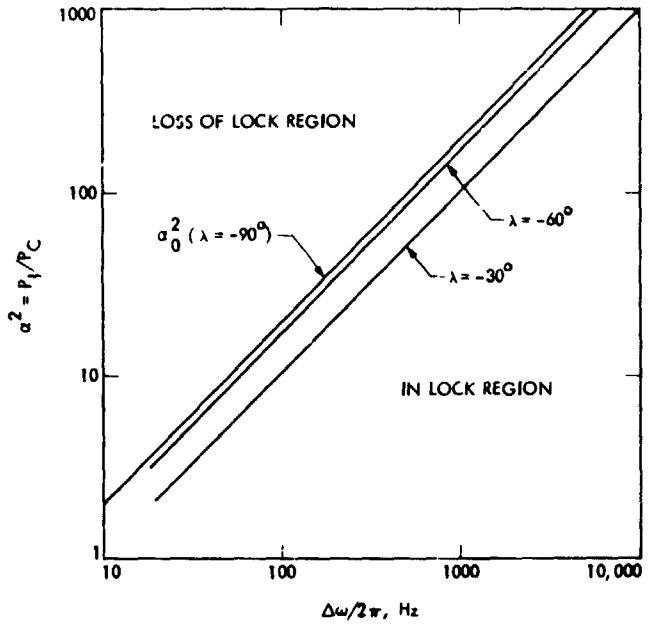

Fig. 1. Limiting interference-to-carrier power levels for loss of lock when $F(s) = \frac{1 + s/8}{1 + 2s}$ and $A\,K_{VCO} = 1000\ s^{-1}$

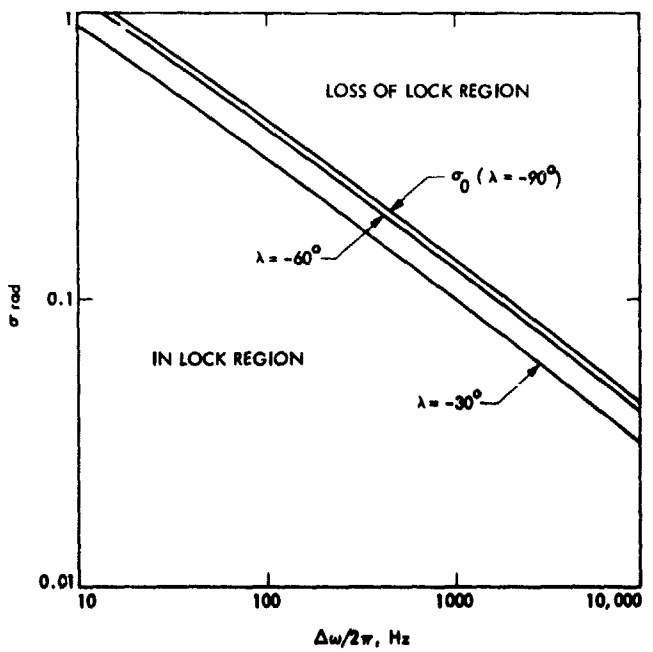

Fig. 2. Corresponding limiting values of σ (phase error beat frequency amplitude)

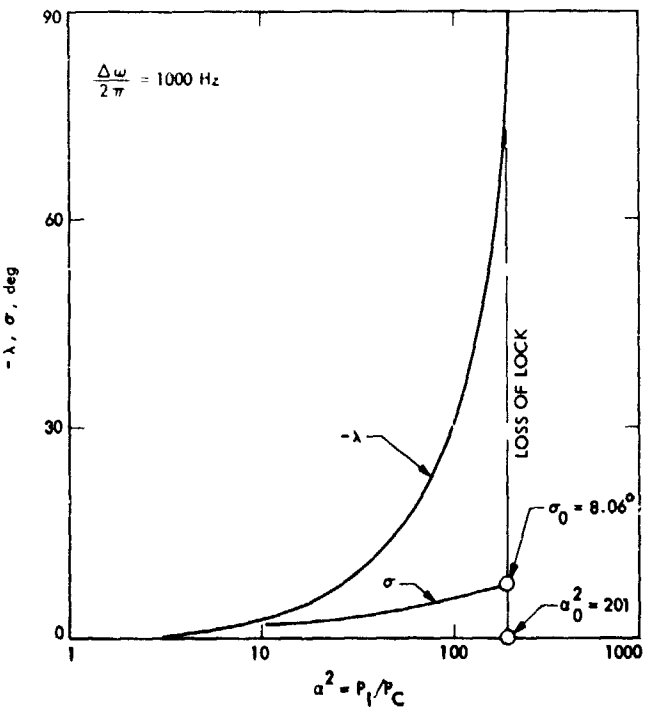

Fig. 3. Lock parameters of previous loop at $\Delta\omega/2\pi$ = 1000 Hz

Appendix A

Derivation of Lock Constraint Approximation

Equations (13) and (14) can be combined to yield the expression

$$\frac{\alpha_o^2}{2\left|\frac{\delta}{\cos\psi}\right|} = J_0(\sigma_o)\left\{\left[\frac{\cos\psi}{2J_1\frac{\sigma_o}{\sigma_o}}\right]^2 + \left[\frac{\sin\psi}{J_0(\sigma_o) - J_2(\sigma_o)}\right]^2\right\}. \tag{A-1}$$

But to order σ_o^4, the Bessel functions above may be approximated by the power series

$$J_0(\sigma_o) \cong 1 - \frac{\sigma_o^2}{4} + \frac{\sigma_o^2}{64},$$

$$2J_1\frac{\sigma_o}{\sigma_o} \cong 1 - \frac{\sigma_o^2}{8} + \frac{\sigma_o^4}{192},$$

$$J_0(\sigma_o) - J_2(\sigma_o) \cong 1 - \frac{3\sigma_o^2}{8} + \frac{\sigma_o^4}{48}. \tag{A-2}$$

Computing the inverse square of the last two polynomials, we find that

$$\left[2J_1\frac{\sigma_o}{\sigma_o}\right]^{-2} \cong 1 + \frac{\sigma_o^2}{4} + \frac{7\sigma_o^4}{192},$$

$$[J_0(\sigma_o) - J_2(\sigma_o)]^{-2} \cong 1 + \frac{3\sigma_o^2}{4} + \frac{73\sigma_o^4}{192}. \tag{A-3}$$

Substituting these expressions into Eq. (1) yields the result

$$\frac{\alpha_o^2}{2\left|\frac{\delta}{\cos\psi}\right|} \cong 1 + \frac{\sigma_o^2}{2}\sin^2\psi\left(1 + \frac{7\sigma_o^2}{16}\right) - \frac{\sigma_o^4}{96} \tag{A-4}$$

Therefore the lowest order in σ_o, Eq. (15) is valid provided the constraint of Eq. (16) is satisfied. The σ_o^4 term is retained in Eq. (16) because it dominates when $\psi = 0$.

Appendix B

Derivation of Extended Range Approximation for σ^2

For $\sigma^2 \ll 8/3$, the Bessel function expressions of Eq. (A-2) simplify to

$$J_0(\sigma) \cong 2J_1\frac{\sigma}{\sigma} \cong J_0(\sigma) - J_2(\sigma) \cong 1 \qquad \text{(B-1)}$$

Substituting Eq. (B-1) into Eqs. (5) and (7) yields the approximations

$$\sin\lambda \cong -\frac{\sigma^2\delta\cos\psi}{2}, \qquad \text{(B-2)}$$

$$\sigma^2 \cong \frac{\alpha^2}{\delta^2 + 2\delta\sin\psi\cos\lambda + \cos^2\lambda} \qquad \text{(B-3)}$$

We want to prove that in the lock region,

$$|\sin\lambda| \leqslant 1, \qquad \text{(B-4)}$$

Eq. (B-3) can be accurately approximated by Eq. (19), provided $\sigma^2 \ll \sqrt{2}$.

When $|\delta\cos\psi| \leqslant \sqrt{2}$, we have

$$|\sin\lambda| = \frac{\sigma^2}{2}|\delta\cos\psi| \leqslant \frac{\sigma^2}{\sqrt{2}} \ll 1 \qquad \text{(B-5)}$$

so that $\cos\lambda \cong 1$ and the desired result follows trivially.

Now consider the region $|\delta\cos\psi| \geqslant \sqrt{2}$. To demonstrate that Eqs. (B-3) and (19) are equivalent, we will prove that the difference between the two denominators is negligible. That is, we want to show that

$$\Delta \equiv |(2\delta\sin\psi + 1) - (2\delta\sin\psi\cos\lambda + \cos^2\lambda)|$$

$$= \sin^2\lambda\left|1 + \frac{2\delta\sin\psi}{1+\cos\lambda}\right| \ll \delta^2 + 2\delta\sin\psi + 1. \qquad \text{(B-6)}$$

To verify Eq. (B-6), it is sufficient to prove that

$$\sin^2\lambda \ll \min_{1\leqslant\eta\leqslant 2}\left[\frac{\delta^2 + 2\delta\sin\psi + 1}{|1 + \eta\delta\sin\psi|}\right] \qquad \text{(B-7)}$$

since $\lambda\epsilon[-\pi/2, \pi/2]$. But for $\sigma^2 \ll \sqrt{2}$,

$$|\sin\lambda| << |\delta\cos\psi|/\sqrt{2}, \qquad \text{(B-8)}$$

and, using Eq. (B-4), this implies that

$$\sin^2\lambda << |\delta\cos\psi|/\sqrt{2}. \qquad \text{(B-9)}$$

So Eq. (B-7) will follow if we can show that

$$\beta \equiv \min_{1\leqslant\eta\leqslant 2}\left[\frac{\sqrt{2}(\delta^2 + 2\delta\sin\psi + 1)}{|\delta\cos\psi|\,|1 + \eta\delta\sin\psi|}\right] \geqslant 1 \qquad \text{(B-10)}$$

From Fig. B-1, it is evident that β may be written in the form

$$\beta = \begin{cases} \dfrac{\sqrt{2}(\delta^2 + 2\delta\sin\psi + 1)}{|\delta\cos\psi|(1 + 2\delta\sin\psi)}; & 0 \leqslant \delta\sin\psi < \infty \\ \dfrac{\sqrt{2}(\delta^2 + 2\delta\sin\psi + 1)}{|\delta\cos\psi|(1 + \delta\sin\psi)}; & -\dfrac{2}{3} \leqslant \delta\sin\psi \leqslant 0 \\ \dfrac{\sqrt{2}(\delta^2 + 2\delta\sin\psi + 1)}{|\delta\cos\psi|(-1 - 2\delta\sin\psi)}; & -\infty < \delta\sin\psi \leqslant -\dfrac{2}{3}. \end{cases} \qquad \text{(B-11)}$$

It can be shown that there is no loss of generality in restricting δ and ψ to the range $-\pi/2 \leqslant \psi \leqslant \pi/2$ and $\delta \geqslant \sqrt{2}/\cos\psi$, since other values of these parameters yield a value of β from this restricted range.

Now, using elementary calculus, for a given value of ψ in this range, β in Eq. (B-11) can be minimized over δ within its range: the results are presented in Table B-1. As shown in the plot of $\beta(\delta_{min})$ vs. ψ in Fig. B-2, β has a minimum value of 1 which occurs at $\psi = 54.74°$ and $\delta = \delta_{min} = 2.45$. This completes our proof.

Table B-1. Variation of minimum value of β with ψ

Range of ψ	$\min_{\delta > \sqrt{2}/\cos\psi} (\beta) = \beta(\delta_{min})$	δ_{min}
$30^\circ \leq \psi \leq 90^\circ$	$(\sqrt{2} \sin\psi \cos\psi)^{-1}$	∞
$8.65^\circ \leq \psi \leq 30^\circ$	$2\sqrt{2}\,(1 - \sin\psi)/\cos\psi$	$(1 - 2\sin\psi)^{-1}$
$0 \leq \psi \leq 8.65^\circ$	$\dfrac{2\cos^2\psi + 4\sqrt{2}\cos\psi \sin\psi + 4}{2\cos^2\psi + 4\sqrt{2}\cos\psi \sin\psi}$	$\sqrt{2}/\cos\psi$
$-11.77^\circ \leq \psi \leq 0$	$\dfrac{2\cos^2\psi + 4\sqrt{2}\cos\psi \sin\psi + 4}{2\cos^2\psi + 2\sqrt{2}\cos\psi \sin\psi}$	$\sqrt{2}/\cos\psi$
$-30^\circ \leq \psi \leq -11.77^\circ$	$-(\sqrt{2} \sin\psi \cos\psi)^{-1}$	∞
$-47.60^\circ \leq \psi \leq -30^\circ$	$2\sqrt{2}\,(1 + \sin\psi)/\cos\psi$	$-(1 + 2\sin\psi)^{-1}$
$-90^\circ \leq \psi \leq -47.60^\circ$	$\dfrac{2\cos^2\psi + 4\sqrt{2}\cos\psi \sin\psi + 4}{-2\cos^2\psi - 4\sqrt{2}\cos\psi \sin\psi}$	$\sqrt{2}/\cos\psi$

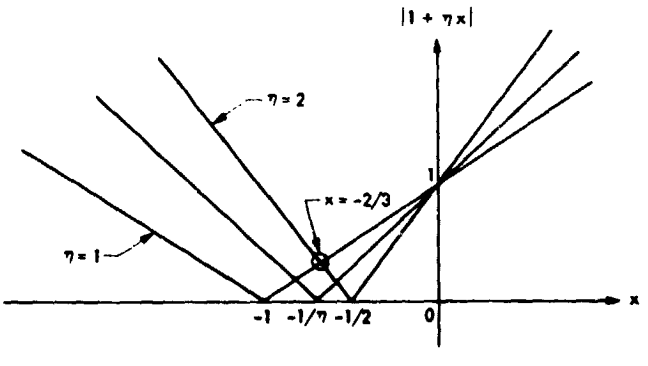

Fig. B-1. Upperbound on $|1 + \eta x|$ for $1 \leq \eta \leq 2$

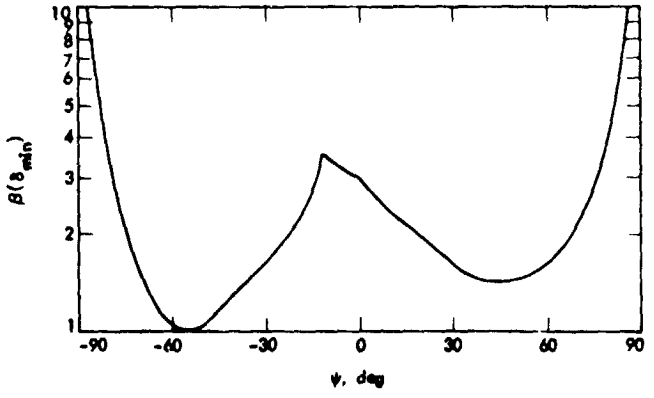

Fig. B-2. Behavior of $\min_{\delta > \sqrt{2}/\cos\psi} (\beta)$ as a function of ψ

ORIGINAL PAGE IS
OF POOR QUALITY

N79-25106

DSS 13 Antenna Monitor System

B. Siev and D. Bayerce
Communications Systems Research Section

A monitor system is being developed for the 26-meter antenna at DSS 13 so that unattended station operation can proceed safely. The antenna has been successfully operating unattended since July 1978. This article documents the part of the monitor system that is currently in use. A later article will be issued which will document the full monitor system.

I. Introduction

The part of the monitor system that is currently functioning at DSS 13 checks system pressures, accumulator pressures, differential pressures, wind velocity, power supplies, fluid temperatures and fluid levels. These system measurements are sent to the antenna controller from a data sampler that interrogates the transducers. The antenna controller decides and takes appropriate action. Some measurements are checked continuously and some measurements are checked as a function of antenna state.

II. Continuous Tests

A. 5-Second Tests

(1) The data sampler
If it is not functioning, the antenna is shut down and the problem is logged.

(2) The wind tower power supply
If it is not functioning, the antenna is shut down and the problem is logged.

(3) Fluid level
If it is greater than 23 cm or less than 11 cm, the antenna is shut down and the problem is logged.

(4) The 2 control room power supplies
If either is not functioning, a warning is logged.

(5) The fluid temperature
If the fluid temperature is too high, the antenna is stowed and the problem is logged.

(6) The lube oil pressure switch
If the system is not pressurized, this test is ignored. If the system is pressurized and the lube oil pressure switch is off, the system is shut down and the problem is logged.

B. 10-Second Tests

(1) Wind velocity and gusts
If the wind velocity exceeds 20 m/s or gusts exceed 25 m/s, the antenna is stowed and the problem is logged.

(2) Wind direction
Wind direction is displayed.

III. Electronics On, Pumps Off

A. Disable Monitor Circuit

If it is off, the antenna is shut down. The monitor system determines which of two conditions caused the problem: loss of the Hydro-Mech 28 v power supply or disable button, and logs the problem.

B. Accumulator Pressures

If any pressure is not within the specified range, the antenna is shut down and the problem is logged.

(1) Azimuth low speed
$5.5 \times 10^6 - 8.3 \times 10^6$ N/m^2

(2) Azimuth high speed #1
$6.9 \times 10^6 - 9.3 \times 10^6$ N/m^2

(3) Azimuth high speed #2
$6.9 \times 10^6 - 9.3 \times 10^6$ N/m^2

(4) Elevation System #1
$8.3 \times 10^6 - 10.3 \times 10^6$ N/m^2

(5) Elevation System #2
$8.3 \times 10^6 - 10.3 \times 10^6$ N/m^2

C. Brakes

If any brake is off, the antenna is shut down and the problem is logged.

IV. Pumps On, Low Speed, No Drive

A. Accumulator Pressures

If any pressure is not within the specified range, the antenna is shut down and the problem is logged.

(1) Azimuth low speed
$8.3 \times 10^6 - 13.1 \times 10^6$ N/m^2

(2) Azimuth high speed #1
$6.9 \times 10^6 - 9.3 \times 10^6$ N/m^2

(3) Azimuth high speed #2
$6.9 \times 10^6 - 9.3 \times 10^6$ N/m^2

(4) Elevation system #1
$8.3 \times 10^6 - 21.7 \times 10^6$ N/m^2

(5) Elevation system #2
$8.3 \times 10^6 - 21.7 \times 10^6$ N/m^2

(6) Elevation low speed
$12.4 \times 10^6 - 20.0 \times 10^6$ N/m^2

B. Brakes

If any brake is off, the antenna is shut down and the problem is logged.

V. Pumps On, High Speed, No Drive

A. Accumulator Pressures

If any pressure is not within the specified range, the antenna is shut down and the problem is logged.

(1) Azimuth low speed
$5.5 \times 10^6 - 8.3 \times 10^6$ N/m^2

(2) Azimuth high speed #1
$8.3 \times 10^6 - 15.5 \times 10^6$ N/m^2

(3) Azimuth high speed #2
$8.3 \times 10^6 - 15.5 \times 10^6$ N/m^2

(4) Elevation high speed
$18.6 \times 10^6 - 21.4 \times 10^6$ N/m^2

(5) Elevation system #1
$18.6 \times 10^6 - 21.4 \times 10^6$ N/m^2

(6) Elevation system #2
$18.6 \times 10^6 - 21.4 \times 10^6$ N/m^2

B. Brakes

If any brake is off, the antenna is shut down and the problem is logged.

VI. Low Speed Drive

A. Differential Pressures

If any pressure exceeds the specified limits for longer than 20 seconds, the antenna is shut down and the problem is logged.

(1) Azimuth low speed
5.5×10^6 N/m^2

(2) Elevation low speed
3.8×10^6 N/m^2

B. Brakes

If any brake is set, the drive command voltage is set to zero, the antenna is shut down and the problem is logged.

VII. High Speed Drive

A. Differential Pressures

If any pressure exceeds the specified limits for longer than 20 seconds, the antenna is shut down and the problem is logged.

(1) Azimuth high speed
13.8×10^6 N/m^2

(2) Elevation high speed
12.8×10^6 N/m^2

B. Brakes

If any brake is set, the drive command voltage is set to zero, the antenna is shut down and the problem is logged.

VIII. Comments

The monitor system has been functioning as planned. It has been used since July 1978. It has performed properly in high winds and has correctly reported all malfunctions that it was designed to identify.

N79-25107

Codes for a Priority Queue on a Parallel Data Bus

D. E. Wallis and H. Taylor
Communications Systems Research Section

The article describes some codes for arbitration of priorities among subsystem computers or peripheral device controllers connected to a parallel data bus. At arbitration time, several subsystems present wire-OR, parallel code words to the bus, and the central computer can not only identify the subsystem of highest priority, but can also determine which of two or more transmission services the subsystem requires. The article contains a mathematical discussion of the optimality of the codes with regard to the number of subsystems that may participate in the scheme for a given number of wires, and also the number of services that each subsystem may request.

I. Introduction

This article describes some codes for arbitration of priorities among subsystem computers or peripheral device controllers connected to a parallel data bus. At arbitration time, several subsystems present wire-OR, parallel code words to the bus, and the central computer can not only identify the subsystem of highest priority, but can also determine which of two or more transmission services the subsystem requires. This article contains a mathematical discussion of the optimality of the codes with regard to the number of subsystems that may participate in the scheme for a given number of wires, and also the number of services that each subsystem may request.

II. Mathematical Discussion

Consider m users strung out along a bundle of n wires, along which they send one of three demands each, to a central terminal. User i can demand action A_i, action B_i, or no action. Each individual wire carries one bit of information (0 or 1) to the central terminal, namely, *no user's signal* is on that wire or *some user's signals* are on that wire.

By way of coding we can design a black box for user i, with buttons A_i and B_i causing two preselected choices of signals for the bundle of wires. Pushing neither button will contribute the Boolean zero; pushing A_i will send one Boolean word of n bits (not all 0); pushing B_i will send another; pushing both A_i and B_i at once will be prevented by a mechanical contrivance inside the black box.

When the system is operating the central terminal is supposed to be able to "understand" every possible message it gets on the bundle of wires. Whatever Boolean word it gets it must identify the user of top priority in that word, as well as the demand of that user.

The example in Fig. 1 has users 1, 2, 3 on a bundle of four wires. Each wire is represented by a column in the figure. For each "button" there is a row representing the Boolean word of four bits that button will contribute. Thus, if user 3 pushes button B_3, user 2 pushes button A_2, and user 1 pushes button B_1, then the word at central will be $w_1w_2w_3w_4 = 0111$, and central will know that the top priority user 3 is "on" and specifically demanding B_3.

To show that the system always works we need an algorithm to analyze any Boolean word $w_1w_2w_3w_4$ which

might appear at the central terminal. One such algorithm is pictured by the decision tree in Fig. 2.

Now more generally we can try for the most efficient priority queue (PQ) on n wires. In the example of Fig. 1 we could handle one more user of higher priority than the others, allowing him just one button. The scheme in Fig. 3 shows a way of putting n users on n wires, giving two buttons each to all the lower priority users and one button to the top priority user.

A clearly defined combinatorial problem arises from the example scheme of Fig. 3. Under the given conditions, could any of the users be given more buttons? Arthur Rubin has given a proof that the answer is "no." Thus the optimality of the scheme in Fig. 3 has been proven.

Here is proof (due to Lloyd Welch) that if there are n users, then there must be at least n wires, and the top priority user can be given only one button.

We assume, of course, that each user has at least one button, and say that the users are $1,2,\cdots,n$ with n having top priority. Consider the following sequence of possibilities.

(1) User 1 (lowest priority) pushes one of his buttons. For central to know it there must be at least one wire - let's call it p_1.

(2) User 1 is on p_1 and user 2 pushes one of user 2's buttons. There must be another wire p_2 just to tell that (higher priority) user 2 is demanding something.

(n) User 1 is on p_1, user 2 is on $p_2,\cdots$, user n-1 is on p_{n-1}, and user n pushes one of his buttons. As in each previous case, there must be another wire p_n different from the wires $p_1,\cdots,p_{n-1}$ just to tell central that user n is demanding something.

Finally, the top priority user cannot be given a second button because that would require yet another wire different from $p_1,\cdots,p_{n-1}$ and different from p_n.

III. Application

The PQ has been used as an arbitration code for parallel arbitration of data-transmission priority among multiple users (subsystem computers) of an optimized, 24-line, bi-directional, digital data I/O and control bus connected to a central computer.

On this bus, it was desired to time-share the data transmissions and the priority arbitrations on the same wires. The purpose of the arbitration by the central computer was to identify, from among many subsystems having simultaneous pending requests for data transmission, that particular subsystem whose priority was the highest at that instant. Further, the scenario for use of the data bus identified two actions (or services) that each subsystem could request:

(1) Data input (subsystem has read and unloaded its data-input register, and is ready for next input).

(2) Data output (subsystem has written and loaded its data-output register, and is ready to output).

It was then desired to *vector* these requests to the central computer, so that the central computer would not have to make any further tests to determine the direction (input or output) of the desired data transmission. It was evident that economy of wire usage would require the subsystem computer to determine, for itself, which direction of transmission was the more important at a given instant. Then, the subsystem would make an interrupt request, and would drive the bus at arbitration time with a parallel code word, the receipt of which at the computer would be sufficient both to identify the subsystem and to identify the desired direction of transmission.

In the bus design, it was desired to arbitrate priorities in a manner which was independent of the relative positions of the various subsystem computers, and the central computer itself, along the bus, i.e., independent of the *electrical closeness* of the subsystems to the central computer. Thus, the parallel, wire-OR connection for driving the arbitration code words onto the bus was adopted. It then became evident that it would be desirable to maximize the number of users that could arbitrate simultaneously on a fixed number of available wires. Thus, the combinatorial study of the various possibilities and their degree of optimality was undertaken.

IV. Conclusion

The number of wires in the data bus is becoming a major cost factor in computer and signalling systems, and it is highly desirable to maximize wire utilization. When parallel arbitration of transmission priorities is used, as for example on the Mod Comp[1] computers of the DSN, more arbitration information can be carried on the wires than is presently transmitted. With 16 data lines and one "request" line, the Mod Comp presently arbitrates 17 priorities, with (in the terminology of this article) one demand per priority. The scheme discussed here, when applied to the same case (where one wire of the 17 is a "request"), also permits 17 priorities, while also affording *two* demands to 15 of these priorities.

[1] "Mod Comp" is a registered service mark of Modular Computer Systems, Inc., Ft. Lauderdale, Florida.

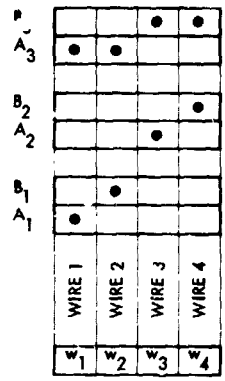

Fig. 1. Example of priority code on four wires with three users and two actions per user

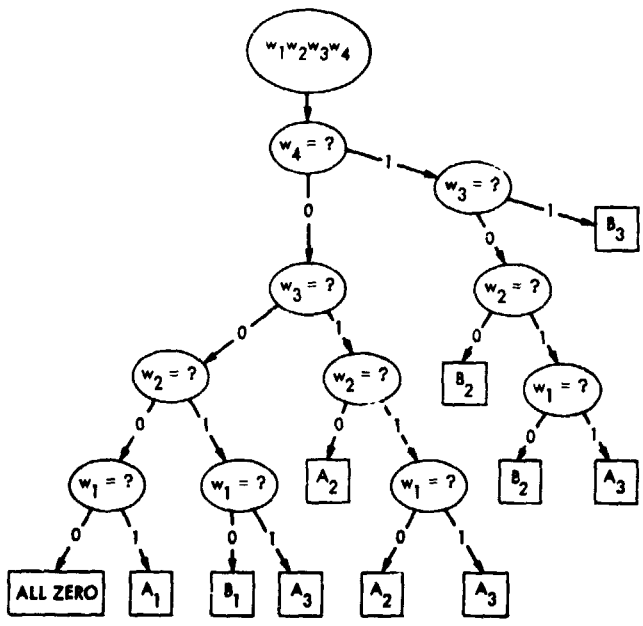

Fig. 2 Decision tree for decoding the example code given in Fig. 1.

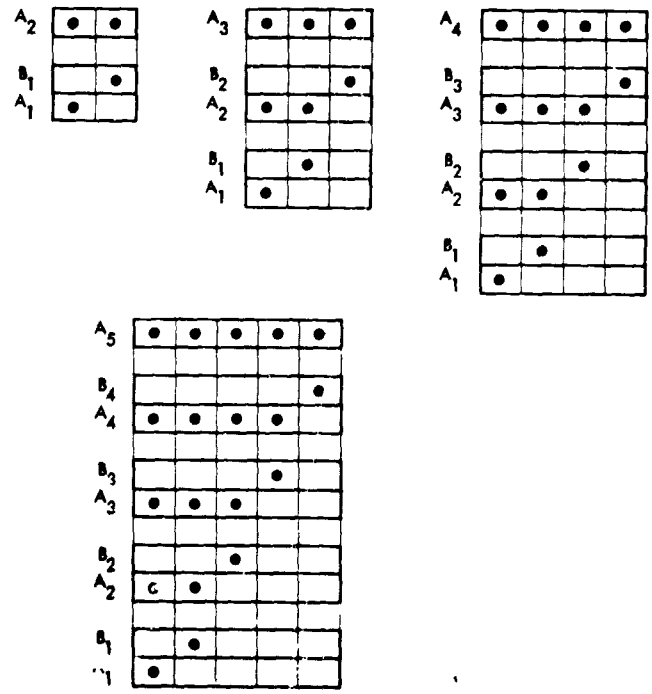

Fig. 3. Efficient priority codes that maximize the number of users on n wires, n = 2, 3, 4, 5

ORIGINAL PAGE IS
OF POOR QUALITY

N79-25108

Mathematical Model for Preventive Maintenance Scheduling

G. Lorden
California Institute of Technology

D. S. Remer
Communications Systems Research Section and Harvey Mudd College

A model is formulated to describe the effect of the time interval chosen for preventive maintenance upon the frequency of failure and frequency of total maintenance (preventive and corrective). Trade-offs between these two frequencies are determined by computation of an optimal interval in the case where the failure distribution is known. For unknown distributions, an adaptive statistical technique is developed that converges to an optimal preventive maintenance interval. A numerical illustration is given.

I. Introduction

The proper goal of a preventive maintenance policy is to improve the availability and reliability of equipment. Such a policy is likely to be cost-effective, however, only if it is designed to take into account and to control the overall cost of corrective and preventive maintenance. DSN experience shows that preventive maintenance is a substantial component of cost (Ref. 1). This article is intended as a first step in the development of effective methods for reducing preventive maintenance costs by performing such maintenance only where and when it is most effective.

The basis for the method studied in this article is a probabilistic model of successive maintenance cycles. Each cycle ends with the performance of preventive maintenance at a scheduled time, or, if failure occurs earlier, with corrective maintenance. Whichever way a cycle ends, the successive cycles are assumed to be generated by independent trials of some failure distribution. The broad class of failure distributions considered allows for the possibility of higher failure rate early in the cycle, e.g., occasional bad effects resulting from maintenance activity.

After formulation of the model and derivation of necessary formulas in Section II, it is determined in Theorem 2 of Section III how to make optimal tradeoffs between the frequency of failure and frequency of maintenance (preventive and corrective combined) by choosing the right time interval for preventive maintenance based on a known failure distribution. Section IV considers a statistical technique for the case of unknown failure distribution. This technique modifies the choice of intervals for preventive maintenance as experience accumulates. The sequence of choices converges in probability to the optimum, as shown in Theorem 3. A numerical example illustrating the required computations is given in Section V. Additional remarks, including possibilities for further investigation, comprise Section VI.

II. The Model

Consider a fixed type of reparable equipment whose times between failures $T_1, T_2, \cdots$ are independent with distribution function F. Assume that F has a continuous density f, and let h be the failure rate function, $f/\bar{F}$, where $\bar{F} = 1 - F$. Thus, $h(t)$ represents the rate of failures in the interval between t and $t + dt$. Suppose that a time interval $m > 0$ is chosen for preventive maintenance. Then if a time m has elapsed since the last failure, preventive maintenance is performed. It will be assumed throughout that preventive maintenance, as well as corrective maintenance, restores the equipment to the condition where its time to next failure has distribution function F.

Theorem 1:

If $m > 0$ is the preventive maintenance interval, then

$$\text{frequency of failure} = \frac{F(m)}{\int_0^m \bar{F}}$$

and

$$\text{frequency of maintenance} = \frac{1}{\int_0^m \bar{F}}$$

the latter including both preventive and corrective maintenance.

Proof:

If $T_1, T_2, \cdots$ are the successive times between failures in the absence of preventive maintenance, then $X_1 = \min(m, T_1)$, $X_2 = \min(m, T_2), \cdots$ are the times between maintenances, and they are independent and identically distributed. Let N be the number of X's until the first failure, i.e., the first time $X_n = T_n$. Since N is distributed like the number of independent flips required to get the first "Heads," where $P(\text{Heads}) = P(T \leq m) = F(m)$, $EN = 1/F(m)$. Let $S_n = X_1 + \cdots + X_n$, $n \geq 1$, and note that the time of first failure is $S_N = X_1 + \cdots + X_N$, after which the whole process repeats itself. Since $ES_N = EN \cdot EX_1$ by Wald's equation for randomly stopped sums, the frequency of failure is

$$\frac{1}{ES_N} = \frac{1}{EN \cdot EX_1} = \frac{F(m)}{EX_1} = \frac{F(m)}{\int_0^m P(X_1 > t)\,dt} = \frac{F(m)}{\int_0^m \bar{F}}$$

Similarly, the frequency of maintenance is $1/EX_1$, which is given by the formula stated in the theorem, and the proof is complete.

III. Optimal Preventive Maintenance for Known F

Suppose that it is desired to choose a maintenance interval $m > 0$ to minimize

$R(m)$ = Frequency of failures + c · frequency of maintenances

$$= \frac{F(m) + c}{\int_0^m \bar{F}}$$

where $c \geq 0$ is chosen in advance. The choice of c determines the tradeoff between the two frequencies. If the choices made for different types of equipment are proportional to the relative costs of maintaining them, then the total spent on maintenance is distributed optimally – that is, minimizes the total failure rate of all equipment types. This is analogous to the determination of optimal allocations of spares to different types of equipment (Ref. 2).

This section considers the case where the failure distribution, F, is known and, hence, also f and h. Though not very practical, it is an instructive case to consider, and the results obtained provide a foundation for the more realistic formulation in the next section.

Theorem 2:

Assume that the failure rate function, h, is continuous and positive on $(0, \infty)$ and is "peak-free," i.e., is either monotonic or else, for some $d > 0$, is nonincreasing on $(0, d)$ and nondecreasing on $[d, \infty)$. Then the limit of h at $+\infty$, $h(\infty)$, exists (possibly infinite) and

(1) If $c \geq h(\infty)\,ET - 1$, then $R(m)$ is nonincreasing and bounded below by its limit at $+\infty$, $(1 + c)/ET$, which is attainable by choosi $m = +\infty$, whereas

(2) If $c < h(\infty)\,ET - 1$, .. the solutions of $R(m) = h(m)$ are an interval $[m_1, m_2]$ (possibly $m_1 = m_2$) such that $R(m)$ is decreasing on $(0, m_1)$, constant on $[m_1, m_2]$, and increasing on $[m_2, \infty)$.

Proof:

The limit $h(\infty)$ exists since h is either nonincreasing or else is eventually nondecreasing. By routine calculation,

$$R'(m) = \frac{Q(m)}{\bar{F}(m)\left(\int_0^m \bar{F}\right)^2} \qquad (1)$$

where

$$Q(m) = h(m)\int_0^a F - |F(m) + c| \qquad (2)$$

and

$$Q(b) - Q(a) = |h(b) - h(a)|\int_0^a \bar{F} + \int_a^b |h(b) - h|\,\bar{F} \qquad (3)$$

It is clear from Eq. (3) that $h(t) \geq h(b)$ for all $t < b$ implies that $Q(t) \geq Q(b)$ also. Hence, Q is nonincreasing on any interval $(0, d)$ where h is. Also, if $h(b) \geq h(a)$, then $Q(b) \geq Q(a)$ and, hence, Q is nondecreasing wherever h is. Thus, Q is peak-free like h and by (2) is also continuous. Since $R(m) \to +\infty$ as $m \downarrow 0$, $R'(m) < 0$ for arbitrarily small positive m and by Eq. (1), therefore, $Q(m) < 0$ for arbitrarily small positive m. Since a peak-free function cannot assume a sequence of values negative-to-positive-to-nonpositive, evidently either Q is never positive or else it is negative on some interval $(0, m_1)$, zero on $[m_1, m_2]$, and positive (as well as nondecreasing) on (m_2, ∞). These two cases occur respectively, as $Q(\infty) = h(\infty)ET - (1 + c)$ is ≤ 0 or > 0. Since, by (1), R' and Q have the same sign, the conclusions about $R(m)$ in the two cases follow immediately and the proof is complete upon noting that, by Eq. (2), $Q(m) = 0$ is equivalent to $R(m) = h(m)$.

Note that if h is differentiable, then

$$Q'(m) = h'(m)\int_0^m \bar{F},$$

and Newton's method can be applied to solve $Q(m) = 0$ numerically.

IV. An Approach to the Optimal m When F is Unknown

Under the assumptions of the preceding sections, we will now show how to choose successive maintenance intervals M_1, $M_2, \cdots$, based on accumulating experience, so that $\{M_n\}$ converges to the optimal interval $[m_1, m_2]$ in probability. The choice of M_{n+1} is based on the observations $Y_1, Y_2, \cdots, Y_n$, where $Y_i = \min(M_i, T_i)$ are the successive times between maintenances, and the choice also takes into account which of the Y_i's are failures (i.e., $T_i \leq M_i$). The method is based upon estimating the "survival function," $\bar{F}(x)$, at every stage by the Kaplan-Meier (ref. 3) Product Limit Estimate (PLE)

$$K(x) = \prod_{t_k < x} \frac{\text{no. of observations surviving } t_k}{\text{no. of observations reaching } t_k}$$

where the t_k's are the points at which failures have been observed. Here the "number of observations reaching t_k" is just the number of Y's $\geq t_k$, while the "number of observations surviving t_k" is the same number minus the number of observed failures at t_k. It is convenient to modify the definition of $K(x)$ by stipulating that $K(x) = 0$ for $x >$ largest observation (failure or not). Note that $K(0) = 1$ and K is a step function with downward jumps at the points where failures have been observed, falling to 0 after the largest observation. It is well-known that $K(x)$ is a consistent estimator of $\bar{F}(x)$ (Ref. 1), i.e., if $K_n(x)$ denotes the estimate after n cycles, $Y_1, \cdots, Y_n$, then

$$K_n(x) \to \bar{F}(x) \text{ with probability one as } n \to \infty$$

for x such that $M_n > x$ for infinitely many n. In fact, this convergence is uniform for such x because the functions $K_n(x)$ are bounded and nonincreasing.

A recipe for choosing $M_1, M_2, \cdots$ can be given as follows. Let $R_n(\cdot)$ denote the estimate of the function $R(\cdot)$ obtained by using $K_n(x)$ in place of $\bar{F}(x)$ in the definition of R (note that $1 - K_n$ replaces F). Then let $M_1 = +\infty$ and for $n \geq 1$,

(1) Let M_n^* denote the value of m minimizing $R_n(m)$.

(2) Choose $M_{n+1} = M_n^*$ with probability $1 - 1/n$
$= +\infty$ with probability $1/n$.

Step (1) is computationally feasible since the numerator of $R_n(m)$ is constant for m between successive failure times, t_k, whereas the denominator increases, and it is easy to verify that the minimum of $R_n(m)$ is attained either at one of the failure times, t_k, or at the largest observation (failure or not). (Note also that the integral in the denominator of $R_n(m)$ is easily calculated since the integrand is K_n, a step function.) The randomization device used in step (2) provides a means of increasing M_n from time to time to gain information about possible m's larger than the ones used so far.

For the scheme of choosing $\{M_n\}$ just described, we obtain the following result:

Theorem 3:

If $b < m_1$, $a > m_2$, then $\lim_{n\to\infty} P(M_n < b) = 0$, $\lim_{n\to\infty} P(M_n > a) = 0$, and $\lim_{n\to\infty} P[R(M_n) > R(m_1) + \epsilon] = 0$ for $\epsilon > 0$.

Proof:

Since $P(M_n^* \neq M_n) = 1/n \to 0$, it suffices to prove all three conclusions with M_n^* in place of M_n. To prove the first conclusion for M_n^*, it suffices to show that for $b < m_1$, with probability one, all but finitely many M_n^*'s are $\geq b$.

Now, since

$$\sum_n P(M_n^* \neq M_n)$$

diverges, infinitely many M_n's equal $+\infty$, and, hence, $R_n(m) \to R(m)$ uniformly on $(0, b+1]$.

Also, for all $m \leq b$, $R(m) \geq R(b) > R(\min(b+1, m_1))$, so that, for sufficiently large n, by the uniform convergence,

$$R_n(m) > R_n(\min(b+1, m_1)) \text{ for all } m \leq b$$

which implies that $M_n^* > b$. Thus, only finitely many M_n^* are less than b, and the first limit in Theorem 3 is proved.

The second limit is shown to be zero by a similar argument. The third limit is zero since by Theorem 2 $R(m) > R(m_1) + \epsilon$ only if $m < b$ or $m > a$ for some $b < m_1$ or $a > m_2$.

V. A Numerical Example

To illustrate the computations needed for the method of the preceding section, suppose that successive cycles of lengths (in days) 47, 26, 26, 19, 27, 16, 18, 20, 20, 35 are observed, where the underlinings denote failures. Assume that $c = 0.5$. The necessary computations are shown in Table 1, and K and the estimated R are graphed in Figs. 1 and 2. Note that the computations only need to be performed at time points where failures occurred and at the largest observation (failure or not). The minimum $R(t)$ is at the largest observation, 47. Thus, $M_{10}^* = 47$ and this value would be chosen as the preventive maintenance time for the next cycle, unless the randomization produced $M_{11} = +\infty$ (the probability of this being 0.1), in which case there would be no preventive maintenance in the next cycle, and the cycle would end at the next failure. At the end of the next cycle, new computations of the entries in Table 1 would be required. If the cycle ended at 17, for example, the "16" column would be unchanged, but the "19" and "26" columns would be recomputed. Also, if the cycle ended with a failure (at a new t-value), then a new column would be inserted for that t-value.

This updating of the columns after each cycle is not difficult because $\Lambda(t)$ is obtained by multiplying the value in the preceding column by a fraction, and the integral of $K(x)$ up to t is obtainable by adding the area of a rectangle to the integral in the preceding column.

VI. Additional Remarks

In practice, the situation is usually slightly more complicated than that described in the preceding section, because one has several pieces of the same type of equipment and simultaneously must set M_n's and accumulate experience from all of them. It is not hard to modify the recipe, however, to deal with this situation. One can simply recalculate $\Lambda(\cdot)$ after each observation (on any of the pieces) and calculate the next M_n desired. If one or more pieces have already exceeded an elapsed time of M_n since their last maintenance, then perform preventive maintenance on them. Thus, one sometimes observes longer cycles than the recipe would call for, but there is no significant change needed in the proof of Theorem 3 or in the carrying out of the recipe.

It is interesting and perhaps useful to try to relax the assumption that preventive maintenance restores the equipment to its original failure distribution, F - say, to allow a separate contribution to the failure rate depending upon the age of the equipment. It is straightforward to modify the "known F" analysis of Section 2 to accommodate this sort of extension — even if the age-contribution is unknown (since it is unaffected by the choice of m and, hence, acts merely as a sort of "background radiation" of failures). The extension in the "unknown F" case, however, seems more difficult. It is perhaps helpful to assume that the age-dependent failure rate is known.

Another promising approach to the determination of preventive maintenance strategies is the use of measurements of "indicator variables" reflecting the need for preventive maintenance. These variables might be levels of contamination, pressure, vibration, etc., or various measures of performance like the rate of random errors. By measuring such variables, one can expect to anticipate failures that could be prevented (or, at least, postponed) by timely maintenance.

References

1. Remer, D. S., and Lorden, G., "Initial Economic and Operations Data Base for DSS-13 Automation Test, *DSN Progress Report 42-49*, Jet Propulsion Laboratory, Pasadena, Calif.

2. I. Eisenberger and Lorden, G., "Dynamic Spares Provisioning for the DSN," *DSN Progress Report 42-42*, Jet Propulsion Laboratory, Pasadena, Calif.

3. Kaplan, E. L., and Meier, P., "Nonparametric Estimation from Incomplete Observations," *J. Amer. Statist. Assoc.*, 53, p. 457-481, 1958.

Table 1. Computational results for illustration

Value of t	16	19	26	47
No. reaching t	10	8	5	1
N[illegible]-viving t	9	7	4	1
K[illegible]	1	0.9	0.788	0.63
[illegible] dx	16	18.7	24.21	37.44
estimated $R(t)$	0.0313	0.0321	0.0294	0.0232

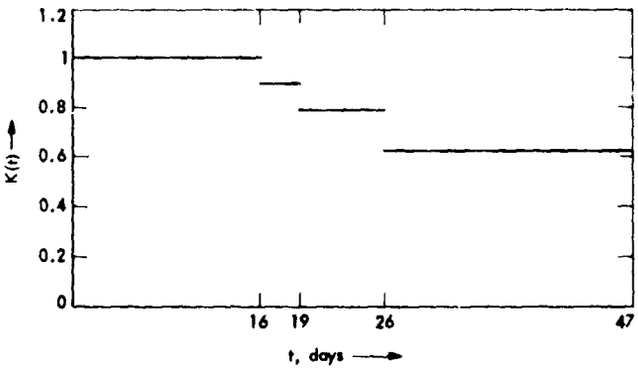

Fig. 1. $K(t)$

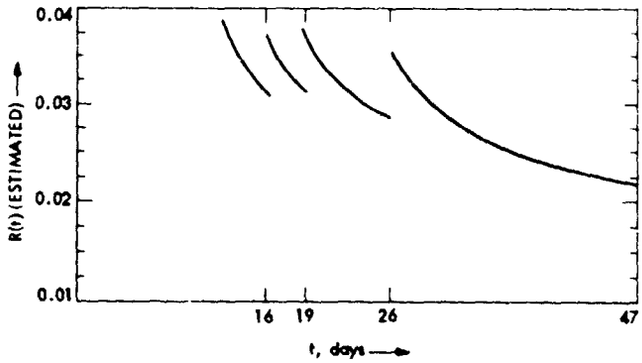

Fig. 2. Estimated $R(t)$

ORIGINAL PAGE IS
OF POOR QUALITY

N79-25109

Preliminary Maintenance Experience for DSS 13 Unattended Operations Demonstration

D. S. Remer
Communications Systems Research Section
and Harvey Mudd College

G. Lorden
California Institute of Technology

This article summarizes the maintenance data base collected for 15 weeks of recent unattended and automated operation of DSS 13. During this period, DSS 13 has been receiving spacecraft telemetry while being controlled remotely from JPL in Pasadena. Corrective and preventive maintenance manhours are reported by subsystem for DSS 13 including the equipment added for the automation demonstration. The corrective and preventive maintenance weekly manhours at DSS 13 averaged 22 and 40, respectively. The antenna hydraulic and electronic systems accounted for about half of the preventive and corrective maintenance manhours. A comparison is presented for overall preventive and corrective maintenance manhours for a comparable attended DSN station, DSS 11.

I. Introduction

The tracking time now available to the end user at a Deep Space Station is reduced by time spent for maintenance, operator training, checkout and calibration. The efficiency of the DSN would be greatly increased if the time for these other functions were decreased. Also, the reliability of the DSN may be increased by reducing the load on operations personnel.

As a result of these potential improvements in DSN efficiency and reliability, a research program was started several years ago at DSS 13. The station has now been automated and is being operated in an unattended mode for spacecraft telemetry reception. Data are now being collected to evaluate this operation.

This article will present the preliminary maintenance experience at DSS 13 for unattended, automated operation. Both corrective and preventive maintenance are considered, and where possible, comparisons are made to a manned operation at DSS 11. Before this maintenance data is presented, the automated system and its capability will be described.

II. DSS 13 Description — Automated Station

DSS 13 is a 26-meter station at Goldstone, California. Central control and monitor for this station are done from JPL in Pasadena by an operator at NOCC. This automated and remote operation only for spacecraft telemetry reception was implemented in 1978. The operator enters configurational

control and predicts. Monitor data are also available to him. The station is (1) powered up, (2) checked out, (3) spacecraft telemetry is acquired and tracked, and, (4) the station is shutdown, all remotely from Pasadena without an operator at the station. There is automatic antenna shutdown capability in case of high winds or certain servo drive failures.

The telemetry stream from DSS 13 is sent to DSS 11 for bit detection and then via high speed data lines to the flight project at JPL. Work is underway so bit detection can be done at DSS 13.

The DSS 13 unattended operations design uses microprocessors or minicomputers on each controlled subsystem for (1) configurational control, (2) monitoring, (3) operation, and (4) checkout.

A central station microprocessor is used for supervision of subsystem monitor and control processors. The antenna, microwave, and receiver subsystems are now under centralized control. Only downlink capability is now available; however, uplink capability will be implemented in 1979. The 100-kilowatt S-band transmitter and exciter subsystem will be added during 1979. While DSS 13 has been in the unattended mode, telemetry data has been provided to the Voyager, Pioneers 10 and 11, and Helios projects.

The following section will describe the maintenance experience during this initial remote unattended operation of DSS 13.

III. DSS 13 Maintenance Data Base

The maintenance data base for DSS 13 operation under remote, automated operation from NOCC in Pasadena is shown in Tables 1 and 2. These data are for the 15-week period of June 18, 1978 through September 24, 1978. The data are summarized in weekly increments. Corrective maintenance is shown in Table 1 and preventive maintenance in Table 2. The maintenance data are broken down by subsystem. An asterisk next to the DSS 13 subsystem means that this equipment has been added for this demonstration.

IV. Discussion of Results

A. DSS 13 Corrective Maintenance

The corrective maintenance at DSS 13 averaged 22.2 manhours per week with a standard deviation of 12.8 during this period. Shown below is the percent of corrective maintenance manhours for each subsystem.

Subsystem	Corrective maintenance manhours %
Antenna electronic systems	38.1
Block III SDA	17.1
Antenna hydraulic systems	10.6
108 kHz subcarrier oscillator microwave link transmission	9.5
Antenna terminet	7.7
Antenna clock	6.1
Block III receiver	4.7
High-speed data line microwave link channel	3.0
Antenna control computer (MOD COMP II/25)	2.6
Maser compressor	0.6
	100.0

The antenna electronic and hydraulic systems and the Block III SDA account for over half of the corrective maintenance manhours. Note that in Table 1 about half of the subsystems, such as the maser refrigerator, required no corrective maintenance.

B. DSS 13 Preventive Maintenance

The preventive maintenance at DSS 13 averaged 39.5 manhours per week with a standard deviation of 14.8. Shown below is the percent of preventive maintenance manhours for each subsystem.

Subsystem	Preventive maintenance manhours %
Antenna hydraulic systems	43.9
Antenna electronic system	15.3
Maser compressor	11.1
Block III receiver	8.8
Block III SDA	6.5
108 kHz subcarrier oscillator	5.1
Antenna control computer (MOD COMP II/25)	4.5
Maser refrigerator	3.8
Station controller (8080 based microcomputer)	0.7
High speed data line microwave link channel	0.3
	100.0

The antenna hydraulic and electronic systems account for over half of the preventive maintenance manhours. About half of the subsystems received no preventive maintenance during this period, as shown in Table 2.

C. Comparison of DSS 13 Corrective and Preventive Maintenance

Several key subsystems had vastly different percentages of corrective and preventive maintenance as shown below.

Subsystem	Percent of total corrective maintenance %	Percent of total preventive maintenance %
Antenna electronic system	38.1	15.3
Block III SDA	17.1	6.5
Antenna hydraulic system	10.6	43.9

For example, while the antenna electronic system accounted for 38.1% of the total corrective maintenance manhours, this system only received 15.3% of the total preventive maintenance manhours. The same relationship was true for the Block III SDA. On the other hand, the antenna hydraulic system received 43.9% of the total preventive maintenance manhours and only 10.6% of the corrective maintenance manhours. These results indicate that perhaps there could be a shift in preventive maintenance to reflect corrective maintenance experience in order to optimize the overall maintenance effort.

D. Maintenance for the Traditional Subsystems Versus the Subsystems Added for This Demonstration

The subsystems added for this demonstration are shown by asterisks in Tables 1 and 2. The percent of preventive and corrective maintenance for these subsystems is shown below.

Subsystem	Preventive maintenance %	Corrective maintenance %
Subsystems added for this demonstration	10.6	28.9
Traditional subsystems	89.4	71.1
	100.0	100.0

The subsystems added for this demonstration required about 29% of the corrective maintenance and received only 11% of the preventive maintenance. Note that some of the "traditional" subsystems were automated for this demonstration, such as the antenna electronic and hydraulic systems.

E. Comparison of Maintenance at DSS 11 with DSS 13

The average weekly maintenance manhours for DSS 11 and DSS 13 are shown below.

Maintenance	Average weekly manhours DSS 11	DSS 13
Corrective maintenance	153.5	22.2
Preventive maintenance	56.4	39.5
	209.9	61.7

The DSS 11 data is from Ref. 1 for the period May 14 through July 9, 1978. Both the corrective and preventive maintenance manhours at DSS 11 are more than at DSS 13. However, DSS 11 has more equipment than DSS 13. For example, DSS 11 has two receivers, two SDA's, two masers, etc., whereas DSS 13 has only one of each. Shown below is the average weekly maintenance manhours for "comparable" systems at DSS 11 and DSS 13.

Maintenance	Average weekly manhours For "comparable" systems DSS 11	DSS 13
Corrective maintenance	153.5	27.2
Preventive maintenance	56.4	51.4
	209.9	78.6[a]

[a](37.5% of 209.9)

In this comparison, we made the conservative assumption that if DSS 13 had had two SDA's, for example, then the preventive and corrective maintenance for SDA's would have been doubled at DSS 13. In actual practice, this factor should be somewhere between one and two. However, even with this conservative assumption, the corrective maintenance at DSS 13 only increased by 22.4% and the preventive maintenance by 30.2% in order to correct for the redundant systems at DSS 11. For comparable systems, we see in the above table that the preventive maintenance manhours are about the same at both stations but the corrective maintenance manhours are much higher at DSS 11.

Another interesting result is that at DSS 11 about three-fourths of the actual maintenance manhours are for corrective maintenance, whereas at DSS 13, about three-fourths of the

actual maintenance manhours are for preventive maintenance, as shown below.

The data suggests that unattended operation may reduce maintenance manhours. There are other factors, however, that may be responsible for the differences between the two stations in total maintenance manhours and the breakdown between preventive and corrective maintenance. For example, DSS 13 has substantially different equipment, schedule of operations, performance verification requirements, and type of personnel than DSS 11.

Maintenance	DSS 11 %	DSS 13 %
Corrective maintenance manhours	73	26
Preventive maintenance manhours	27	74
Total maintenance manhours	100	100

Acknowledgement

We wish to thank Earl Jackson for supplying the DSS 11 and DSS 13 data and for providing insight into station operation.

Reference

1. Remer, D. S., and Lorden, G. "Initial Economic and Operations Data Base for DSS 13 Automation Test," *DSN Progress Report 42-49*, Jet Propulsion Laboratory, Pasadena, Calif. pp. 78-85.

Table 1. DSS 13 corrective maintenance activities in manhours, 1978

	6/18	6/25	7/2	7/9	7/16	7/23	7/30	8/6	8/13	8/20	8/27	9/3	9/10	9/17	9/24	Total	
Corrective Maintenance																	
26-m antenna																	
Hydraulic systems		1.0	0.5		6.0	4.0	13.5	4.0				1.5	5.0			35.5	10.6
Electronic systems	13.0		3.0	4.0	19.5	7.0	42.0	17.0	0.5	6.0		7.0		4.0	4.0	127.0	38.1
*Control computer (MOD COMP II/25)		1.0	2.5	4.0			1.0									8.5	2.6
*Clock		12.0		8.3												20.3	6.1
*Terminet		16.3	1.0										2.0		6.5	25.8	7.7
*Microprocessor																	
Waveguide configuration assembly																	
Low noise amplifier (maser)																	
maser compressor refrigerator										2.0						2.0	0.6
Block III receiver																	
Block III SDA				5.0	7.5						3.0					15.5	4.7
*108 kHz subcarrier oscillator (microwave link transmission)						2.5			18.5	14.0	29.0	6.0	18.5			57.0 31.5	17.1 9.5
*Station controller (8080 based microcomputer)																	
*Star switch controller																	
*SDA controller																	
*Block III receiver controller																	
*Waveguide configuration assembly controller																	
High speed data line																	
*Data set																	
*Microwave link channel										1.5				8.5		10.0	3.0
TOTAL	13.0	30.3	7.0	21.3	33.0	13.5	56.5	21.0	19.0	23.5	32.0	14.5	25.5	12.5	10.5	333.1	100.0

*Equipment added for automation demonstration

Table 2. DSS 13 preventive maintenance activities in manhours, 1978

	6/18	6/25	7/2	7/9	7/16	7/23	7/30	8/6	8/13	8/20	8/27	9/3	9/10	9/17	9/24	Total	%
Preventive Maintenance																	
26-m antenna																	
Hydraulic systems	4.0	6.0	4.0	12.0	19.5	10.0	24.0	15.0	27.5	23.0	29.0	19.5	8.5	52.5	6.0	260.5	43.9
Electronic systems	8.5	14.0	18.5	9.5	3.0	9.0	0.5	10.5	1.0	0.3	7.0		0.5	0.5	8.0	90.8	15.3
*Control computer (MOD COMP II/25)					3.5	6.0					1.5				15.5	26.5	4.5
*Clock																	
*Terminet																	
*Microprocessor																	
Waveguide configuration assembly																	
Low noise amplifier (maser)																	
maser compressor	3.5	26.5	8.5			5.5								12.0	10.0	66.0	11.1
refrigerator	8.0	2.0		5.5			4.0				1.0				2.0	22.5	3.8
Block III receiver	2 .5					2.5	4.0	8.5		1.5	3.0	4.5	1.5			52.0	8.8
Block III SDA		0.5	1.0		0.5	3.0	5.5					9.0	7.0	10.0	2.0	38.5	6.5
108 KHz subcarrier oscillator (microwave link transmission)		2.0	2.0	1.5	2.0		2.5					20.0				30.0	5.1
*Station controller (8080 based microcomputer)															4.0	4.0	0.7
*Star switch controller																	
*SDA controller																	
*Block III receiver controller																	
*Waveguide configuration assembly controller																	
High speed data link																	
*Data Set																	
*Microwave Link Channel								2.0								2.0	0.3
TOTAL	50.5	51.0	34.0	28.5	28.5	36.0	40.5	36.0	28.5	24.8	41.5	53.0	17.5	75.0	47.5	592.8	100.0

*Equipment Added for Automation Demonstration

ORIGINAL PAGE IS
OF POOR QUALITY

LAAS Studies: 26-, 34-, and 40-Meter Elements

W. F. Williams
Radio Frequency and Microwave Subsystems Section

The Large Advanced Antenna Station (LAAS) studies have now included arraying modified 34-meter antennas and new 40-meter antennas. This article discusses the microwave performance expected from these antenna elements when arrayed and fed with the new dual-band coaxial X/S feed. Performance of the 26-meter elements is also discussed for comparison to the new modified antennas.

I. Introduction

The Large Advanced Antenna Station (LAAS) program is an ongoing study to determine a most cost-effective way to obtain a substantial increase in RF performance for a new DSN station, over that presently available with the 64-meter antenna network. Early in this study it was determined that this increase could be provided by a high-grade, 100-meter reflector utilizing specially shaped surfaces and improved feed horns, as well as updated electronic equipment. Later, arrays of smaller antennas were investigated for performing equally to the basic 100-meter unit. Various sizes were considered. These are discussed in Ref. 1. This has led finally to a study of some specific arrays utilizing modified versions of the existing 26-meter antennas of the DSN and STDN, as well as some new antennas.

Subjects to be discussed in this report are the microwave performance of improved 26-meter units, the 34-meter units, which are built by modifying the 26-meter antennas, and 40-meter antennas, which are new.

Improved 26-meter antennas are obtained by relocating the antennas at a common array site and installing new subreflectors more suitable to X-band.

The 34-meter antennas are obtained by expanding these 26-meter antennas to the larger diameter. New surfaces are provided according to special shaping that yields a near-optimum combination illumination and spillover efficiency. The newly developed coaxial X/S horn is used in determining this shaping, and the location of this feed relative to the reflector vertex is held near to that of the present 26-meter antennas so that the present feed cone and feed cone designs can be used. This shaped design is a "best fit" to the 26-meter paraboloids, which minimizes structural changes and suggests that some 26-meter panels might be reused

The new 40-meter shaped antennas are similarly determined, and the existing feed cone design can be used. An alternate 40-meter design is presented that uses a larger coaxial X/S feed, but again the same feed cone. This design permits a larger equivalent focal length to diameter (F/D) ratio that would, perhaps, be more easily constructed.

II. The Antenna Types

A. Relocated 26-Meter Antennas

An example of this antenna is the 26-meter antenna located at DSS 11. These antennas can be used at X-band with the

provision of new subreflectors that are better suited to X-band performance. This subreflector (requiring new tooling) would, relative to the present subreflector, remain at 3-meters diameter, but the outer flange region would be reduced in width and the vertex cone would be smaller.

The radiation pattern of the X-band frequency, X/S horn, was theoretically scattered from this new subreflector design to determine microwave performance. The result is depicted in Fig. 1. The central hole region, ±8 deg from 0 deg, is very noticeable showing the success of the central vertex plate. The calculated efficiencies of this pattern are indicated below:

Forward spillover	0.988
Back spillover	0.998
Illumination	0.832
Cross polarization	0.997
Phase	0.968
Central blockage	0.990
Total RF efficiency	0.784

A dual-hybrid mode corrugated horn has been developed for enhancement of performance at DSS 14. This horn has a pattern shape that results in a higher illumination efficiency when using the standard paraboloid-hyperboloid cassegrain system. The radiation pattern of this horn was also theoretically scattered from the new subreflector with the result shown in Fig. 2. The more uniform illumination function can be noted here when compared to Fig. 1. Below are tabulated the efficiency numbers:

Forward spillover	0.961
Back spillover	0.997
Illumination	0.889
Cross-polarization	0.998
Phase	0.961
Central blockage	0.990
Total RF efficiency	0.809

This represents an improvement of over 2 percent. Although the illumination efficiency improves by over 5 percent, much of this is lost in additional spillover from the sidelobes of the dual-hybrid mode horn. It should be pointed out that in trials using the special shape type of surface, all illumination efficiencies became very good and the dual-hybrid mode offers no particular advantage. To complete this picture, the standard 22-dB gain horn pattern (X-band) was also scattered from the new subreflector. The results below:

Forward spillover	0.960
Back spillover	0.997
Illumination	0.836
Cross polarization	0.997
Phase	0.954
Central blockage	0.990
Total RF efficiency	0.753

This again shows the improvement to be obtained using the dual-hybrid mode horn.

B. 34-Meter and 40-Meter Performance, Special Shapes

The X-band pattern of the new X/S feed horn is used to determine the special shapes for both the modified 34-meter antenna and the new proposed 40-meter antennas. Resulting shapes are similar and the final scattering is similar. Figure 3 depicts the solution for the 40-meter dish. Note that in holding the feed focus at 5.18-meters from dish vertex and using the 17-deg X/S feed, the equivalent F/D has become 0.3, i.e., a very deep dish.

When the X-band pattern is theoretically scattered from the 34-meter and 40-meter shaped subreflectors, the following results:

	34-meter	40-meter
Forward spillover	0.992	0.992
Back spillover	0.996	0.997
Illumination	0.983	0.987
Cross polarization	0.999	0.999
Phase	0.994	0.998
Central blockage	0.985	0.986
Total RF efficiency	0.950	0.960

It should be noted that a slight advantage accrues to the larger antenna. Figure 4 depicts the scattering from the 40-meter antenna subreflector.

When the dual-hybrid mode horn is used for shaping determination, the final reflector is more closely a paraboloid. However, illumination efficiency is no better than the above cases, and forward spillover is worse, with a final result that is 1.5 percent below the 34-meter unit.

C. Using a Larger X/S Horn

It is, of course, possible to use the X/S horn gain-limited technique with different horn flare angles and consequently different illumination angles for the subreflector. For instance, if a narrower flare angle is used with this gain-limited technique, then the beams will be narrower also.

A 14-deg half flare angle horn (instead of a 17.1-deg horn) was chosen to use in a sample shaped antenna design of 40-meter diameter. The constraint was that the feed horn focus have the same location from dish vertex as the other designs, about 5.18-meters, allowing the same feed cone use. The result of this design was an increase in the equivalent F/D from 0.3 to 0.35, which is perhaps mechanically desirable. Further increases in horn size would permit F/D to approach 0.4. Of course, if greater feed location displacements from dish vertex are allowed, then larger F/D values are possible without the larger horns.

The RF efficiency of this configuration was essentially the same as the other 40-meter design, about 96 percent.

III. Other Factors

Surface tolerance efficiency follows the formula of Ruze Ref. 2:

$$\text{surface efficiency} = e^{-\left(\frac{4\pi\epsilon}{\lambda}\right)^2}$$

with ϵ equal to the rms variations of the surface from its prescribed values. The rms variations for the 26-meter antennas are about 1.5 mm, and this results in a surface efficiency of 0.757 for these antennas. The 34-meter modifications would, as discussed above, include mostly new specially shaped reflector sections mounted on the old existing structure. The mechanical design estimates for the rms of this modification are about 1.25 mm. This results in a surface tolerance efficiency for the 34-meter antennas of 0.824. Potential suppliers of new 40-meter antennas have indicated an rms estimate of 0.9 mm, or surface efficiency of 0.903.

The spars or subreflector support legs block or interfere with the aperture distribution. This "spar blockage" efficiency is directly proportional to the percentage area being blocked. It is not quite so simple though, because the spars may be small enough to discount a geometric optics view altogether. Also, because of the real aperture distribution being somewhat greater in the central region, spar shadowing in this central region becomes more important. These factors and past experience leads us to a modification of the spar blockage efficiency rule, as follows

$$\text{spar blockage efficiency} = \left(1 - 1.2\,\frac{A_b}{A_o}\right)^2$$

with A_b the subreflector blocked area and A_o the main reflector aperture area.

Spar area blockage on the 26-meter antennas is about 6 percent, resulting in blockage efficiency of 0.861. For the modified 34-meter antennas, a value of 4.5 percent is expected, for a blockage efficiency of 0.895. An estimate for the larger 40-meter antenna is 5 percent for a blockage efficiency of 0.884.

These antennas are to be arrayed in various ways to achieve a final gain in excess of 77 dB. It is anticipated that in performing this arraying, each antenna will suffer a further loss of 0.17 dB, meaning an additional efficiency term of 0.96, here called the "array efficiency." Also, each horn system will suffer some loss from dissipation and VSWR. This loss, or efficiency term, is estimated at 0.98 for the X/S corrugated horns.

The DSN 26-meter antennas have perforated sheet metal panels for lightening the main reflector. An investigation (Ref. 3) of these holes in a "worse case" indicated that they might add an additional 0.4 Kelvin to noise temperature, which will be ignored.

IV. Final Performance of the Array

Below is tabulated the efficiency performance of each of these antennas as elements of an antenna array.

Antenna	Spar blockage	Surface rms	Array combining	VSWR loss	RF	Percentage total
26-meter	0.861	0.757	0.96	0.98	0.784	48
34-meter	0.895	0.824	0.96	0.98	0.95	66
40-meter	0.884	0.903	0.96	0.98	0.96	72

These larger antennas are compared with the present 26-meter antenna with its standard feed in Table 1.

We note that, everything else being equal, i.e., if all antennas were the same diameter, the improvement from shaping, a more accurate surface, and a more efficient horn feed, is nearly 2 dB.

References

1. *Large Advanced Antenna Station Status Report*, Report 890-74, Jet Propulsion Laboratory, Pasadena, Calif., August 1978 (internal document).

2. John Ruze, Antenna Tolerance Theory - A Review, *Proc. IEEE* Vol. 54, pp. 633-640, Apr. 1966.

3. T. Y. Otoshi, *A Study of Microwave Transmission through Perforated Flat Plates* Technical Report 32-1526, Vol II, Jet Propulsion Laboratory, Pasadena, Calif.

Table 1. Comparison of antennas by size and type

Parameter	26-meter paraboloid			34-meter shaped	40-meter shaped
Feed used	22-dB standard	Dual – hybrid mode	X of X/S	X of X/S	X of X/S
Efficiency, %	46	50	48	66	72
ΔdB (everything else being equal)	−1.95	−1.58	−1.76	−0.38	0

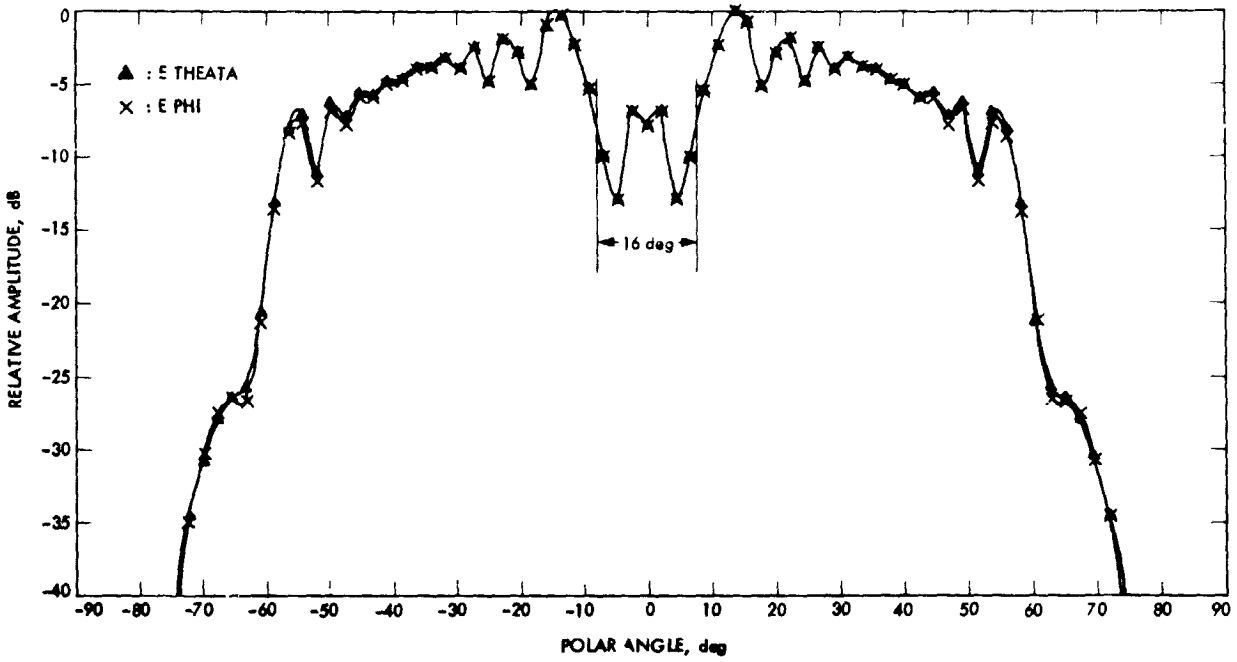

Fig. 1. 55 modes of the theoretical 17.1-deg horn pattern at 8.415-GHz scattering from the subreflector of the 26-meter antenna

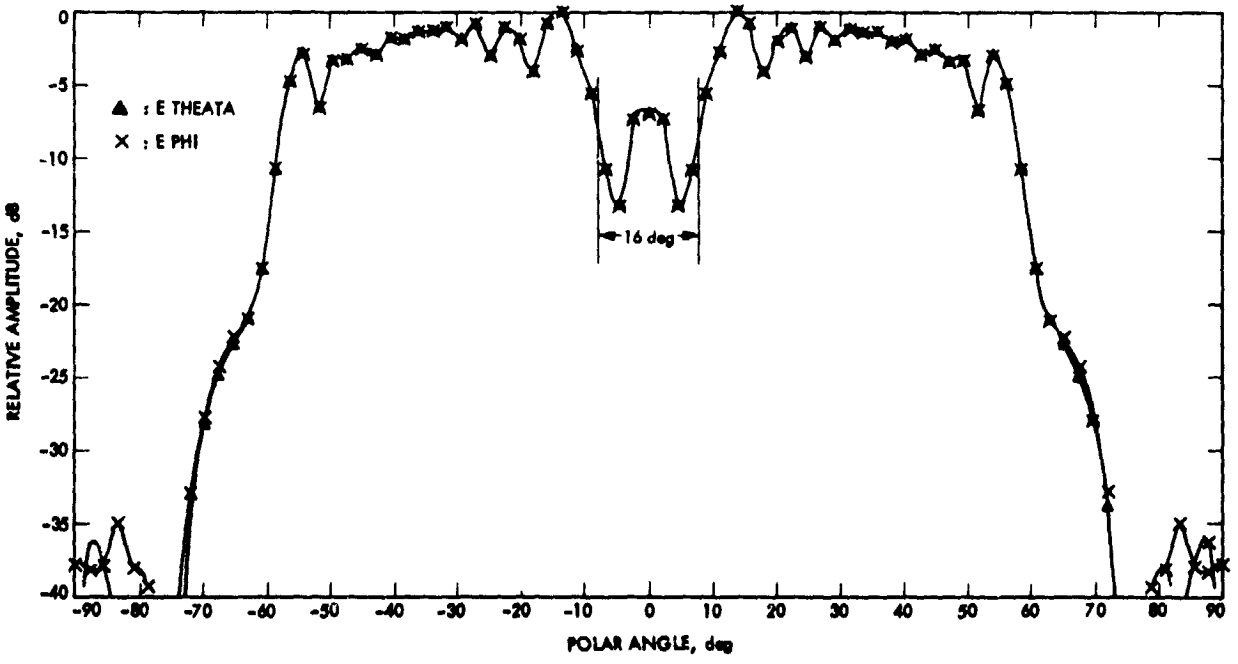

Fig. 2. 55 modes of the dual-mode horn pattern at 8.415-GHz scattering from a 26-meter antenna (54-in. hyperboloid)

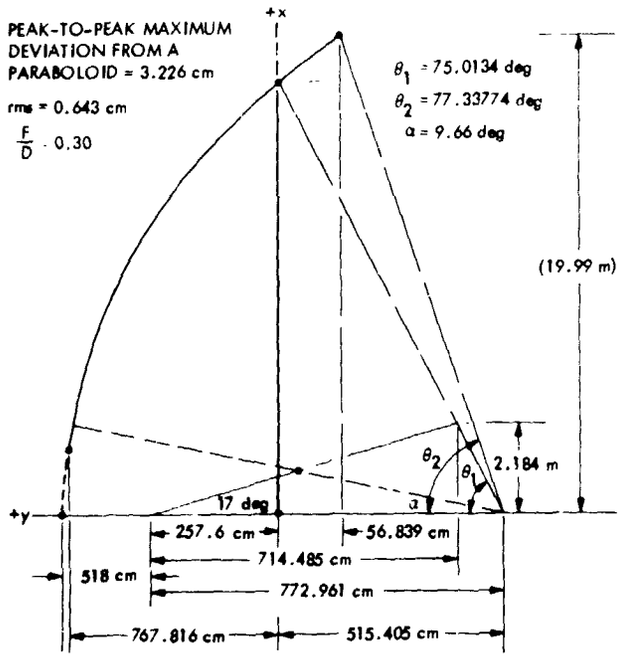

Fig. 3. The "best fit" solution of a 40-m antenna using 8.45 GHz of the X/S horn

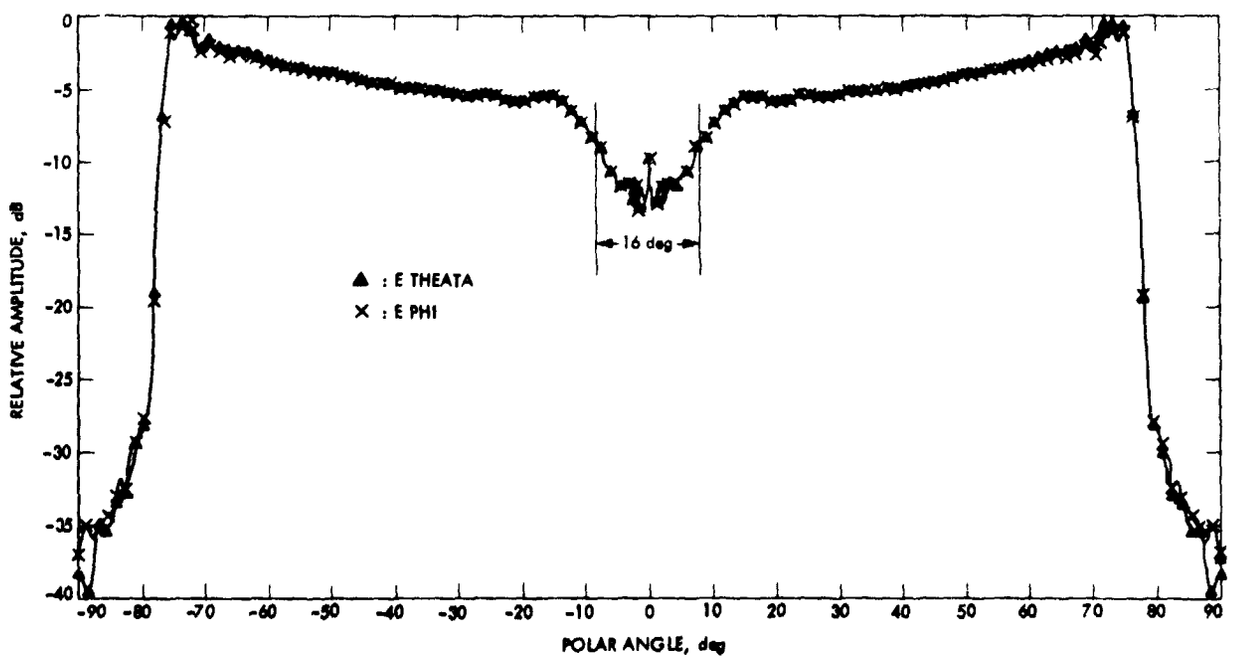

Fig. 4. Scattering of X-band of the X/S horn from the shaped subreflector of the shaped 40-meter antenna

N79-25110

Quick-Look Decoding Schemes for DSN Convolutional Codes

C. A. Greenhall and R. L. Miller
Communications Systems Research Section

The Galileo project will be tracked both by the Tracking and Data Relay Satellite System (TDRSS) and the DSN, whose (7, 1/2) convolutional codes differ in the order of the two symbols in each pair. To resolve this problem, we propose quick-look decoding of the TDRSS data. Quick-look decoding schemes requiring only simple shift registers are given for the DSN (7, 1/2) and (7, 1/3) convolutional codes. These schemes can be used when the communication channel is known to be virtually error free. The schemes not only decode the data, but can also detect symbol errors and the lack of node synchronization.

I. Introduction

The Galileo project will require both the Tracking and Data Relay Satellite System (TDRSS) and the DSN for tracking purposes. The TDRSS will be used for a few hours, the DSN for a few years. A problem has arisen because the TDRSS ground stations and the DSN stations have different Viterbi decoders. The connection vectors for the convolutional code that the TDRSS can decode are reversed from those of the DSN scheme.

This article presents one possible solution to this problem, viz, quick-look decoding. The following conditions are implicitly assumed throughout:

(1) The Galileo spacecraft is equipped with only a DSN-type encoder; TDRSS cannot process these data.

(2) The spacecraft-TDRSS communication channel is virtually error-free.

The second condition allows the possibility of quick-look decoding the data, without attempting to correct any errors. The advantage of quick-look decoding is that it involves only a couple of shift registers of length 7, as against the need to purchase a new Viterbi decoder.

Section II contains a brief description of what the design philosophy of a quick-look decoder should be. Section III presents a tutorial discussion of the theory behind quick-look convolutional decoders. Section IV contains decoding formulas for the DSN (7, 1/2) and (7, 1/3) convolutional codes. We have also included connection diagrams of these codes and their decoders.

II. Design Philosophy

A quick-look decoder should be a simple, fast algorithm that correctly decodes an error-free symbol stream. It does not

attempt to correct errors, but may detect the presence of symbol errors or lack of bit synchronization. Nevertheless, such a decoder should not go looking for trouble. The less it knows, the better. The fewer symbols it has to look at, the fewer symbol errors it will see, and the fewer bit errors it will make. Finally, it must not propagate symbol errors indefinitely far down the decoded bit stream; each decoded bit should depend only on the last few symbols.

III. Theory

A. Inversion Formulas

The method of constructing quick-look decoders is taken from Massey and Sain (Ref. 1). The present exposition is self-contained. Let a convolutional code with constraint length $d+1$ and rate $1/v$, v an integer, be specified by *connection polynomials*

$$C_j(x) = c_{j0} + c_{j1}x + \cdots + c_{jd}x^d, \quad 1 \leqslant j \leqslant v$$

The coefficients are 0 or 1 and arithmetic is performed modulo 2. The sequences of information bits b_n and coded symbol vectors $(s_{1n}, \cdots, s_{vn})$, $-\infty < n < \infty$, are represented by the formal power series,

$$B(x) = \sum_{n=-\infty}^{\infty} b_n x^n$$

$$S_j(x) = \sum_{n=-\infty}^{\infty} s_{jn} x^n, \quad 1 \leqslant j \leqslant v$$

related by

$$S_j(x) = C_j(x)\,B(x), \quad 1 \leqslant j \leqslant v \tag{1}$$

In othe words,

$$s_{jn} = c_{j0}b_n + c_{j1}b_{n-1} + \cdots + c_{jd}b_{n-d},$$

$$1 \leqslant j \leqslant v, \; -\infty < n < \infty$$

Knowing the $C_j(x)$ we must recover $B(x)$. Assume that the greatest common divisor (*gcd*) of $C_1(x), \cdots, C_v(x)$ is 1. By Euclid's Algorithm we can construct *inversion polynomials* $A_1(x), \cdots, A_v(x)$ of degree $< d$ such that

$$A_1(x)\,C_1(x) + \cdots + A_v(x)\,C_v(x) = 1 \tag{2}$$

From Eqs. (1) and (2) we have (dropping the x's now)

$$B = (A_1C_1 + \cdots + A_vC_v)\,B$$

$$B = A_1S_1 + \cdots + A_vS_v \tag{3}$$

for any bit sequence B. Hence the transformation defined by Eq. (1) is one-one and Eq. (3) gives its inverse. If

$$A_j(x) = a_{j0} + a_{j1}x + \cdots + a_{je}x^e, \quad 1 \leqslant j \leqslant v$$

then Eq. (3) says

$$b_n = \sum_{j=1}^{v} (a_{j0}s_{jn} + a_{j1}s_{j,n-1} + \cdots + a_{je}s_{j,n-e}),$$

$$-\infty < n < \infty \tag{4}$$

Conversely, if about the polynomials $C_1(x), \cdots, C_v(x)$ and $A_1(x), \cdots, A_v(x)$ we are given only that Eq. (3) inverts Eq. (1) for all B, then setting $B = 1$ gives Eq. (2) and the conclusion that $gcd\,(C_1, \cdots, C_v) = 1$. Thus:

An inversion formula of form (3) exists if and only if $gcd\,(C_1, \cdots, C_v) = 1$.

B. Symbol Error Detection

Let $gcd\,(C_1, \cdots, C_v) = 1$. Assume that the formal power series $S_1, \cdots, S_v$ are a code stream, i.e., they satisfy Eq. (1) for some B. Then trivially we have

$$C_iS_j = C_jS_i, \quad 1 \leqslant i, j \leqslant v \tag{5}$$

We show that *Eq. (5) is necessary and sufficient for* $S_1, \cdots, S_v$ *to be a code stream.* We just saw that it is necessary. Assume that Eq. (5) holds. Define B by Eq. (3) as before. We show that Eq. (1) holds. It is enough to set $j = 1$. We have

$$C_1B = C_1A_1S_1 + C_1A_2S_2 + \cdots + C_1A_vS_v$$

$$= C_1A_1S_1 + A_2C_2S_1 + \cdots + A_vC_vS_1$$

$$= S_1$$

by virtue of Eqs. (5) and (2). Equation (5) thus yields parity checks of the received symbols.

IV. DSN Codes

We give decoding formulas and parity checks for the DSN (7, 1/2) and (7, 1/3) convolutional codes, whose connection diagrams are given in Figs. (1) and (2).

A. (7, 1/2) Code

The connection and inversion polynomials are

$$C_1(x) = 1 + x^2 + x^3 + x^5 + x^6$$

$$C_2(x) = 1 + x + x^2 + x^3 + x^6$$

$$A_1(x) = x^2 + x^4$$

$$A_2(x) = 1 + x + x^2 + x^3 + x^4$$

The quick-look inversion formula (Eq. (4)) is

$$b_n = s_{1,n-2} + s_{1,n-4} + s_{2,n} + s_{2,n-1} + s_{2,n-2} + s_{2,n-3} + s_{2,n-4} \tag{6}$$

in which b_n is the nth decoded bit and (s_{1n}, s_{2n}) is the nth symbol pair. Thus if we know (s_{1n}, s_{2n}) for $n \geq 0$ we can recover b_n for $n \geq 4$ by this method.

The parity check for detection of symbol errors or lack of bit synchronization (Eq. (5)) is

$$s_{1,n} + s_{1,n-1} + s_{1,n-2} + s_{1,n-3} + s_{1,n-6} + s_{2,n} + s_{2,n-2} + s_{2,n-3} + s_{2,n-5} + s_{2,n-6} = 0 \tag{7}$$

A short burst of parity errors in a good channel indicates one or more symbol errors; a long run of parity bits with a high proportion of errors indicates incorrect node synchronization.

Actual implementations of this code use trivial modifications of it; the DSN inverts the first symbol s_{1n}, and TDRSS transmits s_{1n} and s_{2n} in reverse order. In these situations, Eq. (6), Eq. (7), and Fig. 3 may have to be altered.

B. (7, 1/3) Code

To C_1 and C_2 of the previous code we adjoin a third polynomial

$$C_3(x) = 1 + x + x^2 + x^4 + x^6$$

The three polynomials C_1, C_2, C_3 are pairwise relatively prime. Hence we can treat each of the three subcodes (C_i, C_j), $i < j$, separately. For these, Eq. (2) reads

$$(x^2 + x^4)\,C_1(x) + (1 + x + x^2 + x^3 + x^4)\,C_2(x) = 1 \tag{8}$$

$$(x + x^3)\,C_1(x) + (1 + x^2 + x^3)\,C_3(x) = 1 \tag{9}$$

$$(x^3 + x^4 + x^5)\,C_2(x) + (1 + x + x^4 + x^5)\,C_3(x) = 1 \tag{10}$$

Of course, Eq. (8) comes from the (7, 1/2) code. One could add these to get a single Eq. (3) with $v = 3$, but, according to our design philosophy, there is no point in doing this. The simplest of the above equations is Eq. (9); thus we may as well ignore the S_2 data entirely, use the inversion polynomials $x + x^3$ and $1 + x^2 + x^3$ on S_1 and S_3, and use only S_1 and S_3 for a parity check.

The quick-look inversion formula is

$$b_n = s_{1,n-1} + s_{1,n-3} + s_{3,n} + s_{3,n-2} + s_{3,n-3} \tag{11}$$

in which b_n is the nth decoded bit and (s_{1n}, s_{2n}, s_{3n}) the nth symbol triplet. The parity check is

$$s_{1,n} + s_{1,n-1} + s_{1,n-2} + s_{1,n-4} + s_{1,n-6} + s_{3,n} + s_{3,n-2} + s_{3,n-3} + s_{3,n-5} + s_{3,n-6} = 0 \tag{12}$$

Figure (4) gives the connection diagram of this decoder.

V. Conclusion

We have shown that both the (7, 1/2) and (7, 1/3) convolutional codes can be decoded using quick-look schemes. Such a scheme may be used by the Galileo project to work around the incompatibility between the TDRSS and DSN codes

Reference

1. Massey, James L., and Sain, Michael K., Inverses of Linear Sequential Circuits, *IEEE Trans. Comput.*, Vol. C-17, 1968, 330–337.

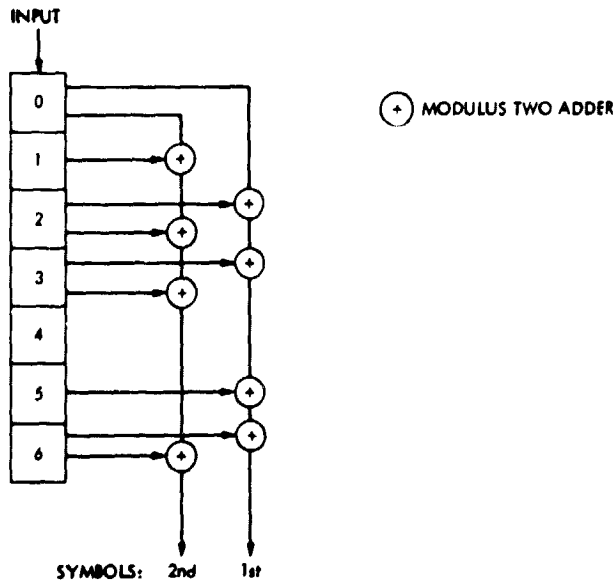

Fig. 1. Connection diagram of unmodified (7, 1/2) code, without symbol inversions or exchanges

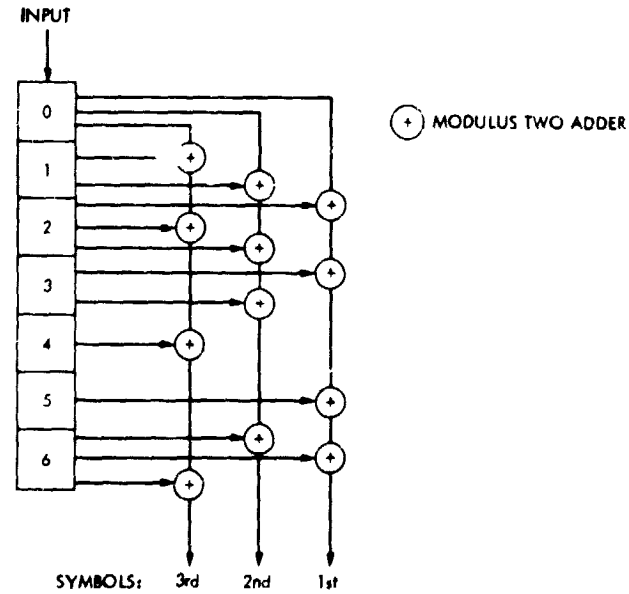

Fig. 2. Connection diagram of (7, 1/3) code

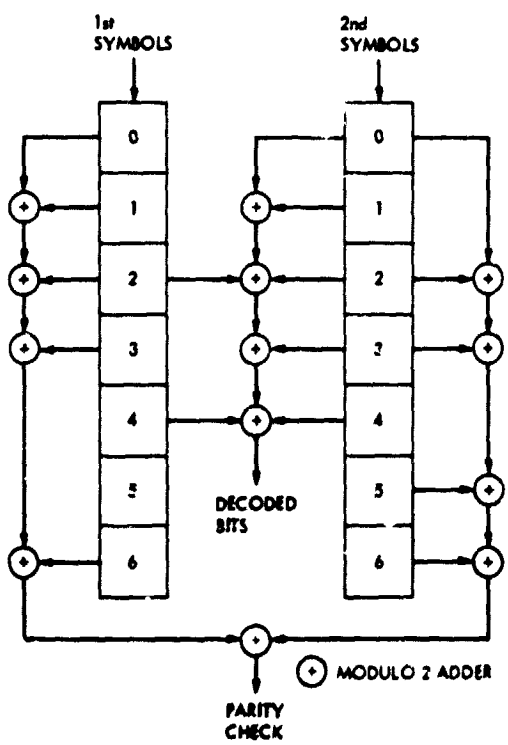

Fig. 3. Connection diagram of quick-look decoder for unmodified (7, 1/2) code, without symbol inversions or exchanges

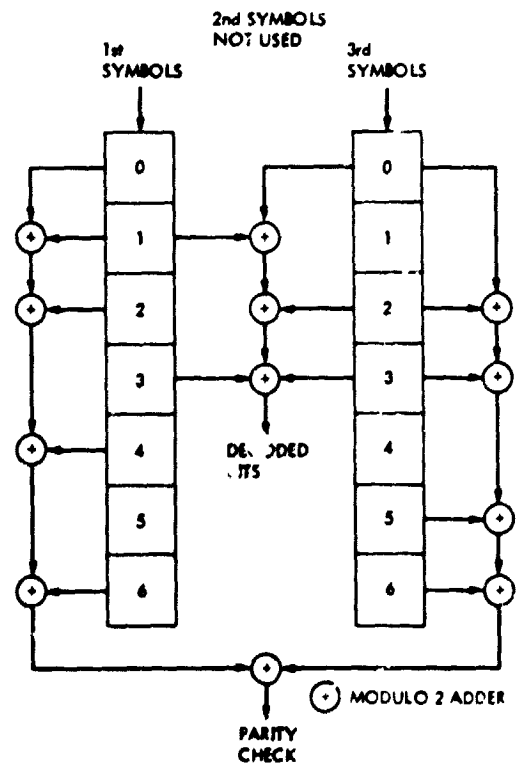

Fig. 4. Connection diagram of quick-look decoder for (7, 1/3) code

N79-25111

DSN Energy Data Base Preliminary Design

E. R. Cole, L. O. Herrera, and D. M. Lascu
DSN Engineering Section

This article describes the initial design and implementation of a computerized data base created to support the DSN Energy Conservation Project with data relating to energy use at Goldstone Deep Space Communications Complex. In addition, it briefly gives the results of development work to date and identifies work currently in progress or in the planning stage.

I. Introduction

The Deep Space Station facilities consume a significant amount of energy, for which the last few years have been the focus for energy conservation. Crucial to any endeavor to reduce energy consumption is the acquisition and maintenance of relevant information. Prior to 1976, information was manually acquired, handled, and processed. In response to limited human resources and considering the emergence of a Centralized Management Data Base System (the DSN Data Base), the DSN Energy Conservation Project commissioned the creation of a computer-based energy data base whose preliminary design was implemented in 1976.

II. The Goldstone Energy Data Base

The concept of an energy data base was conceived from the growing awareness of the need for a readily available and easily accessable source of information relating to the use of energy resources. Initial attempts to gather data for energy studies being conducted at the Goldstone Deep Space Communications Complex (GDSCC) were frustrated by the degree of effort and length of time required to locate and research information. This illustrated the desirability of creating a formal, centralized data base which would provide:

(1) A readily available source of technical and descriptive data.

(2) A central, standardized reference to augment engineering analysis and design.

(3) Information for effective energy management.

(4) A historical record for comparison of actual performance with project goals.

(5) Information for preparing NASA Energy Program Reports.

Using these objectives as a guide, a preliminary energy data base was created and called the Goldstone Energy Data Base. It was implemented in November 1976 and contained sixteen files describing such Goldstone facility parameters as: building architectural construction, utilities, equipment loads, facility operations, and weather, as shown in Fig. 1. The data were collected and placed into a publicly accessable permanent catalog file on the GPCF Univac 1108 titled GOLDSTONE* ENERGY, and an accompanying user document was written and released to explain the design philosophy and provide user access instructions. One application for the data base was to

C-3

provide input data for certain engineering energy analysis and design computer programs such as E-CUBE, NECAP, and the Energy Consumption Program. These programs require information about building construction, operation, and equipment loads. A brief description of each file listed in Table 1 follows.

(1) The interior architectural files, ARC/100 and ARC/200, describe each room of the Goldstone buildings by its wall, floor, and ceiling dimensions, and their construction material U-factor (thermal transmissivity). Both files designate which zone of the building air conditioning system serves each room.

(2) The interior lighting file, INL/100, describes the number of room lighting fixtures and their loads in kilowatts. Both quantities are listed separately by flourescent and incandescent light fixtures. Lighting is also a heating load, which is imposed on a fixed zone of the building air conditioning system. Average light level in foot candles is identified as a requirement for the function and occupancy of the room.

(3) The interior occupancy file, OCC/100, lists the personnel capacity and actual occupancy for each room by eight-hour work shifts for week and weekend day types.

(4) The Interior Electrical Equipment Files, EEQ/100 and EEQ/101, provide a listing by room, number of racks, type of equipment, and total rack power load in kilowatts; also, there is a breakdown by rack of each piece of equipment giving subsystem name and number. Power load in kilowatts, and the corresponding heat dissipated, is given for various operational modes, which include normal station tracking operation, standby, and station closed.

(5) The Exterior Lighting File, EXL/100, describes lighting for the exterior area of each building, which includes number and type of light fixture on each wall, wall orientation, and power in kilowatts.

(6) The Building Airconditioning Plant Files, ACP/100 and ACP/200, identify and locate each air conditioning plant. Each major component is described by size, type and energy load. Air handler size is given in cfm and compressor size in tons. Power used by humidifiers, boilers, heaters, and condensor motors is expressed in kilowatts.

(7) The Power Plant Files, PPL/100 and PPL/200, describe and locate all diesel power plants at Goldstone. The number of frequency convertors, engine generators, and their respective power used or produced is listed.

(8) The Building Utilities File, UTL/100, designates all utilities entering each building, which includes, electrical power by voltage and frequency, telephone, public address, microwave facilities, LP gas, water, and sewer.

(9) The Weather Files, WEA/100, WEA/200, WEA/300, and WEA/400 describe dry bulb temperature, dew point temperature, cloud cover ratio, and wet bulb temperature, respectively. Each file consists of hourly values for each day of a statistically representative year.

III. Preliminary Design Requirements

Certain data base requirements were determined to be desirable by project management. For example, it was considered desirable that all data be "raw" data, due to the past experience of having difficulty in assessing the integrity of acquired data. This meant that, to the extent possible, data values should be directly observed, unconverted, and not derived via computation from other data.

Another requirement was that data should be entered into files in a format that would be human-readable, requiring no interpretive software to produce reports. In part, due to the limited size of the staff available for data base design and implementation, user application software was left to the user for development. Data base files were created on the Univac 1108 as system file elements. Thus they are compatible with MBASIC™ and FORTRAN Programming languages. Plus physical record length was constrained to a maximum of 80 characters to provide both system flexibility and a convenient terminal display format.

Recently, standard guidelines have been published for the design and implementation of data bases on the DSN Data Base System. This DSN Standard Practice document and the recent inclusion of the DSN Energy Data Base into the DSN Technical Facilities Subsystem is currently resulting in the reassessment of DSN Energy Data Base functional design requirements.

IV. Data Base Design

The Goldstone Energy Data Base is designed as a collection of hierarchically structured groups of files (as shown in Fig. 2). This design is intended to provide opportunity for data base growth with minimal structural limitations as well as providing flexibility in its eventual incorporation into the DSN Data Base System.

Data is divided into groups of files containing related data categories as shown in Table 1. All groups consist of one or more files that are structured into three levels: primary, secondary, and tertiary. Each level represents a breakdown of information or other relational association with the files in the

level above. The first file of each level is defined as the initial file. When the logical data record exceeds the maximum length permitted in the initial file, up to eight "continuation files" may be created to provide the required logical record length as shown in Fig. 3.

Files are labeled by a three-character acronym preceeding a three-digit numerical sequence. The acronym identifies the file group while number sequence indicates level and whether it is an "initial" or "continuation" file. File structure, shown in Fig. 4, consists of three record types. The first is the identification record containing information required to identify the file, companion documentation, transaction dates, and the individual responsible for data integrity. The second record is the header record, which provides column headers aligned over each data field that identify the respective data items. The remainder of the file is data records having the same format as established by the header record.

In accordance with design specification, application software was not developed. However, two interactive data access programs were written in MBASIC to provide the casual user with outputs of data base files. The program titled DISPLAY displays files on the users demand terminal while COPY-EG outputs to GPCF line printers.

Description of each file group giving narrative and file composition data was documented into a modularly organized users document entitled: "DSN Energy Project Data Base Facility Parameters for Goldstone". The document describes data base purpose and scope, design structure, description of each file group, and data access instructions. The modular construction of the document provides for addition of sections as new files and groups are added to the data base.

V. Current Status and Future Development

Several additional data categories have been added to the data base since its initial creation. The sixteen original files have grown to nearly thirty, and additional files are in the planning stage. This has resulted in five new groups as well as additional new files to existing groups. Figure 5 and Table 2 show the current and planned growth of the DSN Energy Data Base.

(1) The Energy Consumption Data Group (ECD) consists of seven files with five more in planning. This group lists individual readings from meters that measure consumption of LP gas, diesel fuel, gasoline, electrical power, and water. Also, monthly billing is listed for each respective type. Two additional files complete the group: one lists total monthly energy usage by energy type, and the thermal equivalent that enables the computation of Goldstone total energy consumption. The other is a cross-reference file, providing meter serial number, reading conversion factors, meter location, and installation dates.

(2) The Programmatic Energy Change Group (PGM) consists of three files which keep a historical record of NASA program related changes in energy usage at Goldstone. Such changes include installation or removal of equipment, variation in operational schedules, and operational duty cycle.

(3) The Energy Conservation Change Group (CON) is planned to keep a record similar to the PGM group, but relating to energy conservation actions.

(4) The Building Operation Mode Group (BOM) is still in the planning stage, but is expected to contain facility operational specifications and related data for each building.

(5) The DSN Data Base Interface Group is a special category of four files required by a recently published DSN Standard Practice document. These files, which are in the planning stage, will provide the user with a file catalog, listing files with a narrative description of their purpose and contents. The data dictionary defines each data item and describes its location, type, and size within the data file. The interface group becomes a part of a larger data base interface increment within the DSN Data Base System upon the implementation and transfer of the DSN Energy Data Base to that system.

Not only has the Goldstone Energy Data Base expanded, but there is consideration to extend the data base to include the Australian and Spanish Deep Space Communication Complexes, which would result in the creation of a DSN Energy Data Base.

As mentioned above, the energy data base is being defined as a group with the Technical Facilities subsystem, and considerable review of the data base functional requirements is expected. As a result of new requirements, coupled with the potential for automatic data acquisition suggested by the development of a Technical Facilities Controller (TFC), DSN Monitor and Control (DMC) Mark III, and the creation of the Configuration Control Assembly (CCA), which will contain the DSN Data Base, considerable change to the design of the data base is expected.

In the new design, an elementary data management system will be added consisting of data maintenance software, user access programs, and some applications software.

At the same time of the development of the Goldstone Energy Data Base, a Goldstone Facility Management Data Management System was designed, and an automated data system was implemented (see Ref. 2). This resulted in a Goldstone Facility Management (GFM) Data Base that, among other functions, collected facility energy consumption data for monthly reporting to NASA. The DSN Energy Conservation Project and Goldstone DSCC management decided that the GFM data base was duplicating the Goldstone Energy Data Base in the area of energy related files. Therefore, the DSN Energy Data Base will assume the energy related data management tasks of the GFM Data Base in the new design. This will require the development of some user application software to generate required NASA reports.

VI. Summary

The initial energy data base implemented for Goldstone DSCC provides information support to the DSN Energy Conservation Project. Recent events will lead to an enhanced and expanded data management system design that will not only fulfill these objectives, but may provide other applications for general facility administration and engineering when incorporated into the central DSN Data Base System.

References

1. Date, C. J. *An Introduction to Database Systems*, Second Edition, Addison-Wesley, Reading Mass., 1977.

2. Maiocco, F. R., Hume, J. P., Computerizing Goldstone Facility Maintenance Data for Management Decisions, *DSN Progress Report 42-32*, pp. 310-330, January and February 1976, Jet Propulsion Laboratory, Pasadena, Calif.

Table 1. Goldstone Energy Data Base Content (1976)

Group Name	File Number	File Type	Description
Building Air Conditioning Plant (ACP)	100	Initial primary	Plant and compressor type and size; kilowatts used
Building Air Conditioning Plant (ACP)	200	Continuation primary	Humidifier, boiler and heater type, kilowatts used
Building Utilities (UTL)	100	Initial primary	Electrical and Mechanical type and class
Exterior Lighting (EXL)	100	Initial primary	Location and number of fixtures; kilowatts used
Interior Architectural (ARC)	100	Initial primary	Wall dimensions and U-factor
Interior Architectural (ARC)	200	Continuation primary	Ceiling and floor dimensions and U-factor
Interior Electrical Equipment (EEQ)	100	Initial primary	Number of racks and kilowatts used per room
Interior Electrical Equipment (EEQ)	101	Secondary	Kilowatts used per rack, NDL number
Interior Lighting (INL)	100	Initial primary	Location and number of fixtures; kilowatts used
Interior Occupancy (OCC)	100	Interior primary	Actual occupancy by room; capacity by room
Power Plant (PPL)	100	Initial primary	Station power plant frequency converters
Power Plant (PPL)	200	Continuation primary	Station power plant engine generating power
Weather (WEA)	100	Initial primary	Dry bulb data; Hourly
Weather (WEA)	200	Continuation primary	Dew point data; Hourly
Weather (WEA)	300	Continuation primary	Cloud cover data; Hourly
Weather (WEA)	400	Continuation primary	Wet bulb data; Hourly

ORIGINAL PAGE IS
OF POOR QUALITY

Table 2. Additional DSN Energy Data Bank Contents (1979–1980)

Group Name	File Name	Description
Energy Consumption Data	ECD/100	Monthly LPG meter readings in gallons
	ECD/101[a]	LPG billing data
	ECD/200	Monthly diesel fuel meter readings in gallons
	ECD/201[a]	Diesel fuel billing data
	ECD/300	Monthly water meter readings in gallons
	ECD/301[a]	Water billing data
	ECD/400	Monthly electrical meter readings in kilowatt hours
	ECD/401	Commercial electrical power readings; SCE billing
	ECD/500[a]	Monthly gasoline data in gallons
	ECD/501[a]	Gasoline billing data
	ECD/600	Summary report of monthly total energy use; megawatt hours thermal
	ECD/610	Meter cross-reference between meter codes and S/N; installation and removal dates, meter locations
Programmatic Energy Changes	PGM/100	Summary report of kilowatt-hour changes in use
	PGM/101	Journal entry of duty-cycle and measurement code
	PGM/102	Journal entry of type and load change
Conservation Energy Changes	CON/100[a]	Summary report of kilowatt-hour changes in use
	CON/101[a]	Journal entry of duty-cycle and measurement code
	CON/102[a]	Journal entry of type load change

Table 2 (contd)

Group Name	File Name	Description
Building Operation Mode	BOM/100[a]	Building lighting and HVAC Operational Specifications
	BOM/200[a]	Building lighting and HVAC Operational Specifications
	BOM/300[a]	Building lighting and HVAC Operational Specifications
Data Dictionary	DIC/100[a]	Element name, file name, field length, position data type
	DIC/200[a]	Element definition, and relationships
File Catalog	CAT/300[a]	File name, purpose, and content

[a]These files have not been implemented (planning stage).

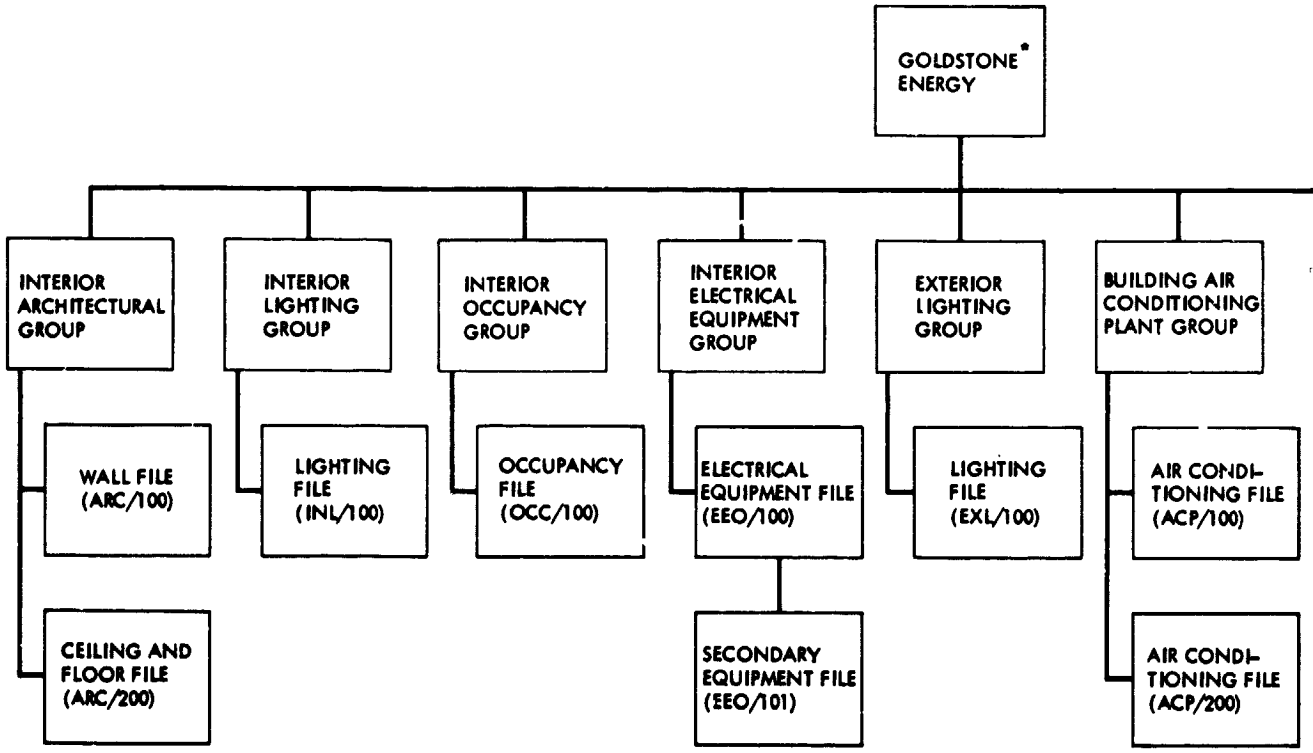

FOLDOUT FRAME

PRECEDING PAGE BLANK NOT FILMED

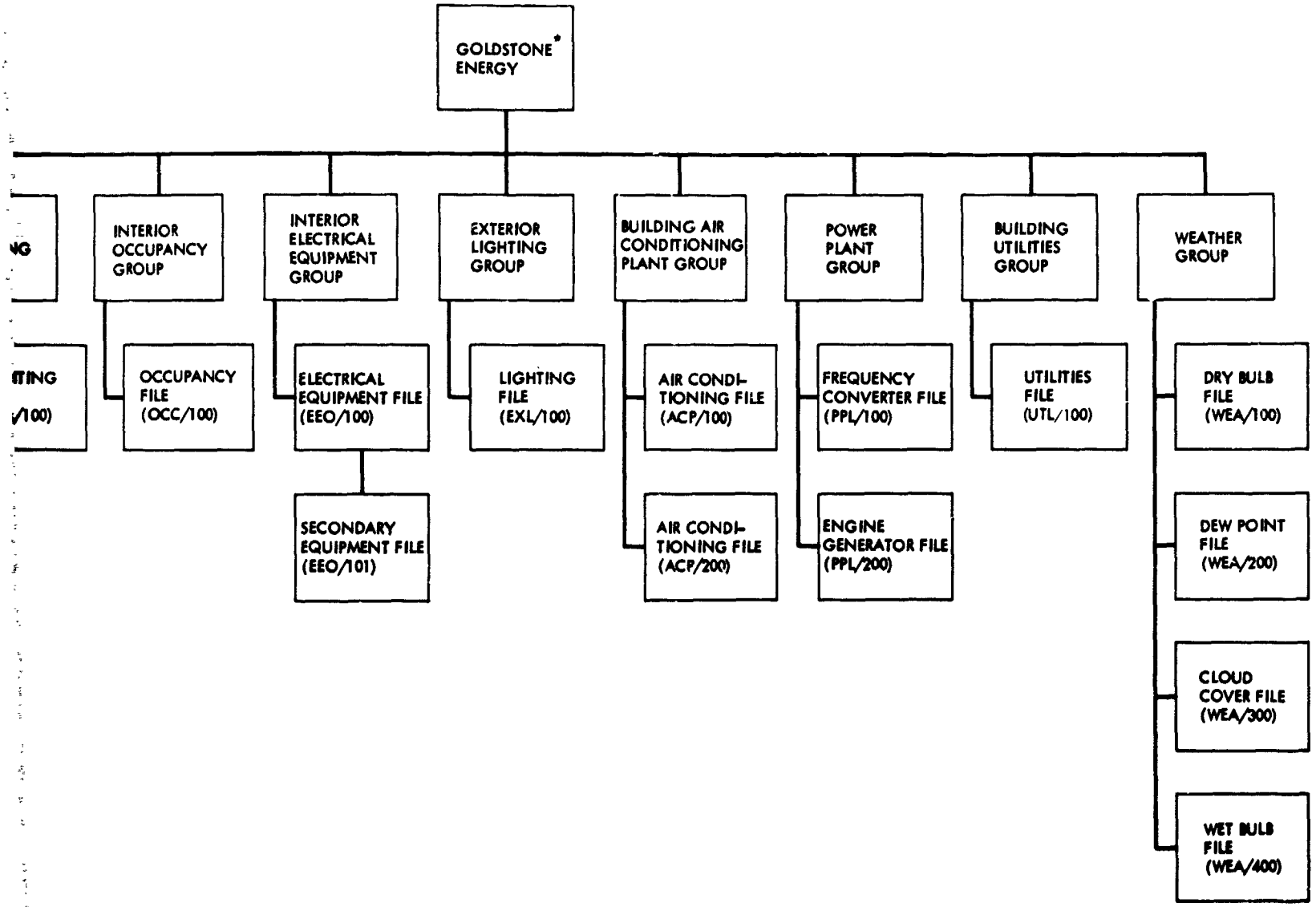

Fig. 1. Goldstone Energy Data Base (1976)

FILMED

PRECEDING PAGE BLANK NOT FILMED

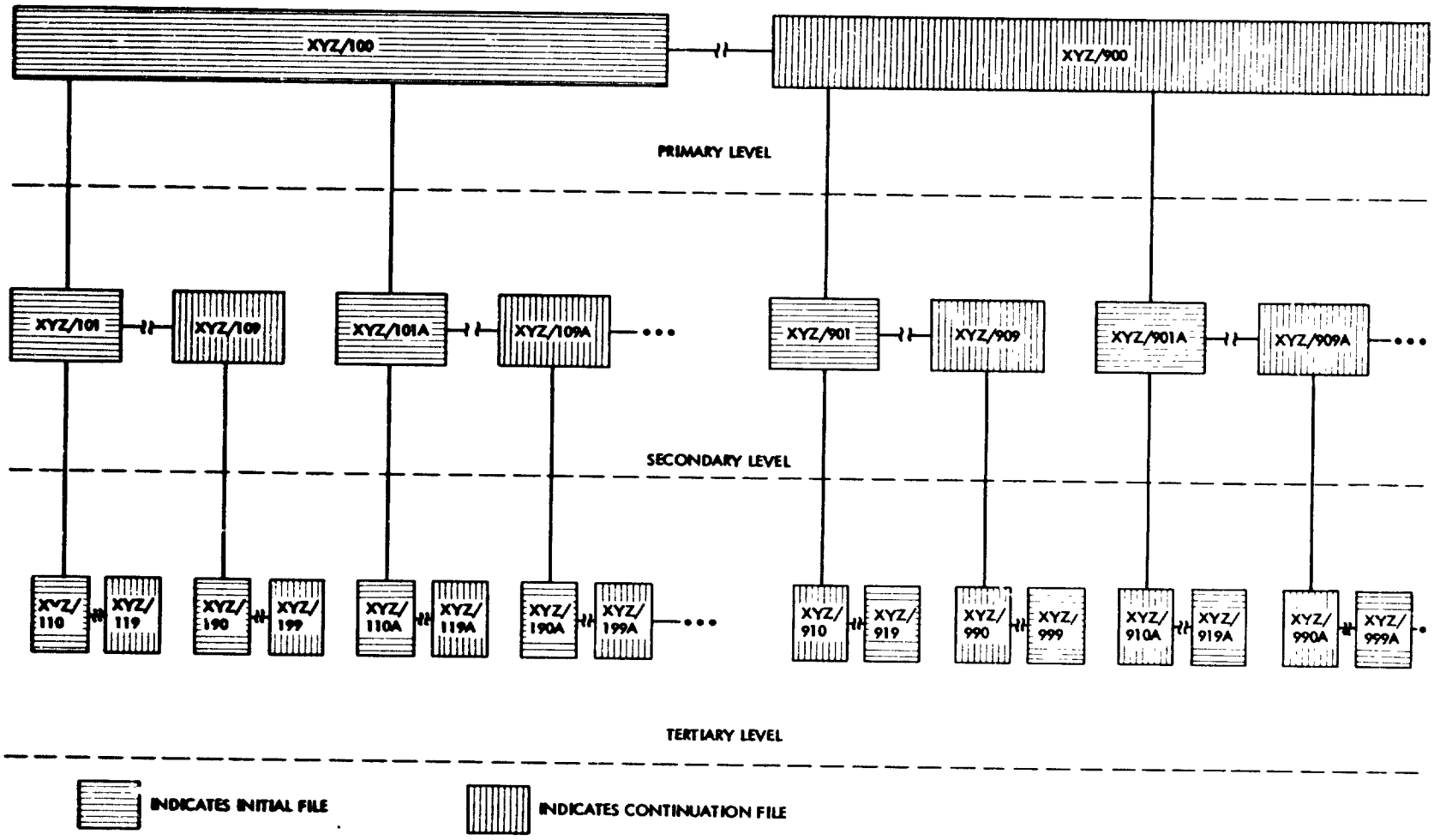

Fig. 2. Group structure hierarchy

INTENTIONALLY BLANK

ORIGINAL PAGE IS OF POOR QUALITY

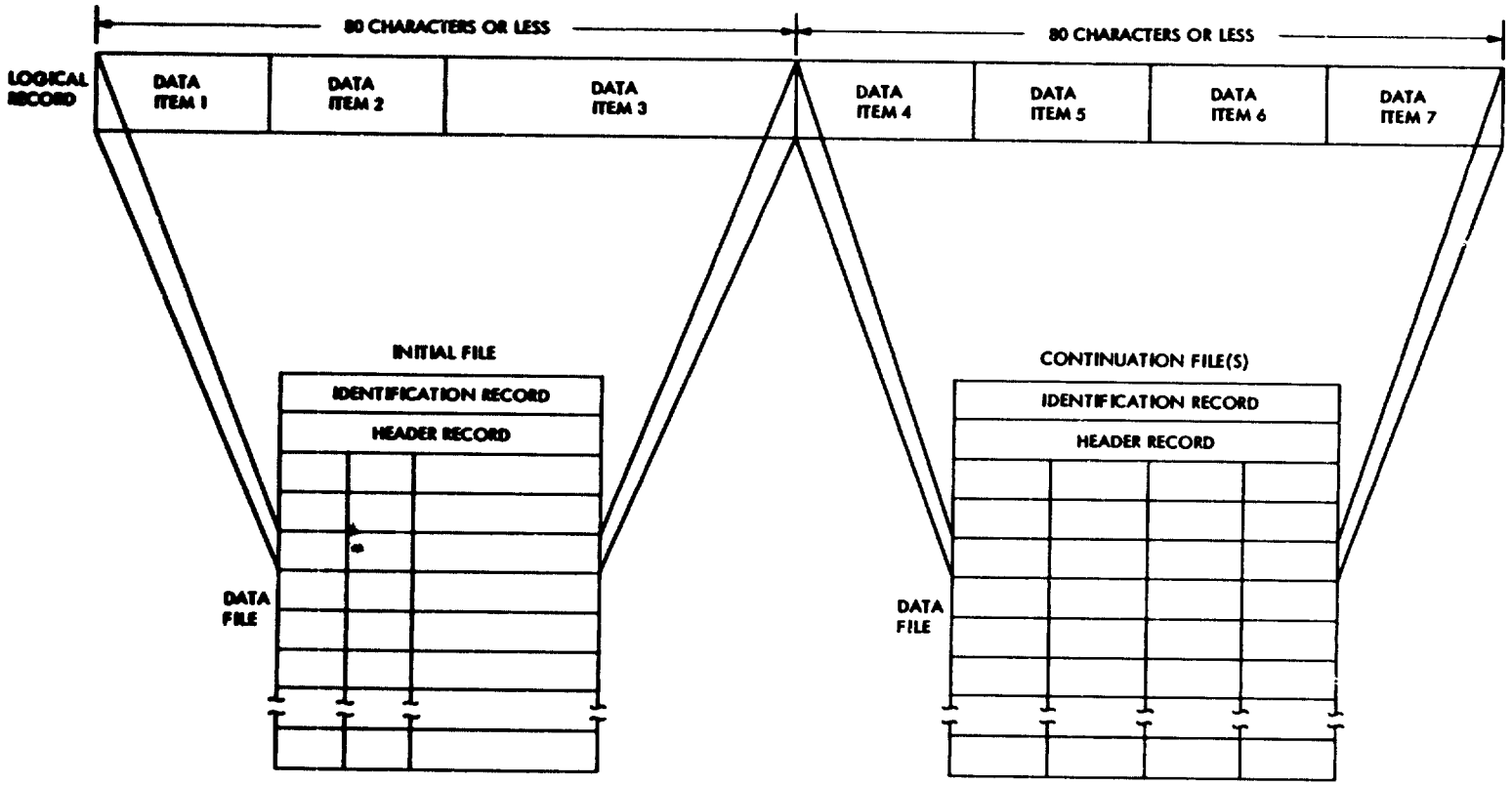

Fig. 3. Example of how a logical record is extended across physical file boundaries

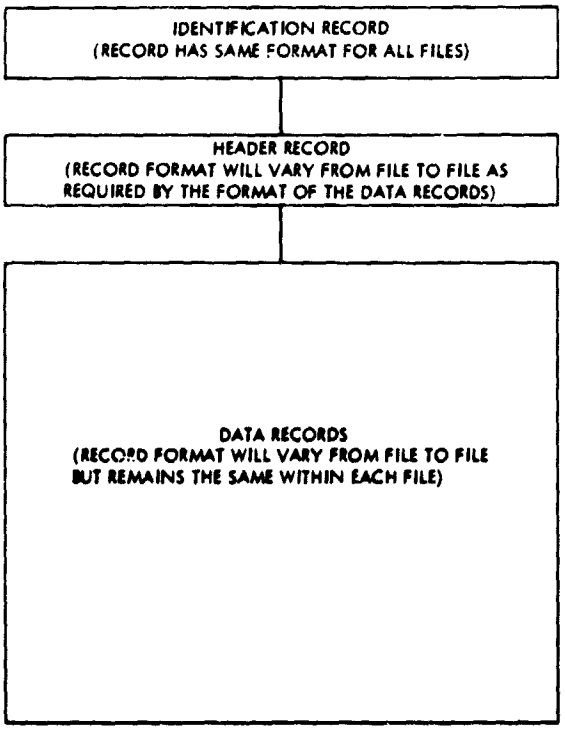

Fig. 4. File structure

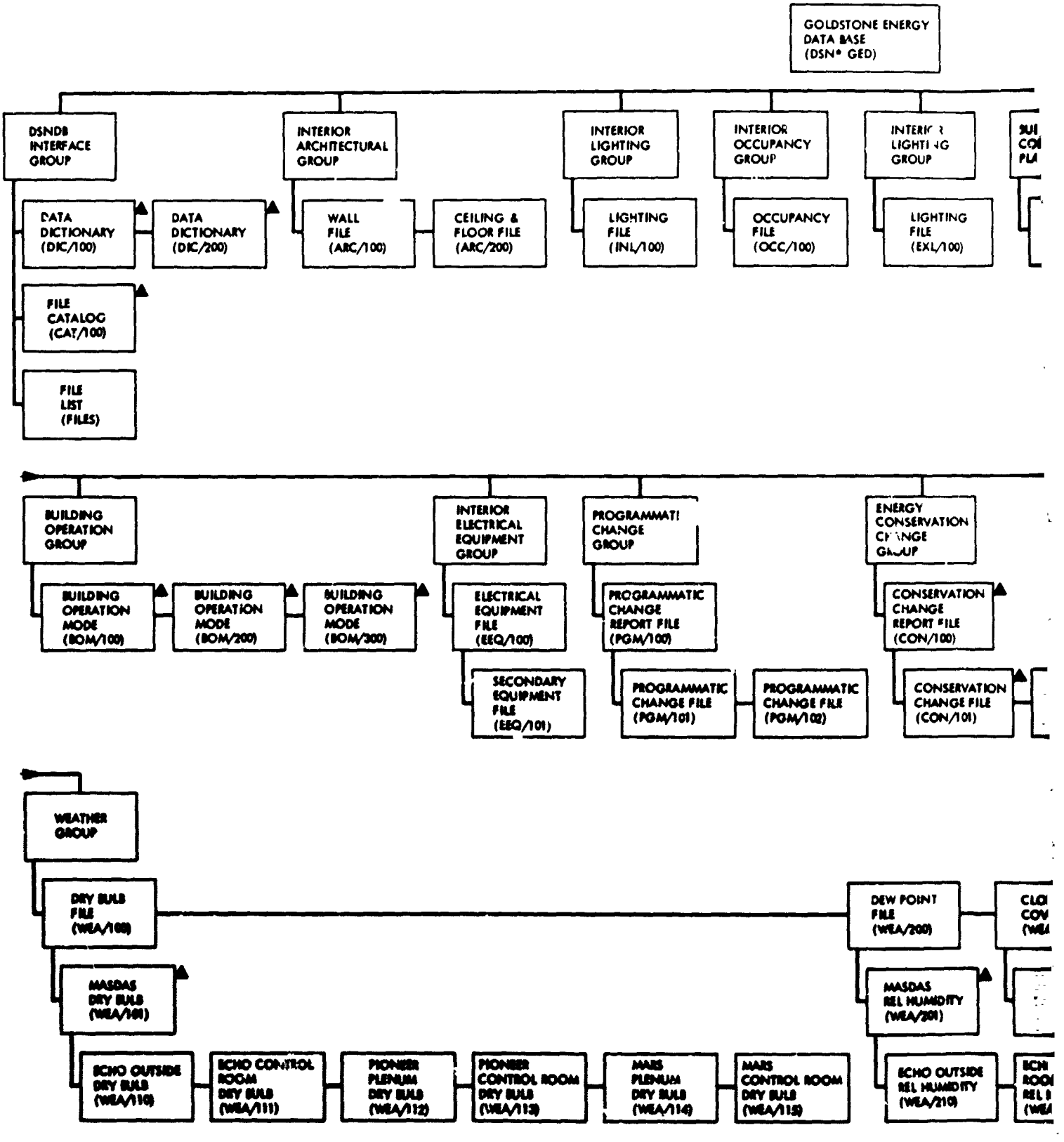

BOLDOUT FRAME

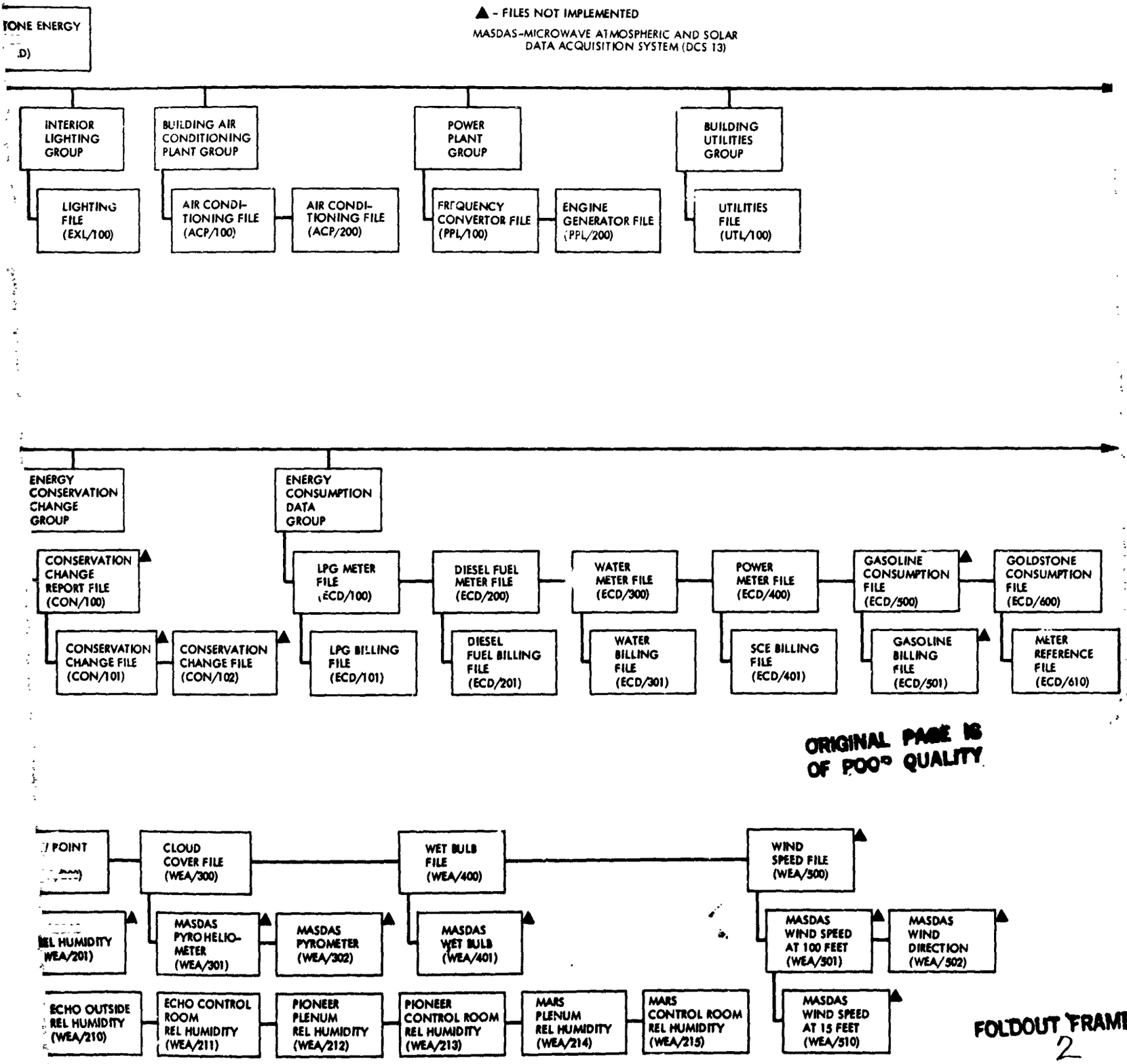

Fig. 5. DSN Energy Data Base (1979–1980)

PAGE 180 INTENTIONALLY BLANK

N79-25112

Microwave Time Delays in the DSN 34- and 64-Meter Antennas

R. Hartop
Radio Frequency and Microwave Subsystems Section

The microwave configurations at the 34- and 64-m stations have changed in the past year due to new equipments. To maintain time delay data logs, new calculations have been made where necessary of both the microwave component delays and the antenna air path delays for each type of antenna.

I. Introduction

Previous articles (Refs. 1 and 2) have discussed the necessity for carefully calculating the group delays within the DSN antenna systems to permit accurate ranging of spacecraft and for various other projects such as VLBI. Because the microwave subsystems are frequently changed to incorporate new equipment with improved capability, it periodically becomes necessary to recalculate the component group delays to update the total time delay within the antenna system. An extreme example of this has occurred in the case of 34-m DSN subnet, in which the antennas and their microwave subsystems have undergone a complete reconfiguration in their growth from 26-m instruments.

This article presents the results and methods used to derive new data for the recent changes to the DSN 34- and 64-m stations at both S- and X-band frequencies.

II. Basic Data

Table 1 presents the calculated parameters that were used throughout. The WC-504 circular waveguide is standard at S-band; the WC-137 is standard at X-band. The WS-90 square waveguide is used only in the orthomode in the new X-band feed. The value of $1.18028543 \times 10^{10}$ inches per second (2.997×10^{10} cm/s) was used for the velocity of light in free space, giving 0.084725271 nanoseconds per inch (0.0333 ns/cm) for the free space delay.

All calculations for feed delays are from the phase center of the horn to the defined output of the feed. Where applicable, the additional delay due to waveguide between the feed output and the TWM coupler input is listed separately below the feed total. Individual component delay calculations are generally very accurate since they rely on the precise physical dimensions of the component. However, certain complex components such as the dual-mode feed horns and the orthogonal mode junction reduce the overall feed delay accuracy to the order of ± 0.2 ns.

III. Feed Delays for 64-Meter Antennas

At DSS 14, the XRO Mod III feed is installed. This contains the orthomode junction with the result that there are, in effect, two feed paths as shown in Table 2. At DSS 43 and DSS 63, the XRO Mod II feed will continue to be used until late in 1979. The data in Table 3, corrected from previous sources, applies. The two travelling wave masers in the feed cone are distinguished by their component designators A17 and A24.

182 INTENTIONALLY BLANK

At S-band frequencies, the SPD cone assembly remains unchanged, so that the delay from the horn phase center to the phase calibration coupler input remains 21.291 ns at 2113 MHz and 18.766 at 2295 MHz.

IV. Feed Delays for 34-Meter Antennas

The X-band feed used in the SXD cone assembly is identical in every respect to the XRO Mod II feed assembly. Thus, the data in Table 3 apply exactly, and the output elbow is the same as for the A17 configuration, giving a total delay of 5.090 ns.

The S-band feed in the SXD cone assembly has the time delays shown in Table 4.

V. Dichroic Plate Correction

At X-band, the signal passes through the dichroic plate with two results. The first effect is an offset in the ray path, making it longer than a direct path. The second effect is that the holes in the plate act as small waveguides with a cutoff wavelength of 1.536 inches (3.90 cm). The resulting group delay of 0.2074 ns per inch (0.082 ns/cm) times the plate thickness of 1.400 inches results in 0.2904 ns delay through the plate. Adding the ray path geometry correction of 0.0296 ns and subtracting the direct free-space delay of 0.1370 ns leaves a residue of 0.183 ns. This is the quantity that must be added at 8420 MHz to any air path delay involving the dichroic plate. The correction does not apply at S-band since the plate is merely a reflector.

VI. Air Path Delays

Air path delays are based on the theoretical geometry of each antenna configuration. No allowance is made for manufacturing tolerances, hyperboloid focussing, or structural deflections. The dichroic plate is treated separately, and a small error was discovered in previous calculation. Thus a new figure is given here for the 64-meter antenna as well as the new 34-meter antennas.

The basic air path delay for the Cassegrain configuration is given by

$$\text{path length} = f + 2a + d$$

where f is the paraboloid focal length, $2a$ is the transverse axis of the hyperboloid, and d is the depth of the paraboloid from vertex to rim. The last parameter arises because it has now become standard to use the aperture plane of the paraboloid as the reference plane for antenna-to-spacecraft path length. To the above basic path must be added the dichroic plate delay for X-band. For S-band, the path length from the horn to the mirrored X-band phase center by way of the ellipsoidal reflector must be added. The theoretical depths of the dishes are calculated from the formula

$$d = \frac{r^2}{4f}$$

where d is the depth, r is the radius of the paraboloid, and f is the focal length as before. The air path delays τ_c for both the 34- and 64-m antennas and presented in Table 5.

References

1. Komarek and Otoshi, *DSN Progress Report 42-36*, pp. 35-40. Jet Propulsion Laboratory, Pasadena, Calif.

2. Otoshi, *DSN Progress Report 42-49*, pp. 45-56. Jet Propulsion Laboratory, Pasadena, Calif.

Table 1. Basic waveguide parameters

Waveguide	λ_{co}, inches (cm)	f, MHz	τ_g, ns/inch	τ_g, ns/cm
WR 430 and WC-504	8.600 (21.84)	2113	0.1057	0.0416
		2295	0.1114	0.0439
WC-125	2.500 (6.35)	8420	0.1023	0.0403
WC-137	2.336 (5.93)	8420	0.1059	0.0417
WS-90	1.800 (4.57)	8420	0.1351	0.0532

Table 2. XRO MOD III Feed Assembly

Item	τ_g, ns	
	Straight path	Side path
Horn	3.050	3.050
Throat	0.477	0.477
Rotary joints (2)	0.424	0.424
Polarizer	0.444	0.444
Orthomode	0.707	0.709
Twist	--	0.511
Switch	0.342	0.342
Feed total	5.444	5.957
Waveguide	0.542	0.460
Total to TWMs	5.986	6.417

Table 3. XRO MOD II Feed Assembly

Item	τ_g, ns	
Horn	2.070	
Spacers (2)	0.675	
Rotary joints (2)	0.424	
Polarizer	0.444	
Transition	0.520	
Switch	0.342	
Feed Total	4.475	
Elbows	0.615 (to A17)	0.844 (to A24)
Total to TWMs	5.090(A17)	5.319(A24)

Table 4. SXD S-Band Feed Assembly

Item	τ_g, ns	
	2113 MHz	2295 MHz
Horn	7.834	7.685
Rotary joints (3)	1.005	0.954
Polarizers (2)	3.452	3.256
Transition	0.794	0.753
Feed total	13.085	12.648
Elbow	1.050	0.996
Total to phase calibration coupler	14.135	13.644

Table 5. Air path delays

Segment	Path length, inches (cm)			
	34 meter		64 meter	
	S	X	S	X
f	432.000 (1097)	432.000	1067.294 (2711)	1067.294
2a	203.247 (516)	203.247	356.057 (904)	356.057
d	259.231 (658)	259.231	371.875 (945)	371.875
Dichroic/ ellipsoid/horn	106.963 (272		106.963	
Total	1001.441 (2544)	894.478 (2272)	1902.189 (4832)	1795.226 (4560)
Delay, τ_c, ns	84.847	75.785	161.163	152.101
Dichroic correction	--	0.183	-	0.183
Total delay, τ_c, ns	84.847	75.968	161.163	152.284

N79-25113

Assessment of 20-kW S-Band Transmitter

R. Dickinson and H. Hansen
Radio Frequency and Microwave Subsystems Section

The recent performance history of the 20-kW S-band transmitter, installed at three 64-meter antennas and six 26-meter antennas in the DSN, is reviewed. An increasing number of failures and Discrepancy Reports are characteristic of the wearout phase of a failure curve. The type of failures are reviewed and four options toward reducing the number and cost of failures are reviewed. These are existing (no change), refurbish (replace worn components), redesign (extensive improvement) and replacement (with completely new transmitter).

The options are compared on a ten-year life cycle cost basis using FY77 expenditures for existing equipment as a base. It is found that benefits, in terms of reduction of outage time, increase with an increase of expenditure toward improvement. The choice of option to be exercised is dependent upon the amount of outage which is acceptable and, of course, upon funds available.

I. Introduction

The 20-kW S-band transmitter subsystem is installed at each of three 64-m antennas and at each of six 26-m antennas in the DSN, making a total of nine transmitters. The installations were completed in 1966. Recent performance has been characterized by an increase in both minutes of outage and number of Discrepancy Reports (DR) on the subsystem. Figure 1 shows a sharp rise in outage and DR's for the years 1977 and 1978. This record was the reason for initiating a study of the transmitter to determine what optimum remedy would reduce this trend in failures. The object of the study is to evaluate the record of recent failure reports and to assess methods of improving performance.

II. Recent Failure Trend

An explanation advanced for the recent rise in failures is increased emphasis on Discrepancy Reporting. This may be a partial cause. However, the reports do cite increased outage time as a result of failures. Further, many failures have resulted from worn bearings, pitted relay contacts, and leaking seals. These troubles suggest that some components are in an "end-of-life" period wherein a more frequent failure pattern is typical. This situation requires attention immediately to prevent reaching a point where failure rate soars prohibitively high. Another reason for searching for options for improvement is that numerous components are becoming obsolete and difficulty has been experienced in locating replacement parts, especially when needed immediately.

For the years 1976 through 1978, the outage time illustrated in Fig. 1 was divided among power amplifier (25%), power supply (25%), heat exchanger (25%), miscellaneous (20%) and procedural (5%) sources. Table 1, which describes the reports for 1977, is representative of the failure pattern and shows many of the large outages which were the reason for the sharp rise in 1977.

Note that total outage due to fan failure, cooling system leaks, arc detector tripping, and insulation faults is 3862 minutes, about 90% of the total.

Some of the outage charged to the power amplifier was described as due to waveguide mismatch. Actually, the transmitter subsystem arc detector is operating as designed and the source of trouble may be in the waveguide, possibly leakage or other problems causing arcing or high voltage standing wave ratio (VSWR). The waveguide is subject to mechanical vibration and probably needs preventive maintenance applied.

The largest source of power supply problems is fan failure due to bearing wearout. Reference 1 considers reliability of blowers to be composed of an electrical component, constant with time, and a mechanical "wearout" component which increases with time. It appears that mechanical components such as the fans may be at the end of life period where the failure rate is increasing rapidly.

Other causes of power supply failures are in relay tripping and insulation breakdown. These, also, suggest aging problems such as contact pitting and insulation deterioration.

Heat exchanger outage shows much time lost due to leaks at seals and fittings. Again, this suggests aging from hardening of packing and gaskets, vibration, bearing wear, etc.

The 926 minutes, under miscellaneous, described as high noise are difficult to explain. A major portion of this outage is ascribed to waveguide arcing which is not a fault within the transmitter.

III. Definition of Options

Possible approaches toward the recent failure history range from "doing nothing" to replacement of the transmitter with a complete new design. "Doing nothing" implies acceptance of probable increased repair cost in future years plus acceptance of greater risk of outage during a scheduled operation when lost data might be irrecoverable. Increased maintenance cost is undesirable at any time. Losing irrecoverable data after having made minimum effort to reduce the likelihood of failure would be inexcusable. Therefore, "doing nothing" is considered a first option but essentially as a starting point in searching for the most advisable plan of action.

A review of Table 1, (plus the details of the associated Discrepancy Reports), suggests that replacement of components subject to wear and/or deterioration would offer a low cost approach to reducing failure rate. For instance, Table 1 shows outage of 479 minutes from fan and air-flow switch failure, 735 minutes from seal and fitting leaks, and 426 minutes due to low flow, fan bearings, etc., in the coolant system. These three areas total 1640 minutes and comprise 38% of a total 4285 minutes outage.

Other failures, such as wiring breakdown, offer additional potential for improvement by replacing components which show the effects of aging or high voltage deterioration.

Thus, refurbishment was chosen as one avenue for improvement which should offer substantial gains, possibly as much as 30% to 40% reduction in outage, and at low cost.

A third option would entail a more complete rebuilding/redesign of the existing transmitter. This would allow replacement of all worn components, replacement of deteriorated insulation with new wiring, and minor improvement in circuitry if deemed advisable from experience. A recommended addition would be expansion of the monitoring circuitry to a built-in test equipment system to aid in faster diagnosis of failures and, thereby, reduce outage time. The proposed redesign would be considerably higher in cost than the refurbishment, but would be limited by using most major components of the high voltage power supply, motor-generator set, heat exchanger, and the klystron.

The potential cost of a redesigned transmitter and the compromises inherent in redesigning any equipment suggest consideration of an entirely new transmitter to replace the existing equipment. The added design cost would be justified by improved performance, high reliability and extensive monitoring and self-test circuitry.

The result of the foregoing considerations was a plan to compare, on a life-cycle cost basis, four options to reduce the rise in failures, shown in Fig. 1:

Option 1. *Existing transmitter.* Continue use without action.

Option 2. *Refurbishment.* Replace worn and obsolete components with new, current items.

Option 3. *Redesign.* Replace additional components, such as obsolescent transistors. Redesign circuitry to remedy known problems, expand monitoring and self-test circuits, redesign cooling system to reduce leaks and vibration caused failures.

Option 4. *New transmitter.* Incorporate highest reliability components, current manufacture, extensive monitoring and self-test circuits. Design to current and anticipated future requirements. Centralized control would be a design objective, with an option for completely unattended

operation. A pre-failure status file would be incorporated with the monitoring circuits to store pre-failure status information.

IV. Cost History

A cost model for the DSN was reported in Ref. 2. This study developed a cost model for the DSN giving maintenance, operations, sustaining, and support costs for each subsystem (see Table 2). For the transmitter subsystem, the 1977 costs were:

Category	Cost
Maintenance	$ 646.000
Operations	501,000
Sustaining	547,000
Support	462,000
Total	$2,156,000

These figures were used as a base for making a cost comparison of the four approaches toward improvement of the transmitter.

V. Estimating Cost to Upgrade Transmitter

A comparison of life cycle cost for each of the four options was desired for the 10 year period beginning in FY80. The subsystem cost figures for FY77 were adjusted to FY80 using an estimated inflation rate of six percent per year. A subsequent allowance for the combined effect of inflation and discount rates was made using a net discount factor of 0.98 per year, per Ref. 3.

The cost for each option was estimated by making an estimate of the cost of implementation. The effect of the changes made toward lowering maintenance, operations, sustaining, and support costs was estimated in terms of percent reduction in expense which might reasonably be expected. A similar estimate was made of the minimum percentage reduction in minutes outage which could be expected. The following assumptions were made for each option:

Option 1: There will be no cost of implementation since no improvement will be made. It is believed that the failure rate is increasing due to aging of mechanical and electrical components. The rate was estimated to increase at five percent per year and this figure was assumed to increase maintenance costs proportionately. While the more frequent failures would have some effect on other costs, it was assumed that operations, sustaining, and support costs would not be increased.

Option 2: A minimum program of refurbishment was assumed:

(a) Replacement of fans with an estimated reduction in fan failures to 25% of the FY77 level.

(b) A thorough rework of coolant lines and fittings will reduce coolant system failures to 25% of FY77 level.

(c) Increased efforts to keep the waveguide mechanically tight, pressurized, and free from impurities will reduce waveguide arcing and will give at least a 20% reduction in arc detector trip-outs.

(d) Efforts to relocate critical controls plus improvement in operating procedures will reduce procedural errors by 33%.

(e) While efforts to improve and replace wiring would be made, most wiring would be unchanged. Therefore, it was assumed that the number of wiring shorts, opens, etc., would be unchanged.

The cost of implementation was estimated as the cost of new fans, coolant fittings, and other hardware to accomplish these improvements, plus the cost of associated labor. The estimated percent reduction in failures was applied to the outage time reported for 1977. The result indicated an approximate 30% reduction in outage time. This reduction was applied to maintenance costs beginning in the second year, assuming one year required for completion of the changes. A reduction of 30% in outage should aid in reducing costs of other functions and it was estimated that the cost of operations, sustaining, and support would be reduced by 10%, 5%, and 10%, respectively.

Option 3: A "best estimate" of the cost of redesign was made, for each subassembly in the transmitter subsystem, to find the cost of implementation.

The redesigned subassemblies would have new, current components and new wiring. Presumably, known problem areas would be eliminated. By this reasoning, it was concluded that improvement in outage would be considerably greater than the 30% reduction predicted in Option 2. Therefore, an estimate of 50% reduction in outage was made as a feasible design goal. This percentage was applied to maintenance to compute a ten year cost.

It was estimated that a 15% reduction in operations, sustaining, and support costs could be expected from less outage, from expanded self-test circuits, and from other refinements. This reduction was used to calculate a ten year cost for operations, sustaining, and support.

Option 4: Being in a conceptual stage, this option was the most difficult on which to make cost estimates. For cost of implementation, a "best guess" estimate was used for cost of design, fabrication and installation, of each assembly.

A major objective in the new transmitter is rapid fault diagnosis and quick repair of failures. For a conservative figure for reduction in outage time, 60% was estimated to be a minimum design goal. This percentage was used to compute maintenance cost.

The self-test circuit, pre-failure status file, and central control operation, should provide a substantial reduction in operations requirements and a 25% reduction was thought to be a realistic, minimum estimate. This figure was used in computing a ten-year cost of operations, sustaining and support.

The specification, design, and procurement of the new transmitter would require at least three years. Therefore, in computing total cost, allowance was made for maintenance cost of the existing transmitter during a three-year design and phase-in cycle.

The assumptions are listed in Table 2 and represent simply a single point selected estimate of the cost benefits which could be expected from each option. Further studies may set more definitive, reasonable goals for achievement.

VI. Results

The result of the estimates and computation of costs for the nine transmitters in the DSN are shown in Table 3 and Fig. 2. As noted above, the computations for Option 4 made allowance for costs of the old transmitter during a three-year design cycle. By way of interest, a computation was made for the new transmitter for FY83 through FY92, i.e., after completion of the design-phase in cycle. These figures, Table 3, make Option 4 especially attractive when charges for the change-over period are deleted.

VII. Conclusions

The reduction in relative outage increases proportionally to expenditure, as would be expected. The figures result from estimates considered to be conservative. The improvement from which reduction in outage was estimated is thought to be the minimum gain possible.

Option 2, refurbishment, gives a high benefit-to-cost ratio. Basically, Option 2 involves replacement of old and worn parts and this program would be the minimum to be initiated.

Additional improvements under Option 3, redesign, and Option 4, a new transmitter, are cost effective also. It appears that the choice of option is dependent upon, first, judgement as to the value of outage reduction in DSN operations, and, second, as to budget which is available for improvement purposes.

Ten years was chosen as the life cycle span to conform with current life cycle cost studies. It is thought that Options 2 and 3 would place the transmitter in condition to serve beyond ten years. A new transmitter per Option 4 should be useful for well beyond a ten-year life.

The figures for DSN expenditures for the S-band transmitter used as a base for costs were determined after a lengthy study (Ref. 2). The cost estimates for the four options were of a "best guess" type in accordance with the improvement to be made. Therefore, accuracy of the total cost is commensurate with the accuracy of the "best guess" estimate. The trend shown in Table 1 and Fig. 2 is valid, however. Basically, the results show that substantial improvement can be obtained for small costs. As more improvements are made, the benefit-to-cost ratio drops and the gain becomes more expensive.

Plans for additional refinement of the figures include contacting cognizant organizations for opinions and estimates on improvements which are required and the effect on outage and on costs if the changes are made. Also, current quotations for hardware requirements will be needed to arrive at more accurate cost figures.

References

1. MIL-HDBK-217B, 20 Sept. 1974, with Notice 1, 7 Sept. 1976, and Notice 2, 17 March 1978.

2. R. W. Burt and J. R. Lesh, "Maintenance and Operations Cost Model for DSN Subsystems," *DSN Progress Report 42-40*, May and June 1977, pp. 91-96.

3. I. Eisenberger and D. S. Remer, "The Role of Interest and Inflation Rates in Life-Cycle Cost Analysis," *DSN Progress Report 42-43*, November and December 1977, pp. 105-107.

Table 1. Discrepancy Report summary, 1977

Assembly	Outage	Description of failure
Power amplifier	351 min	Six arc detector trips, three due to suspected waveguide mismatch.
	405 min	One high reflected power indication, removed by turning on coolant flow to an isolator.
	355 min	RF power limited, required adjustment of attenuator coupler set screw.
	35 min	Beam overcurrent relay tripped.
Power supply	17 min	Arc in high voltage cable, cable replaced.
	479 min	Eight fan or air-flow switch failures required replacing six fans and two air-flow switches.
	21 min	Three relay malfunctions.
	168 min	HV cable insulation breakdown and one loose HV connector.
	165 min	Transmitter could not be turned on because of jammed emergency off switch on remote control console.
Heat exchanger	735 min	Nine leaks at seals, sight glass, fittings, etc.
	426 min	Nine failures due to low flow, lost pressure, fan bearings, etc.
Procedural error	132 min	Outage (3% of total).
Miscellaneous	424 min	High noise, due to waveguide arcing.
	502 min	High noise, cause undetermined, no recurrence.
	70 min	Other miscellaneous.

Table 2. Effect assumed on costs

Option	Maintenance	Operations	Sustaining	Support
1. No improvement	+5%/Year	N/C	N/C	N/C
2. Refurbishment	-30%	-10%	-5%	-10%
3. Redesign	-50%	-15%	-15%	-15%
4. New transmitter	-60%	-25%	-25%	-25%

Table 3. Comparative cost of transmitter options (thousands)

Transmitter option	Total cost	Implementation	Maintenance	Operations sustaining support	Cost reduction	% Outage reduction
Existing	$25,220	No cost	$8,776	$16,444	–	0%
Refurbish	$20,599	$265	$5,241	$15,093	$4,621	30%
Redesign	$18,991	$891	$4,115	$13,985	$6,229	50%
New design	$22,583	$4,406	$4,522	$13,655	$2,637	60%
New design (FY83–FY92)[a]	$18,996	$4,406	$2,983	$11,607	$6,224	60%

[a]Ten year cost after phase-out of old transmitter

ORIGINAL PAGE IS OF POOR QUALITY

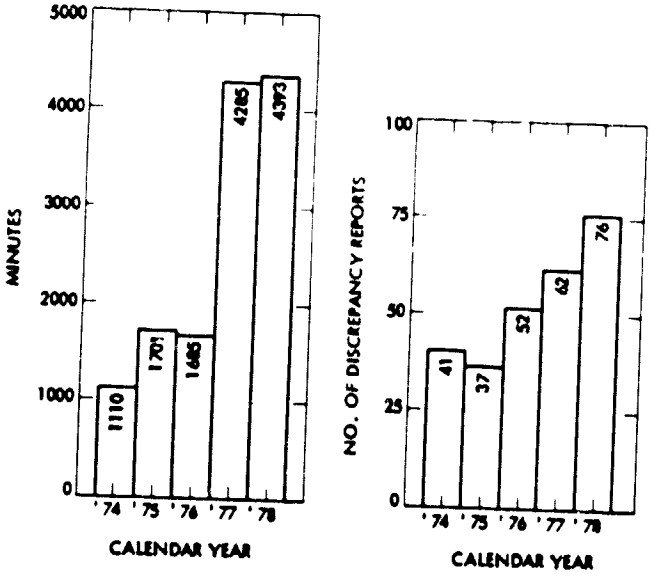

Fig. 1. 20-kW transmitter outage

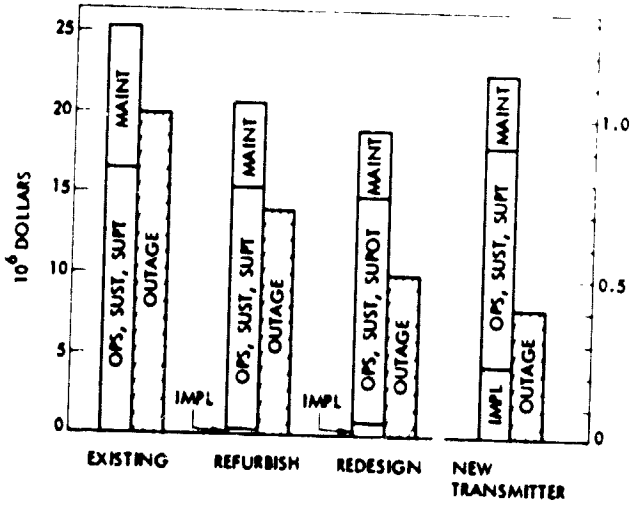

Fig. 2. Relative outage

N79-25114

A Circuit Model for Electromagnetic Properties of Waveguide Arcs

H. C. Yen
Radio Frequency and Microwave Subsystems Section

This is the third article in the series reporting the progress of a waveguide arc study undertaken by the Transmitter Group. In this article, a dielectric model of waveguide arcs is presented to relate measurable electromagnetic quantities to the physical parameters characterizing the breakdown process.

In the course of studying waveguide arcs, the RF power that is reflected from or transmitted through or absorbed by the arcing plasma is often measurable (Refs. 1 and 2). Such measurable quantities reflect the macroscopic electromagnetic properties of the waveguide arcs as seen by a matched waveguide system. In this brief article, we outline an attempt to develop a "dielectric model" relating these measured quantities to the physical parameters characterizing the breakdown such as the electron density, collision frequency, and velocity distribution. We plan to use this model to correlate the arc properties determined by the electromagnetic and optical measurements.

For simplicity, we shall assume the arc plasma behaves like a dielectric with complex dielectric constant $\epsilon = \epsilon' - j\,\epsilon''$ ($j = \sqrt{-1}$) and has a cylindrical shape of diameter d shunting the rectangular waveguide at the center of the broad wall. The imaginary part of the dielectric constant accounts for the losses taking place inside the dielectric. Figure 1 shows the equivalent circuit representation for such a dielectric rod shunting the waveguide (Ref. 3). Z_a and Z_b are given by:

$$\frac{Z_a}{R_0} = \frac{\sqrt{1-m^2}}{8m}\left\{\left(\frac{4}{\alpha^2}+1\right)\frac{\epsilon''}{[(\epsilon'-1)^2+\epsilon''^2]} - \frac{\alpha^4 m^2 \epsilon''}{6}\left[6+(2\epsilon'-3)\alpha^2\right] - j\left[\left(\frac{4}{\alpha^2}+1\right)\frac{(\epsilon'-1)}{[(\epsilon'-1)^2+\epsilon''^2]} - 2S_0 - \frac{\alpha^4 m^2}{12}\left[6(\epsilon'-1) + \alpha^2(\epsilon'^2 - 3\epsilon' + 2 - \epsilon''^2)\right]\right]\right\} \quad (1)$$

$$\frac{Z_b}{R_0} = \frac{\alpha^4 m\sqrt{1-m^2}}{24}\left\{\epsilon''\left[6+2(2\epsilon'-3)\alpha^2\right] + j\left[6(\epsilon'-1)+(2-3\epsilon')\alpha^2+(\epsilon'^2-\epsilon''^2)\alpha^2\right]\right\} \quad (2)$$

with

R_0 : real characteristic impedance of the waveguide system

λ : free-space wavelength

λ_c : cut-off wavelength

a : inner dimension of the broad waveguide wall

$$\alpha = \pi d/\lambda = \frac{\pi d}{2a}\frac{\lambda_c}{\lambda} = \left(\frac{\pi}{2}\right)\left(\frac{d}{a}\right)\left(\frac{1}{m}\right)$$

$$m = \lambda/\lambda_c = \lambda/2a$$

$$S_0 = \ln\left(\frac{4a}{\pi d}\right) - 2 + 2\left\{\sum_{n\ 3,5,\ldots}^{\infty}\left[\frac{1}{n^2 - (1/m)^2}\right]^{1/2} - \frac{1}{n}\right\}$$

Assume the waveguide system is perfectly matched before arcing and neglect the effect of the arc movement. The impedance as seen by the source in the presence of arcing is given by

$$Z_{in} = Z_b + \frac{(R_0 + Z_b)Z_a}{Z_a + Z_b + R_0} \tag{3}$$

and the reflection coefficient is

$$\Gamma = \frac{Z_{in} - R_0}{Z_{in} + R_0} \tag{4}$$

After some lengthy calculation, the ratio of the reflected power P_r to the incident power P_{in} is given by

$$\frac{P_r}{P_{in}} = |\Gamma|^2 = \frac{[1 + Y_b(2Y_a + Y_b) - X_b(2X_a + X_b)]^2 + 4[(X_a + X_b)Y_b + X_b Y_a]^2}{[1 + Y_b(2Y_a + Y_b) - X_b(2X_a + X_b) - 2(X_a + X_b + 1)]^2 + 4[(X_a + X_b)Y_b + X_b Y_a + Y_a + Y_b]^2} \tag{5}$$

where

$$\frac{Z_a}{R_0} = X_a + jY_a$$

$$\frac{Z_b}{R_0} = X_b + jY_b$$

The remaining power is dissipated either in the arc plasma or in the termination. We shall identify them as the power absorbed by and transmitted through the arc respectively.

To carry out the calculation further, we need to know the waveguide dimension, operating frequency, arc plasma size, and its dielectric constant. The arc size (d/a) is estimated to be between 0.1 to 0.2 judging from the arc tracks left behind in some reported S- and X-band experiments (Refs. 1 and 2). The effect on Z_a, Z_b due to the uncertainty of the d/a value is not completely negligible; nevertheless, the arc size can be considered relatively certain. The most important and unfortunately the least known parameter in evaluating Eqs. (1) and (2) is the dielectric constant of the arc plasma as seen below.

Assume local thermodynamic equilibrium (LTE) exists inside the arc plasma (this is usually satisfied for gas pressure larger than 1 atmosphere and probably valid for the waveguide arc also); the collision theory of gases (e.g., Ref. 4) gives the expression of plasma dielectric constant as follows.

$$\epsilon = 1 + \frac{ne^2}{m\omega\epsilon_0} \cdot \frac{4\pi}{3} \cdot \int \frac{1}{\omega - j\nu_c(u)} \cdot \frac{df_0(u,T)}{du} \cdot u^3\, du \tag{6}$$

where ω is the angular frequency of the electromagnetic wave, n is the electron density, e is the electronic charge, m is the electronic mass; ϵ_0 is the vacuum permittivity; $\nu_c(u)$ is the velocity dependent electron collision frequency and $f_0(u,T)$ is the unperturbed electron velocity distribution function. Because the state of the waveguide arc is not well understood, Eq. (6) is hard to evaluate. However, if we can assume a velocity-independent collision frequency, Eq. (6) can be reduced to a much simpler form as follows:

$$\epsilon = 1 - \frac{ne^2}{m\omega\epsilon_0} \cdot \frac{1}{\omega - j\nu_c} \equiv 1 - \frac{\omega_P^2}{\omega(\omega - j\nu_c)} \tag{7}$$

where $\omega_p^2 = ne^2/m\epsilon_0$ is the plasma frequency. Two extreme cases can be readily identified, namely that $\nu_c \ll \omega$ and $\nu_c \gg \omega$. For $\nu_c \ll \omega$, the collision process can be totally neglected and $\epsilon = 1 - \omega_p^2/\omega^2$, i.e., an ideal collisionless plasma. For $\omega < \omega_p$, the dielectric constant is a negative real number resulting in an imaginary propagation constant (evanescent mode). On the other hand, $\omega > \omega_p$ results in a real propagation constant (propagation mode). For $\nu_c \gg \omega$, the collisions are so frequent that they dominate the dielectric constant and $\epsilon = 1 - j\omega_p^2/\omega\nu_c$, resulting in substantial dissipation in the plasma. It is possible that as the arc strikes and forms, the condition may evolve from one realm to the other.

Since we are still in the process of characterizing waveguide arcs, no quantitative evaluation will be carried out at the present time. Further study along this line will be presented and discussed in the future as soon as the physical characterization of an arc plasma is feasible.

References

1. R. F. May, "Characteristics and Effects of CW High Power Breakdown in Waveguide," *IEEE MTT-S Int. Microwave Symp. Digest*, p. 151, 1976.
2. Makoto Nakamura, Takaya Saito, and Minoru Kuramoto, "Characteristics of High Power Breakdown at 28 GHz," *IEEE Trans MTT-26*, p. 354, 1978.
3. *Wave Guide Handbook*, *MIT Radiation Laboratory Series*, Boston Technical Publishers, Inc., Lexington, Mass., 1964, Vol. 10.
4. M. A. Heald, C. B. Wharton, *Plasma Diagnostics with Microwaves*. John Wiley & Sons, Inc., 1965.

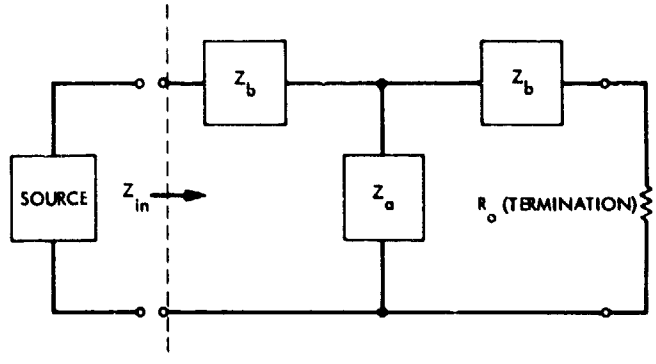

Fig. 1. Equivalent Circuit Representation for Dielectric Shunted Waveguide System

N79-25115

Waveguide Arc Study

H. C. Yen
Radio Frequency and Microwave Subsystems Section

This is the second article in the series reporting the progress of waveguide arc study undertaken by the Transmitter Group. In this article we report some experiments and their preliminary results on the arc study and the arc detector evaluation. Some future experiments are also briefly discussed.

I. Introduction

This is the second article in the series reporting the progress of waveguide arc study and protection undertaken by the Transmitter Group. In this article we briefly describe some experiments that have been or are being carried out to investigate the arc properties and to evaluate the arc detection subsystem performance. Preliminary results are presented where appropriate.

II. Controlled RF Arc Generation

Our arc study will be based on a controlled RF arc established in the laboratory; therefore, a method of generating a suitable arc has to be found. At present, we are experimenting with the idea of establishing an arc inside a resonant structure. During this phase of study, a matched waveguide system with a resonant section was assembled. A block diagram showing the essential components and the signal path is given in Fig. 1. The RF power amplifier used here is capable of delivering more than 10 W into a matched load. The resonant section is made of a 10.16-cm-long standard waveguide (WR430) with both ends enclosed with conducting planes. The coupling is achieved through iris openings in these conducting planes. The width for the input plane is such that, along with the stub tuner, zero-reflected RF power can be achieved at resonance. The iris width on the output plane is such that the loading on the resonator is negligible while providing a measurable signal for monitoring the RF fields inside the resonator.

Preliminary results showed that the unloaded quality factor of the resonator can be as high as 6.5×10^3 at 2 GHz. Since the RF source used in this experiment was not stabilized, the critical coupling state (zero reflection power at resonance) could not be maintained for long before detuning occurs due to oscillator drift and/or thermal effects. At present, we are exploring other alternatives. Among them, the scheme of using a very stable VHF oscillator in cascade with a frequency multiplier seems very promising in providing the necessary stable RF drive.

The idea of using a resonant structure is to sustain a very high RF field inside the structure with a low-power RF source. However, as soon as a breakdown is induced, the loading on the resonator can be such that a large mismatch between the source and the resonator occurs, resulting in substantially reduced fields inside. This, in turn, can quench the arcing unless the already formed arc can be sustained at a much lower field level. (This is in contrast to the arcs generated in a

high-power transmission system where arcs are continuously subject to intense incident RF until the latter is turned off.) Such difficulty is inherent in any experiment using a resonator to study the properties of a not-negligible perturbation introduced to it. Nevertheless, arc study using a resonant structure still merits further pursuit for the following reasons. During the initial breakdown of high-power transmission, arcs evolve from a rapid formative (initiation) state into a more prolonged sustained state. The field and energy balance conditions to bring about an RF arc and to sustain it are believed to be quite different, as is the case for the dc arcs. In view of protecting the transmitter, it is logical and desirable to design an arc detector to be most responsive to the waveguide arc characteristics that are exhibited during the formative stage of arcing, in addition to being responsive to the emission from an established arc. The short-lived (but readily repetitive) pulsed arcs permitted by the resonator are useful in studying the nature of this formation phase of arcing because the RF fields inside the resonator prior to the breakdown can be made to approach that present in the waveguide of a high-power transmission system, and therefore resonator arcs are expected to be good simulations of high-power waveguide arcs as far as this phase is concerned.

Since the arc formation time was reported to be quite short (about 1 microsecond at 5 kW, and much less at higher power), a prudent design requires that the arc detector should also respond positively during the following sustained state. Thus some knowledge about the sustained arcs whether they are moving (such as those that exist further along the transmitter output waveguide) or stationary (such as those that may exist at the klystron window) is also highly desirable. Methods of generating sustained RF arcs inside a resonator are currently being explored so that studies can be done using them as a source. Such arcs are not expected to be fully commensurate with existing high-power transmitter arcs; nevertheless, at this early stage of the detector engineering design, we do not wish to tie up a multimillion dollar, megawatt facility to test arc detector responsitivity. Of course, high power RF arcs are eventually needed for final verification tests.

III. DC Nitrogen Arc Experiment

During this phase of study, we also performed some dc nitrogen arc experiments mainly as an exercise of getting acquainted with the optical instrument as well as the flickering nature and radiation spectrum of nitrogen arcs. A block diagram showing the basic experimental arrangement is given in Fig. 2.

The optical instrument consists entirely of an EG&G 580/585 Spectroradiometer system. It has the capability of performing both spectrometer and radiometer measurements, but is calibrated for only the former mode of operation. When measuring the spectral distribution of a source, order sorting filters are needed for each segment of the spectrum with bandwidth 100 ~ 200 nm wide to eliminate the higher-order contributions from shorter wavelengths for a given grating position. The overall spectral range is determined by the filter type used, grating range, and photomultiplier responsivity. For our system, it covers from 350 to 1200 nm with two different photomultiplier detectors. The accuracy of the wavelength reading is estimated to be ±5 nm mainly due to a mechanical backlash in the grating scanning mechanism.

The arc was generated across a 3.2-mm gap between two tungsten electrodes with voltage of 10 to 15 kV across them. The tube was repeatedly evacuated and refilled with 1 atmosphere of dry nitrogen gas. The maximum arc current is limited by the high-voltage supply to 1 mA and as a result only a very limited light output has been obtained.

A typical raw spectrum covering the visible range is shown in Fig. 3. The spectrum is somewhat distorted because the spectrometer has quite different responsitivities over different portions of the spectral regions. After correcting for this difference, a "true" spectrum is obtained. This is a very time consuming process because it has to be done for each wavelength. Compounding the task are the original uncertainty of the raw spectrum and the possible errors in wavelength designation. In Fig. 3 we also show a sample of a corrected spectrum. As can be seen from there, detail spectral structures cannot be unambiguously resolved because of spectrometer resolution, spectrum fluctuation, wavelength errors, and the correction process for responsitivity difference. Nevertheless, such spectrum can still provide a general sketch of spectral distribution and their relative magnitude.

For wavelengths between 700 and 1200 nm, a thermoelectrically cooled infrared detector has to be used. At present we have some difficulties obtaining a consistent spectrum in this region largely due to the drift and dark current in the detector itself. This seems to imply insufficient cooling power for our detector. Further study of this problem is under way.

One useful parameter to describe the general characteristics of an arc is the arc temperature, especially when local thermodynamic equilibrium prevails. An empirical method has been established (Ref. 1) that can determine this temperature very conveniently. Specifically, for a given pressure, the nitrogen arc radiation (per unit source volume, per unit wavelength bandwidth and per unit solid angle) at wavelength $\lambda = 4955\text{Å}$ is measured. The arc temperature is then read off from an experimentally established calibration curve showing the same quantity as a function of temperature. This particular

wavelength is chosen because, in the vicinity of it, there is no line spectrum contribution (i.e., pure continuum) even at a very elevated temperature. Whereas in other parts of the spectrum, substantial contribution from line spectrum broadening can take place at elevated temperatures even though they are also devoid of line spectrum contribution at a lower temperature. Applying this scheme to our sample spectrum, the temperature was found to be well below 3000 K, which is consistent with the fact that the arc current is limited to less than 1 mA. To our knowledge, there is no nitrogen spectrum at this temperature, pressure, and arc current readily available for comparison; therefore, to establish confidence in our measurement technique, spectra at much higher arc currents are needed.

IV. Transmitter Test Light Upgrading

A nitrogen atmosphere test light would be quite desirable as a light source for arc detector testing. However, until such a unit can be developed and implemented, the xenon-type flash lamp seems to be an interim cost effective test lamp despite the fact that the spectrum it produces is different. In fact, such a lamp can perform almost all the functions that we expect from an ideal nitrogen test light.

A feasibility study of upgrading the existing transmitter test light subsystem was initiated during this phase of study. The goal of this study is to evaluate a commercial solid state electronic camera flash as a candidate for replacing the presently used test light. The attractive features of the flash unit used in this study (Kodak Ektra Electronic Flash) are small size, low-voltage power source (3 V), fast rise time, and intense light output.

The test light is mounted on the transition region from the klystron amplifier output window to a WR430 elbow section. It performs routine arc detector checks, provides a time reference for response time check and can be used in the arc detector sensitivity calibration, which in turn provides the necessary information for setting the detector safety margin.

The unit was slightly modified so that it could be electronically triggered to provide well-controlled and repetitive unambiguous flashings. At the recommended +3 V supply, it required three or four seconds to fully charge the unit with peak charging current as high as 1.5 A. The standard arc detector was used to detect the flash via an optical fiber link at the bend of the elbow. The time delay from the rising edge of the triggering pulse to the rising edge of the arc detector output was measured at several test light levels. The results are summarized in Fig. 4.

Ith is the threshold intensity to produce an observable detector output. Since both pulses have rather short rise times (of the order of nanoseconds), the observed delay can be attributed to the combination of the delay in actual flashing, delay due to light path, delay due to photodiode response, and delay due to voltage comparator (LM211) in the arc detector circuitry. On the time scale of observed delay, it seems that most of the delay is due to the voltage comparator response when the input voltage to it is small (i.e., at very low-light level). This is partially supported from the specification of said comparator where it is shown that substantial response time is required at low input level. To show the weakening effect on the light eventually detected by the photodiode due to the waveguide and optical fiber link, the "dead" time of the system was measured by directly connecting the flash unit output port to the arc detector input port. At maximum flash output, the delay time was measured at 0.7 μs as opposed to the minimal observed time of 6 μs in the actual waveguide configuration.

Clearly, from the results obtained, we conclude, to make an arc detector effective and reliable, every step of caution has to be taken to assure the maximum amount of light reaching the photodiode surface. Assuming that the detector remains unaltered, the following areas for improvement remain: waveguide wall reflectivity, optical acceptance geometry, optical fiber attenuation, and optical fiber-to-photodiode coupling. Among them, the acceptance geometry and fiber-diode coupling seem to offer more room for improvement. Only the coupling problem will be discussed here and we will say more about optical acceptance geometry in the next section.

On a closer examination of our hardware, we found that the optical fiber-to-photodiode coupling was rather poor in our present set up. The problem arises mainly from the physical construction of the fiber itself, which is custom-made and has two input and two output channels. The individual tiny fibers that constitute the main optical fiber are so arranged that whenever there is light in either input channel, it will be equally split into two output channels. Ideally we would like to have the light emerging from the output channel uniformly distributed over the whole cross-section area to maximize the effective interception between this cross section and the photodiode active surface because they are not of the same size and shape. Unfortunately, this is not the case for our fibers. The light emerging from our optical fiber tends to cluster in patches and is distributed irregularly over the cross section. With the active photodiode surface smaller than the optical fiber cross section, the effective light coupling can be severely reduced depending on the actual light distribution.

An attenuation experiment was carried out to investigate the loss due to this "optical mismatch." A monochromatic light source, whose size is the same as the diameter of an

optical probe aperture used for detecting the light at the output end but less than that of the optical fiber, provides a uniform illumination on the input cross section. The results of the measurement were summarized in Table I. Judging from the state of the art of optical fiber technology and taking into account the length involved and the power splitting feature, an attenuation of 5.0 ~ 5.5 dB between channels is regarded as normal. We have incurred an additional attenuation of up to 3.1 dB due to poor coupling. This deficiency in coupling can be corrected without difficulty. If we exchange the roles of input and output channels, we can obtain a uniform light output over the entire cross section at the input channels.

V. LED Array Simulation Experiment

One piece of design information that is useful in maximizing the amount of light received by the detector is the fraction of the light output that enters the optical fiber for a given source and fiber configuration. Not knowing where the breakdown will occur in the general area of the klystron amplifier output window, it is impossible to obtain a specific answer. In the following, we attempt to make an order-of-magnitude estimate of this fraction based on the assumption that the arc will strike across the center of the broad wall of the waveguide at the far end where the test light is situated. A linear LED array was used to simulate the arc. Its dimension is 3.2 mm × 50.8 mm, and at a distance of more than 50 cm away, it can be regarded as an effective point source. The desired fraction is then obtained by taking the ratio of the amount of light received at the input end of the optical fiber to the light intensity of the source. The optical measurement is similar to that shown in Fig. 2 and the essential data are summarized below:

P = Total light emitted from the source per unit solid angle per unit wavelength (i.e., irradiant intensity per unit wavelength)

$= 2.14 \times 10^{-6}$ W/nm-rad

I = Total light received at the input end of the optical fiber per unit wavelength

$= 4.1 \times 10^{-10}$ W/nm

Therefore the effective solid angle subtended is

$$\Omega_{eff} = \frac{I}{P} = 1.9 \times 10^{-4} \text{ rad}$$

However, the apparent solid angle is approximately

$$\Omega_{app} \approx 9.0 \times 10^{-5} \text{ rad}$$

That is, the effective solid angle is twice the apparent solid angle indicating that the contribution of light indirectly scattered into the optical fiber is not insignificant. In fact, it is quite comparable to that from direct scattering. One other aspect worthy of note from the above calculation is that a linear source can radiate into a solid angle of the order of π radians while our effective solid angle is only about 2×10^{-4} radian, i.e., only about 0.01 percent of the light gets detected in our present geometry. It seems reasonable to assume this collection efficiency can be improved somewhat by enlarging the aperture of the optical fiber until the electromagnetic characteristics of the system start to be affected.

Reference

1. J. C. Morris, R. U. Krey and G. R. Bach, "The Continuum Radiation of Oxygen and Nitrogen for Use in Plasma Temperature Determination," *J. Quant. Spectrosc. Radiat. Transfer*, Vol. 6, pp. 727-740.

Table 1. Optical fiber attenuation and one of the test configurations

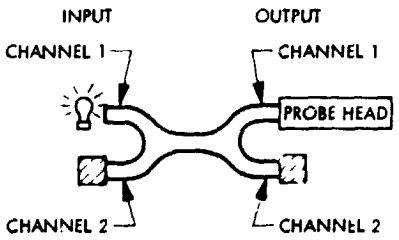

Input channel	Output channel	Attenuation, dB ± 0.3
1	1	6.2
1	2	8.6
2	1	7.6
2	2	6.1

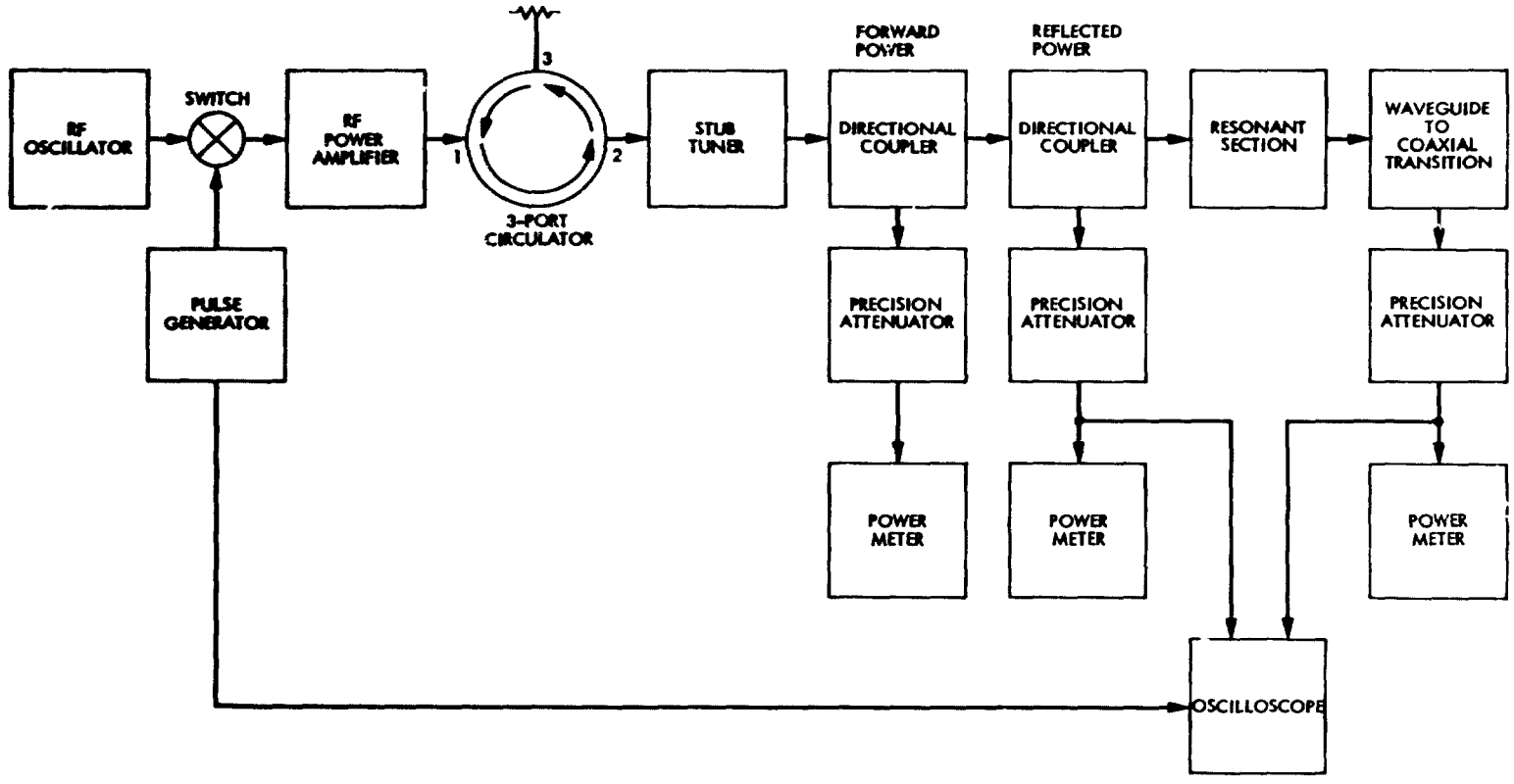

Fig. 1. Block diagram showing the signal path for the experiment of controlled RF arcs

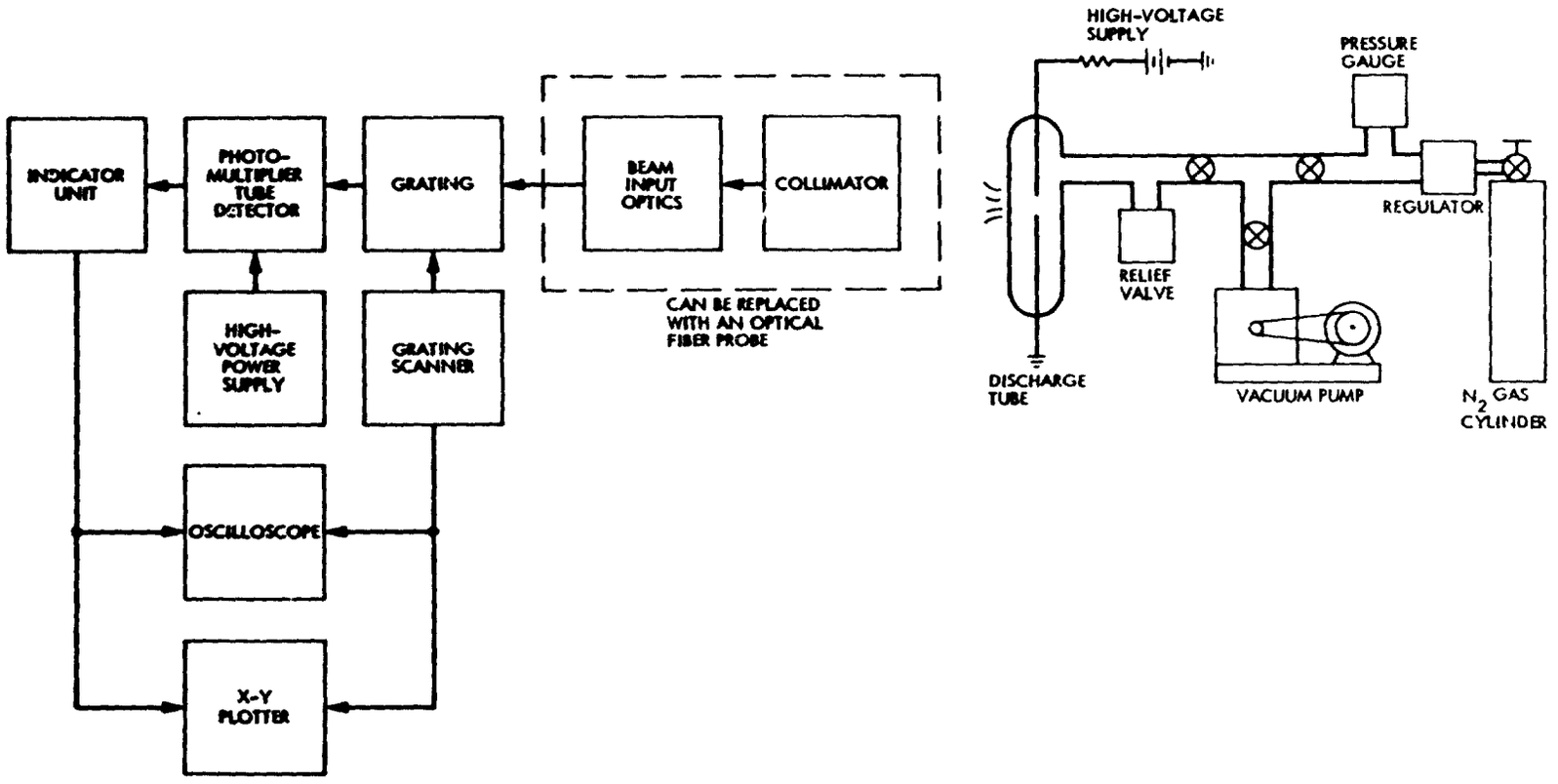

Fig. 2. Experimental set up for dc nitrogen arc study

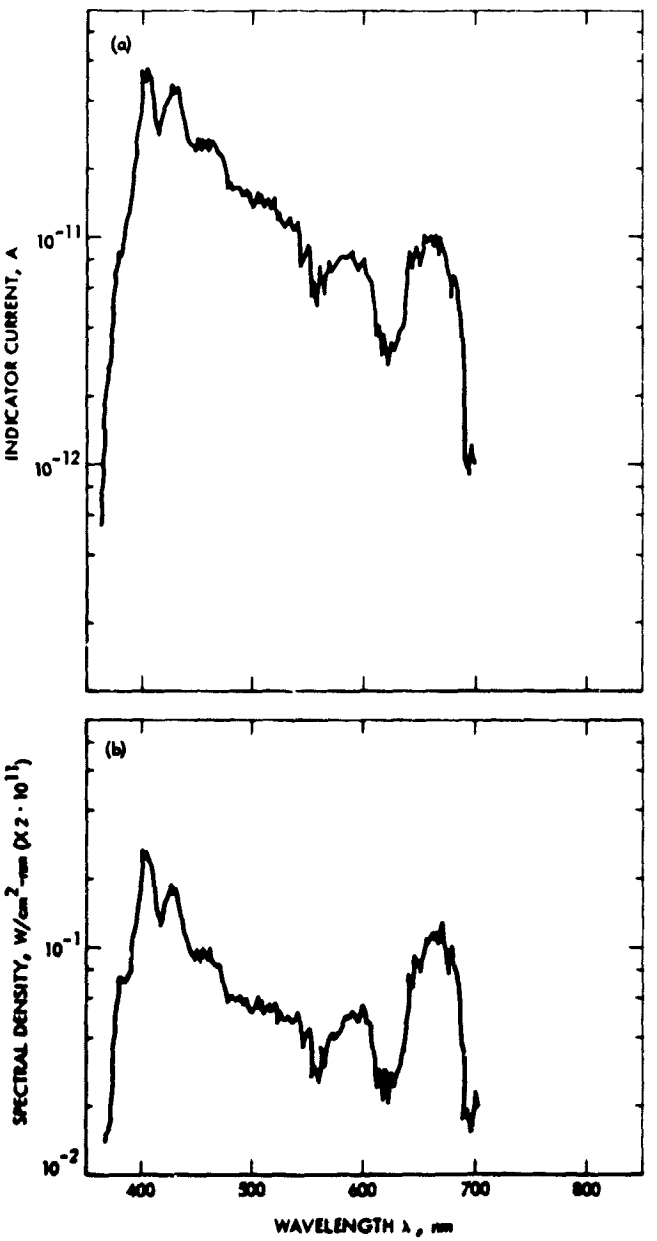

Fig. 3. Nitrogen spectrum: (a) a sample of raw spectrum; (b) the same spectrum after correction

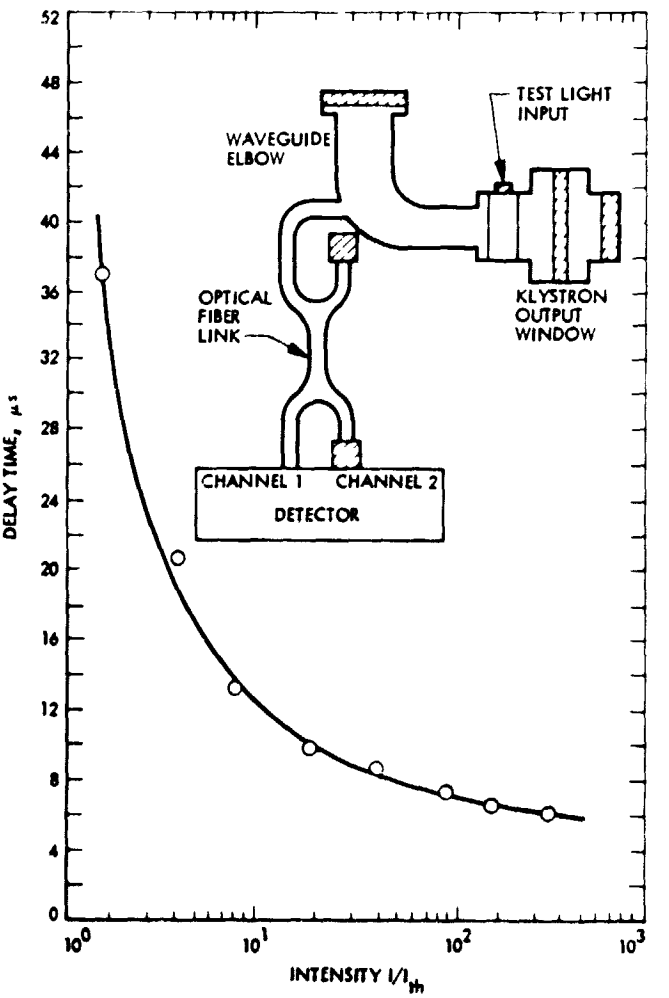

Fig. 4. Delay time versus test light intensity

N79-25116

Radio Frequency Interference Effects of Continuous Wave Signals on Telemetry Data: Part II

P. W. Low
Deep Space Network Operations Section

In a previous report (DSN Progress Report 42-40), the results of the first series of radio frequency interference tests and an empirical telemetry bit SNR degradation model derived for a fixed telemetry data rate and a fixed telemetry data power were presented.

In this report, Part II, the results of a second series of radio frequency interference tests and the derived telemetry bit SNR degradation model, which includes the telemetry data rate and the telemetry data power as independent variables for characterizing the continuous wave interference effects on telemetry data, are presented. This generalized telemetry bit SNR degradation model has been implemented in the second version of the Deep Space Interference Prediction software.

I. Introduction

As part of an ongoing effort to investigate radio frequency interference (RFI) effects on Deep Space Network (DSN) spacecraft telecommunication signals, a series of RFI tests was formulated and conducted with standard Deep Space Station (DSS) equipment to investigate continuous wave (CW) interference effects on telemetry data in 1976. In analyzing the effects, the CW interference was treated as an extraneous noise. Empirical telemetry bit signal-to-noise ratio (SNR) degradation and drop-lock models were then developed based on test data and certain physical characteristics of the telemetry data processing system. These tests and resulting models, which were described in a previous report (Ref. 1), however, were strictly for a telemetry data rate of 2000 bps and a telemetry data power of about -140.5 dBm. To further understand the CW interference effect on telemetry data as a function of the telemetry data rate and the telemetry data power, a second series of RFI tests was conducted at the Goldstone Deep Space Station (DSS 11). This report describes these tests and the new telemetry bit SNR degradation model derived.

II. Telemetry Interference Test

A. Test Objectives

The test objectives were (1) to characterize the telemetry bit SNR degradation as a function of the telemetry data rate and the telemetry data power in the presence of a CW interfering signal, (2) to integrate the results into the previously developed telemetry bit SNR degradation model (Ref. 1) to form a generalized telemetry bit SNR degradation model, and (3) to investigate the CW interference effect on the high-order telemetry subcarrier harmonics.

B. Test Configuration

A block diagram of the test configuration is shown in Fig. 1. The carrier tracking and telemetry data processing system is the standard DSS equipment. The Simulation Conversion Assembly (SCA) was used to generate two binary data streams; each data stream bi-phase-modulated a squarewave subcarrier. The two composite (data plus subcarrier) signals are then mixed and used to phase-modulate a continuous wave carrier. Operations support software was used in the Telemetry and Command Processor (TCP) to provide the telemetry data SNR statistics.

The desired downlink signal used for the test was a typical Viking spacecraft dual-subcarrier downlink signal. However, only the effects on the high-rate subcarrier were investigated. Table 1 summarizes the exact desired downlink signal configuration.

C. Test Cases

Seventy-eight RFI cases were tested. They may be categorized into three different sets:

(1) Telemetry data power variant: The CW signal was placed 1.2 Hz away from the upper telemetry subcarrier. The telemetry data rate was set at 2000 bps. The telemetry data power was set to three different levels; for each data power level, the telemetry data SNR degradation was measured at selected CW signal levels.

(2) Telemetry data rate variant: The CW signal was placed 1.2 Hz away from the upper telemetry subcarrier. The telemetry data was set to four different data rates; for each telemetry data rate, the telemetry data SNR degradation was measured at selected CW signal levels.

(3) CW interfering signal's effect on high-order (through the 27th) telemetry subcarrier harmonics: The telemetry signal level and data rate were fixed at -140.9 dBm and 2000 bps, respectively. The CW signal was placed coincident with each of the telemetry subcarrier harmonics one through twenty-seven (odd numbered harmonic only); for each case, the telemetry data SNR degradation was measured.

Tables 2 through 4 summarize the test cases performed.

III. Bit Signal-to-Noise Ratio Degradation Analysis

A. Summary of Previous Bit SNR Degradation Model

In a previous report (Ref. 1), a telemetry bit SNR degradation model for a fixed data rate of 2000 bps and a fixed telemetry data power of -140.5 dBm (composite average) in the presence of a CW interfering signal was presented. In developing the model, the CW interfering signal was treated as an extraneous noise. Using the basic definition of received bit SNR:

$$SNR_I = 10 \log \left(\frac{P_D T_B}{K T_S} \right)$$

and

$$SNR_{IR} = 10 \log \left[\frac{P_D T_B}{K (T_S + T_R)} \right]$$

where:

SNR_I = received bit SNR when RFI is not present

SNR_{IR} = received bit SNR when RFI is present

P_D = total high-rate data power

T_B = bit (symbol) time ($1/BR$)

K = Boltzmann's constant

T_S = effective system noise temperature when RFI is not present

T_R = increased system noise temperature induced by the CW interfering signal.

Then, defining the received bit SNR degradation as:

$$\Delta SNR_I = SNR_I - SNR_{IR}$$

The mathematical expression of ΔSNR_I was derived:

$$\Delta SNR_I = 10 \log \left(\frac{T_S + T_R}{T_S} \right) \quad (1)$$

Also, using the basic relationships: (See Fig. 2)

$$SNR_O = SNR_I - L_S$$

and

$$SNR_{OR} = SNR_{IR} - L_{SR}$$

where

SNR_O = SSA bit SNR when RFI is not present

SNR_{OR} = SSA bit SNR when RFI is present

L_S = System loss when RFI is not present

L_{SR} = System loss when RFI is present

And, defining the SSA bit SNR degradation as:

$$\Delta SNR_O = SNR_O - SNR_{OR}$$

the mathematical function of ΔSNR_O was expressed as:

$$\Delta SNR_O = \Delta SNR_I - (L_S - L_{SR}) \qquad (2)$$

Having Eqs. (1) and (2) established, the functional relationship of the CW interfering signal and the increased system noise temperature it induces for the case of the CW signal coincident with the telemetry subcarrier was empirically derived from the test data (ΔSNR_O). The result was (NOTE: L_S and L_{SR} were obtained from the Telemetry Analysis Program):

$$T_R \Big|_{\substack{\Delta f_{1sc} = 0 \\ BR = 2K \\ P_D = -140.5\ \text{dBm}}} = \left[\left(10^{8.21e^{.0421 P_{RFI}}}\right)^2 + (40)^2\right]^{1/2} - 39.5 \qquad (3)$$

where:

Δf_{1sc} = frequency separation between the CW interfering signal and the telemetry subcarrier

P_{RFI} = CW interfering signal level (dBm)

Then, the telemetry bit SNR degradation characteristic with the CW interfering signal at various frequency offsets from the subcarrier or subcarrier harmonics (test data included up to the fifth subcarrier harmonic) was investigated. This was done, first, by deriving the telemetry system's magnitude response function, which is:

$$|H(n, \Delta f_{nsc})|^2 = \left(\frac{h\, T_B}{n}\right)^2 \left(\frac{\sin(\pi \Delta f_{nsc}\, T_B)}{\pi \Delta f_{nsc}\, T_B}\right)^2$$

where

h = gain

n = subcarrier harmonic number, $n = 1, 3, 5$, etc

$$\Delta f_{nsc} = \begin{cases} |(f_c + f_{nsc}) - f_{RFI}| & \text{if } f_{RFI} > f_c \\ |(f_c - f_{nsc}) - f_{RFI}| & \text{if } f_{RFI} < f_c \end{cases}$$

f_{nsc} = nth harmonic of subcarrier ($n \cdot f_{sc1}$)
(1st harmonic is also referred to as subcarrier)

f_{RFI} = CW interfering signal frequency

Thus, the power response function of the telemetry system for any CW signal with power, P, would be:

$$P(n, \Delta f_{nsc}) = (P)\left(\frac{h\, T_B}{n}\right)^2 \left(\frac{\sin(\pi \Delta f_{nsc}\, T_B)}{\pi \Delta f_{nsc}\, T_B}\right)^2 \qquad (4)$$

Next, the following relationship (ratio) was formed:

$$\frac{P(n, \Delta f_{nsc})}{P(1, 0)}\Big|_{BR\,=\,2K} = \left(\frac{1}{n^2}\right) \cdot \left(\frac{\sin(\pi \Delta f_{nsc}\, T_B)}{\pi \Delta f_{nsc}\, T_B}\right)^2$$

Expressing it in decibel format, and rearranging terms:

$$P(n, \Delta f_{nsc}) = P(1, 0) - 20 \log(n) + 10 \log\left(\frac{\sin(\pi \Delta f_{nsc}\, T_B)}{\pi \Delta f_{nsc}\, T_B}\right)^2$$

Finally, this relationship was integrated into Eq. (3) along with two adjustment factors (based on test data) to form a generalized expression for T_R:

$$T_R \Big|_{\substack{BR = 2K, \\ P_D = -140.5\ \text{dBm}}} = \left[\left(10^{8.21e^{0.0421 P_I}}\right)^2 + (40)^2\right]^{1/2} - 39.5 \qquad (5)$$

$$P_I = P_{RFI} - (0.94) \cdot (20 \log n) + (0.90) \cdot \left[10 \log\left(\frac{\sin\left(\Delta f_{nsc}\left(\frac{\pi}{BR}\right)\right)^2}{\Delta f_{nsc}\left(\frac{\pi}{BR}\right)}\right)\right] \qquad (6)$$

where

$BR = 1/T_B$

n = number of the subcarrier harmonic which the CW interfering signal is affecting.

Thus, Eqs. (6), (5), (1), and (2) formed the telemetry bit SNR degradation model as presented in Ref. 1.

B. Degradation as a Function of Telemetry Bit Rate and Telemetry Data Power

In this paragraph, the telemetry bit SNR degradation model as described in the preceding paragraph is to be generalized to include the telemetry bit rate and the telemetry data power as independent variables. To do this, an empirical approach is used. The functional relationship of the telemetry bit SNR degradation and the two telemetry parameters (bit rate and data power) in the presence of the CW interfering signal is derived from the test data.

Let us first assume that the effect of the CW interfering signal on the telemetry bit SNR is dependent on the telemetry bit rate and the telemetry data power. Let us further assume that for a CW interfering signal with power, P, input into the telemetry system, its relative effect on the telemetry bit SNR as a function of the telemetry bit rate and the telemetry data power may be expressed in terms of effective CW interfering signal power in the form of:

$$P_e = P \cdot \frac{(BR)^u}{(P_D)^v}$$

where:

P_e = effective CW interfering signal power

u, v = coefficients to be determined from the test data.

Substituting the above relationship into the telemetry system's power response function (Eq. 4), an effective power response function of the telemetry system for any CW signal with power P is obtained:

$$P_e(P_D, BR, n, \Delta f_{nsc}) = P \cdot \frac{(BR)^u}{(P_D)^v}\left(\frac{h}{n \cdot BR}\right)^2 \left[\frac{\sin\left(\pi \frac{\Delta f_{nsc}}{BR}\right)}{\pi \frac{\Delta f_{nsc}}{BR}}\right]^2$$

Combining the BR terms, and expressing the result in decibel format,

$$P_e(P_D, BR, n, \Delta f_{nsc}) = P - v(P_D) + 20\log(h) - 20\log(n) - w(10\log BR) + 10\log\left[\frac{\sin\left(\pi \frac{\Delta f_{nsc}}{BR}\right)}{\pi \frac{\Delta f_{nsc}}{BR}}\right]^2$$

where $w = 2 - u$, the coefficient to be determined from the test data. Let $P_D = -140.5$ dBm, $BR = 2000$, $n = 1$, and $\Delta f_{nsc} = 0$. Then,

$$P_e(-140.5, 2000, 1, 0) = P - v(-140.5) + 20\log h - w(10\log 2000)$$

Thus (in decibel format),

$$P_e(P_D, BR, n, \Delta f_{nsc}) - P_e(-140.5, 2000, 1, 0) = -v(P_D) + v(-140.5) - 20\log n - w(10\log BR) + w(10\log 2000) + 10\log\left[\frac{\sin\left(\pi \frac{\Delta f_{nsc}}{BR}\right)}{\pi \frac{\Delta f_{nsc}}{BR}}\right]^2$$

Or,

$$P_e(P_D, BR, n, \Delta f_{nsc}) = P_e(-140.5, 2000, 1, 0) - v(P_D) + v(-140.5) - 20\log n - w(10\log BR) + w(10\log 2000) + 10\log\left[\frac{\sin\left(\pi \frac{\Delta f_{nsc}}{BR}\right)}{\pi \frac{\Delta f_{nsc}}{BR}}\right]^2$$

Remember that Eq. (3) as described in the preceding paragraph is based on the telemetry bit rate of 2000 bps, telemetry data power of −140.5 dBm, and the interfering signal level P_{RFI} with Δf_{1sc} equal to zero. Thus, applying the above relationship, Eq. (3) may be generalized as:

$$T_R = \left[\left(10^{8.21e^{0.0421\,P_I}}\right)^2 + (40)^2\right]^{1/2} - 39.5 \quad (7)$$

$$P_I = P_{RFI} - 20\log n - v\,(P_D) + v\,(-140.5) - w\,(10\log BR)$$

$$+ w\,(10\log 2000) + 10\log\left[\frac{\sin\left(\pi\frac{\Delta f_{nsc}}{BR}\right)}{\pi\frac{\Delta f_{nsc}}{BR}}\right]^2$$

From the test data, v and w are best determined to be 0.11 and 0.89, respectively. This, however, is done with the retention of the two adjustment factors (0.94 and 0.90), which were introduced into Eq. (6). Thus, P_I becomes:

$$P_I = P_{RFI} - (0.94)\,(20\log n) - (0.11)\,(P_D) + (0.11)\,(-140.5)$$

$$- (0.89)\,(10\log BR) + (0.89)\,(10\log 2000)$$

$$+ (0.90)\left[10\log\left(\frac{\sin\left(\pi\frac{\Delta f_{nsc}}{BR}\right)}{\pi\frac{\Delta f_{nsc}}{BR}}\right)^2\right]$$

Simplifying the above equation, then:

$$P_I = P_{RFI} - (0.94)\,(20\log n) - (0.11)\,P_D$$

$$- (0.89)\,(10\log BR)$$

$$+ (0.90)\left[10\log\left(\frac{\sin\left(\pi\frac{\Delta f_{nsc}}{BR}\right)}{\pi\frac{\Delta f_{nsc}}{BR}}\right)^2\right]$$

$$+ (13.924) \quad (8)$$

Eqs. (7) and (8) may be further simplified by letting:

$$P_R = P_I - (13.924)$$

Substituting this relationship into Eqs. (7) and (8), and then simplifying, the telemetry bit SNR degradation becomes:

$$P_R = P_{RFI} - (0.94)\,(20\log n) - (0.11)\,P_D$$

$$- (0.89)\,(10\log BR)$$

$$+ (0.90)\left[10\log\left(\frac{\sin\left(\pi\frac{\Delta f_{nsc}}{BR}\right)}{\pi\frac{\Delta f_{nsc}}{BR}}\right)^2\right] \quad (9)$$

$$T_R = \left(10^{2.951e^{0.0421\,P_R}} + 1600\right)^{1/2} - 39.5 \quad (10)$$

$$\Delta SNR_I = 10\log\left(\frac{T_S + T_R}{T_S}\right) \quad (1)$$

$$\Delta SNR_O = \Delta SNR_I - (L_S - L_{SR}) \quad (2)$$

Using this generalized model (Eqs. (9), (10), (1), and (2)), ΔSNR_I are calculated and plotted against the test data for test cases 1 through 64 in Figs. 3 and 4.

C. Interfering Signal's Effect on High-Order Telemetry Subcarrier Harmonics

The CW interfering signal's effect on telemetry bit SNR when the CW interfering signal is placed at various high-order subcarrier harmonics is to be investigated in this paragraph. To do this, let us first examine the band-pass characteristic of the telemetry channel of the receiver system used for the test.

The receiver system used for the test is a double-heterodyne phase-locked receiver system. The simplified functional block diagram of the telemetry channel of the receiver system is shown in Fig. 5. As can be seen in Fig. 5, the desired carrier input to the receiver system is being down-converted in two stages to a 10-MHz IF signal, which is then fed into the Subcarrier Demodulator Assembly for carrier and subcarrier demodulation. The overall normalized magnitude response of this 10-MHz IF telemetry channel of the receiver system is shown in Fig. 6. Thus, the CW interfering signal (or any extraneous signal) that passes through the receiver is subjected

to (1) the frequency down-conversion as is the desired carrier, and (2) the corresponding signal level attenuation as characterized by the normalized magnitude response (Fig. 6). Therefore, in evaluating the CW interfering signal's effect on the telemetry bit SNR when the CW interfering signal is at a high-order subcarrier harmonic (or at any frequency away from the carrier), the CW signal level, P_{RFI}, in Eq. (9) must be accounted for its attenuation due to the receiver's magnitude response as shown in Fig. 6. Using Fig. 6 and the telemetry bit SNR degradation model derived in the preceding paragraph, ΔSNR_I are calculated and tabulated against the test data for the test cases 65 through 78 in Table 5.

The receiver's normalized magnitude response curve, as shown in Fig. 6, represents the nominal design characteristics; the actual normalized magnitude response is not presently available. Because of this and the fact that the nominal design normalized magnitude response curve, as shown in Fig. 6, covers only a relatively small frequency domain (about 9 MHz), the receiver's normalized magnitude response function is not presented in this report.

IV. Summary of Analysis Results

When a CW interfering signal is present in the DSS tracking and telemetry data processing system, the telemetry bit SNR is degraded. The telemetry bit SNR degradation as a function of the CW interfering signal power, the frequency separation between the CW interfering signal and the desired telemetry subcarrier, and the effective system noise temperature of the DSS tracking and telemetry data processing system was modeled in the previous report (Ref. 1). In this report, the telemetry bit SNR degradation was found to be also dependent on the telemetry bit rate and the telemetry data power. The bit SNR degradation model was generalized to include all these variables:

$$\Delta SNR_O = \Delta SNR_I - (L_S - L_{SR})$$

$$\Delta SNR_I = 10 \log \left(\frac{T_S + T_R}{T_S} \right)$$

where

$$T_R = \left(10^{2951 e^{0.0421 P_R}} + 1600 \right)^{1/2} - 39.5$$

$$P_R = P_{RFI} - (0.94)(20 \log n) - (0.11) P_D$$

$$- (0.89)(10 \log BR)$$

$$+ (0.90) \left[10 \log \left(\frac{\sin \left(\pi - \frac{\Delta f_{nsc}}{BR} \right)}{\pi \frac{\Delta f_{nsc}}{BR}} \right)^2 \right]$$

When the CW interfering signal is significantly away from (or not coincident with) the desired carrier in frequency, the effective CW interfering signal power is reduced. The reduction is due to the relative attenuation caused by the receiver's normalized magnitude response as shown in Fig. 6. Therefore, in calculating the bit SNR degradation, the P_{RFI} term in the above bit SNR degradation model must be adjusted for its signal level reduction with the corresponding attenuation caused by the receiver's normalized magnitude response. The receiver's normalized magnitude response function was not included in this analysis because of the lack of actual data.

V. Conclusions

Based on the test data obtained from this series of CW interference tests, the telemetry bit SNR degradation model previously developed (Ref. 1) was generalized to include the telemetry data rate and the telemetry data power as independent variables. Test results showed that the telemetry bit SNR degradation is relatively more sensitive to the telemetry data rate than the telemetry data power. The test results of the CW interference effect on the high-order telemetry subcarrier harmonics revealed that when the CW interfering signal is away from the desired carrier in frequency, the effective interfering power is reduced due to the receiver's band-pass characteristics (magnitude response). Thus, when using the telemetry bit SNR degradation model, the CW interfering signal power must be adjusted (reduced) accordingly with the receiver's band-pass characteristic function. Because of the lack of actual data, the receiver's band-pass characteristic function was not derived in this analysis.

Additional tests and analysis are needed to better understand the DSS equipment's RFI susceptibility. Some major tasks will include:

(1) The receiver's band-pass characteristic function and its image rejection capability.

(2) Effects on the telemetry system for various kinds of interference spectrum.

Reference

1. Low, P. W., "Radio Frequency Interference Effects of Continuous Sinewave Signals on Telemetry Data" in *The Deep Space Network Progress Report 42-40*, Jet Propulsion Laboratory, Pasadena, Calif., August 15, 1977.

Table 1. Desired downlink signal configuration

Carrier frequency (f_c)	2293.148160 MHz
Carrier power (P_c)	See Tables 2–4
High rate data	
Subcarrier frequency (f_{sc1})	240 kHz
Data format	Uncoded
Bit rate (BR)	See Tables 2–4
Modulation index	66.54 degrees
Data power (P_D)	See Tables 2–4
Low rate data	
Subcarrier frequency	24 kHz
Data format	Uncoded
Bit rate	33-1/3 bps
Modulation index	19.25 degrees
Data power	(P_c – 9.1) dBm

Table 2. Telemetry data power variant test cases

Test number	P_c, dBm	P_D, dBm	BR, bps	T_S, K	P_{RFI}, dBm	f_{RFI}, Hz
1	−141.5	−134.3	2000	25.2	−165.5	$f_c + f_{sc1} + 1.2$
2					−160.0	
3					−155.0	
4					−150.0	
5					−146.0	
6					−143.0	
7					−140.0	
8					−137.0	
9					−134.5	
10	−141.5	−134.3			−132.0	
11	−148.1	−140.9			−150.5	
12					−149.5	
13					−145.0	
14					−142.5	
15	−148.1	−140.9			−140.0	
16	−155.0	−147.8			−165.0	
17					−160.0	
18					−155.0	
19					−151.0	
20					−148.0	
21	−155.0	−147.8	2000	25.2	−146.0	$f_c + f_{sc1} + 1.2$

ORIGINAL PAGE IS
OF POOR QUALITY

Table 3. Telemetry data rate variant test cases

Test number	P_C, dBm	P_D, dBm	BR, bps	T_S, K	P_{RFI}, dBm	f_{RFI} Hz
22	−157.5	−150.3	200	25.2	−165.0	$f_c + f_{sc1} + 1.2$
23	↓	↓	↓	↓	−160.5	↓
24	↓	↓	↓	↓	−155.0	↓
25	↓	↓	↓	↓	−152.0	↓
26	−157.5	−150.3	200	25.2	−151.0	↓
27	−145.0	−137.8	4,000	25.6	−164.0	↓
28	↓	↓	↓	↓	−160.0	↓
29	↓	↓	↓	↓	−157.0	↓
30	↓	↓	↓	↓	−154.0	↓
31	↓	↓	↓	↓	−151.0	↓
32	↓	↓	↓	↓	−148.0	↓
33	↓	↓	↓	↓	−145.0	↓
34	↓	↓	↓	↓	−142.5	↓
35	↓	↓	↓	↓	−139.5	↓
36	↓	↓	↓	↓	−137.5	↓
37	−145.0	−137.8	4,000	↓	−135.0	↓
38	−138.0	−130.8	20,000	↓	−164.0	↓
39	↓	↓	↓	↓	−160.0	↓
40	↓	↓	↓	↓	−157.0	↓
41	↓	↓	↓	↓	−154.0	↓
42	↓	↓	↓	↓	−151.0	↓
43	↓	↓	↓	↓	−148.0	↓
44	↓	↓	↓	↓	−145.0	↓
45	↓	↓	↓	↓	−142.0	↓
46	↓	↓	↓	↓	−139.0	↓
47	↓	↓	↓	↓	−137.0	↓
48	↓	↓	↓	↓	−135.0	↓
49	↓	↓	↓	↓	−133.5	↓
50	↓	↓	↓	↓	−131.5	↓
51	↓	↓	↓	↓	−129.5	↓
52	−138.0	−130.8	20,000	25.6	−127.5	↓
53	−130.5	−123.3	80,000	25.2	−165.0	↓
54	↓	↓	↓	↓	−160.0	↓
55	↓	↓	↓	↓	−155.0	↓
56	↓	↓	↓	↓	−150.0	↓
57	↓	↓	↓	↓	−146.0	↓
58	↓	↓	↓	↓	−143.0	↓
59	↓	↓	↓	↓	−140.0	↓
60	↓	↓	↓	↓	−136.5	↓
61	↓	↓	↓	↓	−134.0	↓
62	↓	↓	↓	↓	−131.5	↓
63	↓	↓	↓	↓	−128.0	↓
64	−130.5	−123.3	80,000	25.2	−125.0	$f_c + f_{sc1} + 1.2$

Table 4. Test cases of CW interfering signal coincident with various telemetry subcarrier harmonics

Test number	P_C, dBm	P_D, dBm	BR, bps	T_S, K	P_{RFI}, dBm	f_{RFI}, Hz
65	−148.1	−140.9	2,000	25.2	−140.0	$f_c + f_{sc1}$
66					−140.0	$f_c + 3xf_{sc1}$
67					−140.0	$f_c + 5xf_{sc1}$
68					−128.0	$f_c + 7xf_{sc1}$
69					−128.0	$f_c + 9xf_{sc1}$
70					−128.0	$f_c + 11xf_{sc1}$
71					−121.0	$f_c + 13xf_{sc1}$
72					−121.0	$f_c + 15xf_{sc1}$
73					−121.0	$f_c + 17xf_{sc1}$
74					−121.0	$f_c + 19xf_{sc1}$
75					−121.0	$f_c + 21xf_{sc1}$
76					−121.0	$f_c + 23xf_{sc1}$
77					−121.0	$f_c + 25xf_{sc1}$
78	−148.1	−140.9	2,000	25.2	−121.0	$f_c + 27xf_{sc1}$

Table 5. ΔSNR_I vs P_{RFI} for CW interfering signal coincident with various telemetry subcarrier harmonics

Subcarrier harmonic	P_{RFI}, dBm	CW interfering signal attenuation (Fig. 6) (dB)	Measured ΔSNR_I, dB	Calculated ΔSNR_I, dB
1	−140	0	8.63	8.41
3	−140	0.2	2.34	1.86
5	−140	0.4	0.75	0.76
7	−128	0.8	4.08	4.34
9	−128	1.4	1.96	2.68
11	−128	2.3	1.63	1.61
13	−121	3.2	3.97	4.02
15	−121	4.1	3.60	2.75
17	−121	5.1	2.05	1.84
19	−121	6.1	1.92	1.24
21	−121	7.3	1.26	0.82
23	−121	8.4	0.82	0.58
25	−121	9.6	0.42	0.42
27	−121	11.0	0.20	0.31

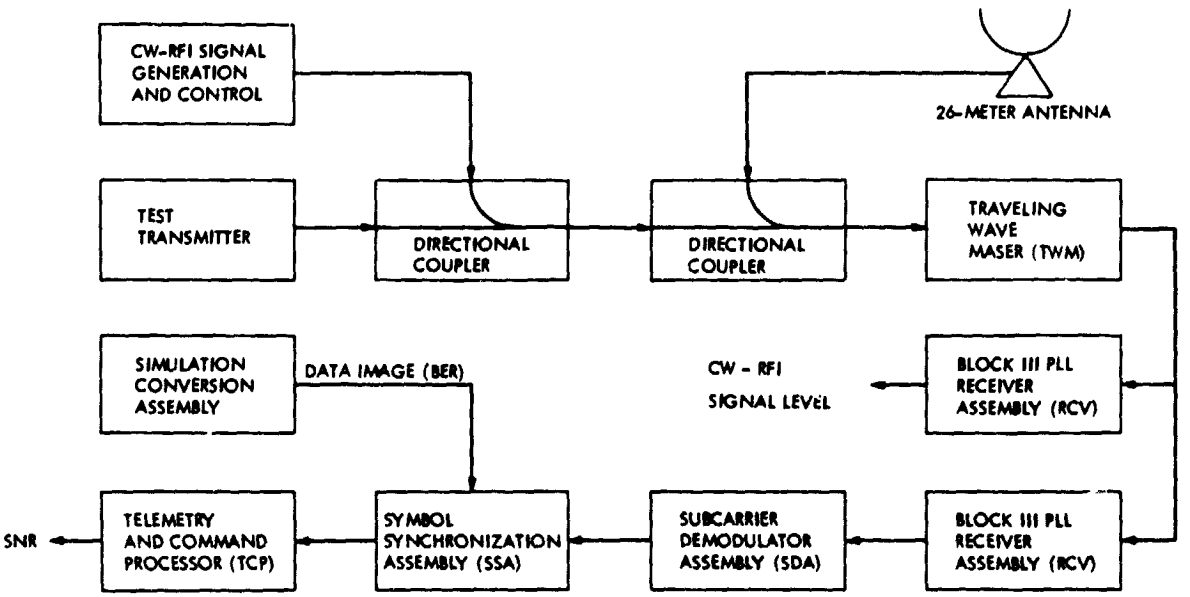

Fig. 1. Test configuration

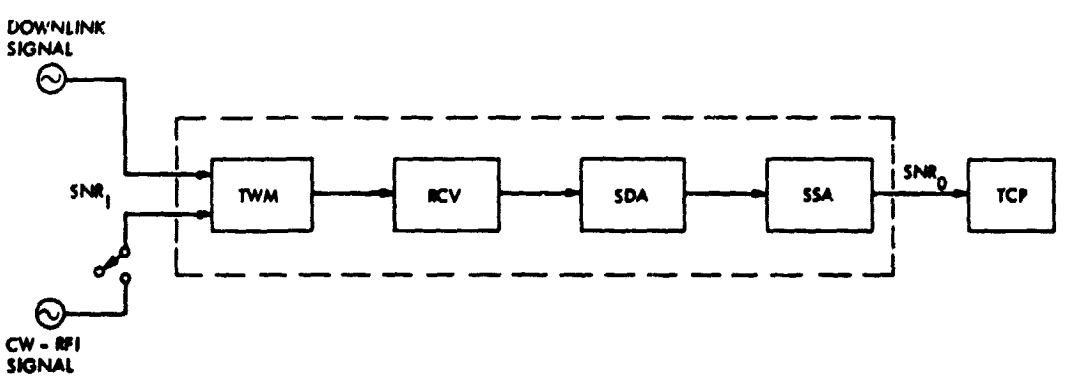

Fig. 2. Simplified carrier tracking and telemetry processing system

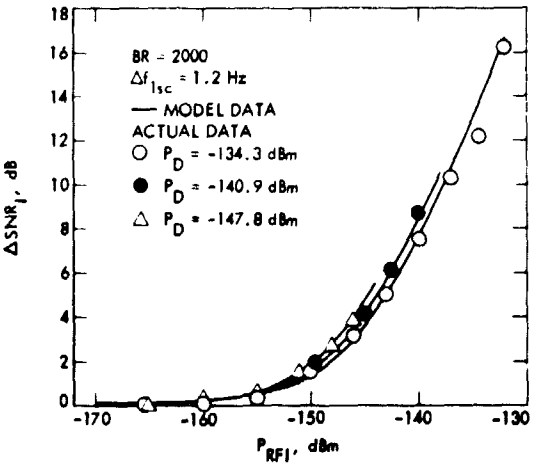

Fig. 3. Δ SNR_I vs P_{RFI} for selected values of P_D

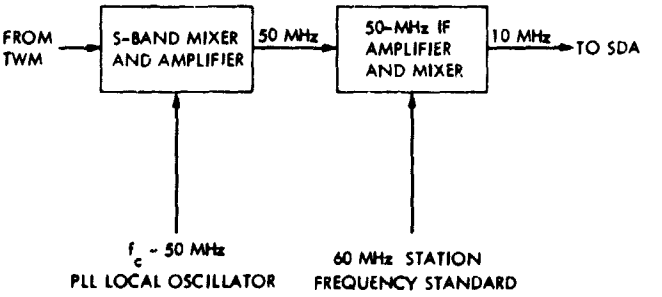

Fig. 5. Block III receiver telemetry function simplified block diagram

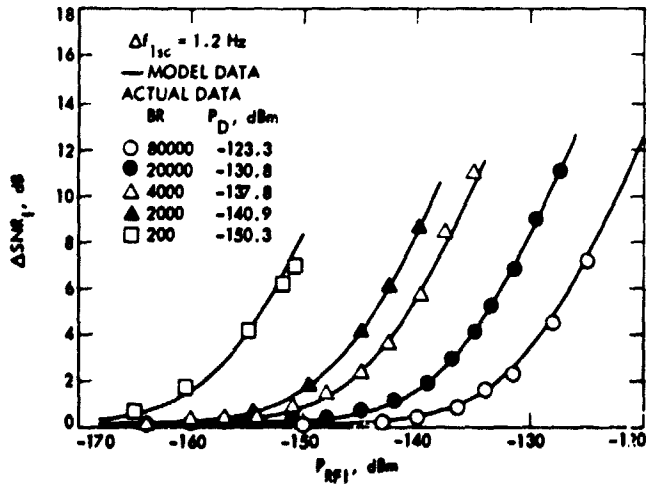

Fig. 4. Δ SNR_I vs P_{RFI} for selected values of BR

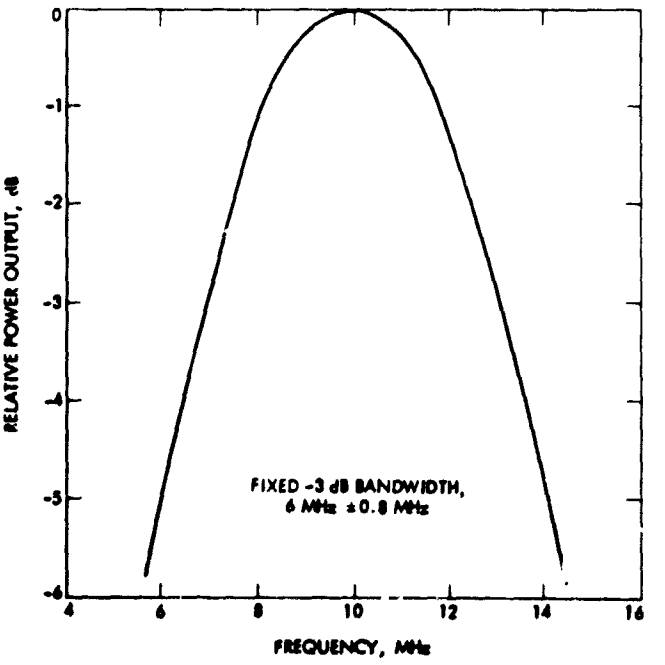

Fig. 6. Block III receiver 10-MHz telemetry output magnitude response characteristics

Bibliography

Ananda, M. P., "Lunar Gravity: A Mass Point Model," *J. Geophys. Res.*, Vol. 82, No. 20, pp. 3049-3064, July 10, 1977.

Anderson, J. D., "Determination of Astrodynamic Constants and a Test of the General Relativistic Time Delay With S-Band Range and Doppler Data From Mariners 6 and 7," *Space Research*, Vol. XI, pp. 105-112, Akademie-Verlag, Berlin, 1971.

Anderson, J. D., et al., "Experimental Test of General Relativity Using Time-Delay Data From Mariner 6 and Mariner 7," *Astrophys. J.*, Vol. 200, No. 1, pp. 221-233, Aug. 15, 1975.

Anderson, J. D., et al., "Tests of General Relativity Using Astrometric and Radio Metric Observations of the Planets," *Acta Astronautica*, Vol. 5, No. 1-2, pp. 43-61, Jan.-Feb. 1978.

Barnum, P. W., et al., *Tracking and Data System Support for the Mariner Mars 1971 Mission: Orbit Insertion Through End of Primary Mission*, Technical Memorandum 33-523, Vol. III, Jet Propulsion Laboratory, Pasadena, Calif., May 15, 1973.

Barnum, P. W., and Renzetti, N. A., *Tracking and Data System Support for the Mariner Mars 1971 Mission: Extended Mission Operations*, Technical Memorandum 33-523, Vol. IV, Jet Propulsion Laboratory, Pasadena, Calif., Dec. 15, 1973.

Barton, W. R., and Miller, R. B., *Tracking and Data System Support for the Pioneer Project: Pioneer 11 - Prelaunch Planning Through Second Trajectory Correction: to May 1, 1973*, Technical Memorandum 33-584, Vol. II, Jet Propulsion Laboratory, Pasadena, Calif., Mar. 15, 1975.

Bartos, K. P., et al., *Implementation of the 64-Meter-Diameter Antennas at the Deep Space Stations in Australia and Spain*, Technical Memorandum 33-692, Jet Propulsion Laboratory, Pasadena, Calif., Jan. 15, 1975.

Bathker, D. A., *Predicted and Measured Power Density Description of a Large Ground Microwave System*, Technical Memorandum 33-433, Jet Propulsion Laboratory, Pasadena, Calif., Apr. 15, 1971.

Bathker, D. A., Brown, D. W., and Petty, S. M., *Single- and Dual-Carrier Microwave Noise Abatement in the Deep Space Network*, Technical Memorandum 33-733, Jet Propulsion Laboratory, Pasadena, Calif., Aug 1, 1975.

Bathker, D. A., *Microwave Performance Characterization of Large Space Antennas*, JPL Publication 77-21, Jet Propulsion Laboratory, Pasadena, Calif., May 15, 1977.

Beatty, R. W., and Otoshi, T. Y., "Effect of Discontinuities on the Group Delay of a Microwave Transmission Line," *IEEE Trans. Microwave Theor. Techniq.*, Vol. MTT-23, No. 11, pp. 919-923, Nov. 1975.

Benjauthrit, B., and Reed, I. S., "Galois Switching Functions and Their Applications," *IEEE Trans. Comput.*, Vol. C-25, No. 1, pp. 78-86, Jan. 1976.

Benjauthrit, B., and Reed, I. S., "On the Fundamental Structure of Galois Switching Functions," *IEEE Trans. Comput.*, Vol. C-27, No. 8, pp. 757-762, Aug. 1978.

Berlekamp, E. R., et al., "On the Inherent Intractability of Certain Coding Problems," *IEEE Trans. Inform. Theor.*, Vol. IT-24, No. 3, pp. 384-386, May 1978.

Berman, A. L., and Rockwell, S. T., *New Optical and Radio Frequency Angular Tropospheric Refraction Models for Deep Space Applications*, Technical Report 32-1601, Jet Propulsion Laboratory, Pasadena, Calif., Nov. 1, 1975.

Berman, A. L., *The Prediction of Zenith Range Refraction From Surface Measurements of Meteorological Parameters*, Technical Report 32-1602, Jet Propulsion Laboratory, Pasadena, Calif., July 15, 1976.

Born, G. H., et al., "The Determination of the Satellite Orbit of Mariner 9," *Celest. Mech.*, Vol. 9, No. 3, pp. 395-414, May 1974.

Born, G. H., and Mohan, S. N., "Orbit Determination for Mariner 9 Using Radio and Optical Data," *J. Spacecraft Rockets*, Vol. 12, No. 7, pp. 439-441, July 1975.

Butman, S., "Rate Distortion Over Band-Limited Feedback Channels," *IEEE Trans. Inform. Theor.*, Vol. IT-17, No. 1, pp. 110-112, Jan. 1971.

Butman, S., and Timor, U., "Interplex An Efficient Multichannel PSK/PM Telemetry System," *IEEE Trans. Commun.*, Vol. COM-20, No. 3, pp. 415-419, June 1972.

Butman, S. A., "Linear Feedback Rate Bounds for Regressive Channels," *IEEE Trans. Inform. Theor.*, Vol. IT-22, No. 3, pp. 363-366, May 1976.

Butman, S. A., et al., "Design Criteria for Noncoherent Gaussian Channels With MFSK Signaling and Coding," *IEEE Trans. Commun.*, Vol. COM-24, No. 10, pp. 1078-1088, Oct. 1976.

Butman, S. A., and Lesh, J. R., "The Effects of Bandpass Limiters on *n*-Phase Tracking Systems," *IEEE Trans. Commun.*, Vol. COM-25, No. 6, pp. 569-576, June 1977.

Chadwick, H. D., and Springett, J. C., "The Design of a Low Data Rate MSFK Communication System" *IEEE Trans. Commun. Technol.*, Vol. COM-18, No. 6, pp. 740-750, Dec. 1970.

Chao, C.-C., "Interstation Frequency Offset Determination Using Differenced 2-Way/3-Way Doppler Data," paper presented at the 1978 Spring Meeting of the American Geophysical Union, Miami, Florida, Apr. 17-20, 1978.

Christensen, C. S., and Reinold, S. J., "Navigation of the Mariner 10 Spacecraft to Venus and Mercury," *J. Spacecraft Rockets*, Vol. 12, No. 5, pp. 280-286, May 1975.

Christensen, C. S., et al., "On Achieving Sufficient Dual Station Range Accuracy for Deep Space Navigation at Zero Declination," paper presented at AAS/AIAA Astrodynamics Specialist Conference, Jackson Hole, Wyo., Sept. 7-9, 1977.

Christensen, E. J., et al., "The Mass of Phobos from Viking Flybys," *Geophys. Res. Lett.*, Vol. 4, No. 12, pp. 555-557, Dec. 1977.

Clark, B. G., et al., "High Resolution Observations of Compact Radio Sources at 13 cm," *Astrophys. J.*, Vol. 161, pp. 803-809, Sept. 1970.

Clauss, R., Flesner, L. D., and Schultz, S., "Simple Waveguide Reflection Maser with Broad Tunability," *Rev. Sci. Instrum.*, Vol. 48, No. 8, pp. 1104-1105, Aug. 1977.

A Collection of Articles on S/X-Band Experiment Zero Delay Ranging Tests, Technical Memorandum 33-747, Vol. 1, Jet Propulsion Laboratory, Pasadena, Calif., Nov. 1, 1975.

Coyner, J. V., Jr., *Radial Rib Antenna Surface Deviation Analysis Program*, Technical Memorandum 33-518, Jet Propulsion Laboratory, Pasadena, Calif., Dec. 15, 1971.

Curkendall, D. W., and Stephenson, R. R., "Earthbased Tracking and Orbit Determination Backbone of the Planetary Navigation System," *Astronaut. Aeronaut.*, Vol. 7, No. 5, pp. 30-36, May 1970.

Curkendall, D. W., "Planetary Navigation: The New Challenges," *Astronaut. Aeronaut.*, Vol. 7, No. 5, pp. 26-29, May 1970.

Curkendall, D. W., "Algorithms for Isolating Worst Case Systematic Data Errors," *J. Guidance Contr.*, Vol. 1, No. 1, pp. 56-62, Jan.-Feb. 1978.

Dickinson, R. M., "The Beamed Power Microwave Transmitting Antenna," *IEEE Trans. Microwave Theor. Tech.*, Vol. MTT-26, No. 5, pp. 335-340, May 1978.

Downs, G. S., and Reichley, P. E., "Observations of Interstellar Scintillations of Pulsar Signals at 2388 MHz," *Astrophys. J.*, Vol. 163, No. 1, Pt. 2, pp. L11-L16, Jan 1971.

Downs, G. S., et al., "Mars Radar Observation, A Preliminary Report," *Science*, Vol. 174, No. 4016, pp. 1324-1327, Dec. 24, 1971.

Downs, G. S., "Martian Topography and Surface Properties as Seen by Radar: The 1971 Opposition," *Icarus*, Vol. 18, No. 1, pp. 8-21, Jan. 1973.

Downs, G. S., Reichley, P. E., and Morris, G. A., "Pulsar Detections at Frequencies of 8.4 and 15.1 GHz," *Astrophys. J.*, Vol. 181, No. 3, Part 2, pp. L143-L146, May 1, 1973.

Duxbury, T. C., Johnson, T. V., and Matson, D. L., "Galilean Satellite Mutual Occultation Data Processing," *Icarus*, Vol. 25, No. 4, pp. 569-584, Aug. 1975.

Edelson, R. E. (ed), *Telecommunications Systems Design Techniques Handbook*, Technical Memorandum 33-571, Jet Propulsion Laboratory, Pasadena, Calif., July 15, 1972.

Edelson, R. E., "An Observational Program to Search for Radio Signals From Extraterrestrial Intelligence Through the Use of Existing Facilities," Preprint IAF-A-76-033, Int. Astronaut. Fed. XXVII Congress, Anaheim, Calif., Oct. 10-16, 1976.

Edelson, R. E., and Levy, G. S., "The Search for Extraterrestrial Intelligence: Telecommunications Technology," *Proceedings of the 1976 National Telecommunications Conference*, Vol. I, Dallas, Tex., Nov. 29-Dec. 1, 1976.

Edelson, R. E., "An Experimental Protocol for a Search for Radio Signals of Extraterrestrial Intelligent Origin in the Presence of Man-Made Radio Frequency Sources," paper presented at the XXVIIIth International Astronautical Congress, Prague, Czechoslovakia, Sept. 25-Oct. 1, 1977.

Efron, L., and Solloway, C. B., *Proceedings of the Conference on Scientific Applications of Radio and Radar Tracking in the Space Program*, Technical Report 32-1475, Jet Propulsion Laboratory, Pasadena, Calif., July 1, 1970.

Esposito, P. B., and Wong, S. K., "Geocentric Gravitational Constant Determined from Mariner 9 Radio Tracking Data," paper presented at the International Symposium on Earth Gravity Models (American Geophysical Union, NASA), St. Louis, Aug. 1972.

Estabrook, F. B., and Wahlquist, H. D., "Response of Doppler Spacecraft Tracking to Gravitational Radiation," *Gen. Relat. Grav.*, Vol. 6, No. 5, pp. 439-447, Oct. 1975.

Estacion Espacial de Madrid: Madrid Space Station, Special Publication 43-26, Jet Propulsion Laboratory, Pasadena, Calif., Aug. 31, 1975.

Ferrari, A. J., and Ananda, M. P., "Lunar Gravity: A Long-Term Keplerian Rate Method," *J. Geophys. Res.*, Vol. 82, No. 20, pp. 3065-3097, July 10, 1977.

Fjeldbo, G., Kliore, A. J., and Seidel, B. L., "Bistatic Radar Measurements of the Surface of Mars with Mariner 1969," *Icarus*, Vol. 16, No. 3, pp. 502-508, June 1972.

Fjeldbo, G., "Radio Occultation Experiments Planned for Pioneer and Mariner Missions to the Outer Planets," *Planet. Space Sci.*, Vol. 21, No. 9, pp. 1533-1547, Sept. 1973.

Fjeldbo, G., et al., "Viking Radio Occultation Measurements of the Martian Atmosphere and Topography: Primary Mission Coverage," *J. Geophys. Res.*, Vol. 82, No. 28 pp. 4317-4324, Sept. 30, 1977.

Flanagan, F. M., et al., *Deep Space Network Support of the Manned Space Flight Network for Apollo: 1962-1968*, Technical Memorandum 33-452, Vol. I, Jet Propulsion Laboratory, Pasadena, Calif., July 1970.

Flanagan, F. M., et al., *Deep Space Network Support of the Manned Space Flight Network for Apollo: 1969-1970*, Technical Memorandum 33-452, Vol. II, Jet Propulsion Laboratory, Pasadena, Calif., May 1, 1971.

Fortenberry, J. W., Freeland, R. E., and Moore, D. M., *Five-Meter-Diameter Conical Furlable Antenna*, Technical Report 32-1604, Jet Propulsion Laboratory, Pasadena, Calif., July 15, 1976.

Freiley, A. J., Batelaan, P. D., and Bathker, D. A., *Absolute Flux Density Calibrations of Radio Sources: 2.3 GHz*, Technical Memorandum 33-806, Jet Propulsion Laboratory, Pasadena, Calif., Dec. 1, 1977.

Gary, B., Olsen, E. T., and Rosenkranz, P. W., "Radio Observations of Cygnus X-3 and the Surrounding Region," *Nature Phys. Sci.*, Vol. 239, No. 95, pp. 128-130, Oct. 23, 1972.

Georgevic, R. M., *Mathematical Model of the Solar Radiation Force and Torques Acting on the Components of a Spacecraft*, Technical Memorandum 33-494, Jet Propulsion Laboratory, Pasadena, Calif., Oct. 1, 1971.

Goldstein, R. M., et al., "Preliminary Radar Results of Mars," *Radio Sci.*, Vol. 5, No. 2, pp. 475-478, Feb. 1970.

Goldstein, R. M., and Rumsey, H., "A Radar Snapshot of Venus," *Science*, Vol. 169, Sept. 1970.

Goldstein, R. M., "Radar Observations of Mercury," *Astron. J.*, Vol. 76, No. 10, pp. 1152-1154, Dec. 1971.

Goldstein, R. M., Holdridge, D. B., and Lieske, J. H., "Minor Planets and Related Objects: XII. Radar Observations of (1685) Toro," *Astron. J.*, Vol. 78, No. 6, pp. 508-509, Aug. 1973.

Goldstein, R. M., and Morris, G. A., "Ganymede: Observations by Radar," *Science*, Vol. 188, No. 4194, pp. 1211-1212, June 20, 1975.

Goldstein, R. M., Green, R. R., and Rumsey, H., Jr., "Venus Radar Images," *J. Geophys. Res.*, Vol. 81, No. 26, pp. 4807-4817, Sept. 10, 1976.

Goodwin, P. S., et al., *Tracking and Data Systems Support for the Helios Project: Project Development Through End of Mission Phase II*, Technical Memorandum 33-752, Vol. I, Jet Propulsion Laboratory, Pasadena, Calif., July 1, 1976.

Goodwin, P. S., et al., *Tracking and Data Systems Support for the Helios Project: DSN Support of Project Helios April 1975 Through May 1976*, Technical Memorandum 33-752, Vol. II, Jet Propulsion Laboratory, Pasadena, Calif., Jan. 15, 1977.

Goodwin, P. S., Jensen, W. N., and Flanagan, F. M., *Tracking and Data Systems Support for the Helios Project DSN Support of Project Helios May 1976 Through June 1977*, Technical Memorandum 33-752, Vol. III, Jet Propulsion Laboratory, Pasadena, Calif., Mar. 1, 1979.

Gordon, H. J., et al., *The Mariner 6 and 7 Flight Paths and Their Determination From Tracking Data*, Technical Memorandum 33-469, Jet Propulsion Laboratory, Pasadena, Calif., Dec. 1, 1970.

Gottlieb, P., et al., "Lunar Gravity over Large Craters from Apollo 12 Tracking Data," *Science*, Vol. 168, No. 3930, pp. 477-479, Apr. 1970.

Gray, R. M., and Tausworthe, R. C., "Frequency-Counted Measurements, and Phase Locking to Noise Oscillators," *IEEE Trans. Commun. Technol.*, Vol. COM-19, No. 1, pp. 21-30, Feb. 1971.

Gulkis, S., and Gary, B., "Circular Polarization and Total-Flux Measurements of Jupiter at 13.1 cm Wavelength," *Astron. J.*, Vol. 76, No. 1, pp. 12-16, Feb. 1971.

Gulkis, S., et al., "Observations of Jupiter at 13-cm Wavelength During 1969 and 1971," *Icarus*, Vol. 18, No. 2, pp. 181-191, Feb. 1973.

Gulkis, S., et al., "An All-Sky Search for Narrow-Band Radiation in the Frequency Range 1-25 GHz," paper presented at the 1976 U.S. National Commission, International Union of Radio Science, Amherst, Mass., Oct. 10-15, 1976.

Hachenberg, O., et al., "The 100-meter Radio Telescope at Effelsberg," *Proc. IEEE*, Vol. 61, No. 9, pp. 1288-1295, Sept. 1973.

Hall, J. R., *Tracking and Data System Support for Lunar Orbiter*, Technical Memorandum 33-450, Jet Propulsion Laboratory, Pasadena, Calif., Apr. 1970.

Harris, A. W., et al., "2290-MHz Flux Densities of 52 High-Declination Radio Sources," *Astron. J.*, Vol. 81, No. 4, pp. 222-224, Apr. 1976.

Havens, W. F., et al., *Scan Pointing Calibration for the Mariner Mars 1971 Spacecraft*, Technical Memorandum 33-556, Jet Propulsion Laboratory, Pasadena, Calif., Aug. 1, 1972.

Higa, W. H., "Time Synchronization via Lunar Radar," *Proc. IEEE*, Vol. 60, No. 5, pp. 552-557, May 1972.

Higa, W. H., "Spurious Signals Generated by Electron Tunneling on Large Reflector Antennas," *Proc. IEEE*, Vol. 63, No. 2, pp. 306-313, Feb. 1975.

Higa, W. H., *The Superconducting Cavity-Stabilized Maser Oscillator*, Technical Memorandum 33-805, Jet Propulsion Laboratory, Pasadena, Calif., Dec. 15, 1976.

Holmes, J. K., "On a Solution to the Second-Order Phase-Locked Loop," *IEEE Trans. Commun. Technol.*, Vol. COM-18, No. 2, pp. 119-126, Apr. 1970.

Holmes, J. K., "First Slip Times Versus Static Phase Error Offset for the First and Passive Second-Order Phase-Locked Loop," *IEEE Trans. Commun. Technol.*, Vol. COM-19, No. 2, pp. 234-235, Apr. 1971.

Holmes, J. K., and Tegnelia, C. R., *Digital Command System Second-Order Subcarrier Tracking Performance*, Technical Report 32-1540, Jet Propulsion Laboratory, Pasadena, Calif., Oct. 1, 1971.

Holmes J. K., "Performance of a First Order Transition Sampling Digital Phase-Locked Loop Using Random-Walk Models," *IEEE Trans. Commun.*, Vol. COM-20, No. 2, pp. 119-131, Apr. 1972.

Hunter, J. A., "Orbiting Deep Space Relay Station, A Study Report," paper presented at AIAA Conference on Large Space Platforms, Future Needs and Capabilities, Los Angeles, Calif., Sept. 27-29, 1978.

Hurd, W. J., and Anderson, T. O., *Digital Transition Tracking Symbol Synchronizer for Low SNR Coded Systems*, Technical Report 32-1488, Jet Propulsion Laboratory, Pasadena, Calif., reprinted from *IEEE Trans. Commun. Technol.*, Vol. COM-18, No. 2, pp. 141-147, Apr. 1970.

Hurd, W. J., "An Analysis and Demonstration of Clock Synchronization by VLBI," *IEEE Trans. Instr. Meas.*, Vol. IM-23, No. 1, pp. 80-89, March 1974.

Jacobson, R. A., McDanell, J. P., and Rinker, G. C., "Use of Ballistics Arcs in Low Thrust Navigation," *J. Spacecraft Rockets*, Vol. 12, No. 3, pp. 138-145, Mar. 1975.

Jordan, J. F., Melbourne, W. G., and Anderson, J. D., "Testing Relativistic Gravity Theories Using Radio Tracking Data From Planetary Orbiting Spacecraft," *Space Research XIII*, pp. 83-92, Akademie-Verlag, Berlin, 1973.

Jurgens, R. F., and Goldstein, R. M., "Radar Observations at 3.5 and 12.6 cm Wavelength of Asteroid 433 Eros," *Icarus*, Vol. 28, No. 1, pp. 1-15, May 1976.

Jurgens, R. F., and Bender, D. F., "Radar Detectability of Asteroids," *Icarus*, Vol. 31, No. 4, pp. 483-497, Aug. 1977.

Katow, M. S., "Evaluating Computed Distortions of Parabolic Reflectors," *Record of IEEE 1977 Mechanical Engineering in Radar Symposium, Arlington, Virginia, Nov. 8-10, 1977*, IEEE Publication 77CH 1250-0 AES, pp. 91-93.

Kellerman, K. I., et al., "High Resolution Observations of Compact Radio Sources at 13 Centimeters," *Astrophys. J.*, Vol. 161, No. 3, pp. 803-809, Sept. 1970.

Kliore, A. J., et al., "Summary of Mariner 6 and 7 Radio Occultation Results on the Atmosphere of Mars," *Space Research*, Vol. XI, pp. 165-175, Akademie-Verlag, Berlin, 1971.

Kliore, A. J., et al., "Mariner 9 S-Band Martian Occultation Experiment: Initial Results on the Atmosphere and Topography of Mars," *Science*, Vol. 175, No. 4019, pp. 313-317, Jan. 1972.

Kliore, A. J., et al., "The Atmosphere of Mars From Mariner 9 Radio Occultation Measurements," *Icarus*, Vol. 17, No. 2, pp. 484-516, Oct. 1972.

Kliore, A. J., et al., "S Band Radio Occultation Measurements of the Atmosphere and Topography of Mars with Mariner 9: Extended Mission Coverage of Polar and Intermediate Latitudes," *J. Geophys. Res.*, Vol. 78, No. 20, pp. 4331-4351, July 10, 1973.

Kliore, A. J., "Radio Occultation Exploration of Mars," *Exploration of the Planetary System* (IAU Symposium, No. 65), pp. 295-316, D. Reidel Publishing Co., Dordrecht, Holland, 1974.

Kliore, A. J., Woiceshyn, P. M., and Hubbard, W. P., "Pioneer 10 and 11 Radio Occultations by Jupiter," *COSPAR Space Research*, Vol. XVII, pp. 703-710, Pergamon Press Ltd., Oxford, 1978.

Kliore, A., et al., "The Polar Ionosphere of Venus Near the Terminator From Early Pioneer Venus Orbiter Radio Occultation," *Science*, Vol. 203, No. 4382, pp. 765-768, Feb. 23, 1979.

Kuiper, T. B. H., and Morris, M., "Searching for Extraterrestrial Civilizations," *Science*, Vol. 196, pp. 616-621, May 6, 1977.

Laeser, R. P., et al., *Tracking and Data System Support for the Mariner Mars 1971 Mission: Prelaunch Phase Through First Trajectory Correction Maneuver*, Technical Memorandum 33-523 Vol. I, Jet Propulsion Laboratory, Pasadena, Calif., Mar. 15, 1972.

Layland, J. W., and Lushbaugh, W. A., "A Flexible High-Speed Sequential Decoder for Deep Space Channels," *IEEE Trans. Commun. Technol.*, Vol. COM-19, No. 5, pp. 813-820, Oct. 1971.

Layland, J. W., "Buffer Management for Sequential Decoding," *IEEE Trans. Commun.*, Vol. COM-22, No. 10, pp. 1685-1690, Oct. 1974.

Leavitt, R. K., *The Least-Squares Process of MEDIA for Computing DRVID Calibration Polynomials*, Technical Memorandum 33-542, Jet Propulsion Laboratory, Pasadena, Calif., May 15, 1972.

Lesh, J. R., *Signal-to-Noise Ratios in Coherent Soft Limiters*, Technical Report 32-1589, Jet Propulsion Laboratory, Pasadena, Calif., Sept. 15, 1973.

Lesh, J. R., "Signal-to-Noise Ratios in Coherent Soft Limiters," *IEEE Trans. Commun.*, Vol. COM-22, No. 6, pp. 803-811, June 1974.

Lesh, J. R., "Sequential Decoding in the Presence of a Noisy Carrier Reference," *IEEE Trans. Commun.*, Vol. COM-23, No. 11, pp. 1292-1297, Nov. 1975.

Levitt, B. K., "Optimum Frame Synchronization for Biorthogonally Coded Data," *IEEE Trans. Commun.*, Vol. COM-22, No. 8, pp. 1130-1134, Aug. 1974.

Levitt, B. K., "Long Frame Sync Words for Binary PSK Telemetry," *IEEE Trans. Commun.*, COM-23, No. 11, pp. 1365-1367, Nov. 1975.

Levy, G. S., et al., "Helios-1 Faraday Rotation Experiment: Results and Interpretations of the Solar Occultations in 1975," *J. Geophys.*, Vol. 42, No. 6, pp. 659-672, 1977.

Levy, R., "Computer-Aided Design of Antenna Structures and Components," *Comput. Struc.*, Vol. 6, Nos. 4/5, pp. 419-428, Aug./Oct. 1976.

Levy, R., and McGinness, H., *Wind Power Prediction Models*, Technical Memorandum 33-802, Jet Propulsion Laboratory, Pasadena, Calif., Nov. 15, 1976.

Levy, R., and Katow, M. S., "Implementation of Wind Performance Studies for Large Antenna Structures," *Record of IEEE 1977 Mechanical Engineering in Radar Symposium, Arlington, Virginia, Nov. 8-10, 1977*, IEEE Publication 77CH 1250-0 AES, pp. 27-33.

Levy, R., "Antenna Bias Rigging for Performance Objective," *Record of IEEE 1977 Mechanical Engineering in Radar Symposium, Arlington, Virginia, Nov. 8-10, 1977*, IEEE Publication 77CH 1250-0 AES, pp. 94-97.

Lieske, J. H., et al., "Simultaneous Solution for the Masses of the Principal Planets from Analysis of Optical Radar and Radio Tracking Data," *Celest. Mech.*, Vol. 4, No. 2, pp. 233-245, Oct. 1971.

Lindsey, W. C., and Simon, M. K., "The Effect of Loop Stress on the Performance of Phase-Coherent Communication Systems," *IEEE Trans. Commun. Technol.*, Vol. COM-18, No. 5, pp. 569-588, Oct. 1970.

Lindsey, W. C., and Simon, M. K., "Carrier Synchronization and Detection of Polyphase Signals," *IEEE Trans. Commun.*, Vol. COM-20, No. 3, pp. 441-454, June 1972.

Lindsey, W. C., and Simon, M. K., "L-Orthogonal Signal Transmission and Detection," *IEEE Trans. Commun.*, Vol. COM-20, No. 5, pp. 953-960, Oct. 1972.

Lindsey, W. C., and Simon, M. K., "On the Detection of Differentially Encoded Polyphase Signals," *IEEE Trans. Commun.*, Vol. COM-20, No. 6, pp. 1121-1128, Dec. 1972.

Lindsey, W. C., *Synchronization Systems in Communication and Control*, Prentice-Hall, Inc., Englewood Cliffs, N.J., 1972.

Lindsey, W. C., and Tausworthe, R. C., *A Bibliography of the Theory and Application of the Phase-Lock Principle*, Technical Report 32-1581, Jet Propulsion Laboratory, Pasadena, Calif., Apr. 1, 1973.

Lindsey, W. C., and Simon, M. K., *Telecommunication Systems Engineering*, Prentice-Hall, Inc., Englewood Cliffs, N.J., 1973.

Liu, A. S., and Pease, G. E., "Spacecraft Ranging From a Ground Digitally Controlled Oscillator," *J. Spacecraft Rockets*, Vol. 12, No. 9, pp. 528-532, Sept. 1975.

Lorell, J., et al., "Icarus: Celestial Mechanics Experiment for Mariner," *Int. J. Sol. Sys.*, Vol. 12, Jan. 1970.

Lorell, J., and Laing, P. A., *Compilation of Lunar Orbiter Tracking Data Used for Long-Term Selenodesy*, Technical Memorandum 33-419, Jet Propulsion Laboratory, Pasadena, Calif., Feb. 1, 1970.

Lorell, J., "Estimation of Gravity Field Harmonics in the Presence of Spin-Axis Direction Error Using Radio Tracking Data," *J. Astronaut. Sci.*, Vol. XX, No. 1, pp. 44-54, Aug. 1972.

Ludwig, A. C., et al., *Gain Calibration of a Horn Antenna Using Pattern Integration*, Technical Report 32-1572, Jet Propulsion Laboratory, Pasadena, Calif., Oct. 1, 1972.

Madrid, G. A., et al., *Tracking System Analytic Calibration Activities for the Mariner Mars 1971 Mission*, Technical Report 32-1587, Jet Propulsion Laboratory, Pasadena, Calif., Mar. 1, 1974.

Martin, D. P., *A Combined Radar-Radiometer With Variable Polarization*, Technical Memorandum 33-570, Jet Propulsion Laboratory, Pasadena, Calif., Oct. 15, 1972.

Martin, W. L., and Zygielbaum, A. I., *Mu-II Ranging*, Technical Memorandum 33-768, Jet Propulsion Laboratory, Pasadena, Calif., May 15, 1977.

Melbourne, W. G., "Planetary Ephemerides," *Astronaut. Aeronaut.*, Vol. 7, No. 5, pp. 38-43, May 1970.

Melbourne, W. G., "Navigation between the Planets," *Sci. Amer.*, Vol. 234, No. 6, pp. 58-74, June 1976.

Miller, R. B., *Tracking and Data System Support for the Pioneer Project: Pioneers 6-9. Extended Missions: July 1, 1972-July 1, 1973*, Technical Memorandum 33-426, Vol. XII, Jet Propulsion Laboratory, Pasadena, Calif., March 1, 1974.

Miller, R. B., *Tracking and Data System Support for the Pioneer Project: Pioneer 10 From April 1, 1972, Through the Jupiter Encounter Period, January 1974*, Technical Memorandum 33-584, Vol. III, Jet Propulsion Laboratory, Pasadena, Calif., June 15, 1975.

Miller, R. B., et al., *Tracking and Data System Support for the Pioneer Project: Pioneer 10 From January 1974 to January 1975; Pioneer 11—From May 1, 1973 Through Jupiter Encounter Period, January 1975*, Technical Memorandum 33-584, Vol. IV, Jet Propulsion Laboratory, Pasadena, Calif., Dec. 1, 1975.

Moyer, T. D., *Mathematical Formulation of the Double-Precision Orbit Determination Program (DPODP)*, Technical Report 32-1527, Jet Propulsion Laboratory, Pasadena, Calif., May 17, 1971.

Mudgway, D. J., *Tracking and Data System Support for the Viking 1975 Mission to Mars: Prelaunch Planning, Implementation, and Testing*, Technical Memorandum 33-783, Vol. I, Jet Propulsion Laboratory, Pasadena, Calif., Jan. 15, 1977.

Mudgway, D. J., and Traxler, M. R., *Tracking and Data System Support for the Viking 1975 Mission to Mars: Launch Through Landing of Viking 1*, Technical Memorandum 33-783, Vol. II, Jet Propulsion Laboratory, Pasadena, Calif., Mar. 15, 1977.

Mudgway, D. J., *Tracking and Data System Support for the Viking 1975 Mission to Mars: Planetary Operations*, Technical Memorandum 33-783, Vol. III, Jet Propulsion Laboratory, Pasadena, Calif., Sept. 1, 1977.

Mudgway, D. J., *Tracking and Data System Support for the Viking 1975 Mission to Mars: Extended Mission Operations December 1976 to May 1978*, Technical Memorandum 33-783, Vol. IV, Jet Propulsion Laboratory, Pasadena, Calif., Dec. 15, 1978.

Muhleman, D. O., et al., "Radio Propagation Measurements of the Solar Corona and Gravitational Field: Applications to Mariner 6 and 7," in *Proceedings of the Conference on Experimental Tests of Gravitational Theories*, California Institute of Technology, Pasadena, Calif., Nov. 1970.

Muhleman, D. O., Esposito, P. B., and Anderson, J. D., "The Electron Density Profile of the Outer Corona and the Interplanetary Medium From Mariner-6 and Mariner-7 Time-Delay Measurements," *Astrophys. J.*, No. 211, No. 3, Part 1, pp. 943-957, Feb. 1, 1977.

Mulhall, B. D., et al., *Tracking System Analytic Calibration Activities for the Mariner Mars 1969 Mission*, Technical Report 32-1499, Jet Propulsion Laboratory, Pasadena, Calif., Nov. 15, 1970.

Muller, P. M., Sjogren, W. L., and Wollenhaupt, W. R., "Lunar Gravity: Apollo 15 Doppler Radio Tracking," *The Moon*, Vol. 10, No. 2, pp. 195-205, June 1974.

Murray, B. C., Gulkis, S., and Edelson, R. E., "Extraterrestrial Intelligence: An Observational Approach," *Science*, Vol. 199, No. 4328, pp. 485-492, Feb. 3, 1978.

The NASA/JPL 64-Meter-Diameter Antenna at Goldstone, California: Project Report, Technical Memorandum 33-671, Jet Propulsion Laboratory, Pasadena, Calif., July 15, 1974.

Newburn, R. L., Jr., et al., *Earth-Based Research on the Outer Planets During the Period 1970-1985*, Technical Report 32-1456, Jet Propulsion Laboratory, Pasadena, Calif., Mar. 15, 1970.

Ohlson, J. E., "Polarization Tracking of a Partially Coherent Signal Using a Double Loop," *IEEE Trans. Commun.*, Vol. COM-23, No. 9, pp. 859-866, Sept. 1975.

Ohlson, J. E., and Reid, M. S., *Conical-Scan Tracking With the 64-m-diameter Antenna at Goldstone*, Technical Report 32-1605, Jet Propulsion Laboratory, Pasadena, Calif., Oct. 1, 1976.

O'Neil, W. J., et al., *Mariner 9 Navigation*, Technical Report 32-1586, Jet Propulsion Laboratory, Pasadena, Calif., Nov. 13, 1973.

Ong, K. M., et al., "A Demonstration of a Transportable Radio Interferometric Surveying System With 3-cm Accuracy on a 307-m Base Line," *J. Geophys. Res.*, Vol. 81, No. 20, pp. 3587-3593, July 10, 1976.

Otoshi, T. Y., Stelzried, C. T., and Yates, B. C., "Comparisons of Waveguide Losses Calibrated by the DC Potentiometer, AC Ratio Transformer, and Reflectometer Techniques," *IEEE Trans. Microwave Theor. Tech.*, Vol. MTT-18, No. 7, pp. 406-409, July 1970.

Otoshi, T. Y., and Stelzried, C. T., "A Precision Compact Rotary Vane Attenuator," *IEEE Trans. Microwave Theor. Tech.*, Vol. MTT-19, No. 11, pp. 843-854, Nov. 1971.

Otoshi, T. Y., "Precision Reflectivity Loss Measurements of Perforated-Plate Mesh Materials by a Waveguide Technique," *IEEE Trans. Instr. Meas.*, Vol. IM-21, No. 4, pp. 451-457, Nov. 1972.

Otoshi, T. Y., and Stelzried, C. T., "Cosmic Background Noise Temperature Measurement at 13-cm Wavelength," *IEEE Trans. Instr. Meas.*, Vol. IM-24, No. 2, pp. 174-179, June 1975.

Phillips, R. J., et al., "Simulation Gravity Modeling to Spacecraft-Tracking Data: Analysis and Application," *J. Geophys. Res.*, Vol. 83, No. B11, pp. 5455-5464, Nov. 10, 1978.

Posner, E. C., "Random Coding Strategies for Minimum Entropy," *IEEE Trans. Inform. Theor.*, Vol. IT-21, No. 4, pp. 388-391, July 1975.

Posner, E. C., "Life Cycle Costing with a Discount Rate," *Utilitas Mathematica*, Vol. 13, pp. 157-188, 1978.

Powell, R. V., and Hibbs, A. R., "An Entree for Large Space Antennas," *Astronaut. Aeronaut.*, Vol. 15, No. 12, pp. 58-64, Dec. 1977.

Reed, I. S., Truong, T. K., and Benjauthrit, B., "On Decoding of Reed-Solomon Codes over GF(32) and GF(64) Using the Transform Techniques of Winograd," *Conference Record, 1978 National Telecommunications Conference*, Vol. 2, Birmingham, Alabama, Dec. 3-6, 1978.

Reid, M. S., et al., "Low-Noise Microwave Receiving Systems in a Worldwide Network of Large Antennas," *Proc. IEEE*, Vol. 61, No. 9, pp. 1330-1335, Sept. 1973.

Renzetti, N. A., *Tracking and Data System Support for the Pioneer Project: Pioneer VI. Prelaunch to End of Nominal Mission*, Technical Memorandum 33-426, Vol. I, Jet Propulsion Laboratory, Pasadena, Calif., Feb. 1, 1970.

Renzetti, N. A., *Tracking and Data System Support for the Pioneer Project: Pioneer VII. Prelaunch to End of Nominal Mission*, Technical Memorandum 33-426, Vol. II, Jet Propulsion Laboratory, Pasadena, Calif., Apr. 15, 1970.

Renzetti, N. A., *Tracking and Data System Support for the Pioneer Project: Pioneer VIII. Prelaunch Through May 1968*, Technical Memorandum 33-426, Vol. III, Jet Propulsion Laboratory, Pasadena, Calif., July 15, 1970.

Renzetti, N. A., *Tracking and Data System Support for the Pioneer Project: Pioneer IX. Prelaunch Through June 1969,* Technical Memorandum 33-426, Vol. IV, Jet Propulsion Laboratory, Pasadena, Calif., Nov. 15, 1970.

Renzetti, N. A., *Tracking and Data System Support for the Pioneer Project: Pioneer VI. Extended Mission: July 1, 1966-July 1, 1969,* Technical Memorandum 33-426, Vol. V, Jet Propulsion Laboratory, Pasadena, Calif., Feb. 1, 1971.

Renzetti, N. A., *Tracking and Data System Support for the Pioneer Project: Pioneer VII. Extended Mission: February 24, 1967-July 1, 1968,* Technical Memorandum 33-426, Vol. VI, Jet Propulsion Laboratory, Pasadena, Calif., Apr. 15, 1971.

Renzetti, N. A., *Tracking and Data System Support for the Pioneer Project: Pioneer VII. Extended Mission: July 1, 1968-July 1, 1969,* Technical Memorandum 33-426, Vol. VII, Jet Propulsion Laboratory, Pasadena, Calif., Apr. 15, 1971.

Renzetti, N. A., *Tracking and Data System Support for the Pioneer Project: Pioneer VIII. Extended Mission: June 1, 1968-July 1, 1969,* Technical Memorandum 33-426, Vol. VIII, Jet Propulsion Laboratory, Pasadena, Calif., May 1, 1971.

Renzetti, N. A., *Tracking and Data System Support for the Pioneer Project: Pioneers VI-IX. Extended Missions: July 1, 1969-July 1, 1970,* Technical Memorandum 33-426, Vol. IX, Jet Propulsion Laboratory, Pasadena, Calif., Aug. 15, 1971.

Renzetti, N. A., and Siegmeth, A. J., *Tracking and Data System Support for the Pioneer Project: Pioneers 6-9. Extended Missions: July 1, 1971-July 1, 1972,* Technical Memorandum 33-426, Vol. XI, Jet Propulsion Laboratory, Pasadena, Calif., May 1, 1973.

Renzetti, N. A., et al., *Tracking and Data System Support for the Mariner Mars 1969 Mission: Planning Phase Through Midcourse Maneuver,* Technical Memorandum 33-474, Vol. I, Jet Propulsion Laboratory, Pasadena, Calif., May 15, 1971.

Renzetti, N. A., et al., *Tracking and Data System Support for the Mariner Mars 1969 Mission: Midcourse Maneuver Through End of Nominal Mission,* Technical Memorandum 33-474, Vol. II, Jet Propulsion Laboratory, Pasadena, Calif., Sept. 1, 1971.

Renzetti, N. A., Linnes, K. W., and Taylor, T. M., *Tracking and Data System Support for the Mariner Mars 1969 Mission: Extended Operations Mission,* Technical Memorandum 33-474, Vol. III, Jet Propulsion Laboratory, Pasadena, Calif., Sept. 15, 1971.

Renzetti, N. A., *A History of the Deep Space Network: From Inception to January 1, 1969,* Technical Report 32-1533, Vol. I, Jet Propulsion Laboratory, Pasadena, Calif., Sept. 1, 1971.

Renzetti, N. A., "Radio Communications at Planetary Distances," paper presented at the International Convention on Radio Communication, Rome and Bologna, Italy, Mar. 1974.

Rusch, W. V. T., *Applications of Two-Dimensional Integral-Equation Theory to Reflector-Antenna Analysis,* Technical Memorandum 33-478, Jet Propulsion Laboratory, Pasadena, Calif., May 1, 1971.

Rusch, W. V. T., "Double Aperture Blocking by Two Wavelength-Sized Feed-Support Struts," *Electron. Lett.*, Vol. 10, No. 15, pp. 296-297, July 25, 1974.

Siegmeth, A. J., Purdue, R. E., and Ryan, R. E., *Tracking and Data System Support for the Pioneer Project: Pioneers 6-9. Extended Missions: July 1, 1970-July 1, 1971,* Technical Memorandum 33-426, Vol. X, Jet Propulsion Laboratory, Pasadena, Calif., Aug. 15, 1972.

Siegmeth, A. J., et al., *Tracking and Data System Support for the Pioneer Project: Pioneer 10 Prelaunch Planning Through Second Trajectory Correction December 4, 1969 to April 1, 1972,* Technical Memorandum 33-584, Vol. I, Jet Propulsion Laboratory, Pasadena, Calif., Apr. 1, 1973.

Simon, M. K., "Nonlinear Analysis of an Absolute Value Type of an Early-Late Gate Bit Synchronizer," *IEEE Trans. Commun. Technol.,* Vol. COM-18, No. 5, pp. 589-596, Oct. 1970.

Simon, M. K., "Optimization of the Performance of a Digital-Data-Transition Tracking Loop," *IEEE Trans. Commun. Technol.,* Vol. COM-18, No. 5, pp. 686-689, Oct. 1970.

Simon, M. K., and Lindsey, W. C., "Data-Aided Carrier Tracking Loops," *IEEE Trans. Commun. Technol.,* Vol. COM-19, No. 2, pp. 157-168, Apr. 1971.

Simon, M. K., "On the Selection of an Optimum Design Point for Phase-Coherent Receivers Employing Bandpass Limiters," *IEEE Trans. Commun.,* Vol. COM-20, No. 2, pp. 210-214, Apr. 1972.

Simon, M. K., "On the Selection of a Sampling Filter Bandwidth for a Digital Data Detector," *IEEE Trans. Commun.,* Vol. COM-20, No. 3, pp. 438-441, June 1972.

Simon, M. K., and Springett, J. C., "The Performance of a Noncoherent FSK Receiver Preceded by a Bandpass Limiter," *IEEE Trans. Commun.,* Vol. COM-20, No. 6, pp. 1128-1136, Dec. 1972.

Simon, M. K., and Springett, J. C., *The Theory, Design, and Operation of the Suppressed Carrier Data-Aided Tracking Receiver,* Technical Report 32-1583, Jet Propulsion Laboratory, Pasadena, Calif., June 15, 1973.

Simon, M. K., and Smith, J. G., "Hexagonal Multiple Phase-and-Amplitude-Shift-Keyed Signal Sets," *IEEE Trans. Commun.,* Vol. COM-21, No. 10, pp. 1108-1115, Oct. 1973.

Simon, M. K., and Smith, J. G., "Carrier Synchronization and Detection of QASK Signal Sets," *IEEE Trans. Commun.,* Vol. COM-22, No. 2, pp. 98-106, Feb. 1974.

Simon, M. K., *Data-Derived Symbol Synchronization of MASK and QASK Signals,* Technical Memorandum 33-720, Jet Propulsion Laboratory, Pasadena, Calif., Dec. 15, 1974.

Simon, M. K., "A Generalization of Minimum-Shift-Keying (MSK) Type Signaling Based Upon Input Data Symbol Pulse Shaping," *IEEE Trans. Commun.,* Vol. COM-24, No. 8, pp. 845-856, Aug. 1976.

Simon, M. K., "An MSK Approach to Offset QASK," *IEEE Trans. Commun.,* Vol. COM-24, No. 8, pp. 921-923, Aug. 1976.

Simon, M. K., "The False Lock Performance of Costas Loops with Hard-Limited In-Phase Channel," *IEEE Trans. Commun.,* Vol. COM-26, No. 1, pp. 23-34, Jan. 1978.

Simon, M. K., "On the Calculation of Squaring Loss in Costas Loops with Arbitrary Arm Filters," *IEEE Trans. Commun.,* Vol. COM-26, No. 1, pp. 179-184, Jan. 1978.

Simon, M. K., "Tracking Performance of Costas Loops With Hard-Limited In-Phase Channel," *IEEE Trans. Commun.,* Vol. COM-26, No. 4, pp. 420-432, Apr. 1978.

Sjogren, W. L., "Lunar Gravity Estimate: Independent Confirmation," *J. Geophys. Res.,* Vol. 76, No. 29, Oct. 10, 1971.

Sjogren, W. L., et al., "Lunar Gravity via Apollo 14 Doppler Radio Tracking," *Science,* Vol. 175, No. 4018, pp. 165-168, Jan. 14, 1972.

Sjogren, W. L., et al., "Gravity Fields," *IEEE Trans. Geosci. Electron.*, Vol. GE-14, No. 3, pp. 172-183, July 1976.

Slobin, S. D., "Beam Switching Cassegrain Feed System and Its Applications to Microwave and Millimeterwave Radioastronomical Observations," *Rev. Sci. Instr.*, Vol. 41, No. 3, pp. 439-443, Mar. 1970.

Spier, G. W., *Design and Implementation of Models for the Double Precision Trajectory Program (DPTRAJ)*, Technical Memorandum 33-451, Jet Propulsion Laboratory, Pasadena, Calif., Apr. 15, 1971.

Springett, J. C., and Simon, M. K., "An Analysis of the Phase Coherent-Incoherent Output of the Bandpass Limiter," *IEEE Trans. Commun. Technol.*, Vol. COM-19, No. 1, pp. 42-49, Feb. 1971.

Stelzried C. T., "Precision Microwave Waveguide Loss Calibrations," *IEEE Trans. Instrum. Measurement*, Vol. IM-19, No. 1, pp. 23-25, Feb. 1970.

Stelzried, C. T., *A Faraday Rotation Measurement of a 13-cm Signal in the Solar Corona*, Technical Report 32-1401, Jet Propulsion Laboratory, Pasadena, Calif., July 15, 1970.

Stelzried, C. T., et al., "The Quasi-Stationary Coronal Magnetic Field and Electron Density as Determined From a Faraday Rotation Experiment," *Sol. Phys.*, Vol. 14, No. 2, pp. 440-456, Oct. 1970.

Stelzried, C. T., "Operating Noise-Temperature Calibrations of Low-Noise Receiving Systems," *Microwave J.*, Vol. 14, No. 6, pp. 41-46, 48, June 1971.

Stelzried, C. T., et al., "Transformation of Received Signal Polarization Angle to the Plane of the Ecliptic," *J. Spacecraft Rockets*, Vol. 9, No. 2, pp. 69-70, Feb. 1972.

Tausworthe, R. C., "Convergence of Oscillator Spectral Estimators for Counted-Frequency Measurements," *IEEE Trans. Commun.*, Vol. COM-20, No. 2, pp. 213-217, Apr. 1972.

Tausworthe, R. C., "Simplified Formula for Mean-Slip Time of Phase-Locked Loops With Steady-State Phase Error," *IEEE Trans. Commun.*, Vol. COM-20, No. 3, pp. 331-337, June 1972.

Tausworthe, R. C., and Crow, R. B., "Improvements in Deep-Space Tracking by Use of Third-Order Loops," *Proceedings of the 1972 International Telemetering Conference, Los Angeles, California, October 10-12, 1972*, pp. 577-583.

Tausworthe, R. C., *Standard Classifications of Software Documentation*, Technical Memorandum 33-756, Jet Propulsion Laboratory, Pasadena, Calif., Jan. 15, 1976.

Textor, G. P., Kelly, L. B., and Kelly, M., *Tracking and Data System Support for the Mariner Mars 1971 Mission: First Trajectory Correction Maneuver Through Orbit Insertion*, Technical Memorandum 33-523, Vol. II, Jet Propulsion Laboratory, Pasadena, Calif., June 15, 1972.

Thomas, J. B., et al., "A Demonstration of an Independent-Station Radio Interferometry System With 4-cm Precision on a 16-km Base Line," *J. Geophys. Res.*, Vol. 81, No. 5, pp. 995-1005, Feb. 10, 1976.

Timor, U., "Equivalence of Time-Multiplexed and Frequency-Multiplexed Signals in Digital Communications," *IEEE Trans. Commun.*, Vol. COM-20, No. 3, pp. 435-438, June 1972.

Toukdarian, R. Z., *Final Engineering Report for Goldstone Operations Support Radar*, Technical Memorandum 33-800, Jet Propulsion Laboratory, Pasadena, Calif., Nov. 1, 1976.

Truong, T. K., and Reed, I. S., "Convolutions Over Residue Classes of Quadratic Integers," *IEEE Trans. Inform. Theor.*, Vol. IT-22, No. 4, pp. 468-475, July 1976.

Truong, T. K., and Reed, I. S., "Convolutions over Quartic Integer Residue Classes," *Proceedings of the International Conference on Information Sciences and Systems*, Patras, Greece, Aug. 19-24, 1976.

Truong, T. K., Liu, K. Y., and Reed, I. S., "Fast Number-Theoretic Transforms for Digital Filtering," *Electron. Lett.*, Vol. 12, No. 24, Nov. 1976.

Truong, T. K., et al., "X-Ray Reconstruction by Finite Field Transforms," *IEEE Trans. Nucl. Sci.*, Vol. NS-24, No. 1, pp. 843-849, Feb. 1977.

Truong, T. K., Golomb, S. W., and Reed, I. S., "Integer Convolutions Over the Finite Field $GF(3 \cdot 2^n + 1)$," *SIAM J. Appl. Math.*, Vol. 32, No. 2, pp. 356-365, Mar. 1977.

Truong, T. K., Reed, I. S., and Liu, K. Y., "Fast Algorithm for Computing Complex Number-Theoretic Transforms," *Electron. Lett.*, Vol. 13, No. 10, pp. 278-280, May 12, 1977.

von Roos, O. H., Yip, K. B. W., and Escobal, P. R., "A Global Model of the Earth's Ionosphere for Use in Space Applications," *Astronautica Acta*, Vol. 18 (Supplement), No. 3, pp. 215-232, Aug. 1974.

Weber, W. J., III, "Performance of Phase-Locked Loops in the Presence of Fading Communication Channels," *IEEE Trans. Commun.*, Vol. COM-24, No. 5, pp. 487-499, May 1976.

Weber, W. J., III, Ackerknecht, W. E., and Kollar, F. J., *Viking X-Band Telemetry Experiment Final Report*, Technical Memorandum 33-794, Jet Propulsion Laboratory, Pasadena, California, Sept. 1, 1976.

Wong, J. S. L., et al., *Review of Finite Fields: Applications to Discrete Fourier Transforms and Reed-Solomon Coding*, JPL Publication 77-23, Jet Propulsion Laboratory, Pasadena, Calif., July 15, 1977.

Wong, S. K., and Reinbold, S. J., "Earth-Moon Mass Ratio From Mariner 9 Radio Tracking Data," *Nature*, Vol. 241, No. 5385, pp. 111-112, Jan. 12, 1973.

Woo, R., and Ishimaru, A., "Remote Sensing of the Turbulence Characteristics of a Planetary Atmosphere by Radio Occultation of a Space Probe," *Radio Sci.*, Vol. 8, No. 2, pp. 103-108, Feb. 1973.

Woo, R. et al., *Effects of Turbulence in the Atmosphere of Venus on Pioneer Venus Radio–Phase I*, Technical Memorandum 33-644, Jet Propulsion Laboratory, Pasadena, Calif., June 30, 1973.

Woo, R., "Measurements of the Solar Wind Using Spacecraft Radio Scattering Observations," in *Study of Traveling Inter-Planetary Phenomena*, pp. 81-100, D. Reidel Publishing Co., Dordrecht, Holland/Boston, 1977.

Woo, R., "Radial Dependence of Solar Wind Properties Deduced from Helios 1/2 and Pioneer 10/11 Radio Scattering Observations," *Astrophys. J.*, Vol. 219, No. 2, Part 1, pp. 727-739, Jan. 15, 1978.

Woo, R. T., "Observations of Turbulence in the Atmosphere of Venus Using Mariner 10 Radio Occultation Measurements," *J. Atmos. Sci.*, Vol. 32, No. 6, pp. 1084-1090, June 1975.

Yuen, J. H., "A Double-Loop Tracking System," *IEEE Trans. Commun.*, Vol. COM-20, No. 6, pp. 1142-1150, Dec. 1972.

Yuen, J. H., *A Practical Statistical Model for Telecommunications Performance Uncertainty*, Technical Memorandum 33-732, Jet Propulsion Laboratory, Pasadena, Calif., June 15, 1975.

NASA - JPL - Comm. L.A. Calif.